Detailed modeling and simulations of Nanosecond Repetitively Pulsed Discharges for Plasma-Assisted Combustion

Nicolas Barleon

THÈSE

En vue de l'obtention du

DOCTORAT DE L'UNIVERSITÉ DE TOULOUSE

Délivré par :

Institut National Polytechnique de Toulouse (Toulouse INP)

Discipline ou spécialité :

Dynamique des fluides

Présentée et soutenue par :

M. NICOLAS BARLEON

le mardi 24 mai 2022

Titre :

Detailed modeling and simulations of Nanosecond Repetitively Pulsed Discharges for Plasma-Assisted Combustion

---

Ecole doctorale :

Mécanique, Energétique, Génie civil, Procédés (MEGeP)

Unité de recherche :

Centre Européen de Recherche et Formation Avancées en Calcul Scientifique (CERFACS)

Directeurs de Thèse :

MME BÉNÉDICTE CUENOT

M. OLIVIER VERMOREL

Rapporteurs :

M. ARNAUD BULTEL, CORIA

MME DEANNA LACOSTE, KING ABDULLAH UNIVERSITY OF SC&TECH

Membres du jury :

M. BENOÎT FIORINA, CENTRALESUPELEC GIF SUR YVETTE, Président

M. FABIEN THOLIN, ONERA, Membre

MME ANNE BOURDON, CNRS PARIS, Membre

MME BÉNÉDICTE CUENOT, CERFACS, Membre

M. OLIVIER VERMOREL, CERFACS, Invité

Résumé

Dans le domaine de la propulsion aéronautique, une tendance actuelle forte est la combustion en régime pauvre, voire très pauvre, afin de limiter les émissions de polluants. Il s'agit cependant d'un défi technologique de taille, puisque la combustion pauvre est peu stable et ne garantit pas les capacités d'allumage et de rallumage en altitude nécessaires à la certification.

Une solution émergente, applicable à une large gamme de configurations, pour permettre l'allumage et la stabilisation de la combustion dans des régimes pauvres, est l'utilisation de décharges électriques de faible énergie près de la flamme. Parmi les différents types de décharge existants, les décharges nanosecondes répétitives pulsées (NRP) sont particulièrement intéressantes. Cependant, malgré une efficacité démontrée, les mécanismes fondamentaux de l'interaction entre la combustion et le plasma généré par la décharge ne sont pas bien compris. De plus, il n'existe pas d'outil numérique opérationnel pour évaluer la performance des décharges NRP dans des configurations pratiques.

L'objectif de cette thèse, réalisée dans le cadre du projet ANR PASTEC, est double. Il s'agit d'abord de développer un code de plasmas froids capable de modéliser la phase plasma. Cette tâche a vu naitre le code parallèle et non-structuré AVIP qui partage la structure de données du code de combustion AVBP développé au CERFACS. Cette modélisation permettra ensuite d'étudier en détail les mécanismes d'interactions entre la le plasma et une flamme dans des configurations pointe-pointe. Pour cela, une chimie détaillée pour la combustion assistée par plasma a été développée et validée avec des données expérimentales dans des configurations de laboratoire. Cette chimie étant trop couteuse pour un calcul multi-dimensionnel, un travail de réduction a été réalisé et un modèle phénoménologique a été proposé. Le mécanisme cinétique réduit est finalement utilisé dans des simulations multi-dimensionnelles couplant les codes AVBP et AVIP afin d'étudier les effets des décharges NRP dans l'air et pour l'allumage d'un mélange methane-air.

Abstract

In the field of aeronautical propulsion, the current trend is to us lean or even very lean combustion regimes, in order to limit pollutant emissions. However, this is a major technological challenge, since lean combustion is prone to instabilities and does not guarantee the ignition and re-ignition capabilities at altitude required for certification.

An emerging solution, applicable to a wide range of configurations, to enable ignition and combustion stabilization in lean regimes is the use of low-energy electrical discharges near the flame. Among the different types of discharges available, the Nanosecond Repetitively Pulsed (NRP) discharges are particularly interesting. However, despite their proven effectiveness, the fundamental mechanisms of the interaction between the combustion and the plasma generated by the discharge are not well understood. Moreover, there is no operational numerical tool to evaluate the performance of NRP discharges in practical configurations.

The objective of this thesis is twofold. The first one is to develop a low-temperature plasma code able to model the plasma phase. This task is done in the parallel and unstructured code AVIP which shares the data structure of the combustion code AVBP developed at CERFACS. In a second step, this modeling will allow to study in detail the mechanisms of interactions between the plasma and a flame in point-to-point configurations. For this purpose, a detailed chemistry for plasma assisted combustion has been first developed and validated against experimental data in laboratory configurations. The detailed chemistry being too expensive for multi-dimensional simulations, a reduction step has been performed and a phenomenological model has been proposed. The reduced kinetic mechanism is finally used in a multi-dimensional calculation, by coupling AVBP and AVIP codes, to study the effects of NRP discharges in air and for the ignition of a methane-air mixture.

Acknowledgements

Je tiens tout d'abord à remercier ma directrice Bénédicte Cuénot et mon co-directeur Olivier Vermorel de m'avoir fait confiance durant ces trois années pour explorer différents aspects de la physique de la combustion assistée par plasma. Je les remercie pour la liberté que j'ai pu avoir pour creuser dans mes idées, tout en me guidant lorsque celles-ci divergeaient trop de l'objectif initial. J'ai également beaucoup apprécié l'ambiance de travail à leur côté grâce à leur bonne humeur au quotidien. Bien que cette physique soit nouvelle pour le laboratoire, mes travaux se sont réalisés dans de bonnes conditions grâce aux nombreux parallèles possible entre les activités traditionnelles du CERFACS et mes travaux de thèse, que ce soit d'un point de vue physique ou bien numérique. Je les remercie également pour tous les conseils qu'ils ont pu me donner ainsi que pour les relectures approfondies des papiers et du manuscrit.

Je remercie également Anne Bourdon d'apporter au CERFACS ses connaissances sur les plasmas froids, que ce soit pour l'équipe PAC ou celle Hall. Ton aide nous est très précieuse et je pense pouvoir dire que toute l'équipe plasma du CERFACS te remercie. Tu as su nous remettre sur la bonne voie, et nous rappeler notre objectif final, quand nous étions bloqués sur nos streamer de quelques nanosecondes, ou bien sur la vibration de N2 qui aurait encore pu nous prendre très longtemps !

Je remercie ensuite l'ensemble des membres de mon jury, pour la relecture du manuscrit et les nombreuses questions qui ont pu être posées lors de la soutenance.

Merci à Deanna Lacoste pour les échanges que nous avons pu avoir, permettant ainsi de confronter les visions expérimentale et numérique. J'espère que ces échanges entre numériciens et expérimentateurs pourront continuer afin d'aller vers des modèles plus prédictifs.

Un grand merci ensuite à tous les doctorants du CERFACS. Ces trois années de thèse n'auraient pas été les mêmes sans vous. En particulier notre petite team plasma avec Lionel, Guillaume et Willca. Merci Lionel pour ces presque 4 ans d'échanges, ce fut un réel plaisir de travailler à tes côtés. Je n'aurai pas pu aller creuser aussi loin sur certains points sans ton talent et ta soif d'apprendre. Malgré les avis parfois divergent, nous avons su nous coordonner durant toutes ces années pour avancer vers nos objectifs et créer de beaux outils au sein du CERFACS qui je l'espère pourront perdurer ! Merci à Guillaume pour la bonne humeur qu'il apporte dans l'équipe et surtout d'avoir accepté de suivre les cours de Professeur Cheng sur le Toro ... j'étais tranquille moi en attendant :p (Rassure toi j'ai aussi passé de durs moments devant le tableau !). Le CERFACS ce n'est pas que du plasma, donc merci aux autres doctorants avec qui j'ai passé de bons moments : Antoine pour qui un magret à eurest peut éliminer tous les problèmes du jour, Jonathan un soutien du Grand Est qui sait que l'Alsace c'est en France ! Clovis qui je l'espère m'expliquera bientôt durant sa soutenance ce que c'est la chorochronie,

Benjamin qui a réussi l'exploit de la promo de finir sa thèse à l'heure ... mais encore beaucoup d'autres Victor, Etienne, Adrien, Théo, les 4 Thomas, Antony, Aurélien ... .

Merci à l'équipe CSG pour le support informatique au CERFACS qui permet un fonctionnement optimal de nos travaux. Merci également à toute l'équipe administrative pour toute l'organisation que nous ne voyons pas en tant que thésard, sans oublier de citer Chantale !

Merci également à tous les copains toulousains, Alex, Enora, Charles, Marie, Antoine, Marine, Sophie, Pierre, Pauline, Aymeric, Théo, Thomas, Nico, Mathias, Mano, Juliette, Adri, Cathy, Hugo ... une thèse c'est long et c'est cool d'avoir des gens sur qui compter pour se changer les idées ! Beaucoup de thésards dans cette liste, courage vous êtes bientôt au bout !

Merci à toute ma famille qui me soutient depuis toujours. Vous avez vu me donner toutes les clés nécessaires à ma réussite. Je ne vous dirai jamais assez à quel point je vous suis reconnaissant ! Je laisse la place à mon frère pour devenir le deuxième docteur de la famille, pour soigner les gens cette fois-ci ;) Bon courage pour tes études je n'ai pas de doute pour ta réussite ;)

Enfin, la thèse est une aventure que l'on vit à deux. Merci à Kim de partager ma vie depuis maintenant plus de 5 ans. Que ce soit dans les moments de joies ou de doutes, tu as toujours été à mes côtés pour m'épauler. Je te remercie d'avoir été compréhensive sur les horaires parfois très étendues, et même des week-ends inexistants sur la fin. De beaux projets sont maintenant devant nous et j'espère pouvoir en entreprendre de nombreux à tes côtés.

Contents

List of symbols

Bold symbols are vectors. Their components and other scalar quantities are in italic.

Symbol	Description	Unit
Roman letters		
$\bar{W}$	Mean molecular weight of the mixture	$\mathrm{kg\,mol^{-1}}$
c_p	Mass heat capacity at constant pressure	$\mathrm{J\,K^{-1}\,kg^{-1}}$
c_v	Mass heat capacity at constant volume	$\mathrm{J\,K^{-1}\,kg^{-1}}$
D_{jk}	Binary mass diffusion coefficient of the species j into the species k	$\mathrm{m^2\,s^{-1}}$
D_k	Effective mass diffusion coefficient of the species k in the rest of the mixture	$\mathrm{m^2\,s^{-1}}$
$\dot{Q}$	External power source term	$\mathrm{J\,m^{-3}\,s^{-1}}$
$\mathbf{dS}$	Orthogonal and infinitesimal surface vector	$\mathrm{m^2}$
$\mathbf{E}$	Electric field vector	$\mathrm{V\,m^{-1}}$
E_{chem}	Discharge chemical energy	J
e_{chem}	Discharge chemical energy density	$\mathrm{J\,m^{-3}}$
E_{exc}	Discharge electronic excitation energy	J
e_{exc}	Discharge electronic excitation energy density	$\mathrm{J\,m^{-3}}$
E_{heat}	Discharge heating energy	J
e_{heat}	Discharge heating energy density	$\mathrm{J\,m^{-3}}$
E_{p}	Total plasma discharge energy	J
e_{p}	Total plasma discharge energy density	$\mathrm{J\,m^{-3}}$
E_{vib}	Discharge vibrational energy	J
e_{vib}	Mean non-equilibrium vibrational energy density	$\mathrm{J\,m^{-3}}$
e^k_{vib}	Mean non-equilibrium vibrational energy density of species k	$\mathrm{J\,m^{-3}}$
F_0	Electron energy distribution function	[-]
f_e	Electron distribution function	[-]
h_k	Molar enthalpy of species k	$\mathrm{J\,mol^{-1}}$
m_e	Electron mass	kg
N_0	Gas number density	$\mathrm{m^3}$
N_{cell}	Number of cells	[-]
n_k	Number density of the species k	$\mathrm{m^3}$
N_{nodes}	Number of nodes	[-]
n^f_v	Number of vertices per cell face	[-]
$\mathbf{q}$	Heat flux vector	$\mathrm{W\,m^{-2}}$
$\mathcal{Q}_j$	Net molar production rate of reaction j	$\mathrm{mol\,m^{-3}\,s^{-1}}$

Symbol	Description	Unit
q_k	Charge number of species k: +1 for positive ions, -1 for negative ions and electron and 0 for neutrals	[-]
r_{AB}	Interaction coefficient between A and B	[-]
$\dot{R}_{VT}$	Vibrational to translational relaxation source term of the vibrational energy	$\mathrm{J\,kg^{-1}\,s^{-1}}$
$\mathbf{S}_f$	Normal surface vector at face f	$\mathrm{m^2}$
$\mathbf{S}_{jk}$	Normal surface vector between node j and k	$\mathrm{m^2}$
T	Gas temperature	K
t	Time	s
Td	Units for reduced electric field	$1 \times 10^{-17}\,\mathrm{V\,cm^2}$
$\mathbf{u}$	Gaseous velocity vector	$\mathrm{m\,s^{-1}}$
u_k	Molar internal energy of species k	$\mathrm{J\,mol^{-1}}$
$\mathbf{v}$	Velocity vector	$\mathrm{m \cdot s^{-1}}$
V_c, V_τ	Cell volume	$\mathrm{m^3}$
V_N	Nodal volume	$\mathrm{m^3}$
W_k	Molecular weight of species k	$\mathrm{kg\,mol^{-1}}$
$\mathbf{x}$	Position vector	m
X_k	Molar fraction of species k	[-]
Y_k	Mass fraction of species k	[-]
Greek letters		
$\Delta\epsilon_k$	Threshold energy of the electron impact process k	eV
Δh_j	Enthalpy change of the reaction j	$\mathrm{J\,mol^{-1}}$
Δt	Time step	s
Δu_j	Internal energy change of the reaction j	$\mathrm{J\,mol^{-1}}$
Δx	Space step	m
$\dot{\omega}_k$	Molar production rate of species k	$\mathrm{mol\,m^{-3}\,s^{-1}}$
$\dot{\omega}_T$	Heat release rate	$\mathrm{J\,m^{-3}\,s^{-1}}$
λ	Thermal conductivity	$\mathrm{W\,m^{-1}\,K^{-1}}$
μ	Mobility	$\mathrm{m^2 \cdot V^{-1} \cdot s^{-1}}$
ν_{kj}	Stoichiometric coefficient of the species k in the reaction j $(\nu''_{kj} - \nu'_{kj})$	[-]
ν'_{kj}	Reactant stoichiometric coefficient of the species k in the reaction j	[-]
ν''_{kj}	Product stoichiometric coefficient of the species k in the reaction j	[-]
ω_k	Molar production of species k	$\mathrm{mol\,m^{-3}}$
ρ	Mass density	$\mathrm{kg\,m^{-3}}$
ρ_c	Space charge	$\mathrm{m^{-3}}$
ρ_k	Mass density of species k	$\mathrm{kg\,m^{-3}}$
σ_k	Cross-section associated to the process k	$\mathrm{m^2}$
$\boldsymbol{\tau}$	Viscous stress tensor	$\mathrm{J\,m^{-3}}$

List of acronyms

1D	One-dimensional
2D	Two-dimensional
3D	Three-dimensional
AE	Advanced Economies
AMR	Adaptive Mesh Refinement
ANR	Agence National de la Recherche
APS	Announced Pledges Scenario: which assumes that all climate commitments made by governments around the world will be met in full and on time.
ARCANE	Analytical Reduction of Chemistry : Automatic, Nice and Efficient
AVBP	A Very Big Project
AVIP	A Very Ionized Project
BOLOS	BOLtzmann equation solver Open Source library
BOLSIG+	BOLtzmann equation Solver for electrons in weakly Ionized Gases
CERFACS	Centre Européen de Recherche et de Formation Avancée en Calcul Scientifique. Laboratory, specialized in high performance computing and reactive flows in Toulouse
DBD	Dielectric Barrier Discharge
DIC	Direct Interaction Coefficient
DRGEP	Directed Relation Graph with Error Propagation
EEDF	Electron Energy Distribution Function
EMDE	Emerging Market and Developing Economies
FGH	Fast Gas Heating
FOU	First Order Upwind
FWMH	Full Width at Half Maximum
HC	HydroCarbons
HPC	High Performance Computing
HRR	Heat Release of Reaction
ICE	Internal Combustion Engine
IEA	Internal Energy Agency
IPCC	Intergovernmental Panel on Climate Change
ISG	Improved Scharfetter-Gummel
LBO	Lean Blow-Out
LDI	Lean Direct Injection
LFA	Local Field Approximation

LIF	Laser Induced Fluorescence (for spectroscopy)
LLW	Limited Lax-Wendroff
LO	Lift-Off
LPP	Lean Partially-Premixed
LW	Lax-Wendroff
MILD	Moderate or Intense Low-oxygen Dilution
NRP	Nanosecond Repetitively Pulsed
NRPD	Nanosecond Repetitively Pulsed Discharge
NRPDs	Nanosecond Repetitively Pulsed Discharges
NZE	Net Zero Emissions by 2050 Scenario
PAC	Plasma-Assisted Combustion
PAI	Plasma-Assisted Ignition
PIC	Particle-In-cell
QSST	Quasi Steady-State Assumption
RQL	Rich-burn - Quick-mix - Lean-burn
SG	Scharfetter-Gummel
SGH	Slow Gas Heating
STEPS	Stated Policies Scenario: which reflects current policy settings based on a sector-by-sector assessment of the specific policies that are in place, as well as those that have been announced by governments around the world.
TALIF	Two-Photon Absorption Laser Induced Fluorescence
TOSU	The Ohio State University
WEO	World Energy Outlook

Chapter 1

General introduction

Contents

1.1 Combustion in the world

1.1.1 Energy consumption

Our everyday life is made possible thanks to the use of an incredible amount of energy which is around around 600×10^{18} J per year during the last decade [1]. This amount of energy represents the work of 700×10^9 humans during a year at a rate of about ten working hours per day. In 2021, more than 80% of this energy has been produced by the combustion of fossil fuels, including oil, natural gas and coal, as shown in Fig. 1.1. In the Stated Policies Scenario (STEPS), which considers the current government policies and those under development, the energy demand will continue to increase until 2050. The reduction of coal consumption will be replaced by natural gas, and the rapid growth of the renewable energies will only compensate for the global demand. The Announced Pledges Scenario (APS), that includes the new policy commitments (COP 26 for instance), predicts a 20% reduction of fossil fuel consumption during the next three decades. Carbon energy will still correspond to more than 50% of the energy consumption in 2050. Finally, in the Net Zero Emissions scenario (NZE), an impressive increase in renewable energy is accompanied by a drastic reduction of fossil fuels usage, representing less than 25% of the energy demand in 2050.

The global renewable energies market is estimated to USD 27 trillion between 2021 and 2050. Part of this renewable energy will still rely on combustion with low carbon fuels such as hydrogen or synthetic fuels produced by renewable energy. In the NZE scenario, carbon-free hydrogen (*i.e.* not produced from fossil fuels by steam reforming of natural gas as in the

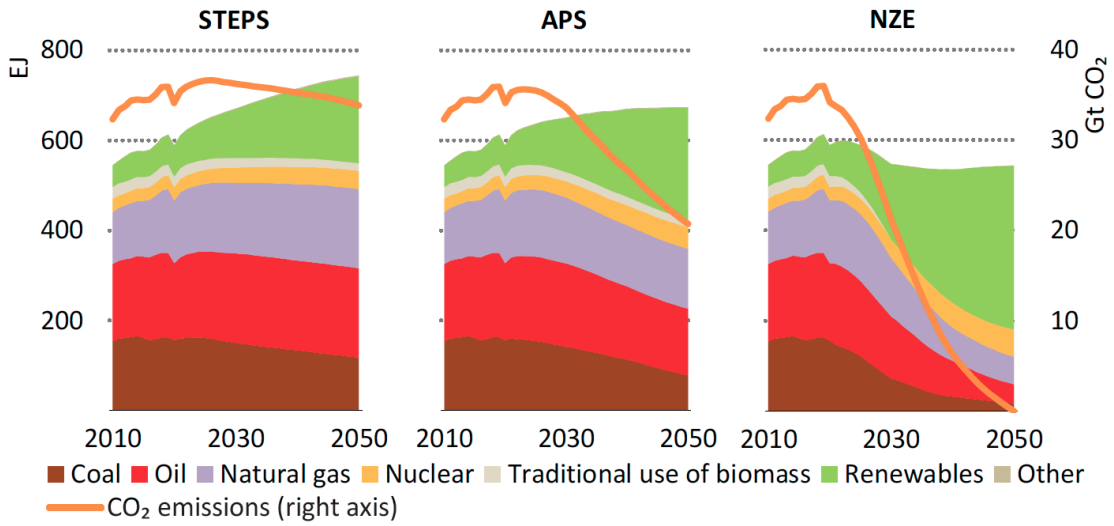

Figure 1.1: Annual world energy consumption history from 2010 to 2021 and different scenarios toward 2050 [Reproduced from the 2021 WEO of the IEA [1]]

current production) will represent 20 EJ in 2030 and 60 EJ in 2050 (10% of the global demand). These new fuels have found favor in important industries such as aeronautics [2]. CERFACS is already participating in the study of these new fuels within the SCIROCCO project [7] for hydrogen-based technologies, and the JETSCREEN [5] project for the use of synthetic fuels. According to the APS scenario, there is also a need for cleaner and more efficient combustion technologies for the remaining fossil energy that will still be important in 2050.

1.1.2 Pollution issues

There is no doubt now that human activities have affected the earth climate in a detrimental way to life on Earth. In its last report, the Intergovernmental Panel on Climate Change (IPCC) said:

> It is unequivocal that human influence has warmed the atmosphere, ocean and land. Widespread and rapid changes in the atmosphere, ocean, cryosphere and biosphere have occurred.

The greenhouse gas emissions from human activities are responsible for atmospheric forcing, resulting in a worldwide temperature rise. The recorded annually averaged surface temperature shown in Fig. 1.2 indicates a sharp increase in the last decades. In particular, the modeled temperature change, including human and natural atmospheric forcing, differs from the natural evolution since 1920. Moreover, the overlapping region between the two models' uncertainties disappears at the beginning of the current millennium.

In the recently adopted Paris Agreement [4], the goal is to limit the global temperature increase to well below 2 degrees Celsius during the 21th century. It is also highly encouraged to limit the increase to 1.5 degrees. Among all the greenhouse gases sources, carbon dioxide is the first contributor to global warming, followed by methane emissions. The different scenarios discussed in Section 1.1.1 were also evaluated in terms of surface temperature change in Fig. 1.3. Only the NZE scenario allows to limit the temperature rise below 2 °C at the end of the century. A significant part of the CO_2 emissions is due to the energy sector, which must radically change its bases and turn to decarbonized energies in the years to come.

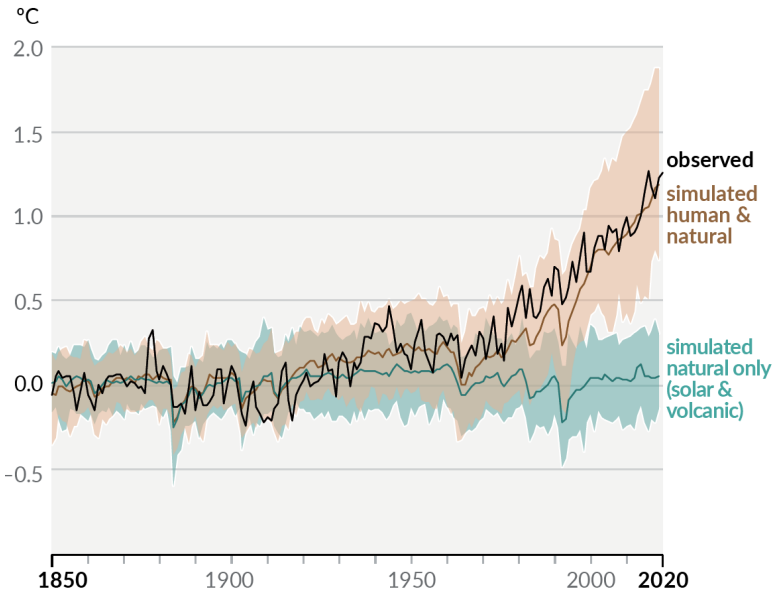

Figure 1.2: Change in global surface temperature (annual average) as observed and simulated using human & natural and only natural factors. SDS (Sustainable Development Scenario) is like the NZE scenario but with zero net emission in 2070. [Reproduced from the Sixth Assessment Report of the IPCC [4]]

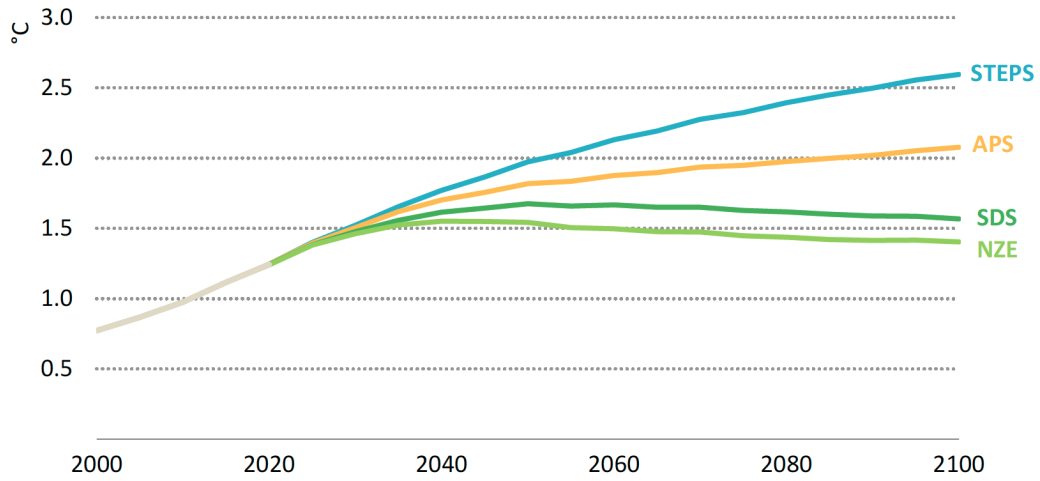

Figure 1.3: Global median surface temperature rise over time in the WEO-2021 scenarios [Reproduced from the 2021 WEO of the IEA [1]]

The fossil fuel combustion does not only results in carbon dioxide emissions. It is accompanied by other combustion products such as carbon oxide CO, unburnt hydrocarbons (HC), nitric oxides NOx, sulfur oxides SOx and soot particles that all contribute to global warming or human health deterioration. More than 90% of the population breathes polluted air, responsible for the premature death of 5 million people per year. The most dangerous particles for human health are those with a diameter of less than 2.5 µm denoted $PM_{2.5}$ because they are qualified as breathable. Figure 1.4 evaluates the part of the population exposed to different densities of $PM_{2.5}$ particles following different scenarios along with the number of premature deaths per year. Both the STEPS and APS scenarios lead to similar results in terms of air pollution, and only the NZE one could significantly reduce the health damages. These observations differ

significantly from those made on temperature rise, where the APS scenario is much preferable to the STEPS scenario. The consequences of pollution are also very unfair from a social point of view since Emerging Market and Developing Economies (EMDE) are much more affected than Advanced Economies (AE). The number of premature deaths due to air pollution could be reduced by 20% (and up to 50% in advanced economies) in the NZE scenario compared to the two others. In addition to greenhouse gas emissions reduction, the new combustion devices must also reduce their emissions of pollutants harmful to human health.

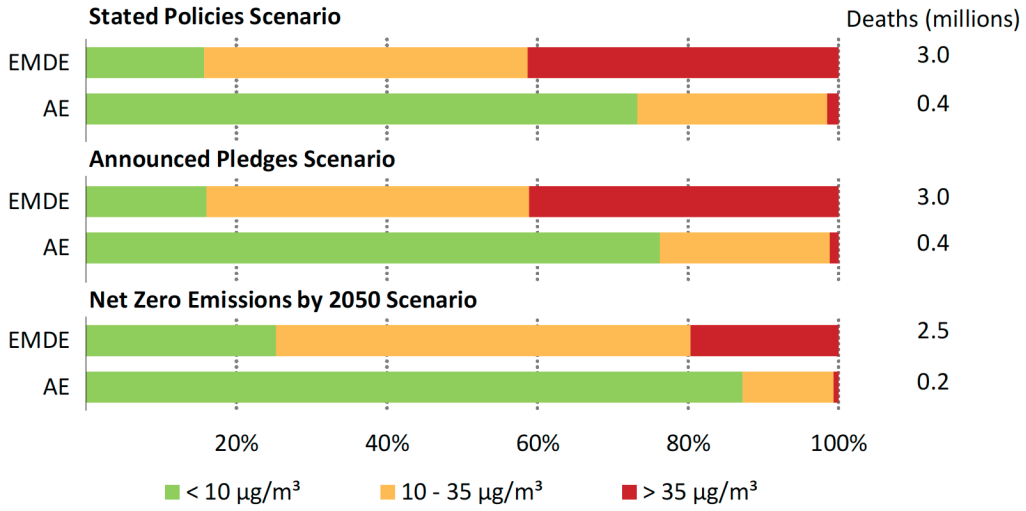

Figure 1.4: Share of population exposed to various $PM_{2.5}$ concentrations and premature deaths from ambient air pollution in 2030 [Reproduced from the 2021 WEO of the IEA [1]]

1.2 Lean combustion regime

Several solutions have been proposed for combustion devices to reduce pollutant emissions and to increase the engine efficiency. Most of them are based on lean premixed or partially premixed combustion regimes. Such regimes produce a lower flame temperature that considerably limits pollutant production. Figure 1.5 shows qualitatively the variation of different pollutants in the exgaust gases of a conventional internal combustion engine using spark-ignition. NO emissions are drastically reduced in the lean regime. In lean premixed flames, most of the NO production is due to the formation of N_2O intermediate, and the thermal NO production following the Zeldovich's mechanism is negligible ($\leq 1\%$) [53]. In a lean regime, complete combustion generally occurs, thus reducing HC and CO emissions. However, the reduction of HC emissions is limited, and they start to grow significantly at low equivalence ratios. The combustion quality becomes poor at such a low fuel/air ratio, and eventually, misfires may occur. It is also preferable to use a homogeneous mixture to limit the possible appearance of rich combustion zones. Figure 1.5 shows the complexity of developing a lean engine in which the reduction of pollutants is associated with uncomplete combustion. The application of these new technologies using lean mixtures to practical systems is still limited by the ability to control ignition and stabilize the flame over a wide range of operating conditions. The difficulty of igniting a lean mixture is explained by the increase in chemical time τ_{chem} as the equivalence ratio decreases. The chemical timescale increase also explains why flame blow-off occurs in lean mixtures. The Damköhler number ($D_a = \tau_{\text{flow}}/\tau_{\text{chem}}$) is often used in design tools to avoid such static instability [57]. It

is generally observed that below a critical Damköhler number, flame blow-off starts to occur. Dynamic instabilities are also a huge topic for gas turbines. These dynamic oscillations may occur when the heat release and pressure field perturbations couple together in a resonant manner. These phenomena refer to as Combustion Instabilities or thermoacoustic instabilities. When the heat release perturbation is in phase with an acoustic wave, the resulting instability can be devastating as shown in Fig. 1.6.

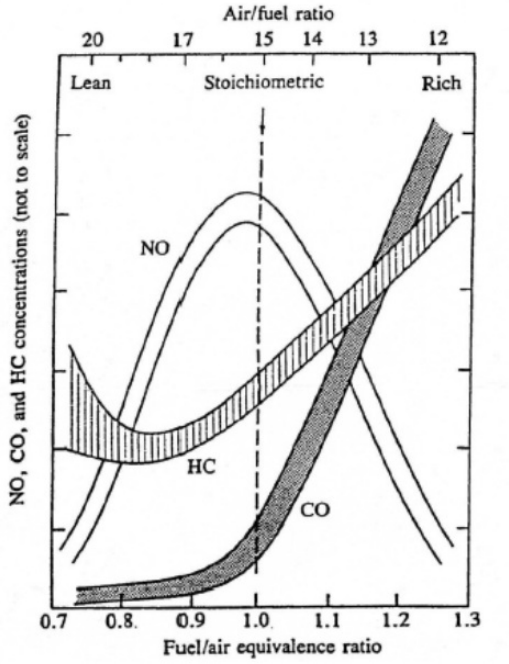

Figure 1.5: Variation of unburnt hydrocarbons (HC), carbone oxide (CO) and nitric oxide (NO) in the exhaust of a conventional spark-ignition engine with fuel/air equivalence ratio [Reproduced from [79]]

Figure 1.6: Burner assembly damaged by combustion instability (left) and new burner assembly (right) [67]

Several concepts relying on lean-burn gas turbines have been developed for ground power generation and aviation in the past two decades. A promising technique makes use of Moderate

or Intense Low-oxygen Dilution (MILD) or flameless combustion regimes [89, 36] in which the mixture reacts in a large zone at relatively low burnt gas temperature and lean conditions. This combustion regime is characterized by a high reactant temperature and low-temperature increase during the process. The reaction zone is much wider than in a conventional flame structure leading to a colorless flame, as shown in Fig. 1.7. The use of MILD regimes allows to produce a large homogeneous temperature distribution that is of great interest in industrial furnaces. Thanks to the lean regime, CO and NOx emissions can be significantly reduced.

(a) (b)

Figure 1.7: Combustion furnace operating on natural gas with a 10 kW heat input for (a) conventional combustion and (b) MILD combustion [Reproduced from [50]]

A conventional RQL (Rich-burn,Quick-mix,Lean-burn) combustion chamber is shown in Fig. 1.8a. It is based on a primary zone, in red, operating in rich conditions with usually $\phi \in [1.2 - 1.6]$. In that case, the NOx formation rates are low due to the low temperature and low oxygen concentration as presented in Fig. 1.8b. Notice that a higher equivalence ratio could reduce even more the NOx emissions but with a drastic increase of soot formation. Moreover, a proper design of the flow pattern in the primary zone must be done to avoid the formation of recirculation zones which would lead to an increase of the residence time, thus leading to NOx production [128]. In addition to the NOx reduction, rich-mixture allows to stabilize the combustion reactions by producing a substantial amount of radial species. However, a high concentration of CO and HC remains in the exit of the primary zone, and oxygen must be added to the mixture to oxidize them. A slow and gradual air injection would lead to an important NOx production following the high NOx route presented in Fig. 1.8b. Thus, the mixture in the blue zone in Fig. 1.8a must be performed as fast as possible (Quick-Mix) to follow the low NOx route presented in Fig. 1.8b. The equivalence ratio in the green zone must be determined to satisfy the emissions requirements as it influences the burnt gases temperature, and usually ranges from 0.5 to 0.7. The high temperature would lead to the formation of thermal NOx, whereas low temperature would not lead to a proper consumption of the remaining CO and HC.

One way to increase the engine core efficiency is to increase the Overall Pressure Ratio. This

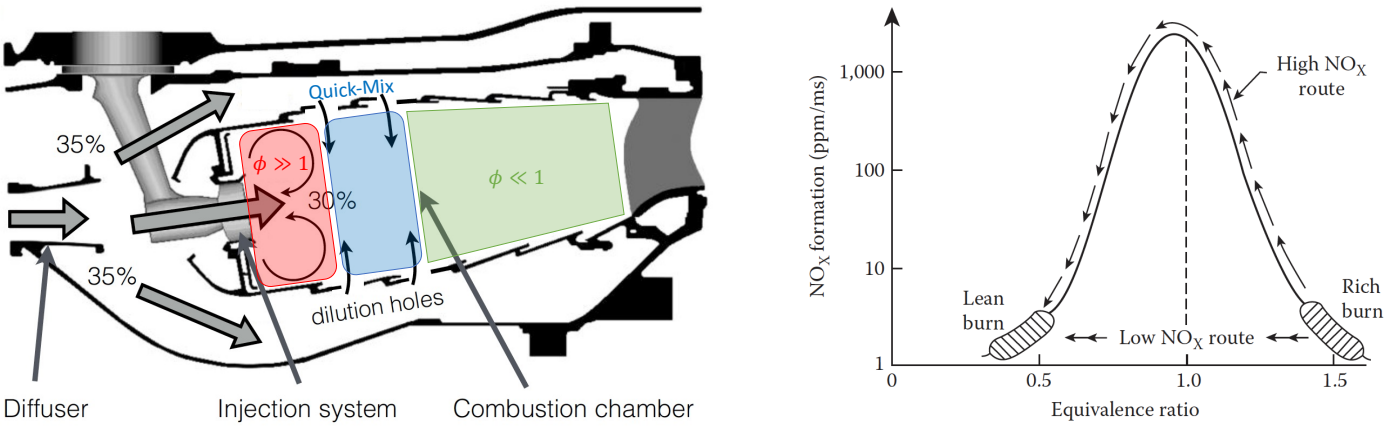

Figure 1.8: Description of a RQL (Rich-Burn | Quick-Mix | Lean-Burn) combustor: (a) sketch adapted from [61] and (b) NOx production routes [107]

has been done in RQL combustors, but it is accompanied by an increase of NOx emissions. Indeed, higher fresh gas pressure leads to higher maximum temperature and consequently higher NOx concentration. Thus, the new combustion chambers that have been designed in the past years mostly rely on lean mixtures such as in the LDI (Lean Direct Injection) and LPP (Lean Premixed Prevaporized) concepts. A lean mixture can be obtained by increasing the amount of fresh gas passing through the injection system, as shown in Fig. 1.9. The NOx production strongly depends on the flow residence time in the combustion chamber, which needs to be shortened. Consequently, hot gas pockets can reach the high-pressure turbines due to temperature heterogeneities, and an efficient cooling system must be designed to avoid damages. Finally, lean premixed combustion in gas turbines is associated with challenges including ignition, flame stabilization, thermoacoustic instabilities, flashback and auto-ignition avoidance.

1.3 Plasma-assisted combustion

As discussed in the previous section, lean homogeneous combustion is prone to misfiring or flame instabilities. Thus, new technologies to control combustion are required. For example, a conventional Spark-Ignition device can fail to ignite a lean mixture in ICE [161]. For gas turbines, the ignition success mainly depends on the flow field, mixture composition and gas temperature [18, 107]. For both applications (*i.e.*, ICE and gas turbine), new ignition devices or concepts are required to tackle the constraints of the novel low-emission burners currently developed. For example in [121], pre-chamber concept in ICE has been used to create multiple hot turbulent jets and provide ignition sites for the lean mixture. Moreover, thermo-acoustic instabilities are a major concern and must be avoided or mitigated. In a recent review made by Ju and Sun [88], non-equilibrium plasma discharges have shown promising capabilities to improve existing combustion systems at a low energy cost. For example in [127], the pre-chamber concept in ICE has been combined with non-equilibrium discharges and compared with a conventional spark plug, showing that faster ignition can be achieved with low-temperature plasma discharges. The last two decades have seen increasing attention in plasma-assisted

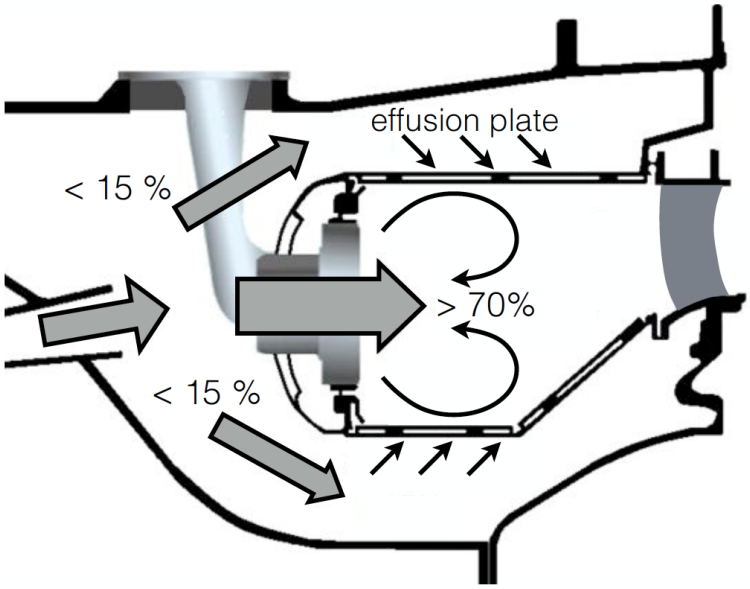

Figure 1.9: Sketch of a low-NOx burner [Reproduced from [61]]

combustion, thus motivating this work.

A wide variety of plasma can be produced depending on the physical conditions and the experimental setup considered (electrode geometry, applied voltage, frequency, gas flow, ...). A large range of electron temperature and number density can be obtained as shown in Fig. 1.10. A simple candle can generate a low-temperature and low-density plasma without any electrical source. Indeed, a flame can produce a small amount of charged species that can be used to influence the flame shape or position with an external electric field [164]. The spark discharges are widely used to ignite a reactive mixture using spark-plug devices. In sparks, the gas is almost fully ionized with a common gas and electron temperature, *i.e.*, the discharge is in thermal equilibrium with the gas. In such equilibrium discharge, a significant part of the discharge energy can be lost into an acoustic wave, radiation, convection and conduction through the electrodes. These energy losses have been analyzed by Phuoc and White [149] in the case of laser-induced spark ignition. They have found that 57 to 70% and 22 to 34% are respectively lost in a shock wave and by radiation. The energy of the remaining hot gas, available for the mixture to ignite, was about 7 to 8% of the spark total energy. Thermal discharges in pin to pin configuration have also been used in [122] to ignition a methane-air mixture. They found that no more than 50% of the discharge energy remains available for the mixture to ignite. They have estimated the energy lost by conduction phenomena through the electrodes between 45 and 70% of the total discharge energy. Thus, the current trend is to investigate non-equilibrium discharge such as corona, radio-frequency, microwave, Dielectric Barrier Discharge (DBD), gliding arc and Nanosecond Repetitively Pulsed NRP discharges. However, determining which kind of plasma is the best option for combustion enhancement in a given environment remains unclear.

The chemistry of plasma-combustion interaction using such discharges is not fully understood yet. The plasma effects on combustion can be divided into three major enhancement channels as detailed in Fig. 1.11: thermal, kinetic and transport. These effects are largely conditioned by the reduced electric field E/N, which is the ratio of the electric field E over the

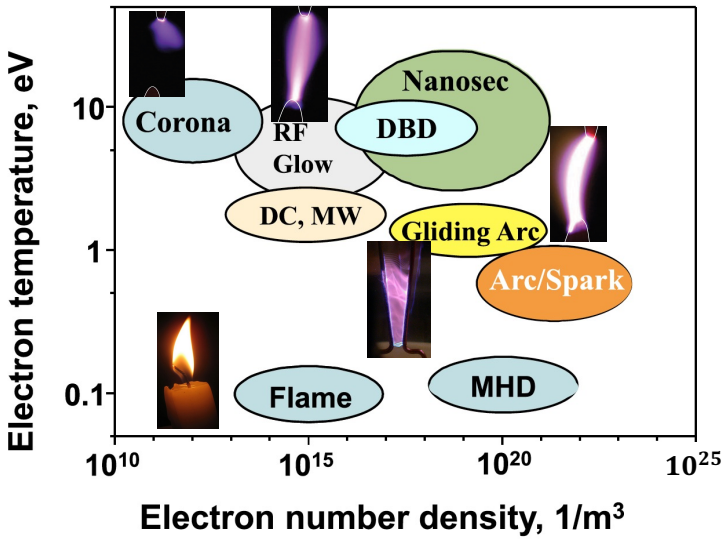

Figure 1.10: Schematic of electron temperature and number density for different discharges, Corona, direct current (DC) discharge, microwave (MW) discharge, dielectric barrier discharge (DBD), radio-frequency discharge (RF), glow discharge, gliding arc, nanosecond repetitively pulsed discharge (NRP), arc, magneto-hydrodynamic discharge (MHD), and flame. [Adapted from [88]]

gas density N, which controls the transfer of energy from the electrons to the gas. The thermal effect results from elastic and inelastic electron collisions on heavy molecules. During the inelastic collisions, part of the electron energy is transferred to the internal energy of the heavy molecules, which become excited rotationally, vibrationally, electronically or ionized. These energetic molecules will further relax their energy into heat and also lead to kinetic effects. The relaxation of electronic states and ionized molecules is responsible for ultra-fast gas heating while vibrational energy is slowly converted to heat through Vibration-Translational (VT) relaxation. For combustion applications, the kinetic effect of plasma discharge is mainly due to the production of active radicals such as O, OH and H, either in the electron impact dissociation process or during the quenching of excited molecules [8]. Vibrational energy can help to reduce the energy barrier of reaction according to the Fridmann-Macheret model [62]. Electronically excited oxygen atoms and molecules can also help to accelerate fuel oxidation. Moreover, long-life species such as O_3 and NO are produced, allowing to accelerate the low-temperature fuel oxidation. The temperature increase directly impacts the kinetics with an increase of chemical reaction rates, which mostly follow an Arrhenius law. The kinetic effects lead to the production of lighter species that can diffuse faster so that the mixture Lewis number decreases. According to [41], this lower Lewis number reduces the critical flame radius necessary for proper ignition. Finally, plasma discharge can be used to modify the flow pattern thanks to the ionic wind which is an induced flow due to heavy charged species collision with neutral molecules. Despite the knowledge of these different effects, it is still difficult to understand them individually because of the strong coupling between them. In this work, a focus is made on the thermal and kinetic effects of NRP discharges that are described in more detail in Chapter 3.

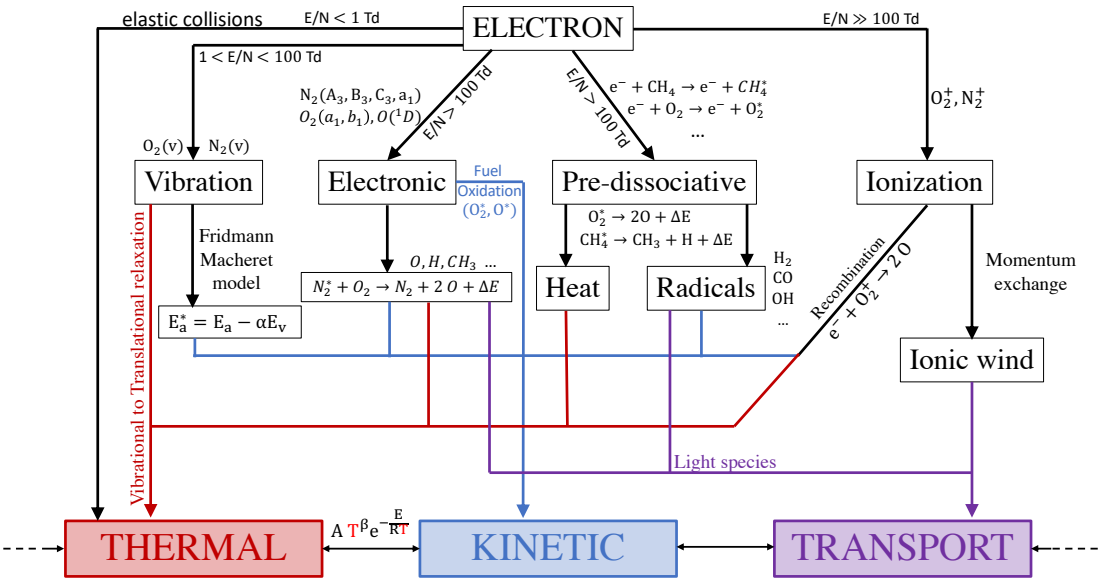

Figure 1.11: Major enhancement pathways of plasma-assisted combustion [Adapted from [88]]

1.4 Overview of plasma-assisted combustion studies

Numerous studies on plasma-assisted combustion have been performed in the past two decades, both experimentally and numerically. Non-exhaustive lists of these studies are given in Tabs. 1.1 and 1.2. They cover a wide range of applications, including ignition, flame stabilization and kinetic effects. Single-pulse ignition was studied by Starikovskaia et al. [178] using a shock tube technique combined with a glow discharge. Thanks to a numerical comparison made by Aleksandrov et al. [11], the efficient chemical effect of the discharge was found to be able to ignite the mixture much faster than the auto-ignition time. The effects of discharge frequency on ignition have been extensively studied in Lefkowitz and Ombrello [108], Lefkowitz et al. [109], who identified different inter-discharge coupling regimes shown in Fig. 1.12a. In Lacoste et al. [103], NRP discharges have been applied in natural gas mixed with air resulting in an increase of the NOx production. The NOx production has been explained by the high degree of oxygen molecule dissociation in such a configuration that promotes NO formation. This effect has also been observed in Kim et al. [90] where the low-temperature plasma can drastically reduce CO emissions while slightly increasing NOx emissions close to the Lean Blow-Off (LBO) limit. As discussed previously, the reduction of NOx emissions in a combustion engine is a significant concern. Thus, the NOx production promoted by plasma discharges when using hydrocarbon fuels (CxHy) must be well understood in order to minimize this drawback. Interestingly, plasma discharge was found to drastically reduce the NOx emission in ammonia combustion (Choe and Sun [45]) as well as increasing the flame speed (Shioyoke et al. [174]). Plasma discharges are also efficient to mitigate flame instabilities, as shown in Fig. 1.12b. Several studies have investigated the plasma effect on LBO limit (Kim and Cohen [91], Kim et al. [90], Zare et al. [201]). An important extension of this limit has been observed with only a small electrical power of the order of 1% of the thermal flame power. Plasma discharges can also help to anchor a lifted flame by reducing the Lift-Off (LO) distance thanks to a combination of thermal and kinetic effects (Shcherbanev et al. [173]) as shown in Fig. 1.12c. Flame stabilization in a burner

representative of an aeronautical combustor has been studied by Barbosa et al. [19]. They have shown an impressive extension of the flamability limit from $\phi = 0.41$ to $\phi = 0.13$ (see Fig. 1.12d). Moreover, the results were sensitive to the electrode position, provided it was placed in a region filled with air and fuel. Improvements of the lean flammability limits and LBO have also been observed by Sabatino and Lacoste [169] at elevated pressure up to 5 bar. Minesi [130] has shown the ability of plasma discharges located in burnt gases to enhance combustion. The effects of plasma discharge in such a mixture are not well understood yet. In a recent work made by Cont-Bernard et al. [47], an academic laminar burner has been designed to answer these questions. This experiment could serve in numerical simulations to isolate the different effects of the plasma-combustion coupling. Close to a practical application, the effect of a gliding arc discharge on kerosene atomization has been studied by Huang et al. [82]. It was found possible to reduce the mean droplet diameter up to 20% at a low pressure of 30 kPa, where liquid atomization is more difficult than at atmospheric pressure. Thus, plasma discharges could be an interesting way to reach engine requirements at low-pressure conditions such as re-light during the cruise phase.

Reference	Mixture	T [K]	Electrodes	Plasma discharge	Effects studied
[178]	CH_4/Air/Ar	≈ 1000	Planar	Glow	Ignition
[103]	Nat. Gas - Air	300	Pin	NRP	NOx
[104]	CH_4/Air	300-2000	Pin-Annular	NRP-glow	Gas heating
[19]	C_3H_8/Air	300-2000	Pin-Annular	NRP	Flame stabilization
[173]	Nat. Gas - Air	2000	Pin-Annular	NRP	Flame anchoring
[108]	CH_4/Air	300	Pin	NRP	Ignition
[109]	CH_4/Air	300	Pin	NRP	Ignition, OH
[47]	CH_4/Air + CO_2/H_2O	300	Pin	NRP-Glow	Flame response, OH
[130]	CH_4/Air + CO_2/H_2O	2000	Pin	NRP-Spark	Flame response
[90]	CH_4/Air	300	Annular	NRP	LBO - CO/NOx
[91]	CH_4/Air	300	Annular	NRP	LBO, NOx, Instabilities
[201]	CH_4/Air	300	Annular	NRP	LBO
[169]	CH_4/Air	300	Annular	NRP	LBO, instability
[82]	Kerosene-Air	290-487	Spherical	Gliding arc	Atomization, Ignition

Table 1.1: Experimental PAC studies

Most of the numerical plasma-assisted combustion studies focused on the simulation of ignition, which can be performed with a few number of pulses and reduced-order models. Non equilibrium plasma effects in pure air have been extensively studied by Popov [159, 157, 158, 160] using a 1D-radial model and detailed chemistry. These works help to understand the major plasma effects on combustion, namely the thermal and kinetic effects. Detailed simulations of plasma-assisted ignition using zero-dimensional models and detailed chemistry have also been made by Aleksandrov et al. [11], Adamovich et al. [8], Mao and Chen [123], DeFilippo and Chen [51]. One-dimensional studies, including some dimensional effects and electric field computation, have been done by Yang et al. [198], Casey et al. [33]. In [198], a multi-scale modeling and theory of Plasma-Assisted Ignition (PAI) is presented including high-voltage pulse $\mathcal{O}$(ns), interpulse period $\mathcal{O}$(µs) and combustion processes $\mathcal{O}$(ms). However, at least a two-dimensional simulation is necessary to study non-planar electrodes widely used in practical Plasma-Assisted Combustion (PAC) applications. Several studies of a single pulse ignition using a 2D-axisymmetric model have been performed using detailed chemistry (Sharma et al. [172]) and simplified chemistry (Tholin et al. [185]). A 2D-planar simulation has also been performed by Breden et al. [28] to better understand the streamer propagation and radical

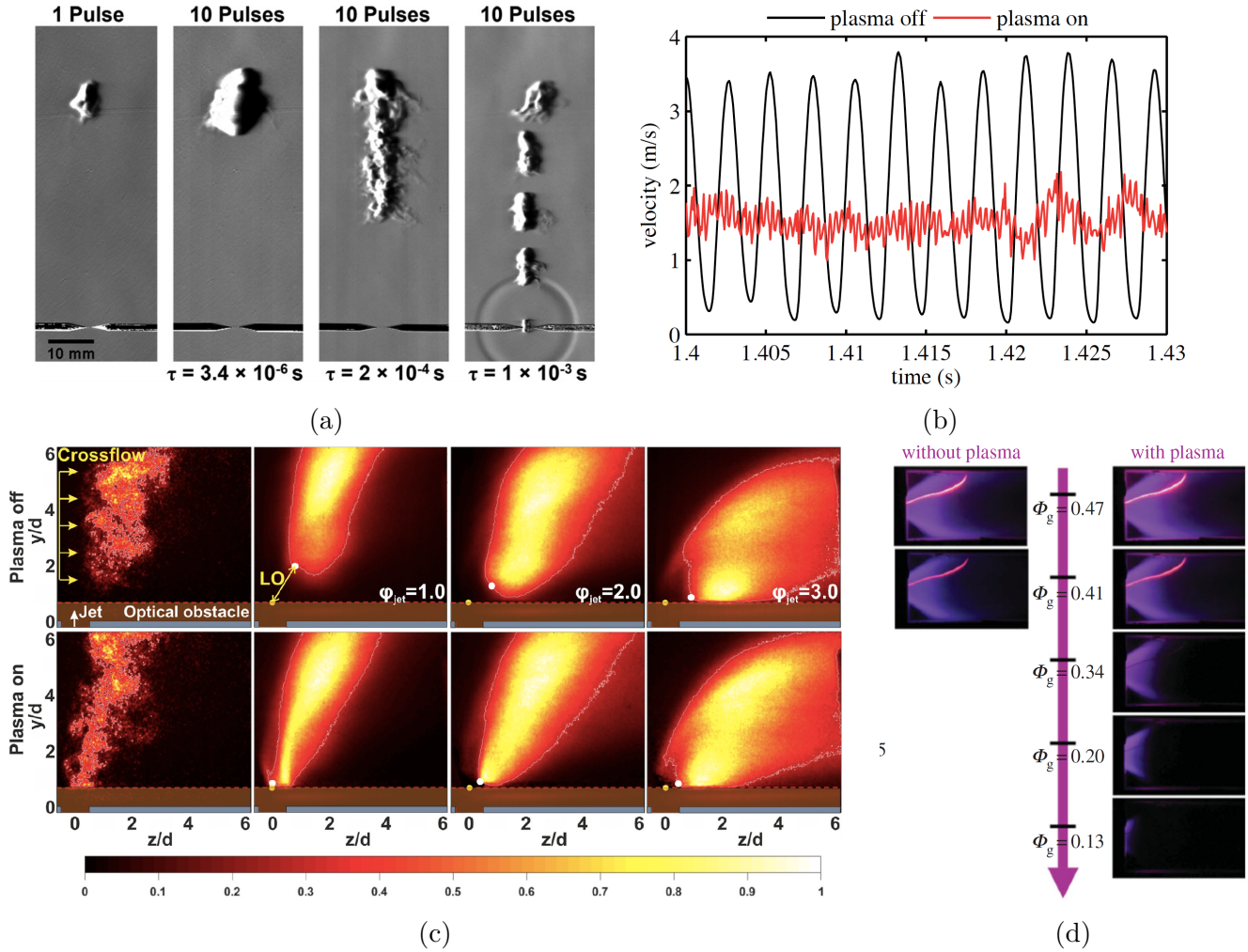

Figure 1.12: Experimental plasma-assisted combustion results: (a) plasma-assisted ignition from Lefkowitz and Ombrello [108], (b) flame instabilities mitigation from Lacoste et al. [102], (c) flame anchoring from Shcherbanev et al. [173] and (d) flammability limits extension from [19].

production in a coaxial configuration. Flame stabilization in 2D-cylindrical coordinates has been studied in Bak et al. [16]. Multiple pulses were simulated using quite detailed chemistry. However, the plasma description has been oversimplified to speed up the computation. The discharge zone is meshed with very coarse cells of 0.2 mm. A detailed Plasma-Assisted Ignition (PAI) simulation of H_2:O_2 mixture has been performed by Sitaraman and Grout [176] using a 3D model. Only the first pulse has been simulated and the effects were supposed to be unchanged for the successive pulses. Finally, a phenomenological model has been developed in Castela et al. [34, 35] to replace the detailed modeling of the plasma phase. This model has been recently used to study methane-air ignition in [21] and flame stabilization in [20]. To the best of my knowledge, there is no study that considers a detailed simulation of NRP discharges using detailed chemistry in two or three dimensions on realistic configurations.

Reference	Dimension	Mixture	Chemistry	Pulse mode	Effects studied
[11]	0D	CH_4/Air/Ar	Detailed	Single-pulse	Ignition
[8]	0D	H_2/C_xH_y/Air	Detailed	Multi-pulse	Ignition
[123]	0D	CH_4/Air	Detailed	Single-pulse	Ignition
[51]	0D	CH_4/Air	Detailed	Single-pulse	Ignition
[158] [160]	1D radial	Air	Detailed	Single-pulse	Fast gas heating Radical production
[198]	1D	CH_4/Air	Detailed	Multi-pulse	Ignition
[33]	1D	CH_4/Air	Detailed	Multi-pulse	Ignition
[172]	2D-axi	H_2/Air	Detailed	Single-pulse	Ignition
[92]	2D-axi	H_2/Air	Detailed	Single-pulse	Discharge phase
[28]	2D	CH_4/Air	Detailed	Single-pulse	Discharge phase Radicals production
[185]	2D-axi	H_2/Air	Reduced	Single-pulse	Ignition
[16]	2D-axi	CH_4/Air	Detailed	Multi-pulse	Stabilization
[34]	2D	CH_4/Air	Modeled	Multi-pulse	Ignition
[35]	3D	CH_4/Air	Modeled	Multi-pulse	Hydrodynamic
[176]	3D	H_2/O_2	Detailed	Multi-pulse	Ignition
[21]	3D	CH_4/Air	Modeled	Multi-pulse	Ignition
[20]	3D	CH_4/Air	Modeled	Multi-pulse	Flame stabilization

Table 1.2: Numerical PAC studies

1.5 Outline of the Dissertation

This work aims to get new insight on plasma-combustion coupling using numerical modeling and simulations. The use of plasma discharges to improve combustion devices is currently investigated by many groups in the world, including the CERFACS through the PASTEC [6] and GECCO [3] ANR projects. Funded by the PASTEC ANR, this work needs to complete the experimental investigations, made at EM2C and CORIA, by developing a numerical framework able to perform detailed simulations including the plasma formation and its interaction with a reactive mixture. Indeed, the development of efficient and reliable numerical tools able to simulate a practical system is a mandatory step toward a better understanding of the complex phenomena occurring between a flame and a plasma discharge. In order to achieve this, the manuscript is organized into three parts that are briefly described below.

Part I The first part of this work aims to develop a robust and accurate code able to simulate the plasma phase. In Chapter 2, a phenomenological description of NRP discharges is first given. Then, the model used for the plasma phase is presented. Chapter 3 presents the numerical discretization of the plasma model that has been implemented in the new low-temperature plasma code AVIP. Finally in Chapter 4, the AVIP code is validated against an international benchmark in which the discharge propagation between two planar electrodes is simulated. Code validation in a pin to pin configuration is also performed to assess the code's ability to work on a fully unstructured grid on a real geometry.

Part II This second part is dedicated to the coupling of the plasma chemistry with combustion kinetics. This is an essential task for detailed PAC modeling. While detailed kinetic mechanisms exist in the literature, their full description and validation are not always clear and validated only in a small range of conditions. In Chapter 5, the canonical zero-dimensional reactors used to study plasma-combustion chemistry are presented. Then, plasma kinetics in air, methane-air

and burnt gases are successively presented in Chapters 6, 7 and 8. These detailed mechanisms are computationally heavy and cannot be used in multi-dimensional simulations. Thus, two methods to reduce the chemistry are presented. In Chapter 9, an automatic kinetic mechanism reduction is applied to reduce the number of species in the mechanism. Chapter 10 presents a new phenomenological model based on all the knowledge gained during the Ph.D in order to get an affordable plasma model for 3D PAC simulations.

Part III In this last part, multi-dimensional simulations of plasma discharges coupled to a gaseous flow are presented. The numerical model that links the low-temperature plasma model to the reactive Navier-Stokes equations is first given in Chapter 11. In Chapter 12, plasma discharges in air are simulated and compared to experiments with a focus on gas heating and atomic oxygen production. Finally in Chapter 13, plasma-assisted ignition is performed. The effect of discharge frequency is investigated by comparison with a single plasma discharge ignition. Moreover, the chemical enhancement from non-equilibrium plasma discharges is emphasized by comparison with heat energy deposition.

Part I

Discharge code development

Chapter 2

Low-temperature plasma discharge modeling

Contents

2.1 NRP discharges

There are two major types of plasma discharges: equilibrium and non-equilibrium. A discharge is at equilibrium when the electron temperature is identical to the gas temperature. It is the case in spark plug devices that have been studied for decades now in the context of internal-combustion engine [153] and gas turbine [18, 14] ignition. During the past two decades, the use of non-equilibrium discharges has gained visibility due to its ability to ignite and stabilize flames. In this kind of discharge, the electrons are not in thermal equilibrium with the gas and their temperature T_e is much higher than the gas temperature T_g with typically $T_e \approx 5\,\text{eV} \simeq 60\,000\,\text{K}$ and $T_g \in [300 - 3000]$ K. However, the high-pressure conditions (≥ 1 bar) encountered in ICE or gas turbines are not favorable to sustain non-equilibrium discharges. Indeed at high pressure, the gas temperature quickly tends to equilibrate with the electron temperature. To overcome this issue, the pulse duration is reduced to a few nanoseconds leading to the so-called

Nanosecond Repetitively Pulse (NRP) discharges. In these discharges, a short pulse of 5-20 kV lasting approximately 10 ns is applied at a high pulse repetition frequency (PRF) ranging from 10 to 100 kHz as depicted in Fig. 2.1. These discharges can be applied between planar electrodes [191], pin-pin electrodes [167] or annular electrodes [169] which are separated by a typical distance of 1 to 10 mm.

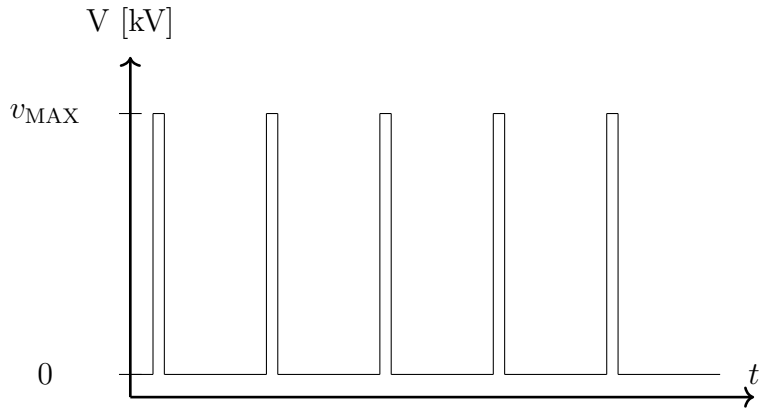

Figure 2.1: Sketch the voltage pulse in NRP discharge application (not in scale)

Despite its unique designation, the NRP discharge can result in very different regimes, as depicted in Fig. 2.2. These different regimes were obtained by varying the applied voltage. It is also possible to switch between corona and spark regimes by decreasing the inter-electrode distance or increasing the pulse duration. The corona regime is characterized by a light emission close to the anode and small pulse energy $\leq 1\,\mu\mathrm{J}$. Diffuse light emission is observed in the glow regime with typical energy per pulse $\leq 100\,\mu\mathrm{J}$. This regime is accompanied by a small gas heating and active species production and becomes attractive for plasma-assisted combustion application [46]. The conductive current remains relatively small ($\leq$ 2 A) in the corona and glow regimes. Then in the spark regime, the conduction current becomes as high as 20-40 A, and intense light emission is observed. The gas heating in such discharges can be higher than 1000 K and a large amount of the oxygen molecules in the air are dissociated [167].

2.2 Charged species processes

During the propagation phase of a plasma discharge, the most important processes involve charged species. Thanks to the strong electric field, these species are accelerated, thus gaining energy. Due to their low mass, electrons quickly accelerate and do not exchange a significant amount of energy through elastic collision processes Eq. (2.1). While the internal energy of particles in process (2.1) is kept constant, the kinetic energy change is proportional to the ratio $m_e/m_A \simeq 10^{-5}$. The low value of this ratio allows the electron to reach energy ranging from 1 to 10 eV.

$$\mathrm{e}^- + \mathrm{A} \longrightarrow \mathrm{e}^- + \mathrm{A} \tag{2.1}$$

When an electron moves, it collides with neutral molecules and inelastic processes may occur. One of the essential processes is the electron impact ionization (2.2) producing a new electron per event. While electrons are also produced by other processes such as photoionization (See Section 2.3.3), electron impact ionization is the main ionization process in most gas discharges.

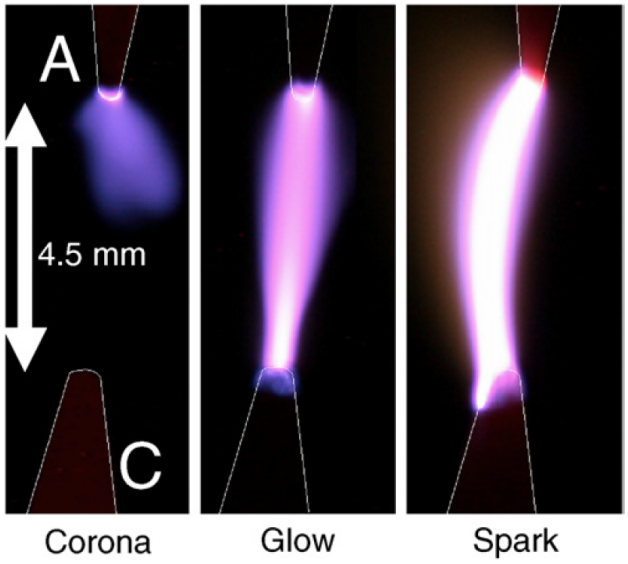

Figure 2.2: Digital camera images of NRP corona, glow and spark regimes in 1 atm air at 1000 K and a PRF of 10 kHz. From left to right the applied voltage is 5 kV, 5.5 kV and 6 kV. [Reproduced from [141]]

$$e^- + A \longrightarrow e^- + e^- + A^+ \tag{2.2}$$

An electron can be lost in two different processes. The first one is the electron attachment process (2.3) which occurs in electronegative gases such as air where electrons can attach on O_2. The reverse reaction corresponds to the electron detachment process (2.4) that can be a source of free-electron. Indeed, a significant amount of negative charge can be stored in negative ions during the inter-pulse period that serves as a memory effect of the preceding discharge. In the air, ionization dominates over the attachment for electric field higher than the so-called breakdown electric field E_b. Electrons can also be lost when they recombine with a positive ion (2.5). The same kind of process occurs for negative ions, which can recombine with a positive ion (2.6).

$$e^- + A \longrightarrow A^- \tag{2.3}$$
$$A^- \longrightarrow A + e^- \tag{2.4}$$
$$e^- + A^+ \longrightarrow A \tag{2.5}$$
$$A^- + A^+ \longrightarrow A + A \tag{2.6}$$

A good description of the discharge propagation can be obtained by only considering the processes described above [98, 136, 49, 184]. However, electrons are also prone to excite neutral particles as described in process (2.7). In that case, electron kinetic energy is converted into internal energy of an excited state A^*. These excited states play a crucial role in plasma-assisted combustion and will be discussed later.

$$e^- + A \longrightarrow e^- + A^* \tag{2.7}$$

2.3 Plasma discharge mechanisms

The mechanism for creating a plasma discharge strongly depends on the operating conditions. One of the critical parameters is the pd product, where p is the ambient gas pressure and d is the inter-electrode distance. For discharges in air where $pd \leq 0.3$ atm.cm^{-1} [126] it is the so-called Townsend mechanism [187] that drives the discharge whereas for $pd \geq 0.3$ atm.cm^{-1} it is the so-called streamer mechanism detailed by Loeb and Meek [116, 117] that describes the propagation of the discharge. In both cases, the electron avalanche process allows describing the origin of the discharge. A discharge can generally occur if the electric field exceeds the breakdown electric field that triggers the electrical breakdown. Electrical breakdown is the process of transformation of a nonconducting material into a conductor one [162]. The concepts of electron avalanche and breakdown field are first described for the Townsend mechanism in Section 2.3.1. Then the streamer formation and propagation are detailed in Section 2.3.2.

2.3.1 Townsend mechanism

Let's start with an initial seed of electrons with a density n_{e0} close to the cathode between two parallel electrodes separated by a distance d as depicted in Fig. 2.3. These electrons give rise to an initial current i_0 at the cathode. These electrons will move against the electric field toward the anode ionizing the gas and generating a so-called electron avalanche. This process is characterized by the Townsend ionization coefficient α. This coefficient expresses the number of electrons created by one electron per unit length and mainly depends on the reduced electric field E/N. This process can be written as:

$$\frac{dn_e}{dx} = \alpha n_e \tag{2.8}$$

from which the electron density at a distance x from the cathode is given by:

$$n_e = n_{e0} e^{\alpha d} \tag{2.9}$$

When reaching the anode, an initial electron has produced $(e^{\alpha d} - 1)$ electrons and the same amount of positive ions A^+. These positive ions produce $\gamma(e^{\alpha d} - 1)$ electrons when arriving at the cathode, thanks to the secondary electron emission (SEE) where $\gamma \in [0.01 - 0.1]$ is the second Townsend coefficient. In the absence of any external ionization source, the discharge can be self-sustained if the number of electrons produced at the cathode following the first and second Townsend processes is at least equal to the initial number of electrons at the cathode:

$$\gamma(e^{\alpha d} - 1) \geq 1 \tag{2.10}$$

In this analysis, the recombination process has been neglected. However, it is possible to account for it by considering a reduced ionization coefficient $\alpha' = \alpha - \eta$ where η is the Townsend attachment coefficient. The breakdown voltage V_b for a self-sustained discharge can be expressed as [162]:

$$V_b = \frac{B\ pd}{C + \ln(pd)} \tag{2.11}$$

where B and C are two constants that depend on the gas and the electrode material [62]. This function has a minimum corresponding to the easiest breakdown conditions and has been measured experimentally in a large range of pd products and gas mixture [62]. Notice that the

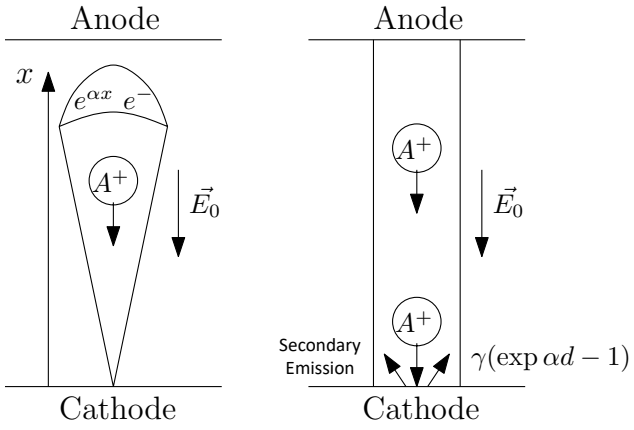

Figure 2.3: Principle of the Townsend mechanism (left) α-process and (right) γ-process

Townsend mechanism is slow as the positive ions, that are much slower than electrons, must reach the cathode to produce new free electrons.

2.3.2 Streamer mechanism

As shown previously, the Townsend mechanism leads to a homogeneous plasma channel, and each electron avalanche develops independently. This process mainly occurs at low values of $pd \leq 0.3$ atm.cm^{-1}. In the case where the pd product is large, the electron avalanche process described in Section 2.3.1 develops rapidly and the space charge in the region of high electron density creates an induced electric field that exceeds the Laplacian electric field E_0 (solution of the homogeneous Poisson equation). The discharge is then no longer controlled by the electric field imposed by the electrodes but by its space charge (See Fig. 2.4) that can be several times higher than the Laplacian field. This localized space charge is called the streamer head. A zoom on a positive streamer head is shown in Fig. 2.5. The space charge layer is very thin with a typical size of around $1/\alpha$. This space charge generates a very high electric field ahead of the streamer, leading to intense ionization in this region. Thus the positive streamer can propagate from left to right as an ionization wave faster than the electron drift-velocity. In the following, the positive and negative streamers are detailed separately.

2.3.2.1 Negative streamer

The negative streamer propagates in the direction of the natural electron movement from the cathode toward the anode, as shown in Fig. 2.6. It is the high-energy electrons at the front of the discharge that ionize neutral molecules thanks to an intense electric field. These electrons produce a multitude of small primary avalanches, which allow a fast propagation of this ionization wave. The head of the negative streamer is thus the seat of a high electron density. Due to their high mass, the positive ions produced during the streamer propagation stay almost immobile during the short discharge duration. Moreover, the main body of the streamer is quasi-neutral, and the electric field is screened within it. Thus, almost no ionization event occurs in the streamer body during its propagation.

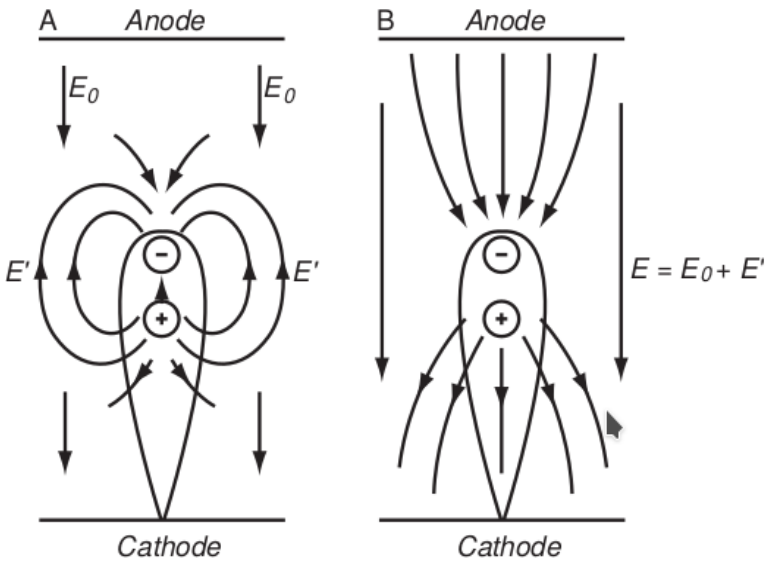

Figure 2.4: Space distribution of the external electric field $\mathbf{E_0}$ and the space charge electric field $\mathbf{E'}$. [Reproduced from [62]]

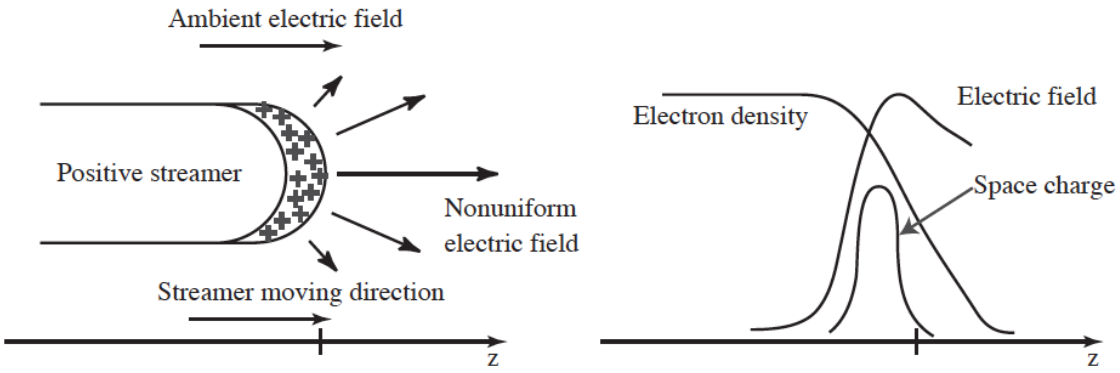

Figure 2.5: Schematic of the head of a positive streamer. [Reproduced from [115]]

2.3.2.2 Positive streamer

The positive streamer propagates in the opposite direction of the natural electron movement from the anode toward the cathode, as shown in Fig. 2.7. In that case, the electrons present upstream of the plasma channel move toward the streamer head by producing a multitude of ionization events. These primary avalanches require the presence of electrons ahead of the streamer, which are naturally present in air or can be produced thanks to the photoionization effect. However, there are few free electrons in ambient air, so that photoionization is critical for positive streamer propagation in ambient air [99]. The photoionization relies on photons emitted in the streamer head region that can ionize molecules upstream of the streamer providing free electrons for new primary avalanches (See Section 2.3.3). After a certain number of pulses, the photoionization becomes less important as a significant pre-ionization level has been reached thanks to a cumulative effect of previous discharges [49, 184].

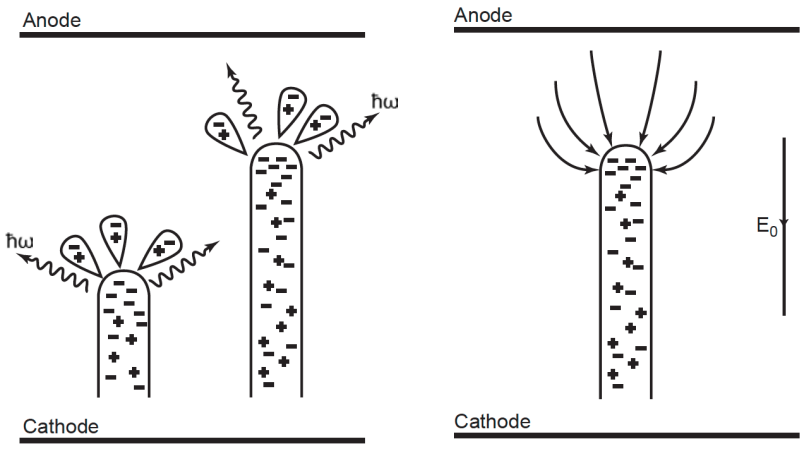

(a) (b)

Figure 2.6: Illustration of the negative streamer: (a) negative streamer propagation, (b) electric field neat the streamer head. [Reproduced from [62]]

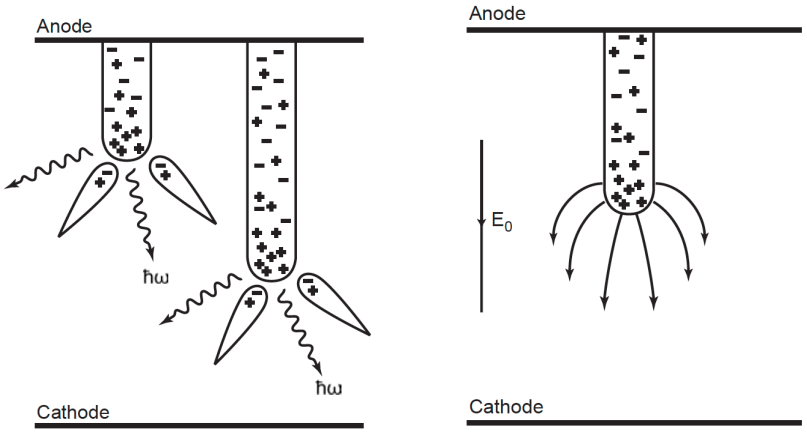

(a) (b)

Figure 2.7: Illustration of the positive streamer: (a) positive streamer propagation, (b) electric field neat the streamer head. [Reproduced from [62]]

2.3.3 Photoionization

In the case of positive streamers detailed in Section 2.3.2, it is essential to have a source of free electrons downstream of the discharge. This source of electrons come from photoionization or from pre-ionized gas [49]. The photoionization process occurs when a photon, characterized by its energy $h\nu$, is absorbed by a gas molecule M leading to the formation of a positive ion:

$$\mathrm{M} + h\nu \longrightarrow \mathrm{M}^{+} + \mathrm{e}^{-} \tag{2.12}$$

In the case of NRP discharges, photoionization is vital during the first pulses [184]. Indeed, ambient air is weakly ionized naturally with $n_e \leq 1 \times 10^{10}\,\mathrm{m}^{-3}$, and positive streamer propagation is difficult in such medium. After several pulses, a high pre-ionized level is reached in the inter-electrode gap and the positive streamer propagation becomes easier.

The photon involved in the process given in Eq. 2.12 must have the necessary energy to ionize the molecule (*i.e.* higher than its ionization potential I_0). In the air, energetic photons

can be produced during the radiative quenching of $N_2(C_3)$ [99] which has an energy close to the O_2 ionization potential. Then, the photon can be absorbed by an oxygen molecule leading to an ionization event. From the emission to absorption, the photon moves at the speed of light. Hence, these two events do not occur at the same location leading to a fundamentally non-local process. The reference model for the photoionization source term S_{ph} is due to the work of Zhelezniak et al. [202]. In this model, the photoionization source term at a location $\mathbf{r}$ is given by:

$$S_{\text{ph}}(\mathbf{r}) = \int_V \frac{I(\mathbf{r}')g(R)}{4\pi R^2} dV \tag{2.13}$$

where $R = |\mathbf{r} - \mathbf{r}'|$. The photon source term is assumed to be proportional to the ionization source term S_i:

$$I(\mathbf{r}) = \frac{p_q}{p + p_q} \xi \frac{\nu_u}{\nu_i} S_i(\mathbf{r}) \tag{2.14}$$

where p is the pressure of the gas, p_q is the quenching pressure which is around 40 mbar (thus $p_q/(p + p_q) = 0.038$ at 1 bar), ξ is the photoionization efficiency, ν_u is the electron impact excitation frequency of the level u, ν_i is the electron impact ionization frequency and $S_i = \nu_i n_e$ is the ionization production term. In Bourdon et al. [27], $\xi\nu_u/\nu_i = 0.06$ was used whereas a value of 0.075 is used in [15]. The g function is a geometrical factor that reads:

$$g(R) = \frac{e^{\chi_{\min} P_{O_2} R} - e^{\chi_{\max} P_{O_2} R}}{R \ln(\chi_{\min}/\chi_{\max})} \tag{2.15}$$

where $\chi_{\min} = 0.035\text{Torr}^{-1}\text{cm}^{-1}$ and $\chi_{\max} = 2\text{Torr}^{-1}\text{cm}^{-1}$.

This model can be an expensive task in streamer simulations performed on multiple processors as each node of the domain must know the ionization source term $I(\mathbf{r})$ over the whole computational domain. It implies the need for massive processor communications that are prohibitive for code scalability. To overcome this issue, a simplified model was proposed by Bourdon et al. [27] who replaced the integral model by a set of Helmotlz differential equations (typically two or three equations [27]) that can be solved similarly to the Poisson equation:

$$\nabla^2 S^j_{\text{ph}}(\mathbf{r}) - (\lambda_j p_{O_2})^2 S^j_{\text{ph}}(\mathbf{r}) = -A_j p^2_{O_2} I(\mathbf{r}) \tag{2.16}$$

where the coefficients λ_j and A_j are fitted to match with the Zhelezniak's model (See [27]). Then the photoionization source term is retrieved from:

$$S_{\text{ph}}(\mathbf{r}) = \sum_j S^j_{\text{ph}}(\mathbf{r}) \tag{2.17}$$

This approach is used in AVIP where the Laplacian operator in Eq. 2.16 is discretized as for the Poisson equation detailed in Section 3.4.1. As discussed in [49], the computation of the photoionization source term can be performed only every ten iterations to limit its computational cost without significant loss of accuracy.

2.4 Low-temperature plasma model

2.4.1 Review of existing models

Over the past decades, several models have been employed for streamer simulations. In terms of modeling, the most straightforward approach is the so-called Particle-In-Cell (PIC) model, which follows the individual motion of charged particles. In this model, collisions are usually included using Monte-Carlo statistical method, which directly relies on cross-sections. This modeling approach has been successfully used for streamer simulation in [39, 182]. However, due to the high computational cost of the particle approach, most of the streamer simulations are performed using fluid models [98, 143, 49, 184]. Fluid models are based on the moments of the Boltzmann equation and are discussed in section 2.4.2. Hybrid models, which rely on particle and fluid models, can also be used following different strategies. One of them consists of modeling some species using a particle approach, while the fluid model is used for the others. Another possibility is to perform partially hybrid computation as done in [111]. In this work, only fluid modeling has been investigated.

2.4.2 Fluid model

Microscopically, particle dynamics can be described by a distribution function $f(\mathbf{r}, \mathbf{v}, t)$ in the phase space $(\mathbf{r}, \mathbf{v})$ obeying the Boltzmann equation:

$$\frac{\partial f}{\partial t} + \mathbf{v} \cdot \nabla f + \frac{\mathbf{F}}{m} \cdot \nabla_v f = \left(\frac{\delta f}{\delta t}\right)_c \tag{2.18}$$

where $\mathbf{F}$ is the force acting on the particle, m its mass and $(\frac{\delta f}{\delta t})_c$ the collision operator. In our case, $\mathbf{F}$ is limited to the Lorentz force $qe(\mathbf{E} + \mathbf{v} \times \mathbf{B})$ where q is the species charge, e the elementary charge, $\mathbf{E}$ the electric field and $\mathbf{B}$ the magnetic field. Moreover, as justified in [49], the magnetic field can be neglected in most of the streamer simulations.

The particle density $n(\mathbf{r}, t)$ is obtained by averaging f over the velocity space:

$$n(\mathbf{r}, \mathbf{t}) = \int f(\mathbf{r}, \mathbf{v}, t) d^3(v) \tag{2.19}$$

We define the mean value of a quantity a by:

$$\langle a \rangle = \frac{1}{n(\mathbf{r}, t)} \int a(\mathbf{v}) f(\mathbf{r}, \mathbf{v}, t) d^3\mathbf{v} \tag{2.20}$$

By taking successively $a = m, m\mathbf{v}, \frac{1}{2}m\mathbf{v}^2$ in Eq. (2.20), one obtains respectively the density ρ, momentum $m\mathbf{V}$ and total energy $E = \frac{1}{2}mV^2 + \frac{3}{2}k_BT$ where $\mathbf{V} = \langle v \rangle$ is the mean velocity. The macroscopic transport equations are obtained by multiplying the Boltzmann equation Eq. (2.18) by a and averaging it over the velocity space. Finally, the mass, momentum and energy conservation equations are given by:

$$\frac{\partial \rho}{\partial t} + \nabla \cdot (\rho \mathbf{V}) = \int \left(\frac{\delta f}{\delta t}\right)_c d^3\mathbf{v} \tag{2.21}$$

$$\frac{\partial \rho \mathbf{V}}{\partial t} + \nabla \cdot (\rho \mathbf{V}\mathbf{V} + \mathbf{P}) = nqe\mathbf{E} + \int m\mathbf{v}\left(\frac{\delta f}{\delta t}\right)_c d^3\mathbf{v} \tag{2.22}$$

$$\frac{\partial \rho E}{\partial t} + \nabla \cdot (\rho E \mathbf{V} + \mathbf{q} + \mathbf{P} \cdot \mathbf{V}) = nqe\mathbf{E} \cdot \mathbf{V} + \int \frac{1}{2} m\mathbf{v}^2 \left(\frac{\delta f}{\delta t}\right)_c d^3\mathbf{v} \tag{2.23}$$

where $\mathbf{P}$ is the pressure tensor and $\mathbf{q}$ the heat flux vector. It appears in Eqs. (2.21)(2.22)(2.23) that there are more unknown than equations leading to the classical issue of system closure that is discussed in Section 2.4.3.

2.4.3 Drift-diffusion approximation

In the widely used drift-diffusion approximation [98, 100, 143, 49, 184], only the particle density is solved through:

$$\frac{\partial mn}{\partial t} + \nabla \cdot (nm\mathbf{V}) = S_0 \tag{2.24}$$

where S_0 corresponds to the chemical source term. This equation lets appear an unknown term which is the mean velocity $\mathbf{V}$ that can be retrieved from the momentum balance equation. Assuming that the velocity distribution is close to isotropic, the pressure tensor $\mathbf{P}$ can be written as a scalar pressure p with $\mathbf{P} = p\mathbf{I} = nk_bT$. The collisional term in the momentum equation 2.22 is often reduced to the collision between the charged species and neutrals with an effective momentum transfer collision frequency ν_{eff} [55]. Moreover, the momentum quickly reaches a steady state and according to [49, 163] the inertial term can also be neglected compared to the friction terms. Then the momentum balance equation 2.22 reduces to:

$$nqe\mathbf{E} - \nabla p - nm\nu_{\text{eff}}\mathbf{V} = 0 \tag{2.25}$$

By expressing the scalar pressure with the temperature the particle flux reads:

$$n\mathbf{V} = nq\frac{e}{m\nu_{\text{eff}}}\mathbf{E} - \frac{k_BT}{m\nu_{\text{eff}}}\nabla n \tag{2.26}$$

This is the well known drift-diffusion particle flux more commonly written:

$$n\mathbf{V} = nq\mu E - D\nabla n \tag{2.27}$$

where $\mu = e/m\nu_{\text{eff}}$ is the mobility coefficient and $D = k_BT/m\nu_{\text{eff}}$ is the diffusion coefficient. The drift-diffusion approach validity is discussed in [110] by comparison with a particle model. Comparison of the drift-diffusion approximation to higher-order fluid model has been performed in [55, 125]. Whereas going to higher-order models can increase the simulation's accuracy, it also requires solving additional equations involving numerical constraints such as time or space steps limitations. In general, the drift-diffusion model is a suitable approximation for collisional plasma at atmospheric pressure. Thus in this work, only the drift-diffusion approximation has been used. Moreover, all the transport coefficients (μ and D) and chemical source terms were assumed to be a function of the local reduced electric field E/N only, to work with the Local Field Approximation (LFA).

2.4.4 Electric field

The charged particles involved in the plasma are strongly coupled due to their response to the presence of an electric field $\mathbf{E}$, which depends on the charged species densities. As discussed in [49], the magnetic field can be neglected in streamer simulation, thus simplifying the Maxwell-Faraday equation to $\nabla \times \mathbf{E} = \mathbf{0}$ (electrostatic approximation). As a consequence, $\mathbf{E}$ is a conservative vector field that is given by the gradient of a scalar potential ϕ:

$$\mathbf{E} = -\nabla\phi \tag{2.28}$$

Injecting Eq. 2.28 into Maxwell-Gauss equation finally leads to the Poisson equation:

$$\Delta\phi = -\frac{1}{\epsilon_0}\sum_k eq_k n_k = -\frac{\rho_c}{\epsilon_0} \tag{2.29}$$

where q_k and n_k are respectively the charge number and particle density of species k and $\rho_c = \sum_k eq_k n_k$ is the charge density. The Equation 2.29 must be supplemented by boundary conditions. Two types of boundary conditions have been considered in this work. The first one applied to the boundary domain $\partial\Omega_\mathrm{D}$ is the Dirichlet condition imposing the potential to a given value ϕ_D. The second one applied to the boundary domain $\partial\Omega_\mathrm{N}$ is the Neumann condition, which imposes the normal derivative of the potential that is equivalent to the normal electric field. These boundary conditions are sumarized by:

$$\phi = \phi_\mathrm{D} \qquad \text{for} \quad \partial\Omega \in \partial\Omega_\mathrm{D} \tag{2.30}$$

$$\nabla\phi \cdot \vec{n} = -E_\mathrm{n} \qquad \text{for} \quad \partial\Omega \in \partial\Omega_\mathrm{N} \tag{2.31}$$

The numerical discretization of the Poisson equation and its boundary conditions is described in Section 3.4.

2.4.5 Transport coefficients and electron impact collision rates

When using the drift-diffusion equation to transport a charged species, two transport coefficients are required: the mobility μ and the diffusion coefficient D. These coefficients usually depend on the electric field, the gas temperature and the gas composition. The coefficients for positive and negative ions are always taken from [136]. In some cases, the electron mobility and electron diffusion coefficient were taken from [15] and [136]. However, when not specified, these coefficients were retrieved from the EEDF solver BOLSIG+ [72] that is embedded in AVIP.

As for the transport coefficients, the chemical source terms are sometimes taken from the literature [15, 136]. However, the general way to compute these rates in AVIP is to use BOLSIG+. In that case, a look-up table is generated during the initializing steps of the simulation using a cross-sections file.

Chapter 3

The discharge code AVIP

Contents

3.1 A low-temperature plasma code

The development of the low-temperature code AVIP has been an on-going task at CERFACS since 2015 and the work of [86, 87]. AVIP is based on the in-house code AVBP [171] developed at CERFACS for more than 20 years now and widely used for combustion and aerodynamics applications [26, 121, 12]. AVBP has proven in the past its HPC performances on fully unstructured grids able to handle complex geometries that are encountered in most industrial applications [64]. As for AVBP, a major objective of AVIP is to deal with realistic configurations for which the use of unstructured grids is essential. When simulating the interaction of

plasma discharges with a gaseous mixture, this approach allows, for example, to easily account for the real shape of the electrodes. This strategy is challenging and original: most of the low-temperature plasma codes rely on structured grids for which high-order numerical discretization can be achieved [115, 49, 192, 184, 60, 120, 182]. As a result, most of these codes are limited to academic configurations such as planar electrodes in rectangle or 3D boxes. In Célestin [49], a Ghost Fluid Method has been used to handle hyperbolic electrodes in the domain. However, this method can not be easily adapted for any electrode configurations. To the best of my knowledge, there are only a few homemade low-temperature plasma codes developed on unstructured grids [63, 200, 172]. There are also licensed codes working on unstructured grids such as COMSOL Multiphysics ©. Moreover, AVIP must be able to perform simulations in cylindrical coordinates that are often used for streamer simulations.

In the following, the unstructured grid formalism of AVIP is first presented in Section 3.2 where the necessary notations are introduced. Then, the drift-diffusion equation used to tranport the charged species is discretized in Section 3.3 followed by the Poisson discretization in Section 3.4.1. Finally, two simplified models for the electric field are presented in Section 3.6.

3.2 Unstructured grid formalism

3.2.1 Vertex centered finite volume integration

AVIP relies on a finite volume discretization of the governing equations, which are integrated over a control volume that must be defined. The equations that need to be solved in AVIP can be written as:

$$\frac{\partial u}{\partial t} + \nabla \cdot \mathbf{F} = 0 \tag{3.1}$$

Several options exist for this, and the most popular one is to consider the cell volume, also called primal volume, as control volume. On the other hand, it is also possible to use the nodal or dual volume that is centered on a mesh node. In AVIP, the variables are stored at the vertices so that two implementations are finally possible: cell-vertex or vertex-centered. In these two formulations, the residuals are now computed in different manners. For a control volume V_i, the residuals R_i is given by:

$$R_i = \frac{1}{V_i} \int_{V_i} \nabla \cdot \mathbf{F} dV \tag{3.2}$$

In the cell-vertex implementation, the residuals are computed on the primal volumes and then redistributed to the dual volumes. This is the option retained for most of the numerical schemes in AVBP. However, this formulation was not easily adaptable to cylindrical discretization. Thus the second option (*i.e.* a vertex-centered formulation) has been prefered. In this formalism, the residuals are directly computed on the dual volume as depicted in red in Figures 3.1a and 3.1b for triangular and quadrangular elements.

To perform the discretization, three different surfaces need to be clearly defined. Note that in 2D, a surface actually corresponds to an edge. The presentation of each surface is done for a triangular element in Fig. 3.2. The first one is the dual surface $\mathbf{S_{ij}^{\tau}}$ (Fig. 3.2a) which corresponds to the surface of the dual volume. This surface is defined for each edge ij of an element τ and verifies $\mathbf{S_{ij}^{\tau}} = -\mathbf{S_{ji}^{\tau}}$. The second surface called primal surface and denoted $\mathbf{S_{ij}}$ corresponds to the surface of an element (or a cell) as shown in Fig. 3.2b. These surfaces are oriented outwards

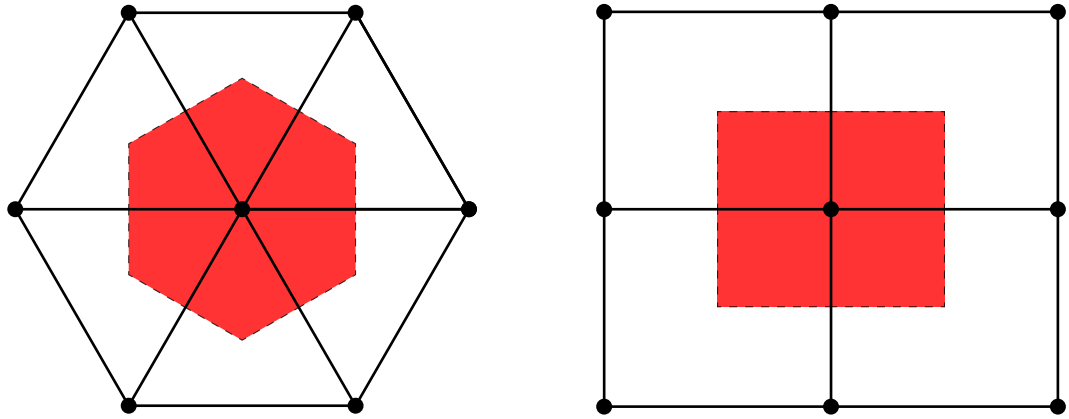

(a) (b)

Figure 3.1: Nodal volume definition in red for (a) a triangular mesh and (b) quadrangular mesh. Data are stored at nodes represented by the black circles.

from the triangle. Finally, the nodal surface $\mathbf{S_i}$ is given by a linear combination of the adjacent primal faces $\mathbf{S_{ij}}$ as in [105]:

$$\mathbf{S_i} = \sum_{j \ni i} -\frac{n_d}{n_v^f} \mathbf{S_{ij}} \tag{3.3}$$

where $j \ni i$ corresponds to the nodes j which share an edge with the node i in the element boundary, n_v^f is the number of vertices of the face f and n_d is the dimension of the domain. Note that for a triangle, the nodal face $\mathbf{S_i}$ is equal to the opposite primal face $\mathbf{S_{jk}}$. The definitions of these surfaces for quadrangular elements are exactly the same and displayed in Fig. 3.3.

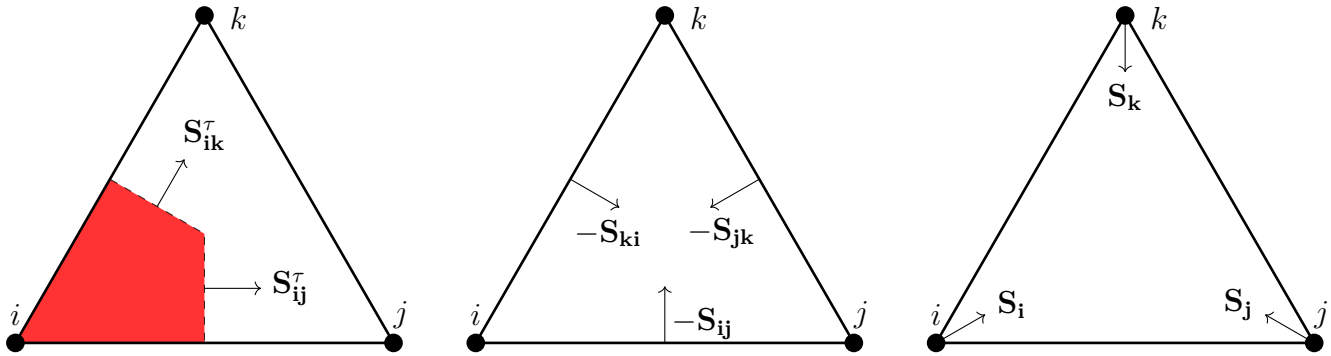

Figure 3.2: Different surfaces encountered in the discretization on triangular meshes: (a) dual faces, (b) primal faces and (c) nodal faces.

3.2.2 Notations

The general notations relative to the grid and mesh are the following. For the sake of clarity, most of these notations will be recalled when first used.

- Ω is the computational domain, $\dot{\Omega}$ its interior and $\partial\Omega$ its boundary.

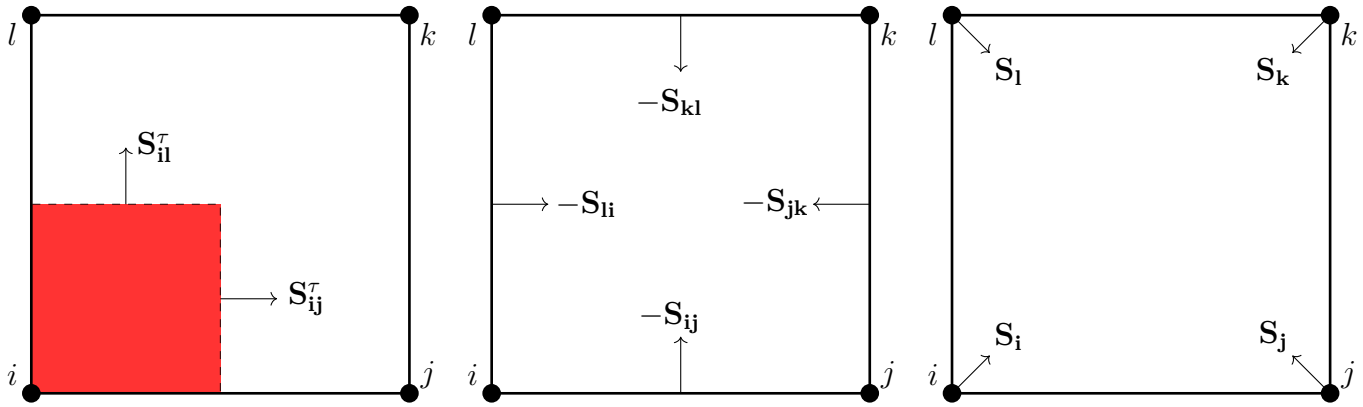

(a) (b) (c)

Figure 3.3: Different surfaces encountered in the discretization on quadrangular meshes: (a) dual faces, (b) primal faces and (c) nodal faces.

- τ is a cell of the domain, V_τ its volume and n_v^τ the number of vertex of the cell.
- V_i is the nodal volume of the node i. The nodal volume boundary ∂V_i is divided in two parts: the interior boundary $\partial \dot{V}_i = \partial V_i \cap \dot{\Omega}$ and the nodal volume boundary at the boundary of the domain $\partial V_i^b = \partial V_i \cap \partial\Omega$
- $\mathbf{S}^{\tau}_{\mathbf{ij}}$ is the dual surface of the edge ij in the cell τ, $\mathbf{S_{ij}}$ is the cell or primal surface associated to the edge ij and $\mathbf{S_i}$ is the nodal surface of the node i defined by Eq. 3.3 (See Section 3.2.1 for more details)
- f is a generic face of the nodal or primal volume.
- $E(i)$ is the set of cells that contain the node i.
- $S(i)$ is the set of nodes which share an edges with the node i.

3.3 Transport equation

3.3.1 Discretization

In the drift-diffusion approximation, the following equation needs to be solved numerically for each species:

$$\frac{\partial n}{\partial t} + \nabla \cdot \mathbf{F} = \frac{\partial n}{\partial t} + \nabla \cdot (n\mathbf{V} - D\nabla n) = 0 \tag{3.4}$$

where $\mathbf{V} = \mu\mathbf{E}$. The integration is performed over the nodal volume V_i and gives:

$$\frac{dn}{dt} + \frac{1}{V_i}\int_{V_i} \nabla \cdot \mathbf{F} dV = 0 \tag{3.5}$$

Then, applying the Green-Ostrogradsky theorem on the volume integral of the flux divergence:

$$\frac{dn}{dt} + \int_{\partial V_i} \mathbf{F} \cdot \mathbf{dS} = 0 \tag{3.6}$$

Moreover, it is necessary to decompose the nodal surface into its interior surfaces $\partial V_i \cap \dot{\Omega}$ and its boundary surfaces $\partial V_i \cap \partial\Omega$ that are treated differently:

$$\int_{\partial V_i} \mathbf{F} \cdot \mathbf{dS} = \int_{\partial V_i \cap \dot{\Omega}} \mathbf{F} \cdot \mathbf{dS} + \int_{\partial V_i \cap \partial\Omega} \mathbf{F} \cdot \mathbf{dS} = \int_{\partial \dot{V}_i} \mathbf{F} \cdot \mathbf{dS} + \int_{\partial V_i^b} \mathbf{F} \cdot \mathbf{dS} \tag{3.7}$$

where $\partial \dot{V}_i = \partial V_i \cap \dot{\Omega}$ and $\partial V_i^b = \partial V_i \cap \partial\Omega$. We first focus on the interior boundary that is decomposed into a sum over the faces f of the nodal surface $\partial \dot{V}_i$:

$$\int_{\partial \dot{V}_i} \mathbf{F} \cdot \mathbf{dS} = \sum_{f \in \partial \dot{V}_i} \int_f \mathbf{F} \cdot \mathbf{dS} \tag{3.8}$$

In pratice, AVIP loops over the cells τ_n as depicted in Fig. 3.4 for a triangular mesh. Then for each edge of the cell (*i.e.* **ij**, **jk** and **ki**), the flux across its associated nodal surface is computed. For example, the flux associated to the edge **ij** in cell τ_1 crosses the surface $\mathbf{S_{ij}^{\tau_1}}$. This residual enters the nodal volume j and leaves the nodal volume i. At the end of the edge loop, the residuals of the nodes i, j and k are updated by the contribution of the cell τ_n (opaque colors in Fig. 3.4). For the node i, it corresponds to the flux crossing the surface $\partial \dot{V}_i \cap \tau_1$:

$$\partial \dot{V}_i \cap \tau_1 = \mathbf{S_{ij}^{\tau_1}} - \mathbf{S_{ki}^{\tau_1}} \tag{3.9}$$

By continuing on cells $\tau_{n\in[1,6]}$, the flux is computed on the whole nodal surface ∂V_i forming the red closed volume of Fig. 3.4. Equation 3.8 can be rewritten as Eq. 3.10 that is closer to the pratical implementation where $\tau \in E(i)$ is the set of cells that contain the node i.

$$\int_{\partial V_i} \mathbf{F} \cdot \mathbf{dS} = \sum_{\tau \in E(i)} \sum_{f \in \partial V_i \cap \tau} \int_f \mathbf{F} \cdot \mathbf{dS} \tag{3.10}$$

Finally, the flux $\mathbf{F}$ is supposed to be constant on the face ij with $\mathbf{F} = \mathbf{F_{ij}}$ allowing to write Eq. 3.11. The computation of the flux $\mathbf{F_{ij}}$ is discussed in detail in Section 3.3.3.

$$\int_{\partial V_i} \mathbf{F} \cdot \mathbf{dS} = \sum_{\tau \in E(i)} \sum_{j \in S(i) \cap \tau} \mathbf{F_{ij}} \cdot \mathbf{S_{ij}^{\tau}} \tag{3.11}$$

where $j \in S(i) \cap \tau$ is the set of nodes sharing an edge with the node i in the cell τ.

For the nodes having a boundary surface (*i.e* $\partial V_i \cap \partial\Omega \neq \emptyset$), the nodal volume is closed by looping on the boundary faces of the domain. Figure 3.5 shows an example of a node i having two boundary faces in blue and red, whereas green-dashed lines correspond to its interior surface already detailed above. The integral over the boundary faces reads:

$$\int_{\partial V_i^b} \mathbf{F} \cdot \mathbf{dS} = \sum_{f \in \partial V_i^b} \mathbf{F_f} \cdot \mathbf{S_f} \tag{3.12}$$

so that for the case of node i in Fig. 3.5 we have:

$$\int_{\partial V_i^b} \mathbf{F} \cdot \mathbf{dS} = \mathbf{F_i^{\tau_1}} \cdot \mathbf{S_i^{b,\tau_1}} + \mathbf{F_i^{\tau_1}} \cdot \mathbf{S_i^{b,\tau_2}} \tag{3.13}$$

where $\mathbf{S_i^{b,\tau_1}}$ and $\mathbf{S_i^{b,\tau_2}}$ are respectively the boundary faces of the node i in cells τ_1 and τ_2.

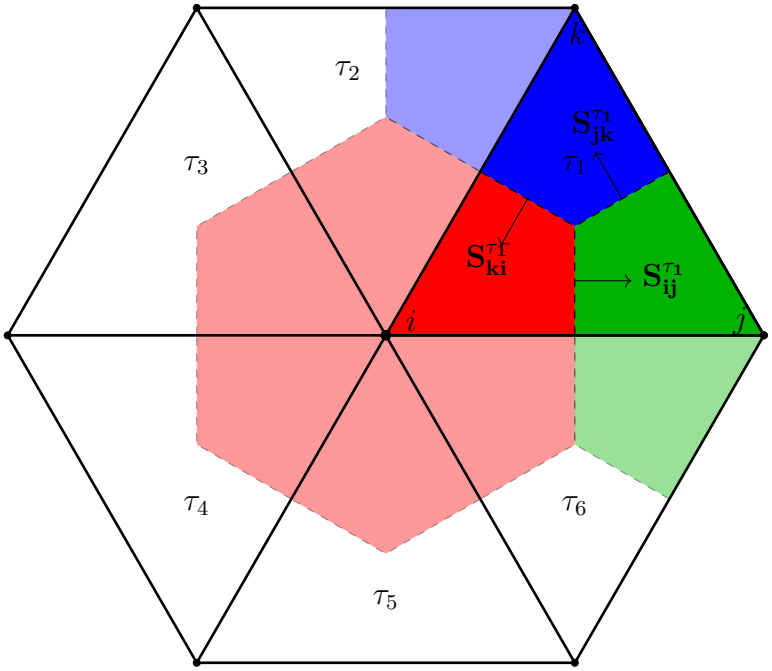

Figure 3.4: Definition of nodal surface vectors for a triangular mesh.

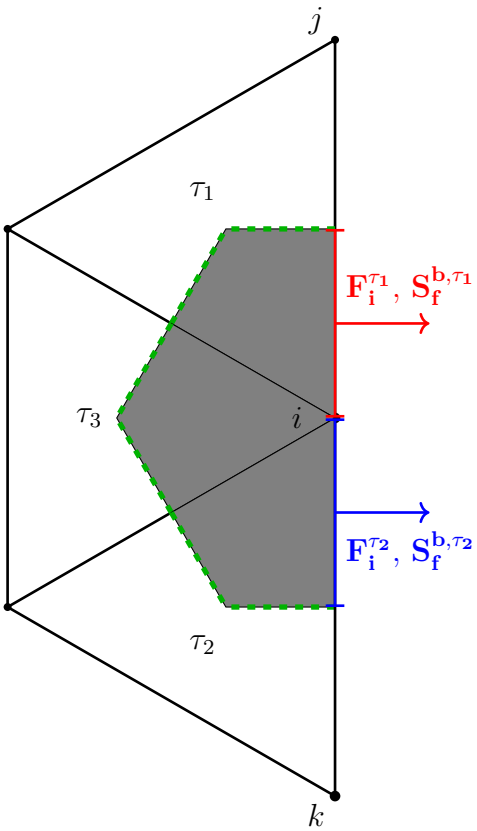

Figure 3.5: Definition of the boundary surfaces for a triangular mesh.

3.3.2 Cylindrical coordinates

Most streamer simulations are performed in cylindrical coordinates (r, θ, z) allowing to model a 3D problem onto a 2D mesh, thus considerably reducing the computational cost. In addition to the simplification $\partial_\theta = 0$, it is also assumed that for all vectors $\mathbf{A} = (A_r, A_\theta, A_z)$ we have $A_\theta = 0$. In cylindrical coordinates, an axisymmetric volume V_i is given by the product of its surface S_i in the $(r,\, z)$-plane and the distance traveled by the surface centroid r_i:

$$V_i = 2\pi r_i S_i \tag{3.14}$$

Then Equation 3.5 becomes:

$$\frac{dn}{dt} + \frac{1}{r_i S_i} \int_{S_i} \nabla \cdot \mathbf{F} r dS = 0 \tag{3.15}$$

In cylindrical coordinates, the product $r\nabla \cdot \mathbf{F}$: reads

$$r\nabla_{\text{cyl}} \cdot \mathbf{F} = r\left(\frac{1}{r}\frac{\partial r F_r}{\partial r} + \frac{\partial F_z}{\partial z}\right) \underbrace{=}_{\partial_z r = 0} \frac{\partial r F_r}{\partial r} + \frac{\partial r F_z}{\partial z} = \nabla_{\text{2D}} \cdot (r\mathbf{F}) \tag{3.16}$$

where $\nabla_{\text{2D}}\cdot$ stands for 2D divergence operator. Using this relation in Eq. 3.15 and applying the Green-Ostrogradsky theorem it gives:

$$\frac{dn}{dt} + \frac{1}{r_i S_i} \int_{\partial S_i} r\mathbf{F} \cdot \mathbf{dl} = 0 \tag{3.17}$$

where $\mathbf{dl}$ corresponds to the normal surface vector weighted by the edge length and similarly to the cartesian case presented in Section 3.3:

$$\int_{\partial S_i} r\mathbf{F} \cdot \mathbf{dl} = \sum_{\tau \in E(i)} \sum_{f \in \partial V_i \cap \tau} \int_f r\mathbf{F} \cdot \mathbf{dl} \tag{3.18}$$

In practice, it is straightforward to adapt a 2D vertex-centered scheme into a cylindrical one as we only need to multiply the surface vectors by the radius of their gravity center.

3.3.3 Numerical schemes for advection-diffusion

The development of the AVIP numerical schemes was driven by two main constraints: good HPC performance on an unstructured mesh and good accuracy. For a structured rectangular mesh, the Scharfetter-Gummel scheme is well adapted and widely used for streamer simulation. However, this scheme is difficult to use on triangular meshes. Regarding the good accuracy of the scheme, it is often accompanied by an increase of the stencil, which is not desirable to keep good parallel performances. To be efficient in parallel computations, the schemes developed in AVIP only require local information at the cell level, thus limiting inter-processor communications. Three numerical schemes for the scalar advection-diffusion transport have been used in this work. A First-Order Upwind (FOU) scheme is first developed in Section 3.3.3.1 and will serve for comparison with the other schemes. Then the Improved Scharfetter-Gummel (ISG) scheme [170, 97] is detailed in Section 3.3.3.2 and adapted for a generic triangular mesh. However, the ISG scheme accuracy exhibits a drastic loss of accuracy on triangular meshes. That is why the Limited Lax-Wendroff (LLW) scheme [80] for scalar transport has been developed. The Lax-Wendroff scheme is second-order accurate and a limiter is applied on top

of it to reduce numerical instabilities. This scheme is described in Section 3.3.3.3. Whereas the ISG scheme treats both the advective and diffusive fluxes, the FOU and LLW schemes are supplemented by a centered scheme for the diffusive fluxes, which is detailed in Section 3.3.3.4. More details concerning the validation of these schemes can be found in [43, 42]. Finally, the boundary conditions are discussed in Section 3.3.3.5.

3.3.3.1 First Order Upwind scheme

The FOU scheme is a first-order scheme that can be used to compare with higher-order schemes. It has the advantages of low computational cost and straightforward implementation. The residual across the face $\mathbf{S_{ij}^{\tau}}$ reads:

$$\int_f \mathbf{F}\cdot\mathbf{dS} = \max\left(0, \mathbf{V_{ij}}\cdot\mathbf{S_{ij}^{\tau}}\right)n_i + \min\left(0, \mathbf{V_{ij}}\cdot\mathbf{S_{ij}^{\tau}}\right)n_j \tag{3.19}$$

where $\mathbf{V_{ij}} = \frac{1}{2}(\mathbf{V_i} + \mathbf{V_j})$.

3.3.3.2 Improved Scharfetter-Gummel scheme

The Scharfetter-Gummel scheme originates from [170] and is very popular for plasma discharge modeling [114, 49, 184, 28, 172, 40]. It is based on the 1D advection-diffusion equation that reads:

$$\frac{\partial n}{\partial t} + \frac{\partial F}{\partial x} = 0 \tag{3.20}$$

with

$$F = nV - D\frac{\partial n}{\partial x} \tag{3.21}$$

Between two nodes i and $i+1$, it is assumed that F, V and D are constant and equal to their value at $i+1/2$. Then, Eq. 3.21 is considered as a differential equation with respect to n on the interval $[x_i,\, x_{i+1}]$ which has an analytical solution:

$$n(x) = \left(n_i - \frac{Fh_i}{D}\int_0^{\xi} e^{\alpha\xi'}d\xi'\right)e^{-\alpha\xi} \tag{3.22}$$

where $h_i = x_{i+1} - x_i$, $\xi = (x - x_i)/h_i$ and $\alpha = h_iV/D$. Evaluating Eq. 3.22 at node $i+1$ (*i.e.* $n(x_{i+1}) = n_{i+1}$) gives the desired expression of the flux at $x_{i+1/2}$:

$$F = \frac{\alpha D}{h_i(1-e^{\alpha})}(n_i - e^{\alpha}n_{i+1}) \tag{3.23}$$

An improved version of the scheme is due to the work of [97] who introduced a linear variation of the electric field in the interval $[x_i,\, x_{i+1}]$. In that case, an analytical solution of the flux F can be obtained assuming that $h_i \ll 2D/\Delta V_i$ where $\Delta V_i = |V_{i+1} - V_i|$. For the electrons, this condition can be expressed in terms of temperature using the Einstein relation that gives:

$$\frac{\Delta E_i h_i}{2T_e} \ll 1 \tag{3.24}$$

where $\Delta E_i = |E_{i+1} - E_i|$ and T_e is the electron temperature in eV. Physically, this condition constraints the potential drop between the nodes i and $i+1$ to be much smaller than the temperature. Thus, a finer spatial discretization must be used to ensure this condition. However, this solution leads to an increase of the computational cost as it requires a mesh refinement. Alternatively, an Improved Scharfetter-Gummel (ISG) scheme was proposed in [97]. The idea is to interpolate the density at virtual nodes L and R on the interval $[x_L, x_R]$ as represented in Fig. 3.6. The distance $h_v = x_R - x_L$ between these two nodes is chosen in order to verify the potential drop condition and verifies:

$$h_v = \sqrt{\epsilon_{\text{SG}} 2D h_i / |\Delta V_i|} \tag{3.25}$$

where $\epsilon_{\text{SG}} \in [0, 1]$ is a parameter which controls the scheme properties. Varying ϵ_{SG} from 0 to 1, the scheme passes from a low-diffusive but dispersive scheme into a monotonic but diffusive one. A recommended value of 0.01 was used in this work when not specified. In this work, the exponential interpolation of the density suggested in [97] has been used as it was easy to implement on an unstructured grid without the need for neighboring information. This

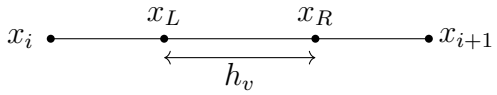

Figure 3.6: Interpolation procedure of the Improved Scharfetter-Gummel scheme.

It is important to notice that the Scharfetter-Gummel scheme was originally developed on a 1D grid and only gives a tangential flux estimate. It is pretty straightforward to adapt it on 2D cartesian grids composed of squares. However, its use on a non-topological mesh is not direct and is still subject to research. Primal cell (*i.e.* an element of the mesh) and nodal cell are topologically dual if they verify Eq. 3.26 for all the edges **ij** of the element. It means that all the element edges are perpendicular to the nodal volume surfaces. This is illustrated in Fig. 3.7 where an equilateral triangle (Fig. 3.7a) verifies this conditions whereas it is obviously not the case for all the triangles (Fig. 3.7b). In the rest of this section, the superscript τ is ignored in the dual surfaces to simplify the notations.

$$\frac{\mathbf{ij}}{||\mathbf{ij}||} = \frac{\mathbf{S}^{\tau}_{\mathbf{ij}}}{||\mathbf{S}^{\tau}_{\mathbf{ij}}||} \tag{3.26}$$

In [24], a flux reconstruction within the cell was performed based on the tangential edges fluxes using the Nedelec elements [138]. While being an elegant solution, an attempt to implement it did not end to a successful conclusion. It is possible that a mistake has been made in the implementation of this method and further work may be necessary. Another strategy was employed here to handle non-topological grids. We introduce the tangential and normal unit vectors respectively denoted $\mathbf{n}^{\parallel}_{\mathbf{ij}}$ and $\mathbf{n}^{\perp}_{\mathbf{ij}}$ defined as:

$$\mathbf{n}^{\parallel}_{\mathbf{ij}} = \frac{\mathbf{ij}}{||\mathbf{ij}||} \ , \quad \mathbf{n}^{\perp}_{\mathbf{ij}} = \mathbf{n}^{\parallel}_{\mathbf{ij}} \times \mathbf{z}$$

where $\mathbf{z}$ in the unit vector normal to the plane. The nodal surface $\mathbf{S_{ij}}$ can be split into tangential and normal components according to Eq. 3.27 and also shown in Fig. 3.7b.

$$\mathbf{S_{ij}} = \left(\mathbf{S_{ij}} \cdot \mathbf{n}^{\parallel}_{\mathbf{ij}}\right) \mathbf{n}^{\parallel}_{\mathbf{ij}} + \left(\mathbf{S_{ij}} \cdot \mathbf{n}^{\perp}_{\mathbf{ij}}\right) \mathbf{n}^{\perp}_{\mathbf{ij}} = S^{\parallel}_{ij} \mathbf{n}^{\parallel}_{\mathbf{ij}} + S^{\perp}_{ij} \mathbf{n}^{\perp}_{\mathbf{ij}} \tag{3.27}$$

The flux F can be split in the same manner:

$$\mathbf{F} = F^{\parallel}\mathbf{n}_{\mathbf{ij}}^{\parallel} + F^{\perp}\mathbf{n}_{\mathbf{ij}}^{\perp} \tag{3.28}$$

In the end, the flux crossing the nodal face $\mathbf{S_{ij}}$ is given by:

$$\mathbf{F} \cdot \mathbf{S_{ij}} = F^{\parallel} S_{ij}^{\parallel} + F^{\perp} S_{ij}^{\perp} \tag{3.29}$$

The parallel flux $F^{\parallel}$ can be obtained directly using the ISG flux along the edge **ij** as in the 1D case. To be consistent with the ISG scheme, the perpendicular flux component $F^{\perp}$ must contain both the advective and diffusive flux. The diffusive flux is always computed using a centered scheme. Two numerical schemes were tested for the advective flux: the FOU scheme described in Section 3.3.3.1 and a centered scheme. It was observed on streamer test cases that the use of a centered scheme for the advective flux leads to better results than with the FOU scheme. Thus, only the centered correction will be used when using the ISG scheme in Chapter 4. Finally, the perpendicular flux $F^{\perp}$ reads:

$$F^{\perp} = \left(\frac{n_i + n_j}{2} \frac{\mathbf{V_i} + \mathbf{V_j}}{2} + \frac{D_i + D_j}{2} \frac{\nabla n_i + \nabla n_j}{2} \right) \cdot \mathbf{n}_{\mathbf{ij}}^{\perp} \tag{3.30}$$

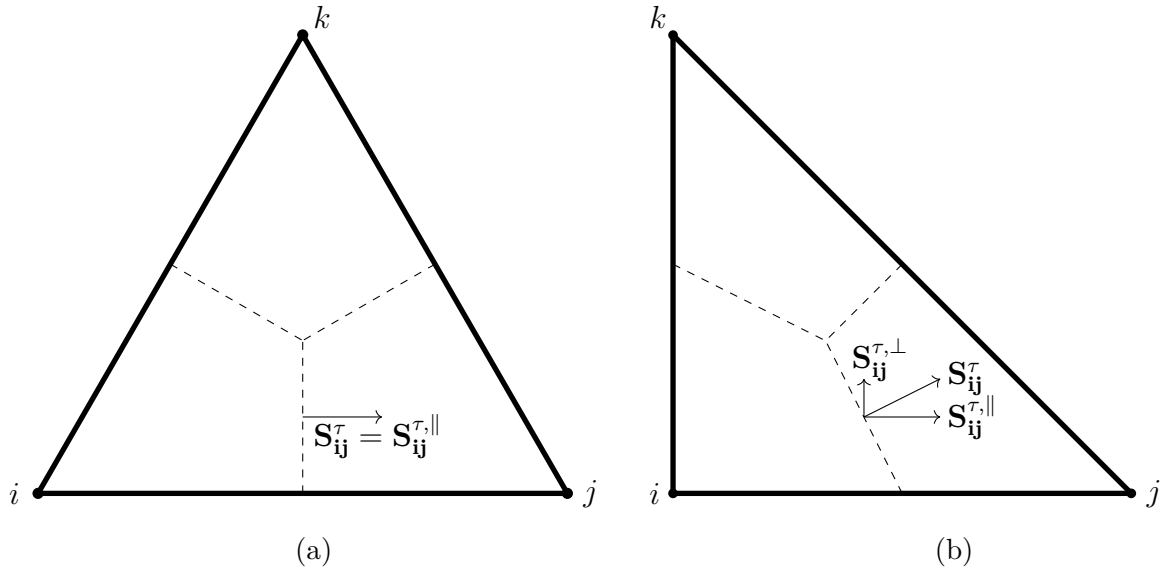

Figure 3.7: Nodal surface splitting on (a) an equilateral triangle and (b) a non-topological triangle.

3.3.3.3 Limited Lax-Wendroff scheme

This scheme has been developed in AVIP in the work of [42] and is briefly detailed here for convenience. The Lax-Wendroff scheme aims to solve the advection equation (Eq. 3.31) starting from a Taylor expansion in time of the variable n.

$$\frac{\partial n}{\partial t} + \nabla \cdot (n\mathbf{V}) = 0 \tag{3.31}$$

Then, the time derivative of n is replaced in the Taylor extension by its expression in Eq. 3.31, and only the three first terms are kept. Assuming a constant velocity along the edge **ij**, the LW flux finally writes:

$$\mathbf{F} = \left(n_{ij} - \frac{\Delta t}{2} \nabla n_{ij} \cdot \mathbf{V_{ij}} \right) \mathbf{V_{ij}} \tag{3.32}$$

where subscript ij refers to the mean value of the edge (*i.e.* $n_{ij} = (n_i + n_j)/2$). To stabilize this scheme, the non-monotonic term of the flux is limited by a Sweby limiter function Ψ [181] to form the Limited Law-Wendroff (LLW) scheme [80]:

$$\mathbf{F} = \left(n_i + \frac{1-\sigma}{2} (n_j - n_i) \Psi(R_i) \right) \mathbf{V_{ij}} \tag{3.33}$$

where σ is the CFL number and R_i is the gradient ratio approximated by Eq. 3.34 on unstructured grids as discussed in [42].

$$R_i = \frac{n_j - n_i - \nabla n_i \cdot \mathbf{ij}}{n_j - n_i} \tag{3.34}$$

Note that in practice, σ is not explicitly computed but is rather estimated by:

$$\sigma (n_j - n_i) = \frac{\Delta t}{2} \nabla n_{ij} \cdot \mathbf{V_{ij}} \tag{3.35}$$

and finally Eq. 3.33 becomes:

$$\mathbf{F} = \left[n_i + \left(\frac{1}{2} (n_j - n_i) - \frac{\Delta t}{2} \nabla n_{ij} \cdot \mathbf{V_{ij}} \right) \Psi(R_i) \right] \mathbf{V_{ij}} \tag{3.36}$$

3.3.3.4 Centered scheme for diffusive flux

The FOU and LLW schemes only compute the advective part of the flux and must be supplemented by another scheme for the diffusion part. In this work, the diffusive flux is computed using a central difference that reads:

$$\mathbf{F_D} = -\frac{D_i + D_j}{2} \frac{\nabla n_i + \nabla n_j}{2} \tag{3.37}$$

3.3.3.5 Boundary conditions

All the fluxes discussed above are applied on the interior surface of the domain $\partial V \cap \tau$. For a boundary node i of a triangular mesh depicted in Fig. 3.5, the nodal volume V_i needs to be closed by the fluxes across the blue and red surfaces:

$$\int_{\partial V_i^b} \mathbf{F} \cdot \mathbf{dS} = \mathbf{F_i^{\tau_1}} \cdot \mathbf{S_i^{b,\tau_1}} + \mathbf{F_i^{\tau_1}} \cdot \mathbf{S_i^{b,\tau_2}} \tag{3.38}$$

Two options have been considered to compute the flux $\mathbf{F_i^{\tau_1}}$:

1. $\mathbf{F_i^{\tau_1}} = 0.75\ \mathbf{F_i} + 0.25\ \mathbf{F_j}$
2. $\mathbf{F_i^{\tau_1}} = \mathbf{F_i}$

In the first option, a linear interpolation is used to approximate the flux at the boundary face center. Whereas it should be more accurate to use this formula, it could lead to numerical instabilities when a strong gradient occurs between the two nodes i and j. To prevent such a problem, the second option was preferred in most simulations.

Finally, two options were also considered for the nodal flux $\mathbf{F_i}$:

1. $\mathbf{F_i} = \mathbf{F_i^C} + \mathbf{F_i^D}$
2. $\mathbf{F_i} = \mathbf{F_i^C}$

where $\mathbf{F_i^C} = n_i \mathbf{V_i}$ and $\mathbf{F_i^D} = -D_i \nabla n_i$. The first option refers to a supersonic boundary condition. The second option assumes that $\nabla n_i \cdot S_i^{b,\tau_1} = 0$ in a weak way (*i.e.* it is not imposed in the solution) and corresponds to a Neumann boundary condition. This second option was used for streamer simulations by Tholin [184] for instance.

These boundary conditions are relatively simple and can not predict any sheath formation. However, they are simple to implement and allow a smooth solution at the electrode surfaces. More realistic conditions could be the subject of future work. For example, the boundary conditions given by Hagelaar et al. [73] include a thermal flux and secondary electron emission at the electrode surface.

3.3.4 Validation cases

The numerical schemes described above are now tested on different test cases to emphasize their major properties. In Section 3.3.4.1, the advection of a profile with constant velocity is analyzed. Then in Section 3.3.4.2, an advection-diffusion problem is solved with a linear velocity profile to demonstrate the usefulness of the Improved Scharfetter-Gummel scheme.

3.3.4.1 One-dimensional advection with a constant speed

A one-dimensional domain is used in this section with the main direction $x \in [-1, 1]$. One cell is used in the second direction y to perform a one-dimensional simulation in a 2D mesh. Both quadrangular and triangular elements are used as presented in Fig. 3.8. It is important to notice that the triangles used to mesh the one-dimensional domain do not form a topological mesh. Thus, the correction made on the ISG scheme will be tested. A periodic boundary condition is applied for the left and right patches, whereas a symmetry condition is applied for the top and bottom patches.

The one-dimensional advection equation is solved with a constant velocity $u = 1\,\mathrm{m\,s^{-1}}$ using two different initial profiles. A gaussian profile is used as a first test case without discontinuities. The profile considered is given by:

$$u(x, t = 0) = A \exp\left(-\frac{x}{\sigma}\right) \tag{3.39}$$

with $A = 1$ and $\sigma = 0.3$ m. A step profile is also used to analyze the scheme behavior when dealing with discontinuities. The step profile is given by:

$$u(x, t = 0) = \begin{cases} 1 & \text{if } x \in [-0.5, 0.5] \\ 0 & \text{otherwize.} \end{cases}$$

The results on a quadrangular mesh are shown in Fig. 3.9 after one full round for both initial profiles. The ISG scheme exhibits very similar behavior as the FOU scheme. Indeed, it can

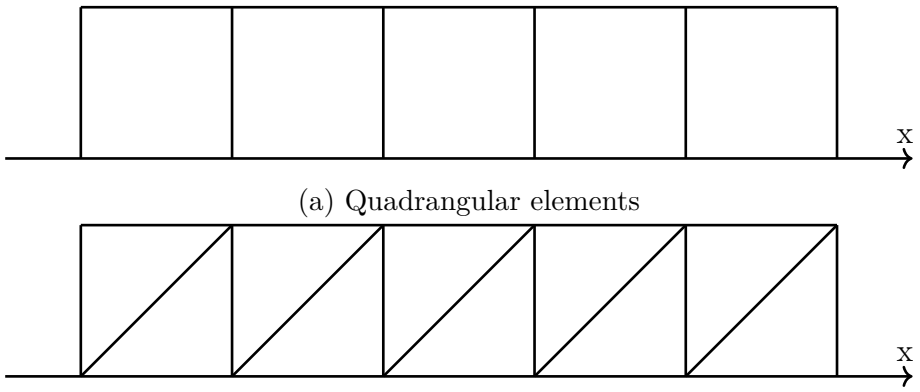

(a) Quadrangular elements

(b) Triangular elements

Figure 3.8: One-dimensional domains used for the advection test case with quandrangular and triangular elements.

be shown that the ISG scheme reduces to the FOU scheme when the velocity is constant and the diffusion coefficient tends toward zero. These two schemes significantly diffuse the gaussian after one round due to their low accuracy order. An excellent agreement is observed for the gaussian advection using the classical Lax-Wendroff (LW) scheme, whereas the profile is slightly damped when using the limited version of the scheme (LLW). However, non-satisfactory results are obtained with the LW scheme on the step profile advection. Significant spurious oscillations are produced close to the steps discontinuities and are amplified during the simulation. The LLW scheme does not produce these oscillations and is also less diffusive than the FOU and ISG schemes.

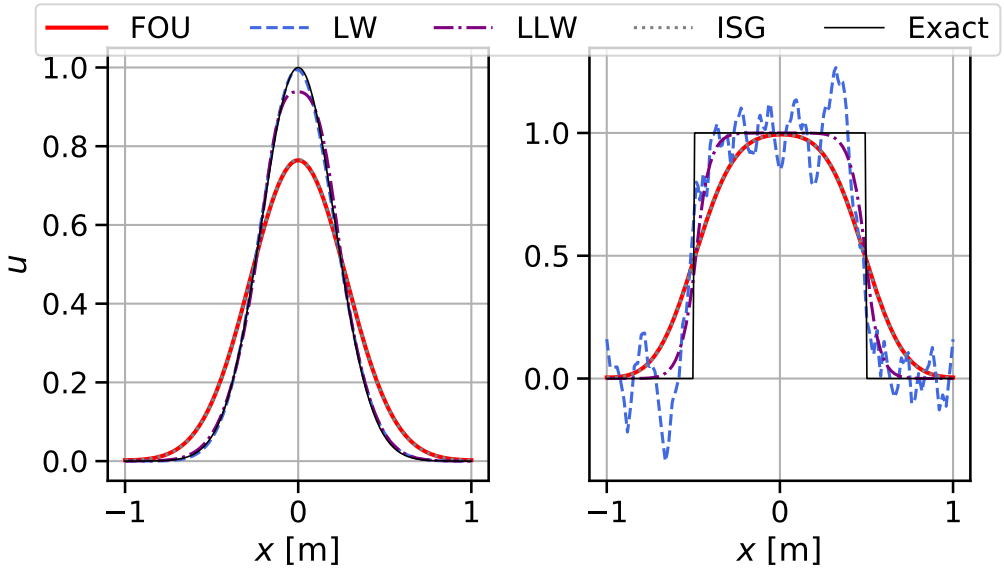

Figure 3.9: Solutions of the one-dimensional advection on quadrangular mesh at 101x2 resolution and CFL=0.3 using different initial conditions and different numerical schemes.

Figure 3.10 shows the results after one round using different schemes on a triangular mesh. Similar observations can be done for the LW and LLW schemes compared to simulations using

quadrangular elements. However, the ISG scheme is a bit less diffusive than the FOU scheme. This is due to the flux correction discussed in Section 3.3.3.2 which is second-order accurate in space. These two test cases validate the correction made on the ISG scheme for a non-topological mesh.

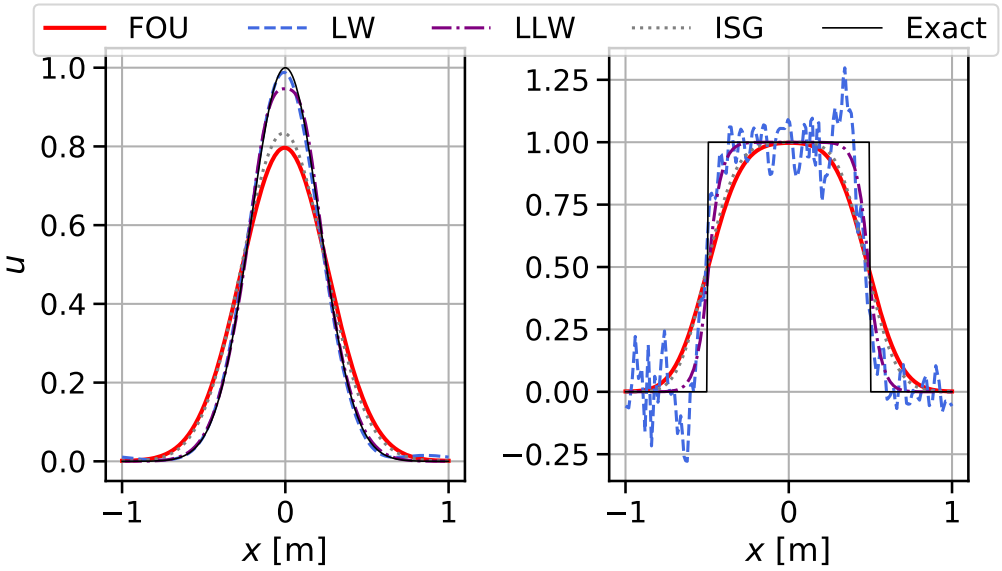

Figure 3.10: Solutions of the one-dimensional advection on triangular mesh at 101x2 resolution and CFL=0.3 using different initial conditions and different numerical schemes.

3.3.4.2 One-dimensional advection-diffusion with a variable speed

This test case is based on the work made by Kulikovsky [97] who developed the ISG scheme. It is used to illustrate the accuracy gain when using the ISG scheme in cases where the velocity varies. This test case aims to solve the 1D advection-diffusion equation given by:

$$\frac{\partial u}{\partial t} - \frac{\partial Axu}{\partial x} - D\frac{\partial^2 u}{\partial x^2} = 0 \tag{3.40}$$

where $W = -Ax$ is the convective speed with $A = 10^4 \mathrm{s}^{-1}$ and $D = 1\,\mathrm{m}^2\,\mathrm{s}^{-1}$ is the diffusion coefficient. This equation corresponds to the drift-diffusion equation with a mobility $\mu = -1$ and a linear electric field $E(x) = Ax$. In the pure advection limit ($D \to 0$), this equation has an exact solution given by [97]:

$$u(x,t) = u_0(xe^{At})e^{At} \tag{3.41}$$

where u_0 is the initial solution profile. The initial condition considered here is given by:

$$u_0(x) = u_1\frac{1}{2}\left[1 + \tanh\left(\frac{x - x_0}{\sigma}\right)\right]u_2 \tag{3.42}$$

where $\sigma = 0.02\,\mathrm{m}$, $x_0 = 0.7\,\mathrm{m}$, $u_1 = 10^2$ and $u_2 = 10^{12}$. This initial solution leads to a very strong gradient with ten orders of magnitude difference representing those encountered in streamer simulations. The results using different schemes are shown in Figs. 3.11a and 3.11b for quadrangular and triangular elements respectively. All the schemes were able to simulate this

test case on a quadrangular mesh with a coarse resolution without any significant numerical oscillation. The FOU scheme is significantly more diffuse than the other schemes. A better agreement is found when using the LW and LLW schemes. Only very small oscillations are present at the top of the gradient using the LLW scheme. Finally, the ISG scheme ($\varepsilon_{SG} = 0.01$) produces the best results, showing the interest of this scheme. It has been observed that the ISG scheme is stable up to CFL=0.6 while the three others are stable up to CFL=1. Now looking at the results on the triangular elements, both FOU and LLW schemes show similar results than in the quadrangular case. A good agreement is found for the front propagation using both the LW and ISG schemes. However, a weird artifact can be observed on the flat part around $x = 0.7\,\mathrm{m}$ and must be further investigated.

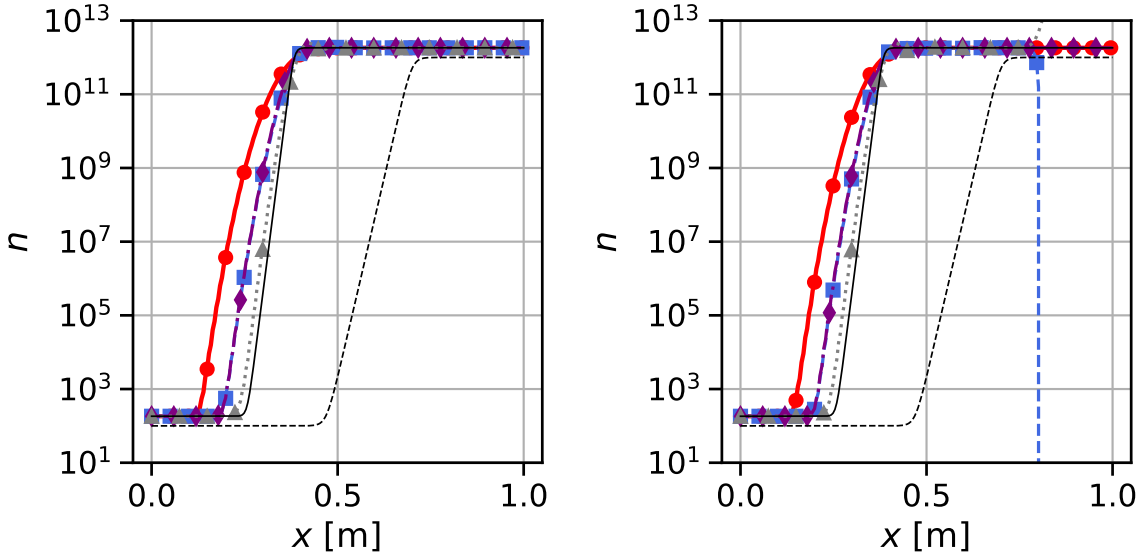

(a) Quadrangular elements

(b) Triangular elements

Figure 3.11: Solutions of the stiff one-dimensional advection on quadrangular and triangular meshes at 101x2 resolution and CFL=0.3 using different numerical schemes: (●) FOU, (■) LW, (♦) LLW, (▲) ISG, (- - -) Initial solution, (—) Analytical solution.

3.4 Poisson equation

In the electrostatic approximation, the electric field **E** can be obtained by solving the Poisson equation as already discussed in Section 2.4.4. This equation involves a Laplacian operator that needs to be discretized. A Vertex-Centered Finite Volume discretization is presented in Section 3.4.1. Then the linear system resolution is briefly discussed in Section 3.4.3.

3.4.1 Discretization of the Poisson equation

The aim of this section is to discretize the Laplacian operator, which appears in the Poisson equation:

$$\nabla^2 \phi = -\frac{\rho_c}{\epsilon_0} \tag{3.43}$$

This equation is now integrated over a nodal volume V_i assuming a constant charge density ρ_c^i in V_i:

$$\int_{V_i} \nabla^2 \phi dV = -\frac{1}{\epsilon_0} \int_{V_i} \rho_c dV = -\frac{\rho_c^i V_i}{\epsilon_0} \tag{3.44}$$

We now focus on the left-hand side of Eq. 3.44 by applying the Green-Ostrogradsky theorem on it:

$$\int_{V_i} \nabla^2 \phi dV = \underbrace{\int_{\partial \dot{V}_i} \nabla \phi \cdot \mathbf{dS}}_{\text{Interior}} + \underbrace{\int_{\partial V_i^b} \nabla \phi \cdot \mathbf{dS}}_{\text{Boundary}} \tag{3.45}$$

In Eq. 3.45, the integral has been divided into the interior surface $\partial \dot{V}_i = \partial V_i \cap \dot{\Omega}$ and the boundary surface $\partial V_i^b = \partial V_i \cap \partial \Omega$ of the node i. As for the drift-diffusion fluxes in Section 3.3.3, the interior surface integral is written as a sum over the faces f of the nodal volume:

$$\int_{\partial \dot{V}_i} \nabla \phi \cdot \mathbf{dS} = \sum_{\tau \in E(i)} \sum_{f \in \partial \dot{V}_i \cap \tau} \int_f \nabla \phi \cdot \mathbf{dS} \tag{3.46}$$

where $\tau \in E(i)$ corresponds to the cells containing the node i and $\partial \dot{V}_i \cap \tau$ is the set of surfaces of the nodal volume V_i in the cell τ. It is assumed that the gradient is constant within a cell τ so that Eq. 3.46 becomes:

$$\int_{\partial \dot{V}_i} \nabla \phi \cdot \mathbf{dS} = \sum_{\tau \in E(i)} \nabla \phi_\tau \cdot \sum_{f \in \partial \dot{V}_i \cap \tau} \int_f \mathbf{dS} = \sum_{\tau \in E(i)} \nabla \phi_\tau \cdot \sum_{j \in S(i) \cap \tau} \mathbf{S_{ij}^\tau} \tag{3.47}$$

where $\mathbf{S_{ij}^\tau}$ is defined in Eq. 3.9 and shown in Fig. 3.4. The cell gradient $\nabla \phi_\tau$ is computed using the Green-Ostrogradsky theorem:

$$\nabla \phi_\tau = \frac{1}{V_\tau} \int_{V_\tau} \nabla \phi \; dV \tag{3.48}$$

$$= \frac{1}{V_\tau} \int_{\partial V_\tau} \phi \mathbf{dS} \tag{3.49}$$

$$= \frac{1}{V_\tau} \sum_{f \in \tau} \phi_f \mathbf{S_f} \tag{3.50}$$

where V_τ is the volume of the cell τ and $\mathbf{S_f}$ a normal surface vector of the cell τ. As in AVBP [105], the nodal surface vector $\mathbf{S_k}$ of the node k is linked to its adjacent cell surface vector $\mathbf{S_f}$ by Eq. 3.3. Then assuming that the face potential ϕ_f is the average of the potential at the neighboring vertices, Eqs. 3.50 and 3.3 give:

$$\nabla \phi_\tau = -\frac{1}{V_\tau n_d} \sum_{k \in \tau} \phi_k \mathbf{S_k} \tag{3.51}$$

where the sum is performed over the vertices k of the cell τ. Following Auffray [13], the nodal volume faces $\mathbf{S_{ij}^\tau}$ are linked to the nodal cell surface $\mathbf{S_k}$:

$$\sum_{j \in S(i) \cap \tau} \mathbf{S_{ij}^\tau} = \frac{\mathbf{S_i}}{n_d} \tag{3.52}$$

By injecting Eqs. 3.51 and 3.52 into Eq. 3.46 it yields:

$$\int_{V_i} \nabla^2 \phi dV = \sum_{\tau \in E(i)} \sum_{k \in \tau} -\frac{\mathbf{S_k} \cdot \mathbf{S_i}}{V_\tau n_d^2} \phi_k \tag{3.53}$$

Finally, the Poisson equation can be reformulated as a linear system:

$$\mathbf{Ax} = \mathbf{b} \tag{3.54}$$

where $\mathbf{A}$ is the Laplacian operator matrix defined by Eq. 3.55 in which the sum is performed over the cells containing the edge ij, $\mathbf{x}^T = [\phi_1, ...\phi_N]$ is the unknwon vector containing the nodal potential values and $\mathbf{b}$ is the rhs term given by Eq. 3.56.

$$a_{ij} = \sum_{ij \in \tau} -\frac{\mathbf{S_i} \cdot \mathbf{S_j}}{V_\tau n_d^2} \tag{3.55}$$

$$b_i = \frac{\rho_c^i V_i}{\epsilon_0} \tag{3.56}$$

After having built this linear system with the interior nodes, it is still necessary to complete the system with the boundary face contributions corresponding to the second term in Eq. 3.45:

$$\int_{\partial V_i^b} \nabla \phi \cdot \mathbf{dS} = \sum_{f \in \partial V_i^b} \nabla \phi_n ||S_f^b|| \tag{3.57}$$

Two boundary conditions have been considered in this work: a Neumann condition which imposes the normal potential gradient $\nabla \phi_n = E_n$ and a Dirichlet boundary condition for which the value of the potential is fixed.

Dirichelet boundary condition The potential ϕ_i of the node i is already known in a Dirichlet boundary condition. To impose this value in the linear system, the i^{th} line of the matrix $\mathbf{A}$ is modified with $a_{ij} = \delta_{ij}$ and the associated component in the rhs vector $\mathbf{b}$ is fixed to the value of the imposed potential ϕ_0.

Neumann boundary condition As shown in Eq. 3.57, the normal surface gradient appears in the boundary term of the Laplacian operator integral. This contribution is taken into account in the rhs vector $\mathbf{b}$ for which a Neumman boundary node i reads:

$$b_i = \frac{\rho_c^i V_i}{\epsilon_0} - \sum_{f \in \partial V_i^b} E_n ||S_f^b|| \tag{3.58}$$

3.4.2 Cylindrical coordinates

As for the transport equations in Section 3.3.2, the Poisson equation needs to be solved in an axisymmetric framework using cylindrical coordinates (r, θ, z) for most streamer simulations. In that case, the integration of the Laplacian operator over the nodal volume V_i gives (see details in Section 3.3.2):

$$\frac{1}{V_i} \int_{V_i} \nabla^2 \phi dV = \frac{1}{r_i S_i} \int_{S_i} \nabla \cdot (\nabla \phi) r dS \tag{3.59}$$

using the properties of the divergence operator in cylindrical coordinates given in Eq. 3.16 it yields:

$$\int_{V_i} \nabla^2 \phi dV = \int_{S_i} \nabla \cdot (r \nabla \phi) dS \tag{3.60}$$

Then applying the divergence theorem and assuming a constant potential gradient in a cell:

$$\int_{V_i} \nabla^2 \phi dV = \sum_{\tau \in E(i)} \nabla \phi_\tau \sum_{j \in S(i) \cap \tau} r \mathbf{S}_{\mathbf{ij}}^\tau \tag{3.61}$$

where $\mathbf{S}_{\mathbf{ij}}^\tau$ is homogeneous to a length. Equation 3.51 remains valid here as $\nabla \phi_\tau$ is a two-dimensional gradient. For a triangular element, two faces are considered to form the nodal surface in the cell τ: $\mathbf{S}_{\mathbf{ij}}^\tau$ and $\mathbf{S}_{\mathbf{ki}}^\tau$. Thus we have:

$$\sum_{j \in S(i) \cap \tau} r \mathbf{S}_{\mathbf{ij}}^\tau = \frac{r_{ij}^\tau + r_\tau}{2} \mathbf{S}_{\mathbf{ij}}^\tau + \frac{r_{ki}^\tau + r_\tau}{2} \mathbf{S}_{\mathbf{ki}}^\tau \tag{3.62}$$

with $r_{ij}^\tau = (r_i + r_j)/2$ the center of the edge ij and $r_\tau = \frac{1}{n_v^\tau} \sum_{k \in \tau} r_k$ the cell center (n_v^τ is the number of vertices in the cell τ). From Auffray [13], there is a simple relation between the normal surfaces of the dual volume $\mathbf{S}_{\mathbf{ij}}^\tau$ and the nodal surfaces $\mathbf{S_i}$ for a triangle:

$$\mathbf{S}_{\mathbf{ij}}^\tau = \frac{1}{6} (\mathbf{S_i} - \mathbf{S_j}) \tag{3.63}$$

that leads to:

$$\sum_{j \in S(i) \cap \tau} r \mathbf{S}_{\mathbf{ij}}^\tau = \frac{1}{24} [(4r_\tau + 2r_i + r_j + r_k)\mathbf{S_i} - (2r_\tau + r_i + r_j)\mathbf{S_j} - (2r_\tau + r_i + r_k)\mathbf{S_k}] \tag{3.64}$$

A very similar expression can be found for quadrangular elements starting from:

$$\sum_{j \in S(i) \cap \tau} r \mathbf{S}_{\mathbf{ij}}^\tau = \frac{r_{ij}^\tau + r_\tau}{2} \mathbf{S}_{\mathbf{ij}}^\tau + \frac{r_{li}^\tau + r_\tau}{2} \mathbf{S}_{\mathbf{li}}^\tau \tag{3.65}$$

Considering the following relation from Auffray [13]:

$$\mathbf{S}_{\mathbf{ij}}^\tau = \frac{1}{4} (\mathbf{S_i} - \mathbf{S_l}) \tag{3.66}$$

it finally gives:

$$\sum_{j \in S(i) \cap \tau} r \mathbf{S}_{\mathbf{ij}}^\tau = \frac{1}{16} [(4r_\tau + 2r_i + r_j + r_l)\mathbf{S_i} - (2r_\tau + r_i + r_j)\mathbf{S_j} - (2r_\tau + r_i + r_l)\mathbf{S_l}] \tag{3.67}$$

3.4.3 Solver and options

The linear system described given by Eqs. 3.54, 3.55 and 3.56 is solved using the external library PETSc [17]. During this Ph.D., the solver options have been taken from PETSc recommendations and are summarized in Tab. 3.1. These options were found to be efficient on triangular meshes in all the cases tested in this work. Moreover, the use of a non-zero initial

guess was found to be very efficient in streamer simulation. Indeed, the potential ϕ does not vary significantly between two iterations and the solution at the iteration $n-1$ can be used as an initial guess at iteration n. Whereas this solution works well for a constant electrode potential, the solver performances are drastically reduced (up to a factor of two) when the applied voltage is varying in time. To solve this issue, the initial guess at iteration n, ϕ_g^n, is multiplied by the voltage ratio between the two successive iterations and reads

$$\phi_g^n = \phi^{n-1} \frac{V^n}{V^{n-1}} \tag{3.68}$$

where V^n is the applied voltage at iteration n.

ksp_type	cg
ksp_norm_type	unpreconditioned
ksp_rtol	10^{-10}
pc_type	gamg
mg_levels_pc_type	sor
mg_levels_ksp_type	richardson
pc_mg_levels	4

Table 3.1: Options used to solve the Poisson equation with the external library PETSc

3.5 Time-step constraints

Time-step limitations must be applied to ensure a simulation's stability and accuracy using an explicit time integration. The Courant-Friedrichs-Lewy (CFL) and Fourier conditions must be verified for an advection-diffusion problem. The CFL condition allows to define a time-step Δt_{CFL} which is related to the convection and is given by Eq. 3.69. For a pure advection problem, the FOU scheme with an Euler time integration is theoretically stable up to CFL=1. Thus, the CFL was set to 0.7 in most simulations.

$$\Delta t_{\mathrm{CFL}} = \frac{\mathrm{CFL}\ \Delta x}{||\mathbf{U}||} \tag{3.69}$$

The Fourier condition ensures the stability of the diffusion fluxes with a limiting time-step Δt_{F} given by Eq. 3.70. The maximum Fourier coefficient F depends on the diffusive fluxes discretization and the dimension. For a 2D case employing a 2^{nd} order centered scheme, we must have $F \leq 0.25$. Thus the value of F was set to 0.1 in most simulations. Note that this constraint can be very restrictive for plasma simulation, which requires very fine spatial discretization.

$$\Delta t_{\mathrm{F}} = \frac{F \Delta x^2}{D} \tag{3.70}$$

When unstructured grids are employed, the definition of the spatial discretization step Δx is not straightforward. It has been estimated at each cell τ using its volume V_τ as $\Delta x = V_\tau^{1/d}$ where d is the dimension of the simulation.

For a charged species system of drift-diffusion equations that are linked together by the Poisson equation, the dielectric (or Maxwell) time-step Δt_{D} given by Eq. 3.71 must also be

taken into account as in [49, 184]. This time-step is characteristic of the electric field screening inside a conducting channel as explained in [183]. As it is inversely proportional to the electron density, it becomes restrictive when the electrical current is important with $\Delta t_{\mathrm{D}} \approx 10^{-15} - 10^{-14}$ s. It was observed that $A_{\mathrm{D}} = 1$ gives good results in most cases and tis value was adopted in this work when not specified. Note that it is possible to relax this condition with a semi-implicit formulation of the Poisson equation as explained in [71, 200]. However, this method was not employed in this work as it would have involved computing the Poisson matrix at each iteration, which is an expensive task.

$$\Delta t_{\mathrm{D}} = A_D \frac{\epsilon_0}{\sum_k |q_k n_k \mu_k|} \simeq A_D \frac{\epsilon_0}{e n_e \mu_e} \tag{3.71}$$

To ensure the stability of the chemical source terms that are integrated explicitly, a chemical time step Δt_{C} was introduced and defined by Eq. 3.72. The coefficient A_{C} can be interpreted as the maximum variation of a species mass due to the chemistry during one iteration. It has been set to 5×10^{-2} in most simulations.

$$\Delta t_{\mathrm{C}} = A_{\mathrm{C}} \min_k \left(\frac{\rho_k}{|\dot{\omega}_k|} \right) \tag{3.72}$$

In the end, the time-step Δt considered in the simulation is given by:

$$\Delta t = \min \left(\Delta t_{\mathrm{CFL}}, \Delta t_{\mathrm{F}}, \Delta t_{\mathrm{D}}, \Delta t_{\mathrm{C}} \right) \tag{3.73}$$

In pratice, the spark model described in Section 3.6.1 is used to evaluate the electric field in order to overcome the dielectric time-step constraint when it becomes lower than an user defined time-step threshold. This value was set to 5×10^{-14} s, which has been determined empirically and is only reached during the spark phase of the discharge. Hence during the spark phase, the time-step is computed using:

$$\Delta t = \min \left(\Delta t_{\mathrm{CFL}}, \Delta t_{\mathrm{F}}, \Delta t_{\mathrm{C}} \right) \tag{3.74}$$

Typical time evolution of the time-step during the high-voltage pulse and the afterglow is shown in Fig. 3.12. Up to $t = 8$ ns, the time-step is limited by the Fourier constraint which gives $\Delta_{\mathrm{F}} \simeq 5 \times 10^{-13}$ s. Then, the time-step is limited by the dielectric constraint up to 10 ns and sharply decreases to small values on the order of 10^{-14} s. The spark model is activated to overcome this constraint, leading to a significant increase of the time-step during the spark phase of the discharge. At the end of the pulse ($t = 18$ ns), the ambipolar model discussed in Section 3.6.2 is used to suppress the Fourier constraint from the electrons. During the first instant of the afterglow, the chemical time-step limits the time-step. The chemical time-step quickly increases as the short-life species start to be consumed. Finally, the time-step is stabilized and reaches Δt_{F} at 200 ns with $\Delta t \simeq 5 \times 10^{-11}$ s.

3.6 Simplified models for electric field

Simplified models to compute the electric field were used in this work when possible to save computational time based on the work of Tholin [184].

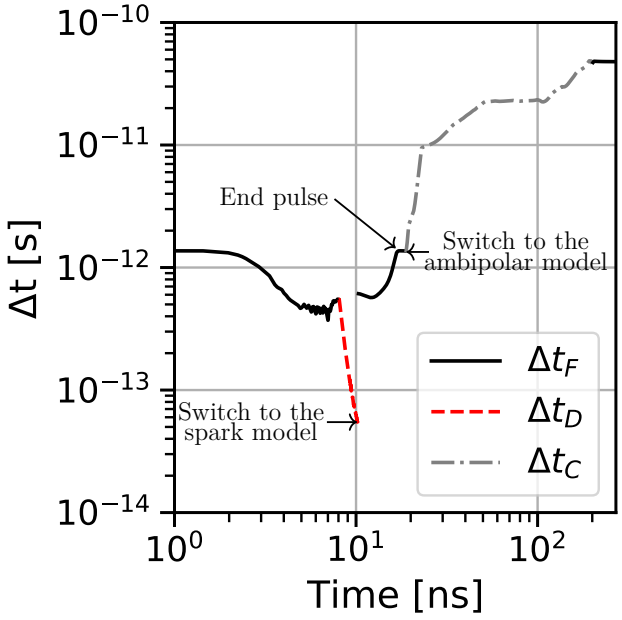

Figure 3.12: Typical timestep in a streamer simulation during the high-voltage pulse and the afterglow taken from the simulation performed in Section 12.2.3.

3.6.1 Spark model

As its name suggests, this model is used when the discharge enters in the spark phase characterized by a high electrical current. As a consequence of the high current, the dielectric time-step sharply decreases to values lower than 1×10^{-15} s, and the computational cost rises. During this phase, the electric field is nearly uniform within the inter-electrode gap while the electron density continues to grow if the Laplacian electric field is above the breakdown field. Thus, to overcome the dielectric time-step limitation, the Poisson equation is replaced by a simple model developed in [184] and briefly described here. The spatial shape of the electric field is assumed to stay constant and its magnitude varies as the potential V at the anode. Starting from an initial electric field computed with the Poisson equation, the time evolution of the electric field magnitude is given by:

$$||\mathbf{E}||^{-1} \frac{\partial ||\mathbf{E}||}{\partial t} = V^{-1} \frac{\partial V}{\partial t} \tag{3.75}$$

From Gauss's law, space charge ρ_c must evolve as the electric field:

$$\rho_c^{-1} \frac{\partial \rho_c}{\partial t} = V^{-1} \frac{\partial V}{\partial t} \tag{3.76}$$

This space charge variation is ensured by an electron source term $\dot{S}_e^{\text{spark}}$ that reads:

$$\dot{S}_e^{\text{spark}} = \left(\frac{V(t + \Delta t)}{V(t)} - 1 \right) \frac{m_e}{e \Delta t} \rho_c \tag{3.77}$$

3.6.2 Ambipolar electric field

At the end of the high-voltage pulse, the applied voltage is usually small with some reflected pulses as observed, for example, in Rusterholtz et al. [167]. Thus, in this work, the applied

voltage was set to zero during the interpulse period and the Laplacian electric field is null. In that case, electrons diffuse faster than ions because of the four orders of magnitude between their diffusion coefficients [136]. This difference leads to the formation of a thin space charge layer at the edge of the plasma channel that produces the so-called ambipolar electric field $\mathbf{E}_{\text{amb}}$ which slows down the electrons and accelerates the ions to preserve the quasi-neutrality (*i.e.* $\rho_{\text{c}} = 0$) of the plasma channel. As a result, the electrons and ions diffuse at the same speed. To preserve the quasi-neutrality, the balance of charged species fluxes $\mathbf{F_k}$ must verify:

$$\sum_k q_k \mathbf{F_k} = \mathbf{0} \tag{3.78}$$

where $\mathbf{F_k} = n_k q_k \mu_k \mathbf{E}_{\text{amb}} - D_k \nabla n_k$. Then, the ambipolar electric field is given by:

$$\mathbf{E}_{\text{amb}} = \frac{\sum_k q_k D_k}{\sum_k n_k \mu_k} \tag{3.79}$$

It is interesting to note that a good estimate of the charged species fluxes $\mathbf{F_k}$ can be obtained by assuming that all charged species k diffuse at the velocity of the positive ions (*i.e.* $\mathbf{F_k} = -D_p \nabla n_k$ with D_p the positive ion diffusion coefficient and $E_{\text{amb}} = 0$) as discussed in [184, 140]. The validity of this assumption was verified in [184] at $T = 300\,\text{K}$ and $T = 1000\,\text{K}$ with less than 20% error compared to the use of Eq. 3.79. At $T = 300\,\text{K}$, charged species are dominated by positive and negative ions while electron density quickly vanishes. Both the mobilities and diffusion coefficients of positive and negative ions are very close in the air. At $T = 1000\,\text{K}$, electron density remains high of the same order of magnitude as the positive ions. Neglecting the presence of negative ions, the positive ion flux $\mathbf{F_p}$ using $\mathbf{E}_{\text{amb}}$ from Eq. 3.79 is given by:

$$\mathbf{F_p} = -\nabla n_p \left(D_p + \frac{\mu_p}{\mu_e} D_e \right) \tag{3.80}$$

At 1000 K, you have $D_p \approx 5\frac{\mu_p}{\mu_e} D_e$ that justifies to diffuse all the species with the positive ions diffusion coefficient. Thus in practice, when the ambipolar electric field model is used, all the species fluxes reduce to:

$$\mathbf{F_k} = -D_p \nabla n_k \tag{3.81}$$

From a numerical point of view, this assumption significantly speeds up the computation of the interpulse period. Indeed, the Fourier condition mostly restricts the time-step during this phase. At $1000\,\text{K}$ $D_e \simeq 1 \times 10^{-1}\,\text{m}^2\,\text{s}^{-1}$ and $D_p \simeq 1 \times 10^{-4}\,\text{m}^2\,\text{s}^{-1}$ which, for a typical cell size of $10\,\mu\text{m}$, give respectively a Fourier time-step of $1\,\text{ns}$ and $1\,\mu\text{s}$. Thus, in most cases, the charged species' diffusive time-step is not effective during the interpulse period when considering the positive ions diffusion coefficient.

Chapter 4

Streamer simulations

Contents

This chapter aims to verify the capacity of the code to simulate streamer propagation under different conditions. A code verification is first performed in Section 4.1 by comparing AVIP to six other low-temperature plasma codes [15]. In this first test case, a positive streamer propagation between two parallel electrodes is simulated with different initial conditions. This test case includes different degrees of difficulty by varying the density gradient and also validates the photoionization source term. Closer to the configurations simulated in Part III, the propagation of positive and negative streamers are simulated between two hyperbolic electrodes in Sections 4.2. This last case takes advantage of the AVIP's capacity to handle unstructured meshes that can easily mesh any electrode shapes.

4.1 Streamer benchmark

In this section, the AVIP code is compared to six other low-temperature plasma codesreferenced in the benchmark of Bagheri et al. [15]. This benchmark is quite challenging for AVIP, which is a fully unstructured code. Indeed, four of the six group's results compared in [15] are obtained with structured codes on which it is easier to build high-order numerical methods for instance.

Only the commercial code COMSOL Multiphysics© relies on unstructured grids in [15], all the other self-implemented codes relying on structured grids. Table 4.1 summarized the numerical features of the codes used in [15] as well as those of AVIP.

Group name	CWI	ES	FR	CN	TUE	DE	CERFACS
Code name	Afivo	ARCoS	-	COMSOL©	PLASIMO	COMSOL©	AVIP
Method	FV	FV	FV	FE	FV	FE	FV
Unstructured grid	No	No	No	Yes	No	Yes	Yes
Spatial discretization order	2	2	2	1	2	1	1 to 2
Implicit time discretization	No	No	No	Yes	Yes	Yes	No
Time discretization order	2	2	2	1 to 2	1	1 to 5	1
Adaptive Refinement	Yes	Yes	No	Yes	No	No	No
Parallel	Yes	No	Yes	Yes	No	Yes	Yes

Table 4.1: A summary of the code implementations adapted from [15, Table 1] (FV: Finite Volume, FE: Finite Element)

4.1.1 Numerical setup

In all the cases presented in Section 4.1, a positive streamer is simulated between two parrallel electrodes in dry air (80% N_2 and 20% O_2) at $T = 300$ K and $P = 1$ bar. These conditions correspond to a neutral background density of $2.414 \times 10^{25}\,\mathrm{m}^{-3}$. The electrodes are separated by 1.25 cm with an anode potential fixed at $\phi = 18.75$ kV as depicted in Fig. 4.1. This applied voltage corresponds to a Laplacian electric field of $-1.5\,\mathrm{MV\,m}^{-1}$ which is much lower than the breakdown field in these conditions (see Section 4.1.2). To locally enhance the electric field and trigger the propagation of a positive streamer, a non-neutral initial solution is used, including a gaussian seed of positive ions that reads:

$$n_p(x, r) = n_b + N_0 \exp\left(-\frac{r^2 + (x - x_0)}{\sigma^2}\right) \tag{4.1}$$

where n_b is an homogeneous background ionization level which can vary, $N_0 = 5 \times 10^{18}\,\mathrm{m}^{-3}$, $x_0 = 1$ cm and $\sigma = 0.4$ mm. This initial seed is schematically represented in red in Fig. 4.1.

For the Poisson equation, Dirichlet boundary conditions are used for the electrodes, while a Neumann boundary condition is applied for the top and bottom patches. The resulting initial electric field is shown in Fig. 4.2. The electric field is strongly enhanced close to the positive ions seed with a peak value around $8.3\,\mathrm{MV\,m}^{-1}$. This value is much higher than the breakdown electric field allowing to initiate the propagation of a positive streamer.

A symmetry boundary condition is applied on the cylindrical axis patch for the drift-diffusion equation, while the others are treated with Neumann boundary conditions.

Different meshes have been used in this study to evaluate the influence of the cell type (quadrangle or triangle) and the numerical scheme. As for most of the groups in [15], the mesh is refined near the axis ($r \leq 2$ mm) with a cell size ranging from 1 to 5 µm. Then, the mesh is expanded up to $r = 1.25$ cm with coarser cells. The three numerical schemes presented in Chapter 3 are investigated and are referred to as FOU (First Order Upwind), LLW (Limited Lax-Wendroff) and ISG (Improved Scharfetter-Gummel) with a CFL coefficient of 0.7 and a Fourier coefficient of 0.1.

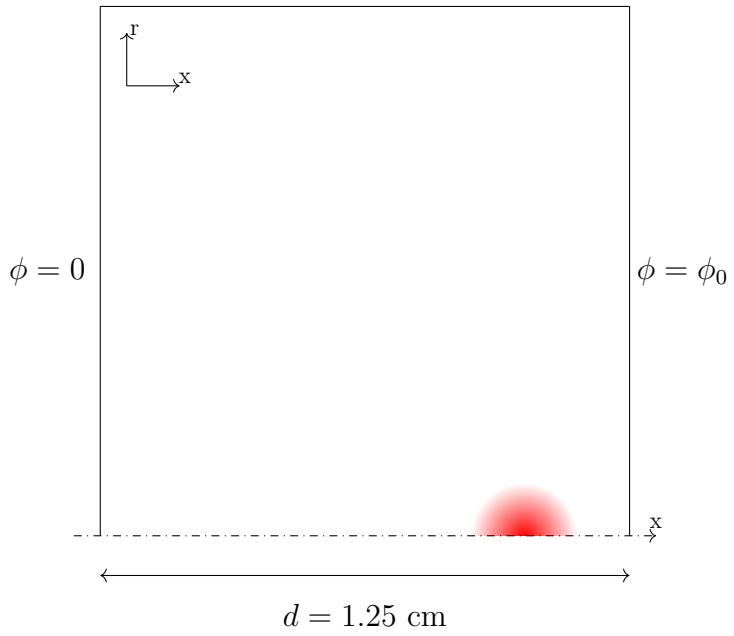

Figure 4.1: Sketch of the configuration used in Bagheri et al. [15]. The red area schematically corresponds to the initial seed of positive ions.

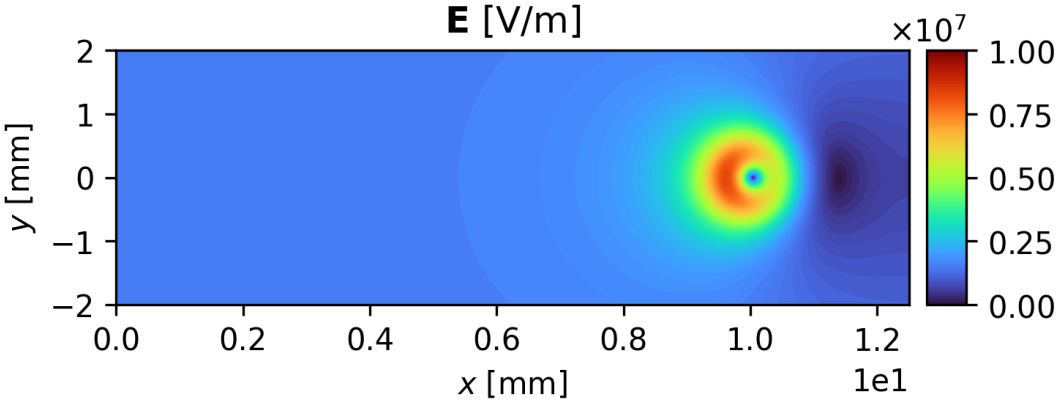

Figure 4.2: Initial electric field resulting from the initial conditions used in [15]

4.1.2 Simplified chemistry and transport parameters

A very simple chemical model for streamer propagation is used in this study. The charged species are only composed of electrons and a global positive ion. Moreover, the positive ions are not transported as the simulations last no more than a few nanoseconds and they do not have time to move significantly. Thus, the governing equations read:

$$\frac{\partial n_e}{\partial t} + \nabla \cdot (-n_e \mu_e \mathbf{E} - D_e \nabla n_e) = \bar{\alpha} |\mathbf{v_e}| + S_{ph} \tag{4.2}$$

$$\frac{\partial n_p}{\partial t} = \bar{\alpha} |\mathbf{v_e}| + S_{ph} \tag{4.3}$$

where $\mu_e > 0$ is the electron mobility, D_e is the electron diffusion coefficient, $\bar{\alpha} = \alpha - \eta$ is the effective ionization coefficient, $\mathbf{E}$ is the electric field, $\mathbf{v_e} = -\mu_e \mathbf{E}$ is the electron drift-velocity

and S_{ph} is the photoionization source term. The electric field is obtained by solving the Poisson equation through the electrostatic approximation. All the coefficients of the model (*i.e.* $\bar{\alpha}$, μ_e and D_e) are assumed to be a function of the reduced electric field only, so that we use the Local Field Approximation. These coefficients are taken from [58, 74] and depend on the gas temperature. At the physical conditions considered here, they read:

$$\mu_e = 2.3987|\mathbf{E}|^{-0.26}\ \mathrm{m^2\,V^{-1}\,s^{-1}} \tag{4.4}$$

$$D_e = 4.3628\times10^{-3}|\mathbf{E}|^{0.22}\ \mathrm{m^2\,s^{-1}} \tag{4.5}$$

$$\alpha = \left(1.1944\times10^{6} + 4.3666\times10^{26}|\mathbf{E}|^{-3}\right)\exp\left(-2.73\times10^{7}/|\mathbf{E}|\right)\ \mathrm{m^{-1}} \tag{4.6}$$

$$\eta = 340.75\,\mathrm{m^{-1}} \tag{4.7}$$

These coefficients correspond to a breakdown electric field ($\bar{\alpha} = 0$) of $2.4\,\mathrm{MV\,m^{-1}}$ which is higher than the Laplacian electric field created by the planar electrodes. Finally, the photoionization source term S_{ph} is modeled by a set of Helmholtz equations following the work of [49] as detailed in Section 2.3.3.

4.1.3 Case 1: High background pre-ionization

In this first test case, a quite high background density $n_b = 10^{13}\mathrm{m^{-3}}$ is used to reduce the streamer head stiffness. This value is representative of the plasma density after several pulses or can mimic the effect of the photoionization process which was neglected here to start with a simple numerical model. The photoionization will be included in a third case that is discussed in Section 4.1.5.

The solution of a reference simulation on a quadrangular mesh with $\Delta x = 3\,\mu\mathrm{m}$ using the ISG scheme is shown in Fig. 4.3. This simulation does not exhibit numerical oscillation and is in good qualitative agreement with the results presented in [15]. A stable propagation from right to left is obtained up to 16 ns. Starting at $0.8\times10^{7}\,\mathrm{V\,m^{-1}}$, the maximum electric field in the streamer head increases to $1.6\times10^{7}\,\mathrm{V\,m^{-1}}$ and remains almost constant up to 12 ns. Then, the streamer becomes a bit wider at 16 ns. After 12 ns, the electron density starts to diffuse to the right of the initial seed with a density around $1\times10^{18}\,\mathrm{m^{-3}}$ which looks like a weak negative streamer with an electric field close to the breakdown field at $t = 16$ ns.

AVIP is faced with the other codes by comparing the streamer length L and the maximum electric field along the axis. The streamer length $L(t)$ is defined as the distance between the initial seed and the maximum electric field location. AVIP results on a quadrangular mesh with $\Delta x = 3\,\mu\mathrm{m}$ are shown in Fig. 4.4. This mesh size is representative of those used in the benchmark paper where $\Delta x \in [2, 4.3]$ µm for the different simulations of the case 1. The LLW scheme gives acceptable results and is very similar to the slower discharge propagation in [15]. As shown in Fig. 4.4b, the LLW scheme leads to oscillations on the maximum electric field that some groups also observed. These oscillations do not seem to be physical as they disappear during the mesh convergence in [15]. The consequences of these oscillations are clearly visible in Fig. 4.5a in which two electron density bumps are present at $x \simeq 0.55$ and 0.9 mm. The FOU scheme leads to faster propagation than all the other codes. This result is in agreement with the observations made in [49] when comparing the FOU scheme to a higher-order one. In addition, the FOU scheme exhibits a 10% higher electric field peak compared to all the other simulations. A 2D map of the streamer propagation using the FOU scheme at 15 ns is shown in Fig. 4.5b. At the beginning of the streamer propagation, the electron density is higher and

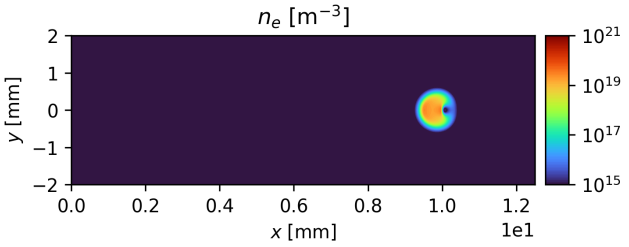

(a) $t = 1$ ns

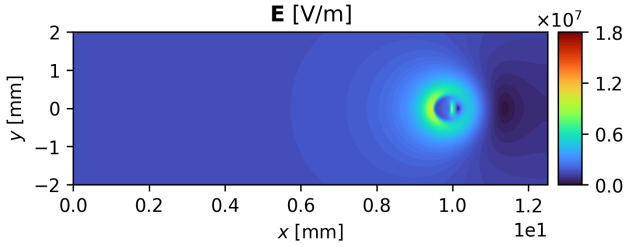

(b) $t = 1$ ns

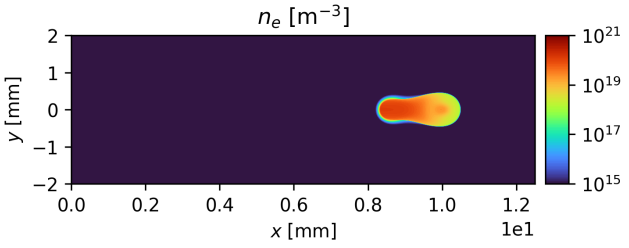

(c) $t = 4$ ns

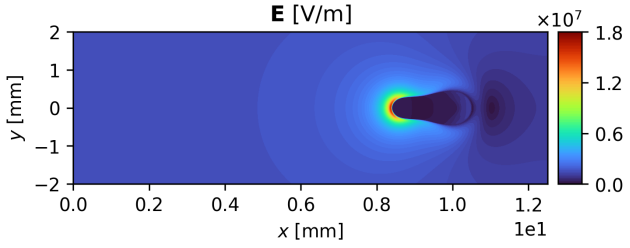

(d) $t = 4$ ns

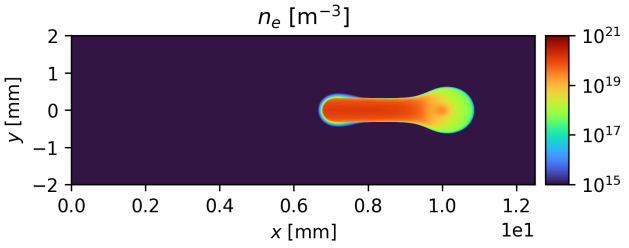

(e) $t = 8$ ns

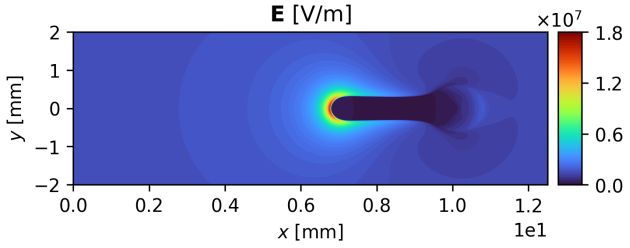

(f) $t = 8$ ns

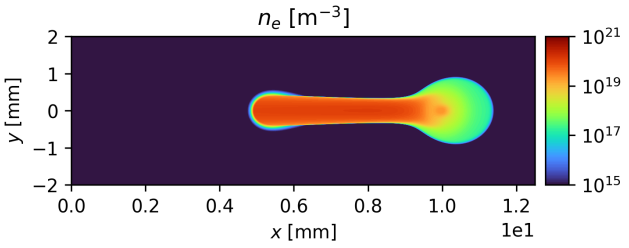

(g) $t = 12$ ns

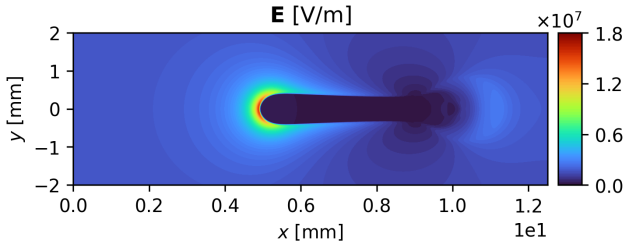

(h) $t = 12$ ns

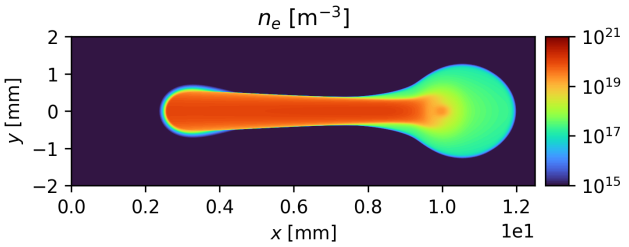

(i) $t = 16$ ns

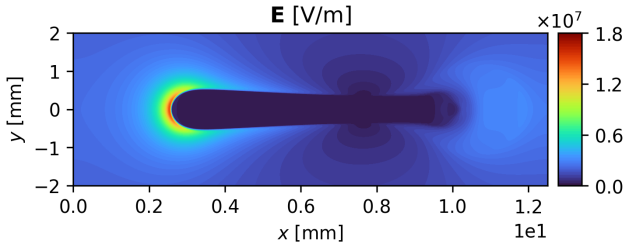

(j) $t = 16$ ns

Figure 4.3: Electron density (left) and electric field magnitude (right) at different instants of the case 1 streamer propagation using the ISG scheme with $\varepsilon_{\mathrm{SG}} = 0.01$ on a quadrangular mesh with $\Delta x = 3\,\mu\mathrm{m}$.

much more focused on the axis than with the LLW scheme. Finally, the ISG scheme gives good results for the streamer length and electric field peak. The electron density map shown in Fig. 4.5c is similar to that of the LLW scheme without any mark of oscillation.

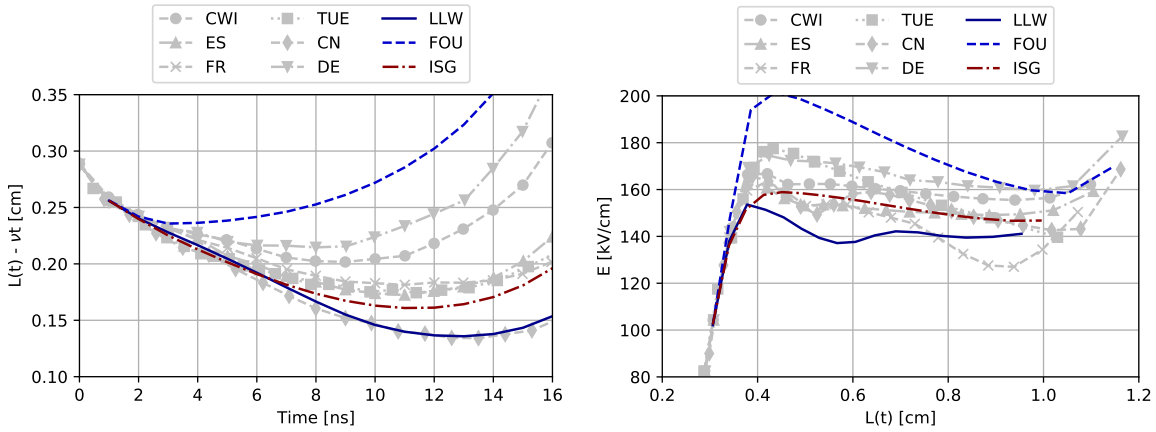

(a) (b)

Figure 4.4: Comparison of the AVIP results with the results of Bagheri et al. [15] on case 1 using quadragular elements and $\Delta x = 3\,\mu\text{m}$: (a) $L(t) - \nu t$ versus time ($\nu = 0.05\,\text{cm ns}^{-1}$) and (b) maximum electric field versus streamer length.

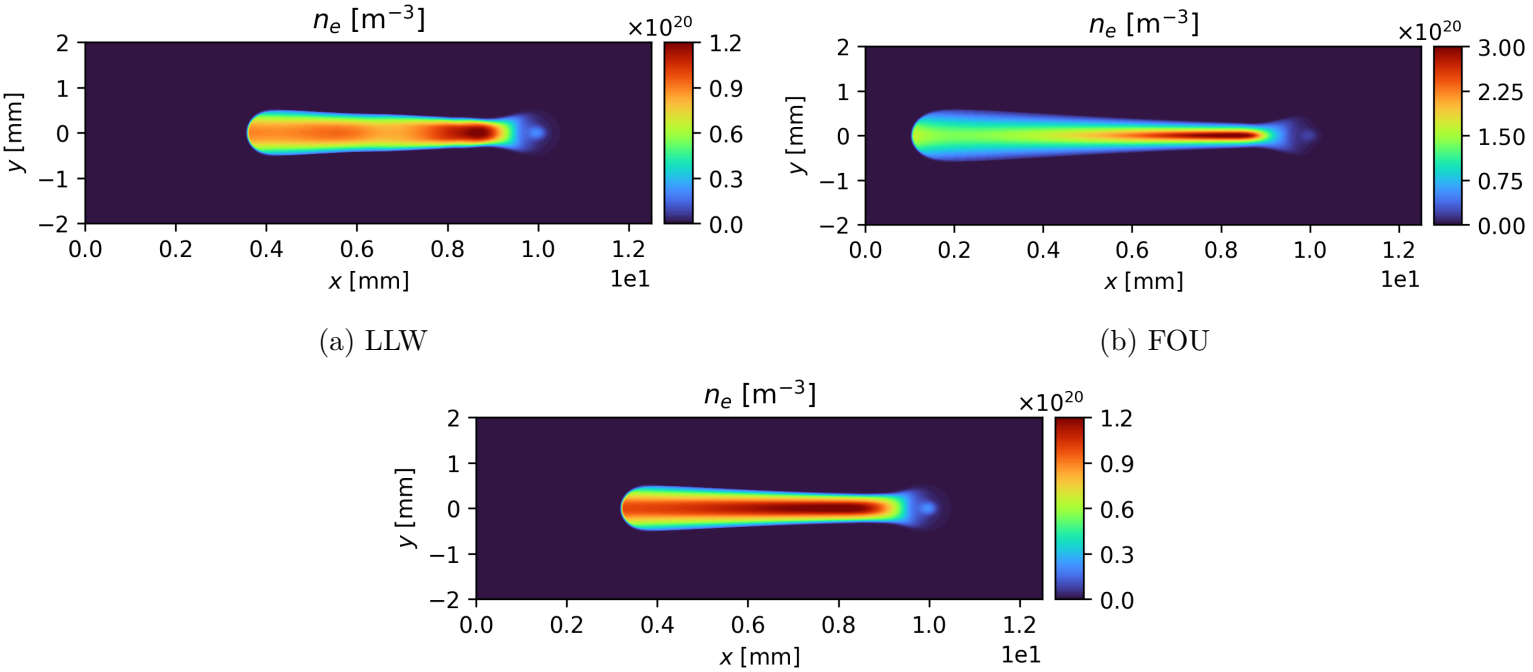

(a) LLW

(b) FOU

(c) ISG

Figure 4.5: Electron density at $t = 15$ ns on a quadrangular mesh ($\Delta x = 3\,\mu\text{m}$) using the (a) LLW scheme, (b) FOU scheme and (c) ISG scheme.

Despite the promising results obtained using the ISG scheme on quadrangular meshes, the main goal of AVIP is to perform reliable simulations of streamer propagation on unstructured

grids using triangular elements. Thus, the case 1 has also been simulated using triangular meshes on which only the ISG and LLW schemes could propagate the streamer properly. The cell size has been varied from 2 to 5 µm to analyze the influence of the grid resolution when using the LLW scheme. The grid resolution needs to be reduced to 1 µm for the ISG scheme to simulate the streamer propagation with triangular elements. The use of the ISG scheme was found possible for very small cell size around 1 µm indicating a strong reduction of the scheme accuracy in a non-topological mesh. The use of the ISG scheme on non-topological will be further investigated in the cases presented in Section 4.2 for which only triangular meshes can be used. A comparison with the benchmark results is shown in Fig. 4.6. Good results were obtained for the streamer length compared to the other codes. The streamer length seems only slightly sensitive to the mesh size when using the LLW scheme. However, significant oscillations are observed on the maximum electric field in Fig. 4.6b when using the coarsest spatial resolutions ($\Delta x = 4 - 5$µm). These oscillations are significantly reduced for $\Delta x = 3$ µm and are almost mitigated for $\Delta x = 2$ µm. Maps of the electron density at $t = 16$ ns using the LLW scheme are shown in Fig. 4.7 for different mesh resolutions. For $\Delta x \geq 4$ µm, several numerical branching initiation of the streamer can be observed. On the 3 µm-mesh, the streamer does not branch, but oscillations are still present. There is no significant numerical artefact for $\Delta x \leq 2$ µm.

AVIP has also shown good performance using a bi-socket Intel node with 2 x 18 core Xeon Gold 6140 (2.3 GHz clock speed and 96 Gb memory) compared with the reference simulations performed in Bagheri et al. [15]. The Afivo code from CWI is the fastest one and performed the simulation of case 1 in 20 min core time (Run time × Number of CPU cores). The core times of the five other groups range from 6 h to 90 h. For the simulation using the LLW scheme on the 3 µm triangular mesh, the AVIP core time was 3.7 h, which places the code in second place in the benchmark in terms of performance.

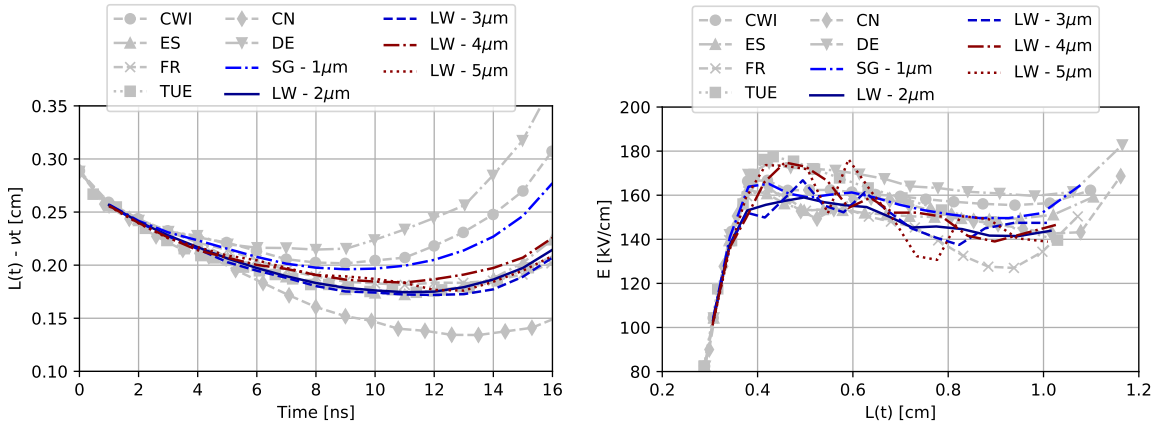

(a) (b)

Figure 4.6: Comparison of AVIP results with those of Bagheri et al. [15] for case 1 using triangular elements: (a) $L(t) - \nu t$ versus time ($\nu = 0.05\,\mathrm{cm\,ns^{-1}}$) and (b) maximum electric field versus streamer length.

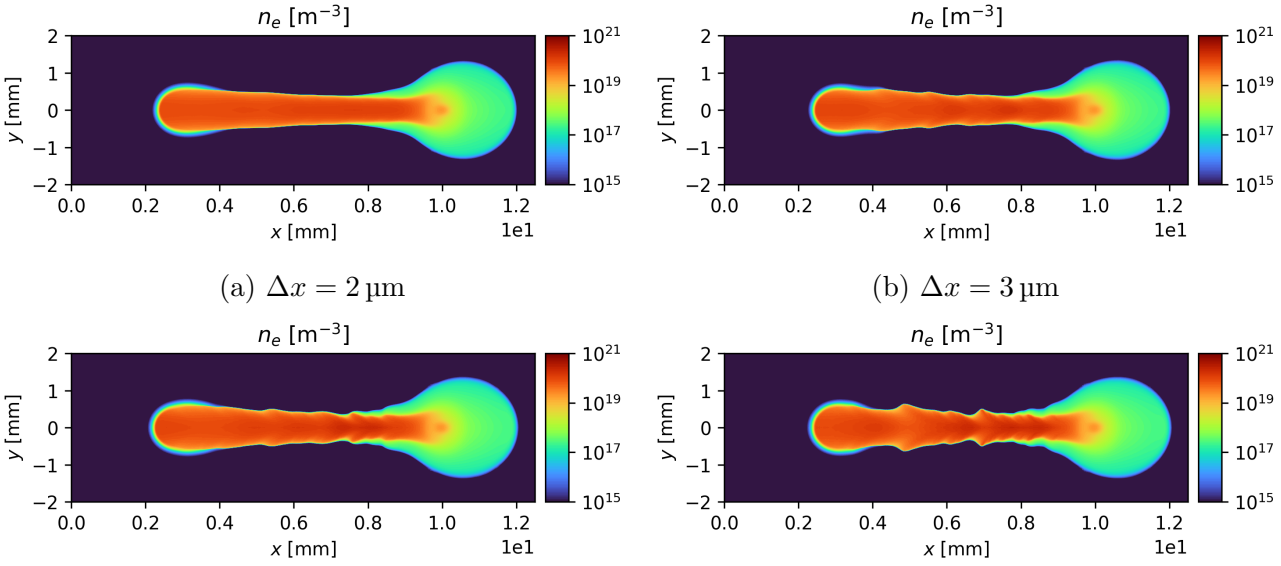

(a) $\Delta x = 2\,\mu\text{m}$ (b) $\Delta x = 3\,\mu\text{m}$

(c) $\Delta x = 4\,\mu\text{m}$ (d) $\Delta x = 5\,\mu\text{m}$

Figure 4.7: Electron density at $t = 16$ ns on a quadrangular mesh using the LLW scheme and different mesh resolutions. Case 1 of Bagheri et al. [15].

4.1.4 Case 2: Low background pre-ionization

The second test case considers a much lower background ionization level compared to case 1 with $n_b = 1 \times 10^9\,\text{m}^{-3}$. The resulting positive streamer has a smaller radius, higher electric field, and higher density gradients than in case 1. This second case is therefore much more computationally and numerically challenging than the first one. Only three of the six groups (CN, CWI, FR) in [15] were able to propagate the streamer up to $t = 20$ ns without numerical branching or crash. The simulation of the DE group was stopped at 14 ns, whereas numerical branching seems to occur at 17 ns for the ES group [15, Figure 8]. In AVIP, only the ISG scheme used on a quadrangular mesh with $\Delta x = 2\,\mu\text{m}$ was able to propagate the positive streamer as shown in Fig. 4.8. The electric field in the streamer head is around $2.2\,\text{MV}\,\text{m}^{-1}$ which is 30% higher than in case 1. It must be noticed that a small attempt to numerical branching occurs at 4 ns but is quickly quenched. A good agreement is found regarding both streamer length and electric field peak in Fig. 4.9. Unfortunately, none of the simulations were able to propagate such a streamer using triangular elements and the LLW scheme even for $\Delta x = 1\,\mu\text{m}$. All of these simulations have led to streamer branching, as shown in Fig. 4.10 where only the most refined case is displayed. Nevertheless, these simulation conditions are not very physical since photoionization should be accounted for when using such a low pre-ionization level. Thus, the third case discussed in Section 4.1.5 is more representative of positive streamer propagation at a low pre-ionization level.

4.1.5 Case 3: Photoionization effect

This third case aims to validate the photoionization model discussed in Section 2.3.3. A low pre-ionization level of $1 \times 10^9\,\text{m}^{-3}$ is used to exacerbate the photoionization effect on the streamer propagation. This case has been simulated by all the groups of the benchmark paper except the TUE group. This case is much less computationally challenging than case 2 due to the presence

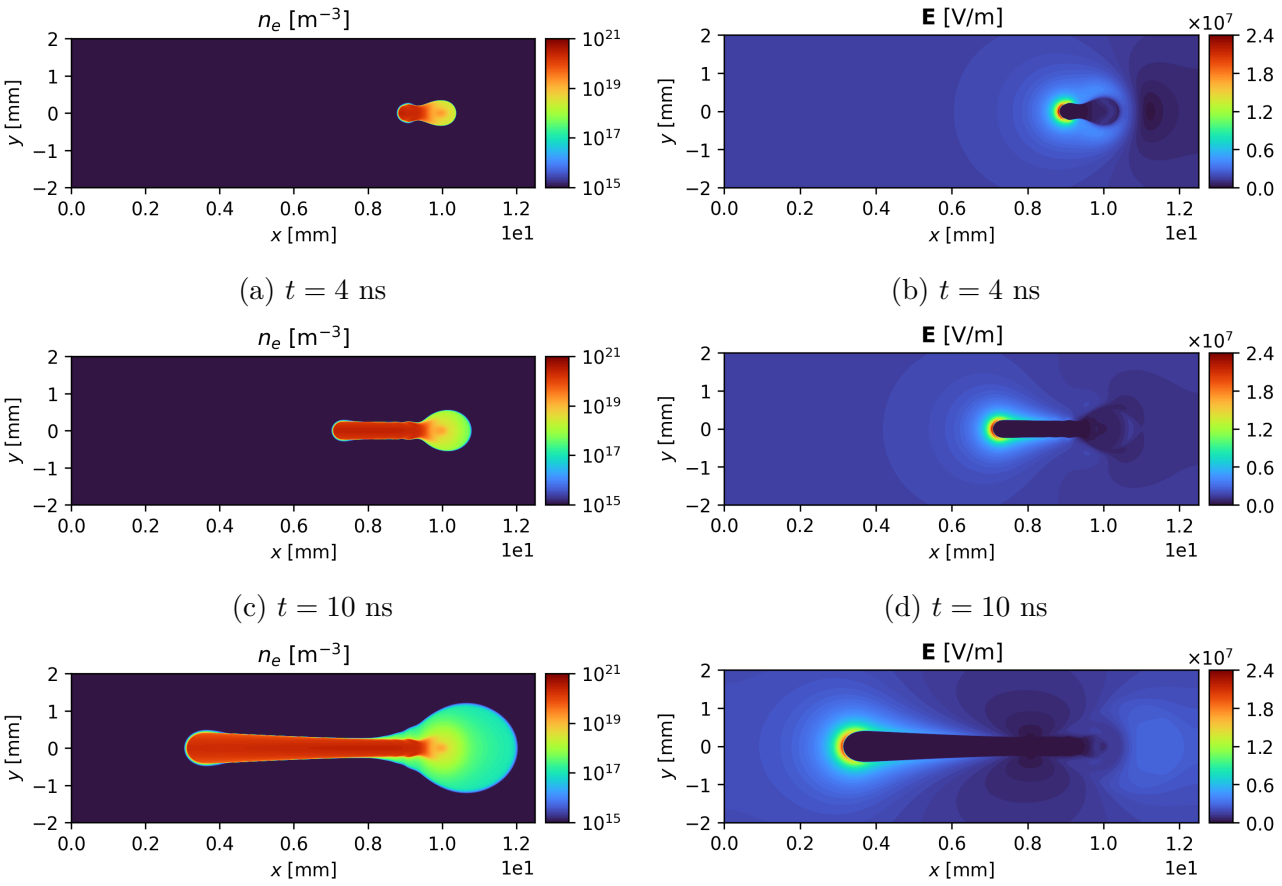

(a) $t = 4$ ns (b) $t = 4$ ns

(c) $t = 10$ ns (d) $t = 10$ ns

(e) $t = 20$ ns (f) $t = 20$ ns

Figure 4.8: Electron density (left) and electric field magnitude (right) at different instants of the streamer propagation using the ISG scheme with $\varepsilon_{\text{SG}} = 0.01$ on a quadrangular mesh with $\Delta x = 2\,\mu\text{m}$. Case 2 of Bagheri et al. [15].

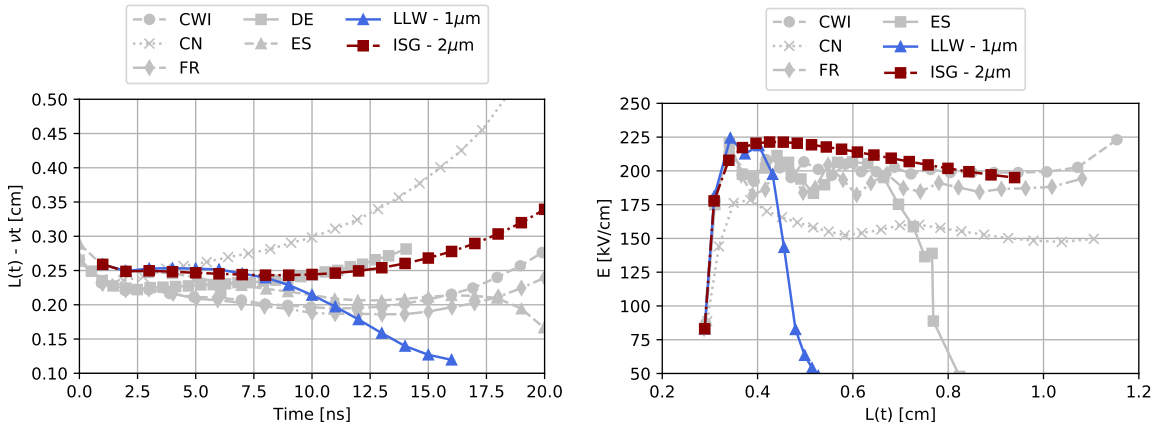

(a) (b)

Figure 4.9: Comparison of AVIP results with those of Bagheri et al. [15] for case 2: (a) $L(t) - \nu t$ versus time ($\nu = 0.03\,\text{cm}\,\text{ns}^{-1}$) and (b) maximum electric field versus streamer length.

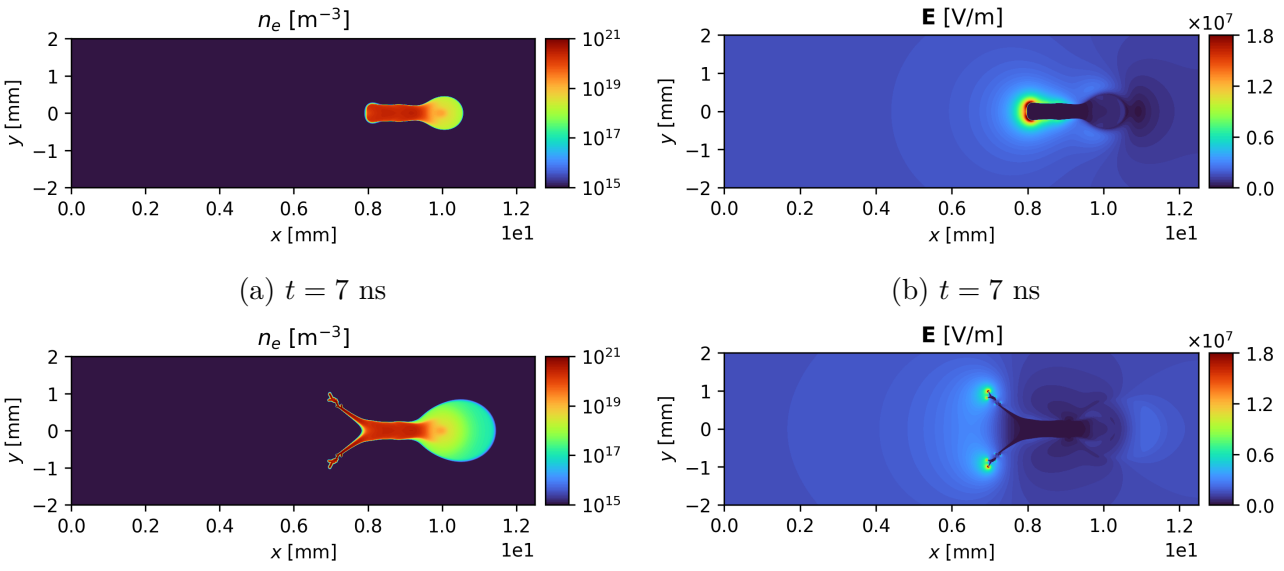

(a) $t = 7$ ns

(b) $t = 7$ ns

(c) $t = 16$ ns

(d) $t = 16$ ns

Figure 4.10: Electron density (left) and electric field magnitude (right) at different instants of the streamer propagation using the LLW scheme on a triangular mesh with $\Delta x = 1\,\mu$m. Case 2 of Bagheri et al. [15].

of an intense photoionization source term in front of the streamer head as shown in Fig. 4.11 This source term increases the electron density in the ionization region, thus reducing all the gradients. Both the ISG scheme on quadrangular mesh and the LLW scheme on triangular mesh can propagate the positive streamer properly. The comparisons made in Fig. 4.12 show good agreements with the other codes. When considering photoionization, it validates the AVIP capacity to propagate a positive streamer on triangular meshes at a low pre-ionization level.

4.1.6 Conclusion

AVIP was successfully confronted with six other codes for positive streamer propagation. It was able to properly propagate a positive streamer with a high pre-ionization level representative of repetitive discharges. Simulations on triangular meshes are proned to numerical branching and require finer cell size compared to quadrangular meshes. For the conditions considered in case 1, a typical cell size of 2-3 µm is required for the LLW scheme on a triangular mesh to avoid numerical instabilities. The second case of the benchmark was found too difficult using triangular meshes, and only the ISG scheme on a quadrangular mesh was able to propagate the streamer correctly. The third case considering a low pre-ionization level and photoionization has been successfully simulated on a triangular mesh using the LLW scheme. This last case also validates the photoionization source term implemented in AVIP.

To conclude, AVIP can propagate a positive streamer between two planar electrodes using the LLW scheme on triangular meshes. A typical cell size of 3 µm is required to get good results on both cases 1 and 3, which represent typical conditions encountered in the practical application of NRP discharges in a PAC framework. The comparison of AVIP to six other codes developed independently and using different numerical methods allows to assess the validity of the numerical implementations made in AVIP.

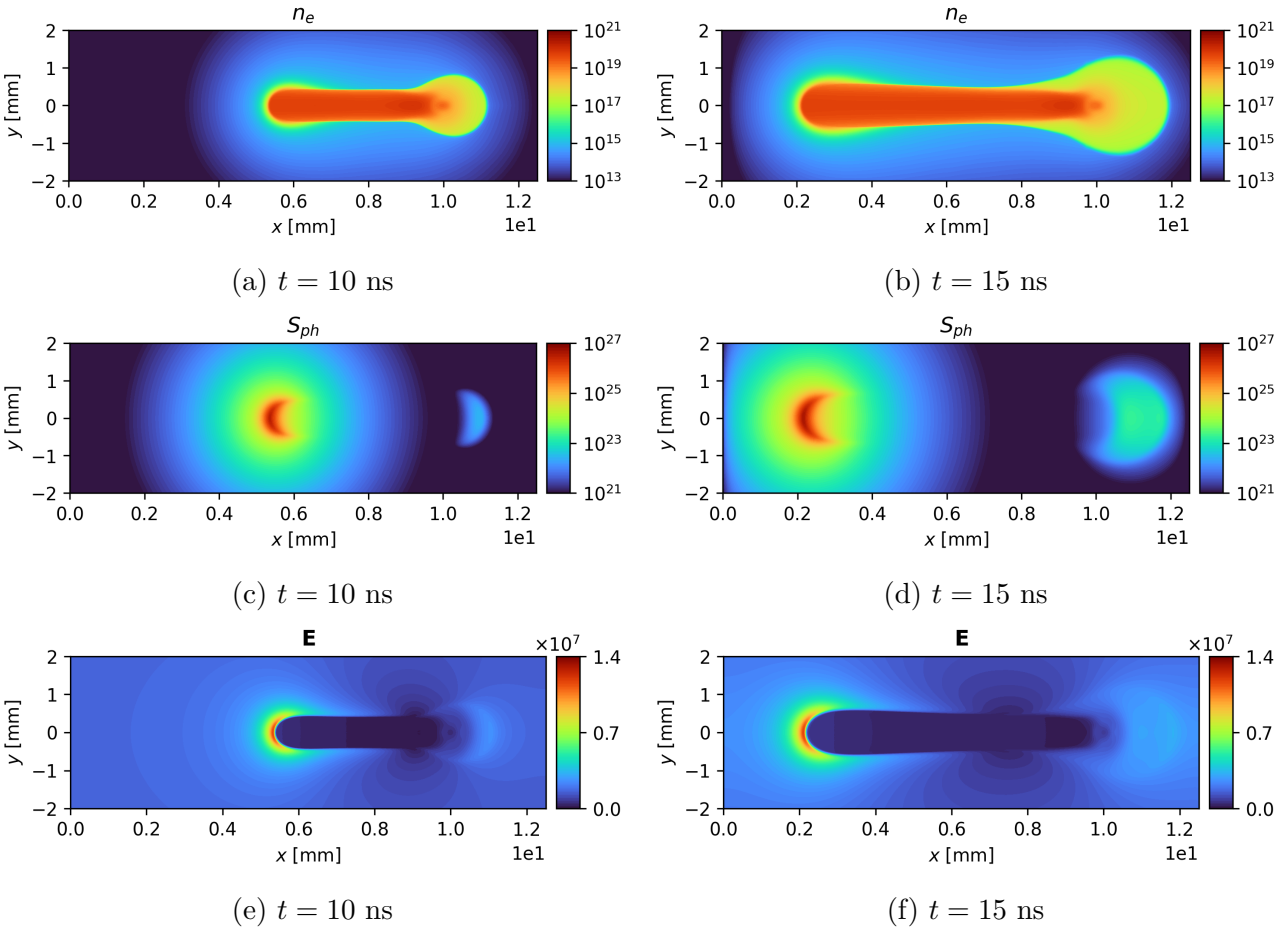

(a) $t = 10$ ns (b) $t = 15$ ns

(c) $t = 10$ ns (d) $t = 15$ ns

(e) $t = 10$ ns (f) $t = 15$ ns

Figure 4.11: Electron density, and electric field magnitude and photionization source term at different instants of the case 3 streamer propagation using the LLW scheme on triangular mesh with $\Delta x = 3\,\mu\text{m}$.

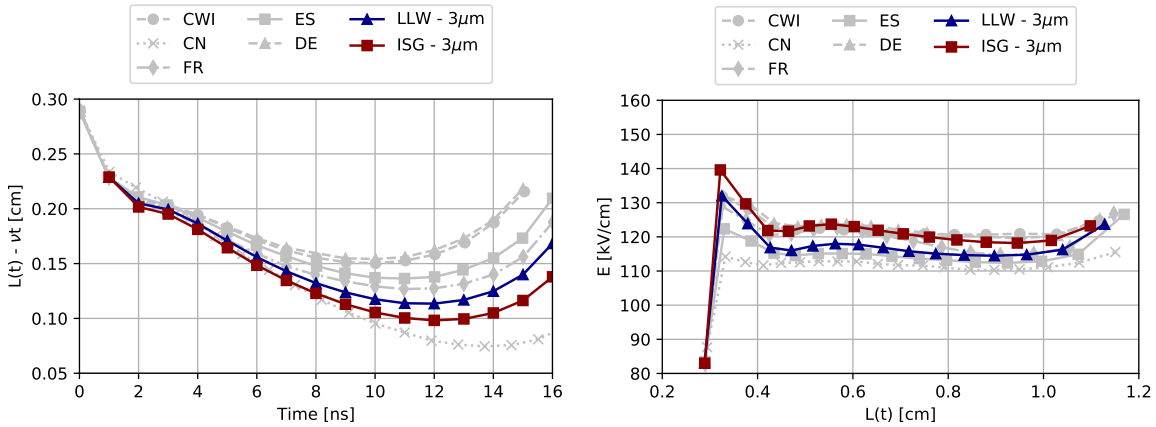

(a) (b)

Figure 4.12: Comparison of the AVIP results on case 3 with results of Bagheri et al. [15]: (a) $L(t) - \nu t$ versus time ($\nu = 0.06\,\text{cm ns}^{-1}$) and (b) maximum electric field versus streamer length. Marker used for AVIP results corresponds to the cell type used.

4.2 Hyberbolic electrodes

Hyperboloid electrodes are now investigated to approximate the real electrode shapes used in pin-pin experiments such as in [167, 133, 142, 47]. A realistic electrode shape is schematically represented in Fig. 4.13 by a cylinder with a diameter $D/2$ that is rounded at one of its extremity. The electrode tip can be well estimated by a hyperboloid electrode that is thus used as a first step toward a realistic electrode.

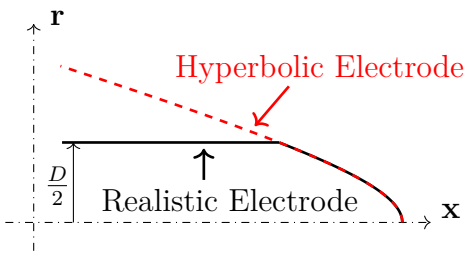

Figure 4.13: Approximation of a realistic electrode by an hyperbolic electrode.

Compared to planar electrodes, the curvature radius R_c of a hyperbolic electrode allows to locally enhance the electric field at its extremity to create favorable conditions for streamer initiation. For two infinite hyperbolic electrodes, there is an analytical solution of the potential from which the electric field can be deduced [49]. Figure 4.14 shows the reduced electric field at 300 K along the axis for typical values of curvature radius $R_c = 200\,\mu$m, inter-electrode gap distance $d = 5$ mm and applied voltage $V_A = 12$ kV. The electrode tips are located at $x = \pm 2.5$ mm and the solution of the reduced electric field is symmetric with respect to x, so that only $x \geq 0$ is shown in Fig. 4.14. The reduced electric field is very high and peak ≈ 600 Td close to the electrode ($x = 2.5$ mm). This value is much higher than the breakdown electric that is about 110 Td in this condition leading to favorable conditions for electron amplification close to the electrode tip. It is interesting to notice that for the same applied voltage and gap distance, the reduced electric field for two planar electrodes is lower than the breakdown field.

4.2.1 Numerical setup

The pin-pin configuration considered in this work is depicted in Fig. 4.15. It is composed of two hyperbolic electrodes with a curvature radius $R_c = 200\,\mu$m separated by a distance $d = 5$ mm. The cathode potential is grounded (*i.e.* $V_C = 0$) and the anode potential is set to a constant voltage $V_A > 0$. Taking advantage of the unstructured grid, the domain has been extended up to 10 cm with a small number of cells and a Neumann boundary condition is applied on this far-field patch. A simple Neumann boundary condition is employed for charged species on the electrode surfaces as in [49] whereas a free inlet-outlet is applied on the far-field. All the boundary conditions for the Poisson and drift-diffusion equations are summarized in Tab. 4.2. When not specified, the simulations are performed using a CFL of 0.7 and a Fourier coefficient of 0.1.

All the simulations are performed at atmospheric pressure $P_0 = 1$ atm. Two initial temperatures were investigated: a case at 300 K representative of a streamer discharge in standard condition and another at 1000 K representative of discharges in pre-heated conditions (either in a high-temperature flow or due to previous discharges). As discussed in [115], the charged species density n scale as $n = n_0(N/N_0)^2$ with n_0 and N_0 a reference charge species and background densties respectively and N the gas number density. Thus for a given pressure, the

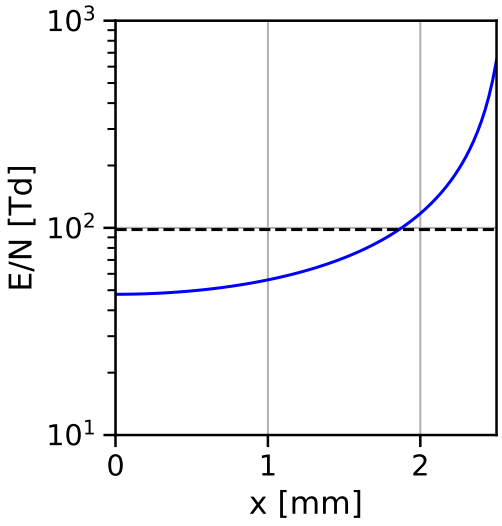

Figure 4.14: Axial profile (r=0) of the reduced electric field (in blue) at $T = 300$ K for two hyperbolic electrodes of radius $R_c = 200\,\mu$m separated by $d = 5\,$mm with an applied voltage of 12 kV. The black dashed curve corresponds to the equivalent reduced electric field for two planar electrodes.

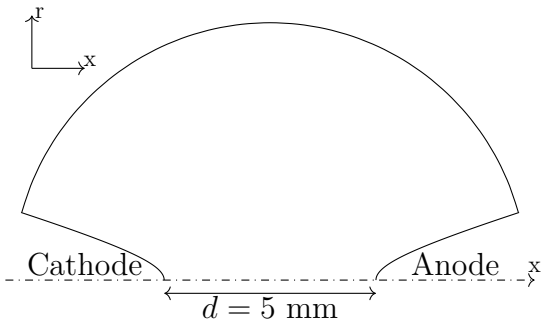

Figure 4.15: Sketch of the pin-pin configuration

	Cathode	Anode	Axis	Farfield
Poisson	Dirichlet ($V_C = 0$)	Dirichlet ($V_A \geq 0$)	Neumann ($\nabla\phi = 0$)	Neumann ($\nabla\phi = 0$)
Transport	Neumann	Neumann	Symmetry	Outlet

Table 4.2: Boundary conditions used for the Poisson and charged species transport equations for the pin-pin configuration.

charge species densities decrease with the gas temperature. As a consequence, the smaller gradients at higher temperatures are expected to reduce the numerical difficulty of streamer propagation as observed between cases 1 and 2 in Bagheri et al. [15]. As shown in Section 4.1, numerical branching can occur depending on the cell size and the numerical scheme used. Different meshes summarized in Tab. 4.3 have been used to investigate this effect and establish some criteria for numerical stability of a discharge propagation between two hyperbolic electrodes. All the simulations are performed with triangular elements to handle the complex shape of the electrodes.

	M1	M2	M3	M4	M5	M6	M7
$\Delta_x^{\min}$	1 µm	2 µm	3 µm	4 µm	5 µm	7.5 µm	10 µm
N_{nodes}	3.5×10^6	1.1×10^6	0.55×10^6	0.36×10^6	0.27×10^6	0.21×10^6	0.18×10^6

Table 4.3: Characteristics of the triangular meshes used in the pin-pin configuration.

4.2.2 Chemistry and transport parameters

A simplified chemistry for streamer propagation in air [136] successfully employed in [49, 184] is used here as a first step toward more detailed chemistries. The transport coefficients (*i.e.* μ_k and D_k) are also taken from [136]. Three charged species are considered: the electrons, the positive ions and the negative ions. Thus, the complete set of governing equations reads:

$$\frac{\partial n_e}{\partial t} + \nabla(-n_e\mu_e\mathbf{E} - D_e\nabla n_e) = (\nu_\alpha - \nu_\eta - \beta_{\text{ep}}n_p)n_e + \nu_{\text{det}}n_n \tag{4.8}$$

$$\frac{\partial n_n}{\partial t} + \nabla(-n_n\mu_n\mathbf{E} - D_n\nabla n_n) = -(\nu_{\text{det}} + \beta_{\text{np}}n_p)n_n + \nu_\eta n_e \tag{4.9}$$

$$\frac{\partial n_p}{\partial t} + \nabla(n_p\mu_p\mathbf{E} - D_p\nabla n_p) = -(\beta_{\text{ep}}n_e + \beta_{\text{np}}n_n)n_p + \nu_\alpha n_e \tag{4.10}$$

where ν_α is the ionization frequency (Eq. 2.2), ν_η the attachment frequency (Eq. 2.3), ν_{det} the detachment frequency (Eq. 2.4), β_{ep} the recombation rate of electrons with positive ions (Eq. 2.5) and β_{np} the recombination rate of positive and negative ions (Eq. 2.6). It is assumed that all these parameters only depend on the reduced electric field E/N (LFA).

The ionization and attachment frequencies at 300 K and 1000 K are shown in Fig. 4.16a versus the reduced electric field. When plotted versus the reduced electric field, the two frequencies have very similar trends at both temperatures as they approximately scale with the gas number density N. Figure 4.16 allows to easily identify the breakdown electric field, which is around 2.6 MV m^{-1} at 300 K and 0.8 MV m^{-1} at 1000 K corresponding to a reduced electric field of about 108 Td. Hence, a lower voltage can be applied at 1000 K compared to 300 K to trigger the streamer propagations.

As discussed in [49], a typical length of charge separation in a streamer head can be estimated by α^{-1}, where α is the first Townsend coefficient discussed in Section 2.3.1. This characteristic streamer size versus the reduced electric field is shown in Fig. 4.17 for the two temperatures considered here. At high reduced electric representative of the streamer head ($E/N \simeq 1000$ Td), the characteristic sizes at 300 K and 1000 K are respectively 4 µm and 14 µm. Thus, smaller gradients are expected as the temperature increases.

4.2.3 Discharge at 300 K

The discharge at 300 K is first investigated. The initial densities of electrons and positive ions are set to 1×10^{14} m^{-3} in order to mimic the effects of the photoionization that is not considered here as discussed in [49]. The applied voltage is set to $V_A = 12$ kV allowing to create a reduced electric field much higher than 110 Td close to the electrode as shown previously in Fig 4.14.

Before comparing the different numerical schemes and spatial discretizations, a reference simulation using the limited Law-Wendroff scheme is performed on the finer mesh M1 to analyze the discharge propagation. The resulting electron density and electric field are shown in Fig. 4.18. Both positive and negative streamers start to propagate after a few nanoseconds and

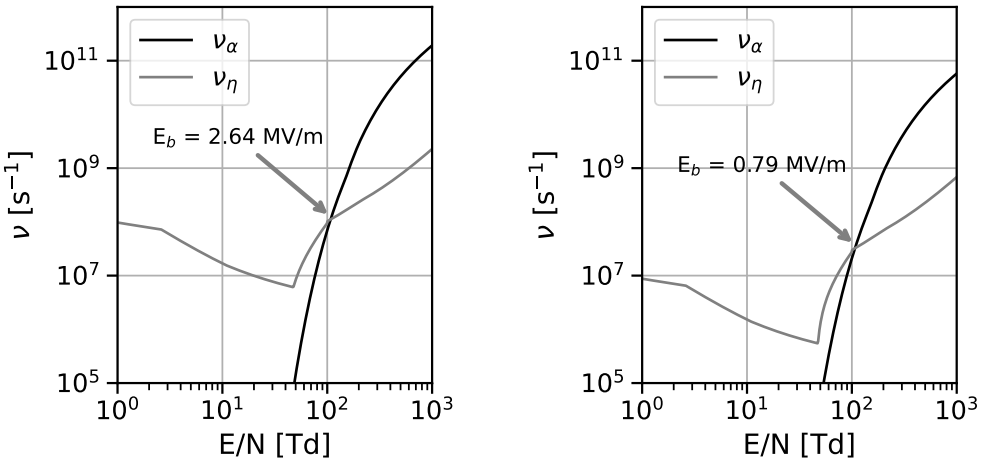

(a) $T = 300$ K (b) $T = 1000$ K

Figure 4.16: Ionization and attachment frequencies against the reduced electric field using coefficients from Morrow and Lowke [136] at (a) 300 K and (b) 1000 K.

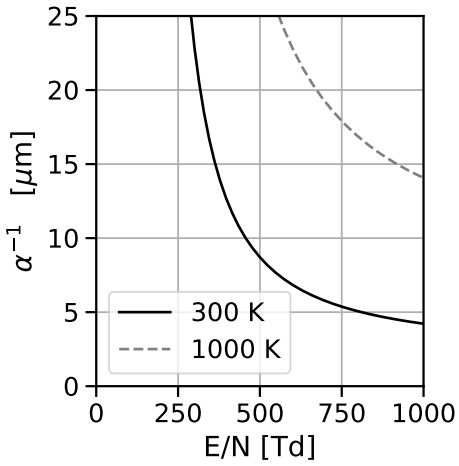

Figure 4.17: Characteristic length scale versus the reduced electric field for streamer propagation using the first Townsend coefficient from [136] at 300 K and 1000 K.

their heads are already detached from the electrode surface at 2 ns. The electric field peak in the positive streamer head is about ten times the breakdown field. The negative streamer is moving faster and more diffusely than the positive one during the first instants of the propagation. This is also illustrated in Fig. 4.19 in which the electron density and the electric field are shown along the axis at different instants. After 1 ns, the negative streamer already traveled 0.5 mm whereas the positive is still attached to the anode. Then the negative streamer nearly moves at a constant speed while the positive streamer accelerates. Finally, the positive and negative streamers nearly merge at mid-gap as shown in Fig. 4.18. Finally, they form a conducting channel at time $t \geq 10$ ns.

During their propagation, no streamer branching or oscillations were observed. Thus it is highly likely that no physical branching or oscillation must occur in the conditions studied. Consequently, any branching or oscillations in the simulation must be associated with a numer-

ical artifact. Hence, these conditions are considered to be a suitable test case to study discharge propagation's numerical stability in a pin-pin configuration.

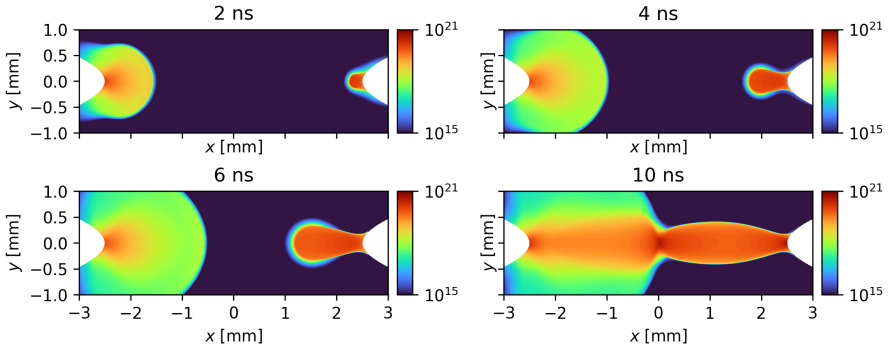

(a) n_e [m^{-3}]

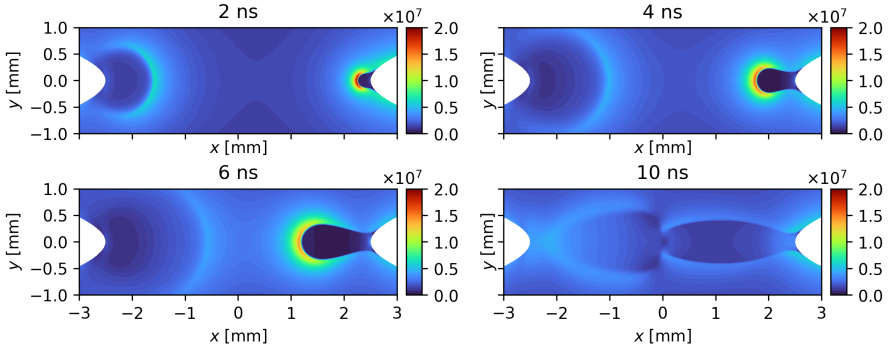

(b) $||\mathbf{E}||$ [V/m]

Figure 4.18: Streamer propagation at 300 K for two hyperbolic-shaped electrodes having a 200 µm-curvature radius separated by 5 mm using LLW scheme on the mesh M1.

The impact of the mesh resolution using the LLW scheme is first investigated. The results using meshes M1 to M4 are shown in Fig. 4.20 while mesh M5 is not displayed as it crashes before 1 ns. Quite similar results are obtained for the meshes M1 to M3 at 7 ns with only a minor increase of the positive streamer velocity as the cell size increases. This is clearly visible in Fig. 4.22 where the electron density and the electric field are shown at $t = 7$ ns for meshes M1 to M3. On the coarser mesh M3, the solution exhibits a slightly faster positive streamer propagation whereas there is no noticeable difference between meshes M1 and M2. For all these three meshes, the negative streamer propagation velocity is unchanged, indicating that the negative streamer head is already well discretized with $\Delta x = 3$ µm. When increasing the cell size to 4 µm (mesh M4), the simulation crashes after only 2 ns and the positive streamer shape does not look like the reference simulation of Fig 4.18 at the same physical time. Performing a zoom on the anode area, Figure 4.21 spotlights the wrong behavior of the discharge close to the axis with an electric field about 50% higher than in the reference case. When reducing the Fourier coefficient F to 0.05 for the diffusion time step, the simulation can be continued up to 10 ns and the streamers can merge. However, the positive streamer is affected by numerical oscillations, as shown in Fig. 4.20e that could eventually evolve into a streamer branching.

The First Order Upwind (FOU) scheme is now investigated to analyze the effect of the scheme accuracy on streamer propagation. It was already observed in [49] the high numerical diffusion of this scheme leads to faster positive streamer propagation. This behavior is associated with the scheme's numerical diffusion that decreases with the scheme order. This is

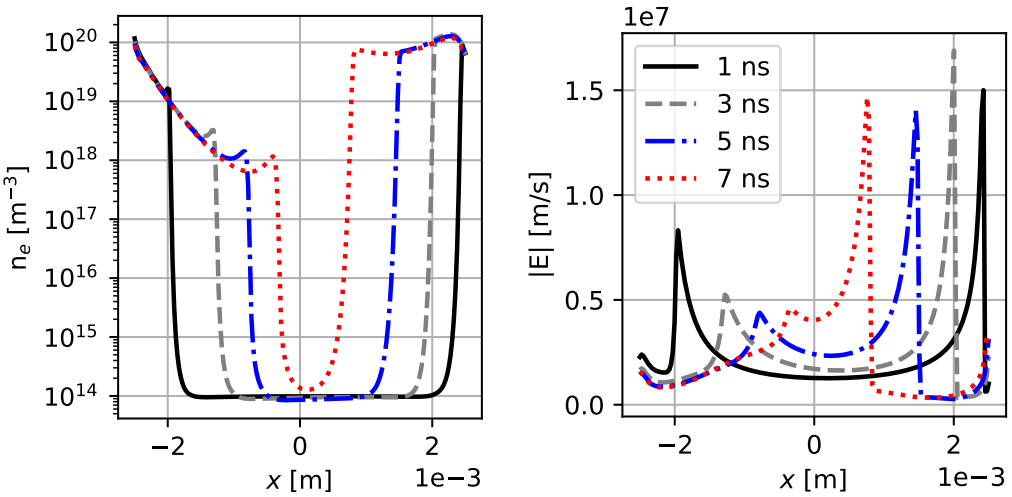

(a) n_e [m^{-3}] (b) $||\mathbf{E}||$ [V/m]

Figure 4.19: Electron density (left) and electric field (right) along the axis at different instants of the streamer propagation at 300 K for two hyperbolic-shaped electrodes having a 200 µm-curvature radius separated by 5 mm using LLW scheme on the mesh M1.

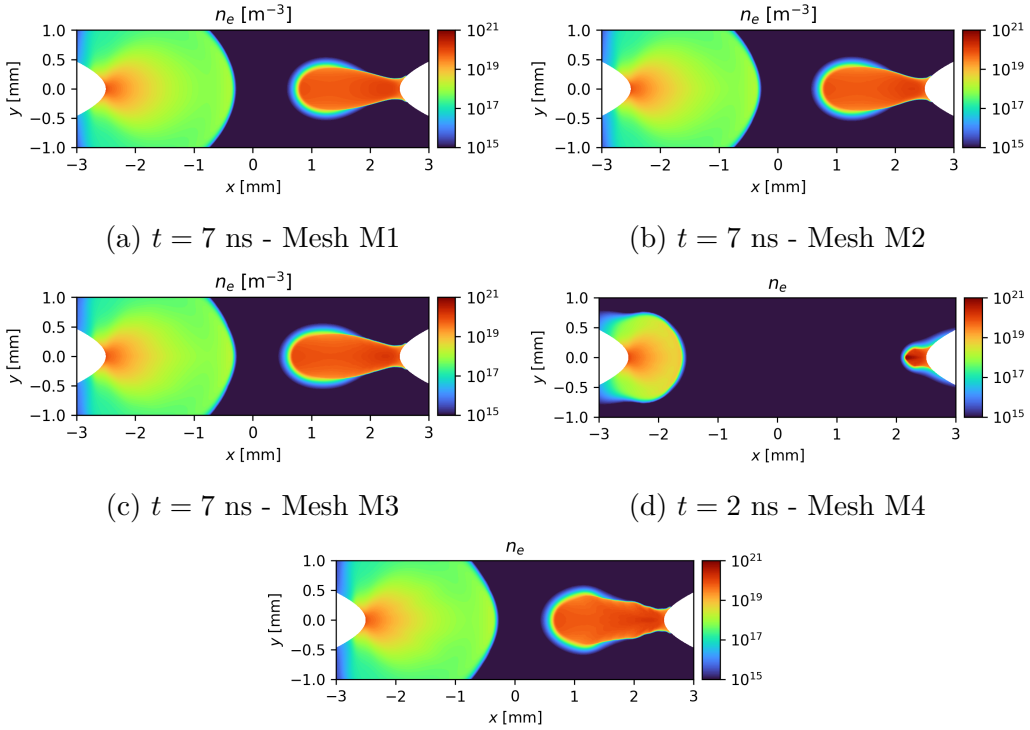

(a) $t = 7$ ns - Mesh M1 (b) $t = 7$ ns - Mesh M2

(c) $t = 7$ ns - Mesh M3 (d) $t = 2$ ns - Mesh M4

(e) $t = 7$ ns - Mesh M4 - Fourier 0.05

Figure 4.20: Cell size influence on the streamer propagation at 300 K for two hyperbolic-shaped electrodes having a 200 µm-curvature radius separated by 5 mm using the LLW scheme.

observed for the simulations on meshes M1 to M3 of Fig. 4.23 that use the FOU scheme by comparing them to the simulations using the LLW scheme previously described in Fig. 4.18. A comparison of the electron density and the electric field along the axis for the different scheme

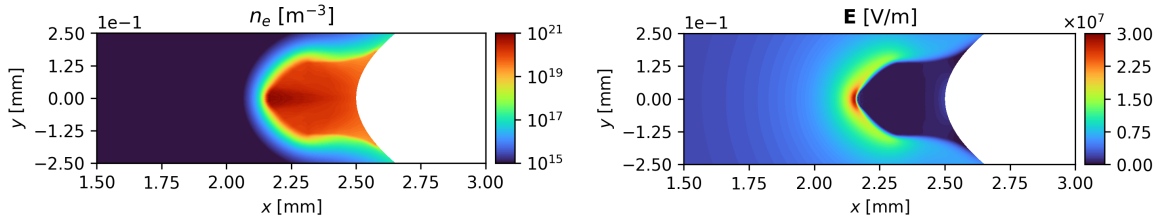

(a) n_e [m^{-3}] (b) $||\mathbf{E}||$ [V/m]

Figure 4.21: Zoom on the anode region at $t = 2$ ns using the LLW scheme on mesh M4 - 300 K

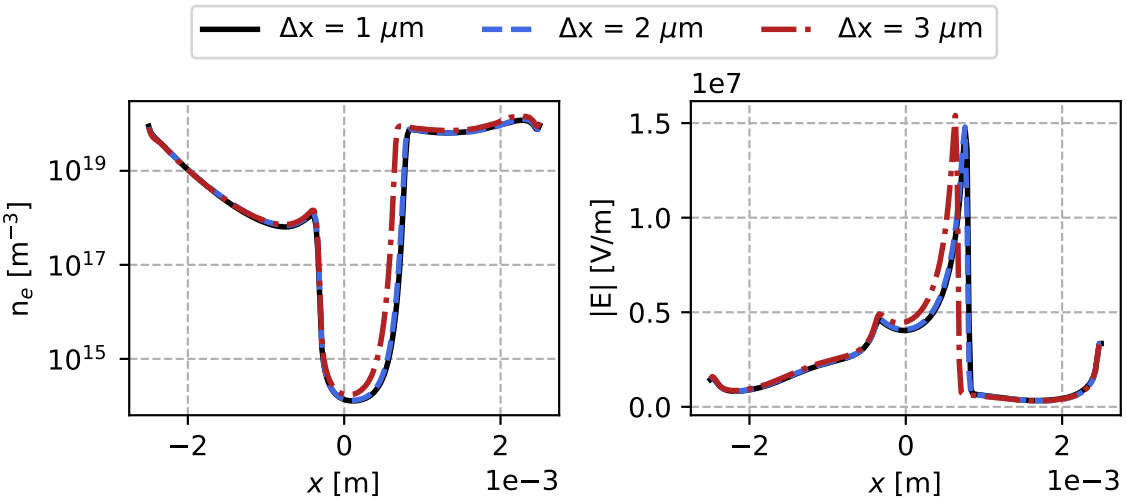

Figure 4.22: Electron density (left) and electric field (right) along the axis at $t = 7$ ns of the streamer propagation at 300 K for two hyperbolic-shaped electrodes having a 200 µm-curvature radius separated by 5 mm using the LLW scheme on different triangular meshes.

on mesh M3 can be shown in Fig. 4.24. Whereas the negative streamer propagation are similar with both the LLW and the FOU schemes, the positive streamer propagation is much faster with the FOU scheme than with the LLW scheme. The use of the FOU scheme requires excessive mesh refinement to get a converged solution as shown in Fig. 4.25. A small numerical artifact on the negative streamer at $y = 0.5$ mm is observed and corresponds to a mesh transition (the cell size is doubled for $y \geq 0.5$ mm). As this behavior was not observed on the LLW-cases, it could be a piece of evidence that the LLW scheme is more robust on mesh transition. When increasing the mesh size to 4 µm (Fig. 4.23d) and 5 µm (Fig. 4.23e), numerical branching is observed and becomes more prononced as the cell size increases. However, the simulations can be continued up to 10 ns in all cases and show a proper propagation of the negative streamer even on mesh M5.

The Improved Scharfetter-Gummel scheme is widely used in the literature for streamer propagation simulation and is one of the most efficient schemes on topologically dual meshes. However, as discussed in Section. 3.3.3, the original version of this scheme is not applicable on a generic triangular element. The potential of this scheme is now investigated to analyze the benefits provided by the correction discussed in Section. 3.3.3. All the simulations were performed with $\epsilon_{SG} = 0.02$ and no significant change was observed by decreasing it. For a sufficient resolution (*i.e.* $\Delta x \leq 3$ µm), the corrected Scharfetter-Gummel scheme gives accurate

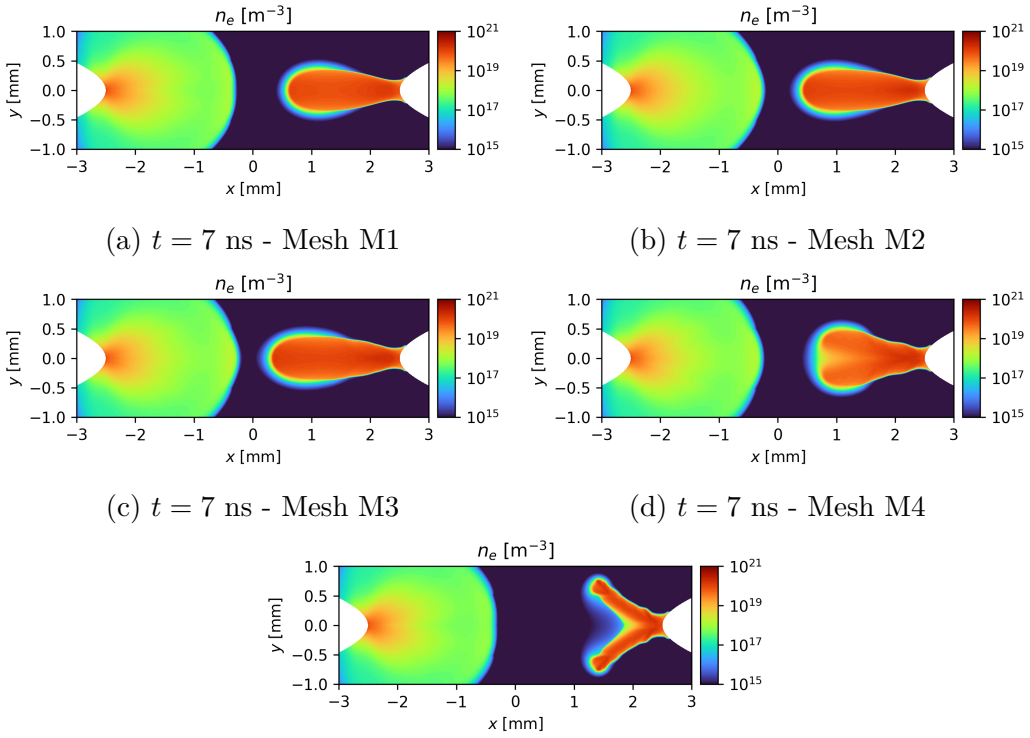

(a) $t = 7$ ns - Mesh M1

(b) $t = 7$ ns - Mesh M2

(c) $t = 7$ ns - Mesh M3

(d) $t = 7$ ns - Mesh M4

(e) $t = 7$ ns - Mesh M5

Figure 4.23: Cell size influence on the streamer propagation at 300 K for two hyperbolic-shaped electrodes having a 200 µm-curvature radius separated by 5 mm using the FOU scheme.

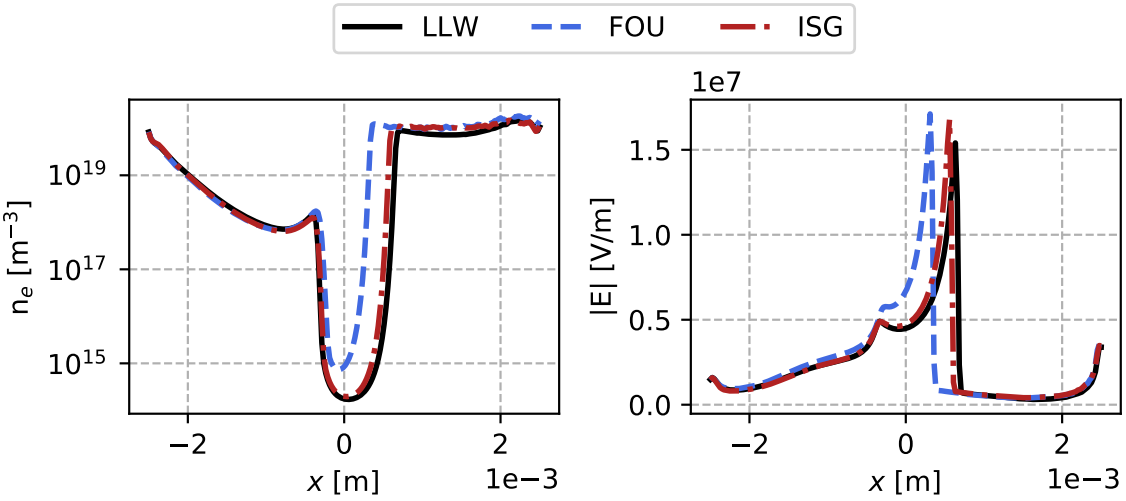

Figure 4.24: Electron density (left) and electric field (right) along the axis at $t = 7$ ns of the streamer propagation at 300 K for two hyperbolic-shaped electrodes having a 200 µm-curvature radius separated by 5 mm using different scheme on mesh M3.

results comparable to the LLW-cases. For 4 µm-cell size, a quite good result is obtained up to 5 ns where the LLW scheme crashes at 2 ns with an incorrect positive streamer shape. Using the ISG scheme, only a slight departure from the axis is observed in Fig. 4.26d and the overall positive streamer shape is well reproduced. However, the simulation crashes before reaching

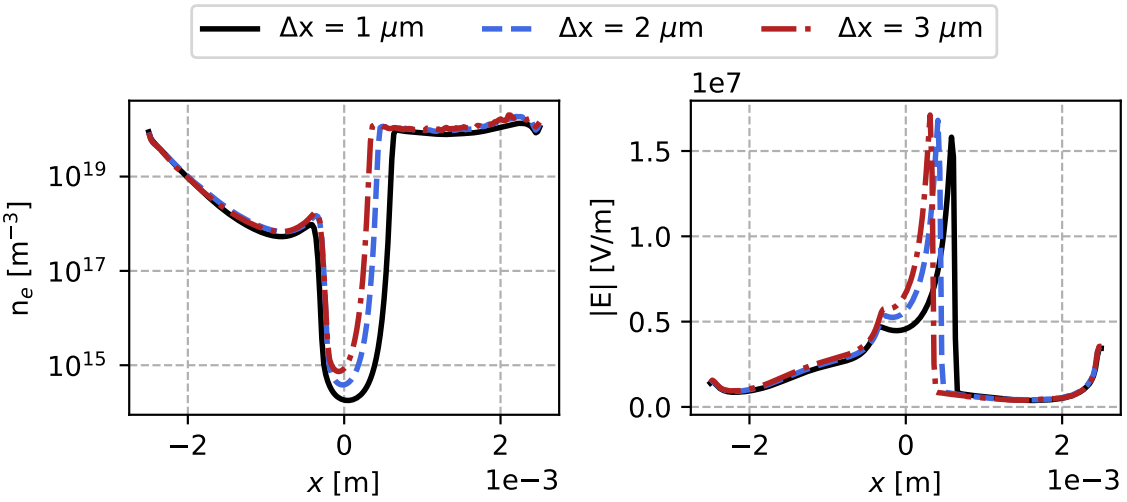

Figure 4.25: Electron density (left) and electric field (right) along the axis at $t = 7$ ns of the streamer propagation at 300 K for two hyperbolic-shaped electrodes having a 200 µm-curvature radius separated by 5 mm using the FOU scheme on different triangular meshes.

6 ns due to numerical oscillations in the radial direction in the positive streamer side. This issue is also observed on mesh M5 and occurs earlier. The ISG scheme is still under development and crash issues when using it on triangular meshes are not well understood yet. This scheme seems to be able to propagate a positive streamer at a lower resolution on triangular meshes than the LLW and FOU schemes, provided that the issues on the radial streamer propagation are corrected.

4.2.4 Discharge at 1000 K

The same geometry of the previous section (*i.e.* $R_c = 200$ µm and $d = 5$ mm) is now used to investigate a discharge in air at 1000 K. As discussed in Section 4.2.2, the applied voltage V_A needs to be reduced to account for the temperature variation and is set to 5 kV. This value corresponds to a slightly higher reduced electric field ($V_A/(dN) \simeq 140$ Td) than in the 300 K case ($V_A/(dN) \simeq 100$ Td). Initial conditions for the charged species are the same as in the 300 K-case. Notice that below 5 kV, no positive streamer can propagate and only a diffusive negative streamer is observed.

A reference simulation is performed using the LLW scheme on mesh M2 and snapshots of electron density and electric field magnitude at different instants are shown in Fig. 4.27. As in the 300 K-case, the negative streamer is already moving fastly after 2 ns while the positive streamer remains almost attached to the anode until 4 ns. At $t = 6$ ns, the positive streamer moves fastly and the conduction channel is formed at $t = 12$ ns. Despite the higher initial reduced electric field, the streamers inception occurs about 3 ns later than at 300 K. Moreover, the electron density is about one order of magnitude lower at 1000 K compared to 300 K.

A mesh convergence is now performed using the LLW scheme, and results are shown in Fig 4.29. The same conclusion as for the 300 K discharge can be done except that the streamer propagation remains stable up to a 7.5 µm-cell size (mesh M6). The FOU scheme exhibits faster positive streamer propagation whereas the LLW and ISG schemes leads to very similar propagation speed as shown in Fig. 4.28. For $\Delta x = 10$ µm (mesh M7), the simulation quickly

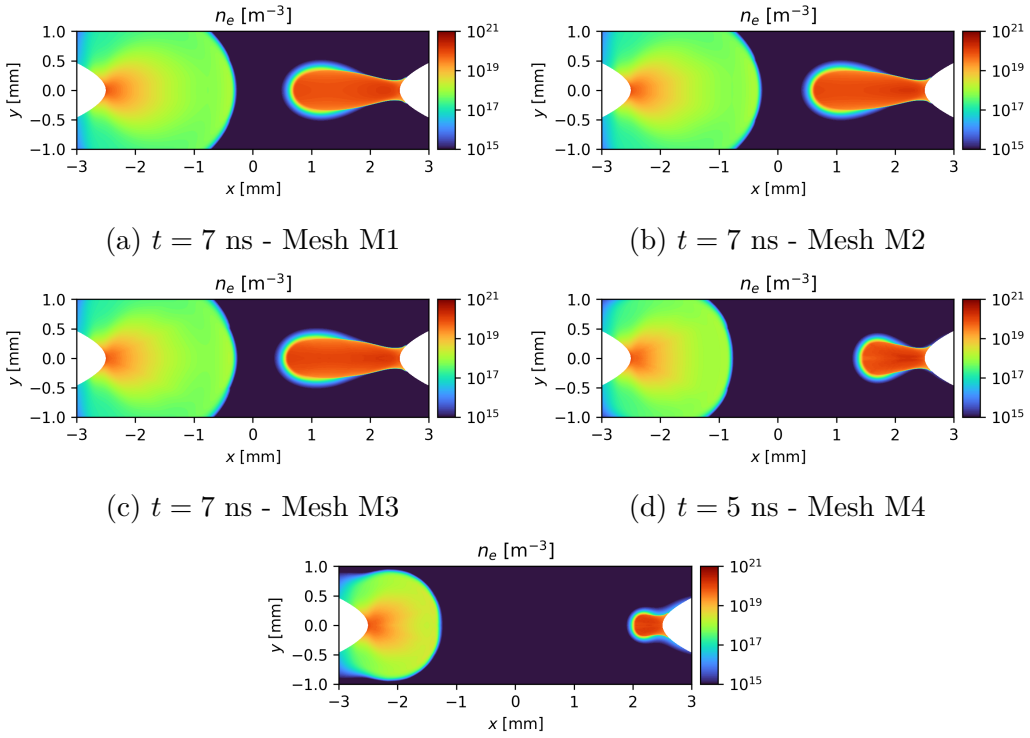

(a) $t = 7$ ns - Mesh M1

(b) $t = 7$ ns - Mesh M2

(c) $t = 7$ ns - Mesh M3

(d) $t = 5$ ns - Mesh M4

(e) $t = 3$ ns - Mesh M5

Figure 4.26: Cell size influence on the streamer propagation at 300 K for two hyperbolic-shaped electrodes having a 200 µm-curvature radius separated by 5 mm using the ISG scheme.

crashes at $t = 3$ ns following the same kind of positive streamer distortion. As shown in Fig. 4.30, the FOU scheme is also stable up to $\Delta x = 7.5$ µm. However, the increase of the positive streamer velocity due to numerical diffusion of the FOU scheme is more pronounced than in the LLW simulations. For a 10 µm-cell size, the positive streamer branches after only 2 ns leading to an unphysical propagation. Finally, the ISG scheme produces promising results with a stable positive streamer propagation for a cell size of 10 µm as shown in Fig. 4.31. Moreover, only a minor change in streamer velocity is observed when varying the cell size. The success of the ISG scheme at 1000 K seems to be attributed to the smoother positive streamer head compared with the case at 300 K.

4.2.5 Concluding remarks on hyperbolic electrodes

The numerical stability and mesh convergence of streamer propagation in pin to pin configuration have been assessed using three numerical schemes. Two different initial temperatures (T=300 K and 1000 K), representing the conditions in which NRP discharges are used, were investigated. At both temperatures, the LLW scheme is more accurate and less prone to numerical branching than the FOU scheme. Although LLW crashes on the coarser meshes, the FOU scheme exhibits numerical branching so that both schemes cannot propagate a positive streamer properly at poor spatial resolution. Moreover, positive streamer sensitivity to the mesh size is more pronounced for the FOU scheme compared to the LLW scheme. It would lead to a significant increase of the computational cost without a significant accuracy gain. The correction made on the ISG scheme to make it applicable on triangular meshes has shown

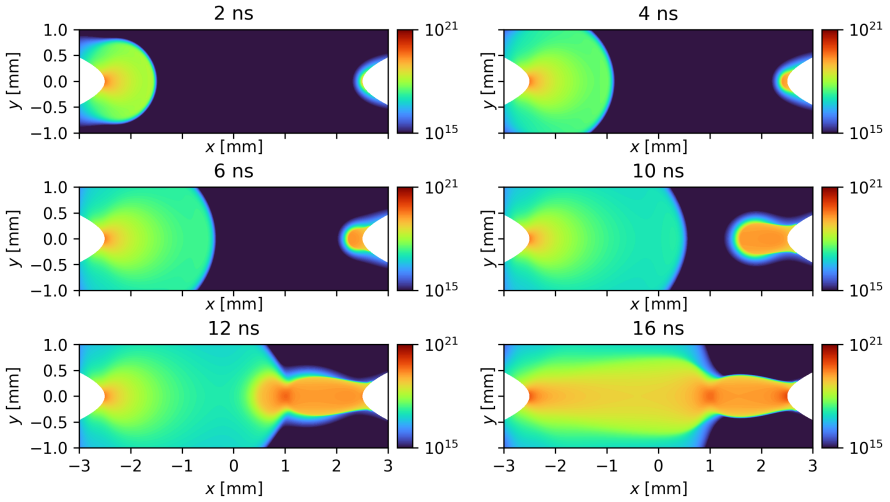

(a) n_e [m^{-3}]

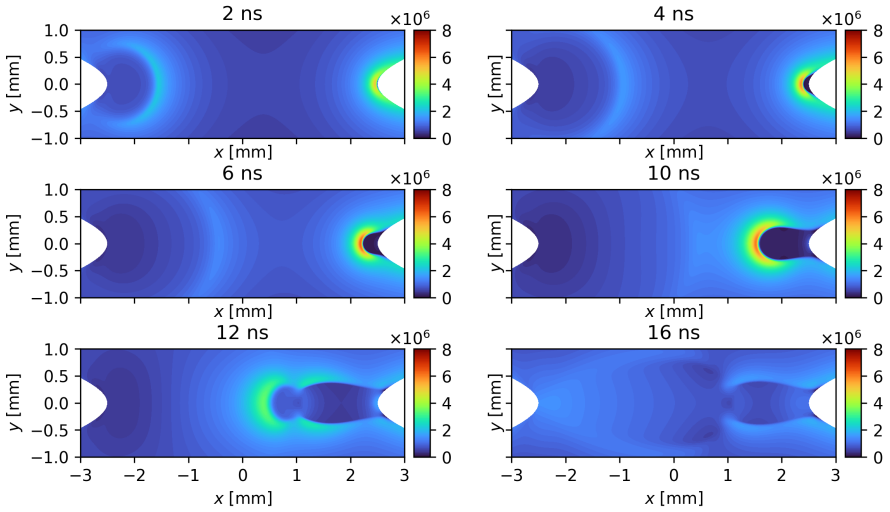

(b) $||\mathbf{E}||$ [V/m]

Figure 4.27: Streamer propagation at 1000 K for two hyperbolic-shaped electrodes having a 200 µm-curvature radius separated by 5 mm using the LLW scheme on the mesh M2.

encouraging results and an effort needs to be made to stabilize it. At 300 K, the ISG scheme leads to similar positive streamer propagation than the LLW scheme. Stability of the positive streamer propagation is kept for $\Delta x \leq 3\,\mu$m as for the LLW and FOU schemes. For $\Delta x = 4\,\mu$m, the positive streamer starts to propagate correctly with only minor branching and shows better results than the LLW scheme. At 1000 K, the ISG scheme is even more stable than the LLW scheme with a proper discharge propagation even at 10 µm.

More generally, the negative streamer was found to be very easy to propagate regarding the spatial discretization independently of the scheme used. This is due to the lowest density gradient in the negative streamer head compared with the positive streamer head. Consequently, the negative streamer region can be discretized with larger cells ($\Delta x \geq 5\,\mu$m) to decrease the computational cost. The positive streamer needs fine cell size to propagate correctly. A comparison of the positive streamer head structure at 300 K and 1000 K is shown in Fig. 4.32. As discussed previously following the discussion concerning the similarity laws in [115], the electron density

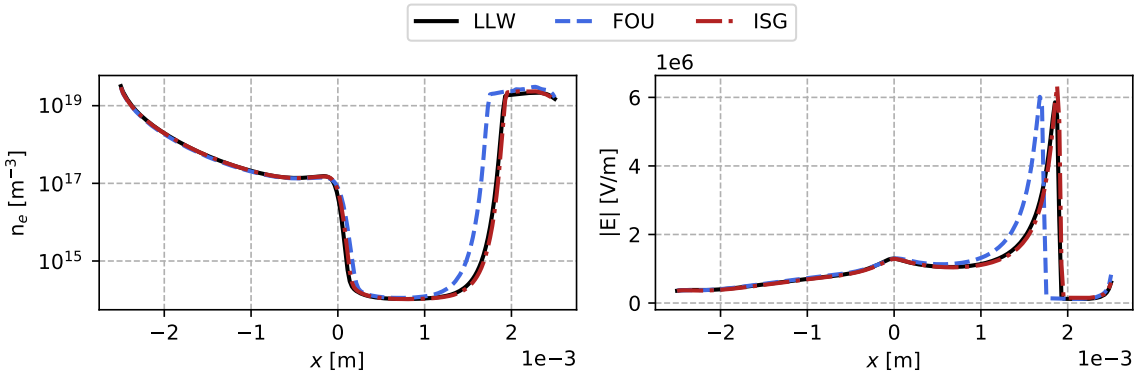

Figure 4.28: Electron density (left) and electric field (right) along the axis at $t = 10$ ns of the streamer propagation at 1000 K for two hyperbolic-shaped electrodes having a 200 µm-curvature radius separated by 5 mm using different scheme on mesh M5.

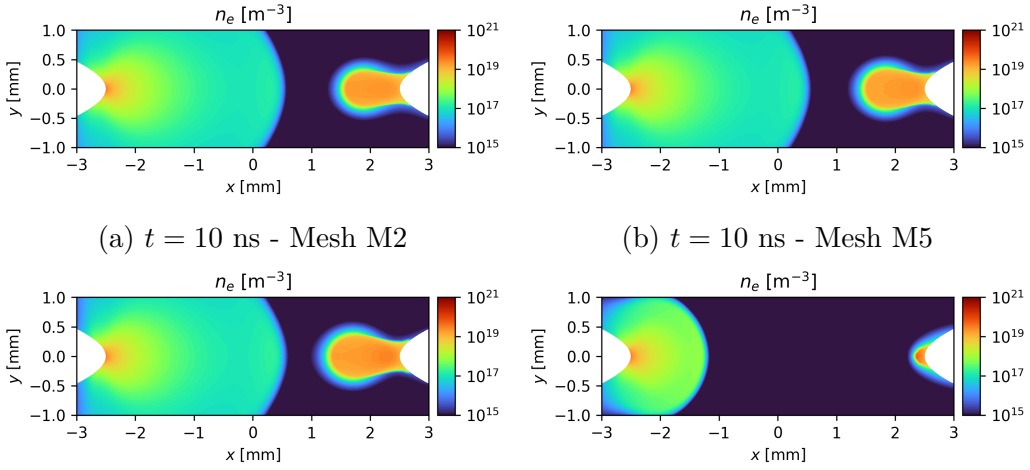

(a) $t = 10$ ns - Mesh M2

(b) $t = 10$ ns - Mesh M5

(c) $t = 10$ ns - Mesh M6

(d) $t = 3$ ns - Mesh M7

Figure 4.29: Cell size influence on the streamer propagation at 1000 K for two hyperbolic-shaped electrodes having a 200 µm-curvature radius separated by 5 mm using the LLW scheme.

is much higher at 300 K compared with the case at 1000 K, leading to higher gradients. Another consequence is the shape of the space charge ρ_c presents in the RHS of the Poisson equation. This RHS is more intense and narrower at 300 K compared with the case at 1000 K. Based on Fig. 4.32, the FWHM of the space charge, which is a good estimate of the stremer head width, is estimated to 32 µm and 45 µm at 300 K and 1000 K respectively. From the mesh convergence performed in this section with the LLW scheme, the maximal cell size $\Delta x_{\max}$ required for stable propagation increases with the temperature: 3 µm at 300 K and 7.5 µm at 1000 K. These two mesh sizes respectively correspond to 10 and 6 points in the positive streamer head. Moreover, the characteristic length introduced previously in Fig. 4.17 seems to be a good first guess for the required mesh size. Indeed, at 300 K we observed $\Delta x_{\max} \times \alpha = 1.33$, while at 1000 K we have $\Delta x_{\max} \times \alpha = 1.86$. To conclude, the mesh size can be estimated a priori with $\Delta x \in [\alpha^{-1}/2, \alpha^{-1}]$. Based on a first solution, it should be verified that the streamer head is correctly discretized with 6 to 10 points in the space charge FWHM.

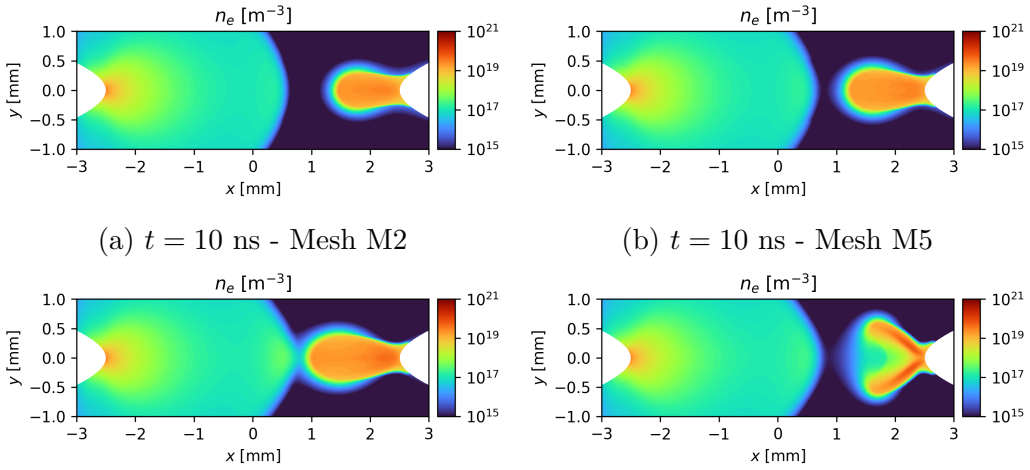

(a) $t = 10$ ns - Mesh M2

(b) $t = 10$ ns - Mesh M5

(c) $t = 10$ ns - Mesh M6

(d) $t = 10$ ns - Mesh M7

Figure 4.30: Cell size influence on the streamer propagation at 1000 K for two hyperbolic-shaped electrodes having a 200 µm-curvature radius separated by 5 mm using the FOU scheme.

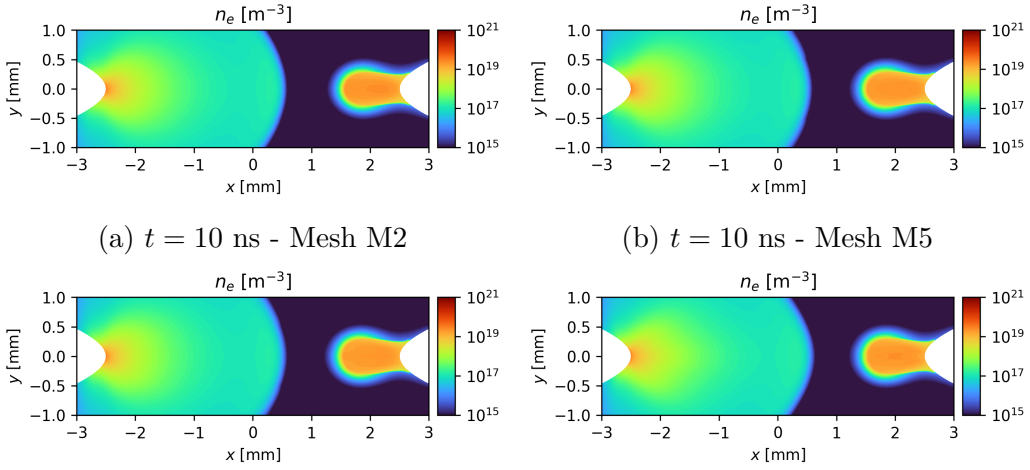

(a) $t = 10$ ns - Mesh M2

(b) $t = 10$ ns - Mesh M5

(c) $t = 10$ ns - Mesh M6

(d) $t = 10$ ns - Mesh M7

Figure 4.31: Cell size influence on the streamer propagation at 1000 K for two hyperbolic-shaped electrodes having a 200 µm-curvature radius separated by 5 mm using the ISG scheme.

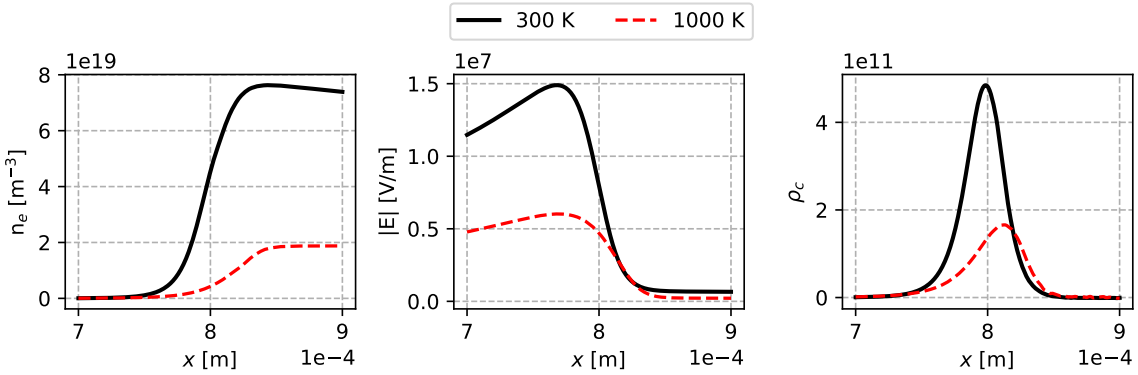

Figure 4.32: Structure of the positive streamer head at 300 K (t=7 ns) and 1000 K (t=10 ns) using the LLW scheme respectively on mesh M1 and M2. The positive streamer at 1000 K has been shifted by 0.75 mm to the left. ρ_c corresponds to rhs of the Poisson equation representative of the streamer head width and amplitude.

Part II

Plasma-assisted combustion chemistry

This part deals with the plasma-assisted combustion chemistry that is crucial for detailed simulation of the plasma-combustion coupling. The Chapter 5 presents the chemistry modeling adopted. The Chapters 6 and 7 aim to develop and validate a plasma chemistry in air and CH_4-air mixture and are partially taken from the published work [44]. Then, Chapter 8 extends the previously validated kinetic mechanism to vitiated mixtures in which NRP discharges often occur. As the detailed chemistry is not affordable for multi-dimensional simulations, reduced chemical mechanisms are generated in Chapter 9 and an existing phenomenological model [34] is improved in Chapter 10 based on the learning we made in the whole part.

Chapter 5

Chemistry modeling

Contents

The study of detailed chemistry requires simplified cases which can describe the essential features of the chemical mechanism. In this work, the CANTERA library [66] has been used to benefit from all its capabilities in combustion modeling. Moreover, the reduction tool ARCANE [37] developed at CERFACS and Cornell University relies on CANTERA. Thus we could also benefit from all the developments made on the reduction tool during the past few years. The classical 0D and 1D cases available in CANTERA and used in this work are briefly summarized in Section 5.1. Then in Section 5.2, a 0D reactor dedicated to plasma-combustion simulations is presented.

5.1 Canonical combustion cases

Combustion chemistries are classically studied employing zero-dimensional reactors or one-dimensional steady flames. These simplified representations allow evaluating some important combustion properties with detailed chemistry containing hundreds of species and thousands of reactions. The 0D reactors allow to study the time evolution of a spatially homogeneous reactive mixture and are very convenient for studying the auto-ignition delay time. The 1D flame case allows the study of the flame spatial structure including the transport processes, which are absent in 0D cases.

5.1.1 Isochoric reactor

In a zero-dimensional isochoric reactor, the mass fractions Y_k and the gas temperature T are governed by [165]:

$$m\frac{\mathrm{d}Y_k}{\mathrm{d}t} = V\dot{\omega}_k \tag{5.1}$$

$$mc_v\frac{\mathrm{d}T}{\mathrm{d}t} = V\dot{\omega}_T \tag{5.2}$$

where m is the mass of the mixture, t is the time, $\dot{\omega}_k$ is the volumic mass production rate of species k, P is the pressure, V is the volume, c_v is the mass heat capacity at constant volume and $\dot{\omega}_T$ is the volumic heat release rate.

The species source term $\dot{\omega}_k$ relies on the chemical mechanism used, which can include different types of reactions described in Section 5.1.3. The heat release rate is given by:

$$\dot{\omega}_T = -\sum_k \dot{\omega}_k u_k \tag{5.3}$$

where u_k is the internal energy per kg of species k.

5.1.2 1D freely propagating flame

This canonical case is used to study the structure of a 1D premixed flame. In addition to the thermo-chemical properties of the mechanism, the solution also depends on the species transport. The coupled chemistry and transport models must be able to predict the flame speed and the burnt gas temperature, which are two fundamental combustion properties. In the steady laminar premixed flame, the conservation equations for perfect gas read along the z-direction [165]:

$$\frac{\partial \rho u}{\partial z} = 0 \tag{5.4}$$

$$\rho u\frac{\partial Y_k}{\partial z} = -\frac{\partial j_{k,z}}{\partial z} + \dot{\omega}_k \tag{5.5}$$

$$\rho u c_p\frac{\partial T}{\partial z} = \frac{\partial}{\partial z}\left(\lambda\frac{\partial T}{\partial z}\right) - \sum_k c_{pk} j_{k,z}\frac{\partial T}{\partial z} - \sum_k h_k\dot{\omega}_k \tag{5.6}$$

where u is the gaseous speed, $\dot{\omega}_k$ is the mass production rate of species k, $j_{k,z}$ is the diffusive mass flux of species k, c_p is the mass average specific heat, $c_{p,k}$ is the specific heat of species k, λ is the thermal conductivity and h_k is the internal enthalpy of species k. These equations are supplemented by an ideal gas law $\rho = \frac{p\bar{W}}{RT}$ where $\bar{W}$ is the mean molecular weight of the mixture. In CANTERA, the species diffusive mass flux $j_{k,z}$ is computed using a mixture-average formulation following the Hirshfelder and Curtis approximation [81] with a correction velocity to ensure that the sum of the diffusion fluxes is zero. These steady-state equations describe a wave propagating from the burnt to the fresh gas at the so-called laminar flame speed S_L, so that $\rho u = \text{cte} = \rho_0 S_L$. In CANTERA, these equations are solved iteratively as described in [165, Section 15.1.3]

5.1.3 Chemical mechanism

A chemical mechanism is composed of N species that are coupled through a set of M chemical reactions. Each chemical reaction $j \in [1, M]$ can be written as:

$$\sum_{k=1}^{N} \nu'_{kj} \mathcal{M}_k \rightleftharpoons \sum_{k=1}^{N} \nu''_{kj} \mathcal{M}_k \tag{5.7}$$

or equivalently

$$\sum_{k=1}^{N} \nu_{kj} \mathcal{M}_k = 0 \tag{5.8}$$

where $\mathcal{M}_k$ symbolizes a species k, ν'_{kj} and ν''_{kj} are the molar stoichiometric coefficients of the species k in the reaction j for respectively the reactants and the products, $\nu_{kj} = \nu''_{kj} - \nu'_{kj}$. From the whole set of reactions, the mass production rate $\dot{\omega}_k$ of a species k reads:

$$\dot{\omega}_k = W_k \sum_{j=1}^{M} \nu_{kj} \mathcal{Q}_j \tag{5.9}$$

where W_k is the molecular weight of species k and $\mathcal{Q}_j$ is the net progress rate or net molar production rate of the reaction j expressed in $[\mathrm{mol\,m^{-3}\,s^{-1}}]$. The molar production rate is usually expressed as:

$$\mathcal{Q}_j = K_{fj} \prod_{k=1}^{N} [\mathcal{M}_k]^{\nu'_{kj}} - K_{rj} \prod_{k=1}^{N} [\mathcal{M}_k]^{\nu''_{kj}} \tag{5.10}$$

where K_{fj} and K_{rj} are the forward and reverse rates of reaction j and $[\mathcal{M}_k]$ is the molar concentration of the species k. For an irreversible reaction, K_{rj} is set to zero. For most of the reactions encountered in combustion, the forward reaction rate can be modeled using an Arrhenius law:

$$K_{fj} = A_j T^{\beta_j} \exp\left(-\frac{E_j}{RT}\right) \tag{5.11}$$

where A_j is the pre-exponential constant, β_j is the temperature exponent and E_j is the activation energy. Other kinds of reactions are available in CANTERA, including three-body reactions, pressure-dependent reactions and falloff reactions (See [165] for more details). The reverse reaction rate K_{rj} can be computed through its relation with the forward rate K_{fj} and the equilibrium constants K_c:

$$K_c = \frac{K_{fj}}{K_{rj}} = \left(\frac{p_0}{RT}\right)^{\sum_{k=1}^{N} \nu_{kj}} \exp\left(\frac{\Delta_r S_j^0}{R} - \frac{\Delta_r H_j^0}{RT}\right) \tag{5.12}$$

where $p_0 = 1\,\mathrm{bar}$, $\Delta_r S_j^0$ is the reaction entropy change and $\Delta_r H_j^0$ is the reaction enthalpy change. The computation of the equilibrium constant relies on the thermodynamics properties of the species that are computed using NASA polynomial. Most of these coefficients can be retrieved from Burcat's database [29].

Any chemical reaction j is accompanied by a heat release linked to the species internal energy or enthalpy change of reaction respectively denoted Δu_j and Δh_j. The use of the internal energy reaction change Δu_j is used for fixed volume system (*i.e.* in the c_v formulation) wheareas the enthalpy reaction change Δh_j is used for open system at fixed pressure (*i.e.* in the c_p formulation). The global heat release rate $\dot{\omega}_T$ provided by all the reactions of the mechanism can be computed through:

$$\dot{\omega}_T = \sum_{j=1}^{M} \mathcal{Q}_j \Delta u_j \quad \text{or} \quad \dot{\omega}_T = \sum_{j=1}^{M} \mathcal{Q}_j \Delta h_j \tag{5.13}$$

or equivalently as a sum over the species:

$$\dot{\omega}_T = \sum_{k=1}^{N} \dot{\omega}_k u_k \quad \text{or} \quad \dot{\omega}_T = \sum_{k=1}^{N} \dot{\omega}_k h_k \tag{5.14}$$

The second option is usually preferred as $N \ll M$ in most cases and is thus less expensive to compute. However, the first one allows controlling the heat release rate of each reaction and will be considered in Section 6.4.

5.2 Zero-dimensional plasma reactors

This section aims to develop a low-dimensional representation of the plasma interaction with a reactive mixture. It is based on the conventional 0D isochoric or isobaric reactors available in CANTERA, on which plasma-specific features have been added. Only the isochoric plasma reactor is detailed in the following, but a very similar isobaric plasma reactor was also implemented in CANTERA during this work.

5.2.1 Governing equations

The governing equations used for the species mass fractions and the gas temperature are essentially the same as in the classical isochoric reactor detailed in Section 5.1.1. Indeed, the isochoric plasma reactor is a subclass of the isochoric reactor and inherits all its capacities.

$$m \frac{\mathrm{d}Y_k}{\mathrm{d}t} = V \dot{\omega}_k \tag{5.15}$$

$$m c_v \frac{\mathrm{d}T}{\mathrm{d}t} = V \dot{\omega}_T + \dot{Q} \tag{5.16}$$

where $\dot{Q}$ is an external power source term that is used to manage some features of the discharge energy transfer to the gas.

In typical NRP discharge conditions, the electrons are far from equilibrium and their energy must be treated separately. In low-temperature plasmas, the ionization degree, *i.e.*, the molar fraction of the charged species in the mixture, is relatively low, reaching at most 10^{-4} to 10^{-3}. Despite this low concentration, the electrons can transfer a significant amount of energy to the mixture in a very efficient way during so-called electron impact collisions. Indeed, thanks to the strong electric field in plasma discharges, electrons are much more energetic than other heavy species, having a temperature as high as 5 to 10 eV ($\geq 50\,000$ K). The resulting electron-neutral collisions can efficiently produce reactive species such as radicals or excited states, driving the electron distribution far from a Maxwellian one. It is thus important to know the electron distribution function $f_e(\mathbf{r}, \mathbf{v}_e, t)$, with $\mathbf{r}$ the position and $\mathbf{v}_e$ the electron velocity, which obeys the Boltzmann equation:

$$\frac{\partial f_e}{\partial t} + \mathbf{v}_e \cdot \nabla f_e - \frac{e\mathbf{E}}{m_e} \cdot \nabla_v f_e = \left(\frac{\delta f_e}{\delta t} \right)_c \tag{5.17}$$

where $\mathbf{E}$ is the electric field and m_e the electron mass. ∇_v corresponds to gradient in velocity space. The collision term $(\delta f_e/\delta t)_c$ is computed from a complete set of cross sections σ_j containing mostly electron-neutral collisions.

Assuming a two-term expansion, the electron distribution function f_e can be written as the product of the Electron Energy Distribution Function (EEDF) F_0 and the electron density n_e [72]. The Boltzmann equation (5.17) is then recast in terms of F_0 and solved. This allows to compute the reaction rate k_j associated to the cross-section σ_j and the effective electron temperature T_e by integrating over energy ε [72]:

$$k_j = \gamma \int_0^\infty \varepsilon \sigma_j F_0 d\varepsilon \tag{5.18}$$

$$T_e = \frac{2}{3} \int_0^\infty \varepsilon^{3/2} F_0 d\varepsilon \tag{5.19}$$

with $\gamma = \sqrt{\frac{2e}{m_e}}$ a constant and $\varepsilon = (v/\gamma)^2$ the electron energy in electron-volt. In typical discharges, T_e rises up to 5 eV. In this work, an EEDF solver has been implemented in CANTERA, based on an open-source version of BOLSIG+ [72] named BOLOS, written by Alejandro Luque. Some features such as the energy grid adaptation from the open-source solver LOKI-B [52] have been introduced in our EEDF solver.

Finally, the mean non-equilibrium vibrational energy e^k_{vib} of a ground state species k is governed by:

$$\frac{de^k_{\text{vib}}}{dt} = \dot{E}^k_{\text{vib}} - \dot{R}^k_{\text{VT}} \tag{5.20}$$

where $\dot{E}^k_{\text{vib}}$ corresponds to the vibrational excitation of the species k by the plasma discharge and $\dot{R}^k_{\text{VT}}$ is a sink term which relaxes the vibrational energy into translational energy (*i.e.*, into gas heating). Thus, this sink term appears as a source term in the gas temperature equation with:

$$\dot{Q} = \sum_k \dot{R}^k_{\text{VT}} \tag{5.21}$$

More details concerning the vibrational energy modeling will be given in Section 6.5.

5.2.2 Plasma reactions

In addition to the classical reactions described in Section 5.1.3, an extension of the Arrhenius law, including an electron temperature dependency, has been added to CANTERA. This reaction is referred to as `plasma_reaction` and reads:

$$k_j = A_j T^{\beta_j} \exp\left(-\frac{E_j}{RT}\right) T_e^{\beta'_j} \exp\left(-\frac{E'_j}{RT_e}\right) \exp\left(-\frac{T}{T_j}\right) \tag{5.22}$$

where A_j is the pre-exponential constant, β_j and β'_j are the gas temperature and electron temperature exponents, E_j is the activation relative to the gas temperature, and E'_j is the activation energy relative to the electron energy. The last exponential term involving the temperature T_j is only used for very few reactions and is not computed when T_j is not specified in the reaction.

Chapter 6

Plasma chemistry in air

Contents

Plasma discharges in the air have been extensively studied in the past, and their chemistry is relatively well-known [94, 32]. A good description of the chemical mechanisms in pure air is a keystone for any plasma-assisted combustion mechanism, as usually N_2 and O_2 remain the dominant components of the mixture in combustion applications. In the following, a detailed plasma kinetic mechanism for NRP discharges in the air is presented and validated against experiments.

6.1 Discharge energy branching in air

We first describe the discharge energy branching which explains how the electro-magnetic power P_{EM} is transferred into the heavy molecules of the gas. The electron power loss is the sum of the elastic power loss P_{el} and the inelastic power loss P_{inel} which read respectively [72]:

$$P_{\mathrm{el}} = \sum_{k=\mathrm{elastic}} P_{\mathrm{el}}^{k} = \sum_{k=\mathrm{elastic}} \gamma n_k \frac{2m_e}{M_k} \int_0^{\infty} \left[\sigma_k \left(\epsilon^2 F_0 + \frac{k_B T}{e} \frac{\partial F_0}{\partial \epsilon} \right) \right] d\epsilon \tag{6.1}$$

$$P_{\mathrm{inel}} = \sum_{k=\mathrm{inelastic}} P_{\mathrm{inel}}^{k} = \sum_{k=\mathrm{inelastic}} n_k k_k \Delta\epsilon_k \tag{6.2}$$

where n_k is the number density of the target particle involved in the process k, M_k is its mass, σ_k is the cross-section associated to the process k, T is the gas temperature of target particle, k_k is the reaction rate of the process k and $\Delta\epsilon_k$ is the energy threshold of the process k. The elastic power is composed of two contributions: the first one corresponds to the kinetic energy lost to the collinding particles and the second one reflects the energy gained by the electron from the collinding particles which follow a Maxwellian distribution. Notice that in Eq. 6.2, the super-elastic processes are not considered. When neglecting the electron growth power [72] and power loss due to the electron-ion Coulomb collisions, the solution of BOLSIG+ [72] verifies

$$P_{\mathrm{EM}} = P_{\mathrm{el}} + P_{\mathrm{inel}} \tag{6.3}$$

The power fraction r_{inel}^{k} that is transferred from the electrons to the gas in the inelastic process k is given by Eq. 6.4. In this work, the elastic power loss ratio r_{el} is always computed as a global loss over all the mixture components using Eq. 6.5. Moreover, as rotational states are not considered explicitly in this work, the power transferred to the particles in such state is merged with the elastic power loss.

$$r_{\mathrm{inel}}^{k} = \frac{P_{\mathrm{inel}}^{k}}{P_{\mathrm{EM}}} \tag{6.4}$$

$$r_{\mathrm{el}} = \frac{P_{\mathrm{el}}}{P_{\mathrm{EM}}} \tag{6.5}$$

The Phelps database [148] is used within BOLSIG+ to compute the power ratio of the different processes in a N_2:O_2:80:20 mixture representative of air. The processes considered with these cross-sections along with the associated reactions are detailed in Tab. 6.1 for N_2 and Tab. 6.2 for O_2. The inelastic processes are grouped into generic processes which are the vibrational excitation, electronic excitation, electron attachment, dissociation and ionization.

The resulting discharge energy branching is shown in Fig. 6.1 as a function of the reduced electric field for a representative mixture of the ambient air. First of all, the sum of elastic and rotational powers is only substantial at low electric field $E/N \leq 10$ Td. For $E/N \leq 10$ Td, most of the electron energy is spent to vibrationally excite O_2. Then vibrational excitation of O_2 sharply decreases to reach a negligible part of the power at $E/N \geq 100$ Td. At an intermediate reduced electric field $10 \leq E/N \leq 100$ Td, almost all the electron energy serves to excite nitrogen vibrational states $N_2(v)$. Above 100 Td, which is of primal interest in our work, the nitrogen electronic states $N_2{}^*$ are efficiently produced, representing around 50 % of the discharge energy at 200 Td. Nitrogen electronic excitation remains the dominant discharge energy channel

#	Process	Reaction	$\Delta\epsilon$ [eV]	ΔE [eV]	Type
(CS1.1)	$N_2 \longrightarrow N_2(\text{rot})$	$e^- + N_2 \longrightarrow e^- + N_2 + \Delta E$	0.02	0.02	Elastic
(CS1.2)	$N_2 \longrightarrow N_2(v_1)$	$e^- + N_2 \longrightarrow e^- + N_2(v{=}1)$	0.29	0.0	Vibration
(CS1.3)	$N_2 \longrightarrow N_2(v_1\text{res})$	$e^- + N_2 \longrightarrow e^- + N_2(v{=}1)$	0.29	0.0	Vibration
(CS1.4)	$N_2 \longrightarrow N_2(v_2)$	$e^- + N_2 \longrightarrow e^- + N_2(v{=}2)$	0.59	0.0	Vibration
(CS1.5)	$N_2 \longrightarrow N_2(v_3)$	$e^- + N_2 \longrightarrow e^- + N_2(v{=}3)$	0.88	0.0	Vibration
(CS1.6)	$N_2 \longrightarrow N_2(v_4)$	$e^- + N_2 \longrightarrow e^- + N_2(v{=}4)$	1.17	0.0	Vibration
(CS1.7)	$N_2 \longrightarrow N_2(v_5)$	$e^- + N_2 \longrightarrow e^- + N_2(v{=}5)$	1.47	0.0	Vibration
(CS1.8)	$N_2 \longrightarrow N_2(v_6)$	$e^- + N_2 \longrightarrow e^- + N_2(v{=}6)$	1.76	0.0	Vibration
(CS1.9)	$N_2 \longrightarrow N_2(v_7)$	$e^- + N_2 \longrightarrow e^- + N_2(v{=}7)$	2.06	0.0	Vibration
(CS1.10)	$N_2 \longrightarrow N_2(v_8)$	$e^- + N_2 \longrightarrow e^- + N_2(v{=}8)$	2.35	0.0	Vibration
(CS1.11)	$N_2 \longrightarrow N_2(A_3, v{=}0\text{-}4)$	$e^- + N_2 \longrightarrow e^- + N_2(A_3)$	6.17	0.0	Electronic
(CS1.12)	$N_2 \longrightarrow N_2(A_3, v{=}5\text{-}9)$	$e^- + N_2 \longrightarrow e^- + N_2(A_3) + \Delta E$	7.0	0.83	Electronic
(CS1.13)	$N_2 \longrightarrow N_2(A_3, v{=}10\text{-})$	$e^- + N_2 \longrightarrow e^- + N_2(A_3) + \Delta E$	7.8	1.63	Electronic
(CS1.14)	$N_2 \longrightarrow N_2(B_3)$	$e^- + N_2 \longrightarrow e^- + N_2(B_3)$	7.35	0.0	Electronic
(CS1.15)	$N_2 \longrightarrow N_2(W_3)$	$e^- + N_2 \longrightarrow e^- + N_2(B_3) + \Delta E$	7.36	0.01	Electronic
(CS1.16)	$N_2 \longrightarrow N_2(B'_3)$	$e^- + N_2 \longrightarrow e^- + N_2(B_3) + \Delta E$	8.16	0.81	Electronic
(CS1.17)	$N_2 \longrightarrow N_2(a'_1)$	$e^- + N_2 \longrightarrow e^- + N_2(a_1)$	8.4	0.0	Electronic
(CS1.18)	$N_2 \longrightarrow N_2(a_1)$	$e^- + N_2 \longrightarrow e^- + N_2(a_1) + \Delta E$	8.55	0.15	Electronic
(CS1.19)	$N_2 \longrightarrow N_2(w_1)$	$e^- + N_2 \longrightarrow e^- + N_2(a_1) + \Delta E$	8.89	0.49	Electronic
(CS1.20)	$N_2 \longrightarrow N_2(a''_1)$	$e^- + N_2 \longrightarrow e^- + N_2(a_1) + \Delta E$	12.25	3.85	Electronic
(CS1.21)	$N_2 \longrightarrow N_2(C_3)$	$e^- + N_2 \longrightarrow e^- + N_2(C_3)$	11.03	0.0	Electronic
(CS1.22)	$N_2 \longrightarrow N_2(E_3)$	$e^- + N_2 \longrightarrow e^- + N_2(C_3) + \Delta E$	11.87	0.84	Electronic
(CS1.23)	$N_2 \longrightarrow N_2(\text{SUM})$	$e^- + N_2 \longrightarrow e^- + N + N(^2D) + \Delta E$	13.0	0.90	Dissociation
(CS1.24)	$N_2 \longrightarrow {N_2}^+$	$e^- + N_2 \longrightarrow 2\,e^- + {N_2}^+$	15.6	0.0	Ionization
(CS1.25)	$N_2 \longrightarrow {N_2}^+(B_2\text{SIGMA})$	$e^- + N_2 \longrightarrow 2\,e^- + {N_2}^+ + \Delta E$	18.8	3.2	Ionization

Table 6.1: List of processes in the Phelps database [148] for N_2 and the associated reactions considered in this work.

#	Process	Reaction	$\Delta\epsilon$ [eV]	ΔE [eV]	Type
(CS2.1)	$O_2 \longrightarrow O_2(\text{rot})$	$e^- + O_2 \longrightarrow e^- + O_2 + \Delta E$	0.02	0.02	Elastic
(CS2.2)	O_2 (ATT)	$e^- + O_2 + M \longrightarrow {O_2}^- + M$	0.0	0.0	Attachment
(CS2.3)	$O_2 \longrightarrow O^- + O$	$e^- + O_2 \longrightarrow O^- + O$	0.0	0.0	Attachment
(CS2.4)	$O_2 \longrightarrow O_2(v_1)$	$e^- + O_2 \longrightarrow e^- + O_2(v_1)$	0.19	0.0	Vibration
(CS2.5)	$O_2 \longrightarrow O_2(v_1\text{res})$	$e^- + O_2 \longrightarrow e^- + O_2(v_1)$	0.19	0.0	Vibration
(CS2.6)	$O_2 \longrightarrow O_2(v_2)$	$e^- + O_2 \longrightarrow e^- + O_2(v_2)$	0.38	0.0	Vibration
(CS2.7)	$O_2 \longrightarrow O_2(v_2\text{res})$	$e^- + O_2 \longrightarrow e^- + O_2(v_2)$	0.38	0.0	Vibration
(CS2.8)	$O_2 \longrightarrow O_2(v_3)$	$e^- + O_2 \longrightarrow e^- + O_2(v_3)$	0.57	0.0	Vibration
(CS2.9)	$O_2 \longrightarrow O_2(v_4)$	$e^- + O_2 \longrightarrow e^- + O_2(v_4)$	0.75	0.0	Vibration
(CS2.10)	$O_2 \longrightarrow O_2(a_1)$	$e^- + O_2 \longrightarrow e^- + O_2(a_1)$	0.977	0.0	Electronic
(CS2.11)	$O_2 \longrightarrow O_2(b_1)$	$e^- + O_2 \longrightarrow e^- + O_2(b_1)$	1.627	0.0	Electronic
(CS2.12)	$O_2 \longrightarrow O_2(4.5\,\text{eV})$	$e^- + O_2 \longrightarrow e^- + O_2(A_3)$	4.5	0.0	Electronic
(CS2.13)	$O_2 \longrightarrow O_2(6.0\,\text{eV})$	$e^- + O_2 \longrightarrow e^- + 2\,O + \Delta E$	6.0	0.78	Dissociation
(CS2.14)	$O_2 \longrightarrow O_2(8.4\,\text{eV})$	$e^- + O_2 \longrightarrow e^- + O + O(^1D) + \Delta E$	8.4	1.26	Dissociation
(CS2.15)	$O_2 \longrightarrow O_2(9.97\,\text{eV})$	$e^- + O_2 \longrightarrow e^- + O + O(^1S) + \Delta E$	9.97	0.63	Dissociation
(CS2.16)	$O_2 \longrightarrow {O_2}^+$	$e^- + O_2 \longrightarrow 2\,e^- + {O_2}^+$	12.06	0.0	Ionization

Table 6.2: List of processes in the Phelps database [148] for O_2 and the associated reactions considered in this work.

up to 600 Td above which it is replaced by N_2 dissociation and ionization. This result differs from [179, Fig. 21.a] where nitrogen electronic excitation is presented as the dominant channel

between 100 and 1000 Td. This difference is attributed to the process (CS1.23) in the Table 6.1 in which we assume N_2-dissociation as in [157]. The oxygen dissociation is the second most important process up to $\simeq$ 300 Td, with a peak value of $\approx$ 20 % at 200 Td. Concomitantly, the nitrogen vibrational excitation drastically decreases above 100 Td but remains non-negligible up to 300 Td. At a very high reduced electric field $E/N \gg 600$ Td, ionization and N_2-dissociation processes convert a substantial part of the electron energy, with around 35 % each at 1000 Td.

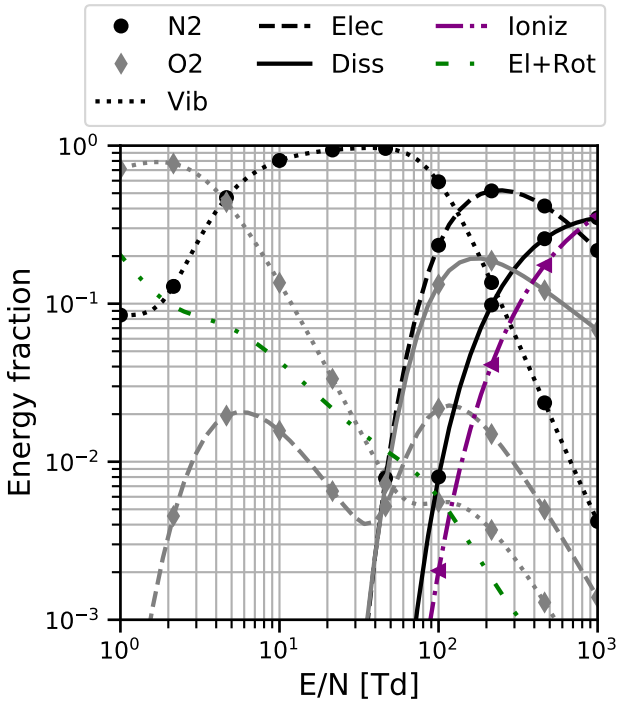

Figure 6.1: Discharge energy branching in air ($X_{O_2} = 0.2, X_{N_2} = 0.8$) computed with BOLSIG+ [72].

6.2 The two-step mechanism

A well-established mechanism in air called the two-step mechanism in Popov [159, 157, 160], is responsible for a significant amount of atomic oxygen production and intense fast gas heating (FGH) during the discharge. This mechanism is summarized by the following reactions that occur consecutively:

$$e^- + N_2 \longrightarrow e^- + N_2{}^* \tag{R1}$$
$$N_2{}^* + O_2 \longrightarrow N_2 + 2\,O + \text{Heat} \tag{R2}$$

where $N_2{}^* = N_2(A_3, B_3, C_3, a_1)$. The reaction rates for reactions (R1) are computed using BOLSIG+ [72] using the previously described complete set of N_2 cross-sections of the Phelps' database [148]. The triplet and singlet electronic states $N_2(B_3)$ and $N_2(a_1)$ are lumpings of $N_2\,(B^3\Pi_g)$, $N_2\,(B'^3\Sigma_u^-)$, $N_2\,(W^3\Delta_u)$ and $N_2\,(a^1\Pi_g)$, $N_2\,(a'^1\Sigma_u^-)$, $N_2\,(w^1\Delta_u)$ states respectively as usually assumed [157], $N_2(B_3)$ and $N_2(a_1)$ representing the lowest excited states of each group.

The difference of energy between the lower state and the higher states in the group is assumed to be transferred into translational energy (*i.e.*, as a heating term).

The super-elastic collisions of $N_2{}^*$ with electrons were not considered in this work. Then, the excited nitrogen can be lost in radiative or collisional quenching. Radiative quenching occurs when the excited state emits a photon as described in the reaction (R3). In that case, N_2' can be another lower excited state or the ground state $N_2(X)$. At standard conditions, only the optical transition $N_2(C_3) \longrightarrow N_2(B_3)$ that occurs at nanosecond timescale is relevant. The other transitions occur at a much higher timescale [32].

$$N_2{}^* \longrightarrow N_2' + h\nu \tag{R3}$$

Most of the electronic states of N_2 are consumed through the collisional quenching processes. Among them, the dissociation of O_2 represented by the reaction (R2) plays an important role. The reaction rates of the reaction (R2) are given in Tab. 6.3. The rate of reaction (A1) is the recommended rate of reaction $N_2 + O_2 \longrightarrow$ *products* from [78], multiplied by a factor of 0.77 as suggested by [65] for O_2 dissociation. For reaction (A3), different dissociative channels were considered as discussed in [157]: the ratios for the production of $O(^3P) + O(^3P)$, $O(^3P) + O(^1D)$ and $O(^3P) + O(^1S)$ were respectively 0.46, 0.52 and 0.02. Finally, the rate of reaction of (A4) is taken from [124] and will be discussed in more detail in Section 6.3.

#	Reaction	k_f [$\mathrm{cm^3\,s^{-1}}$]	Ref
(A1)	$N_2(A_3) + O_2 \longrightarrow N_2 + 2\,O$	$8.356 \times 10^{-14} \times T_g^{0.55}$	[78]
(A2)	$N_2(B_3) + O_2 \longrightarrow N_2 + 2\,O$	3×10^{-10}	[32]
(A3)	$N_2(C_3) + O_2 \longrightarrow N_2 + 2\,O$	$3 \times 10^{-10} \times (T_g/300)^{0.3}$	[167]
(A4)	$N_2(a_1) + O_2 \longrightarrow N_2 + 2\,O$	4.3×10^{-10}	[124]

Table 6.3: Reaction rates of dissociative quenching of $N_2{}^*$ by O_2

The kinetics of electronically excited nitrogen must be completed with their collisional quenching by other molecules to properly describe their dynamics. Table 6.4 summarizes all the reactions considered in this work along with the rates used. Most of these rates were taken from [32] and some of them were modified according to the works of Popov [159, 157] and [94]. All these reactions strongly participate in the fast gas heating occurring during NRP discharges and more details are given in Section 6.4.

6.3 Dissociative quenching of O_2 by $N_2(a_1)$

While global agreement on the dissociative quenching rates of O_2 by $N_2\,(A^3\Sigma_u^+)$, $N_2\,(B^3\Pi_g)$ and $N_2\,(C^3\Pi_u)$ is reached in the literature, the case of $N_2\,(a^1\Pi_g)$ is ambiguous. In most of the plasma-assisted combustion studies [157, 8], the rate for $N_2\,(a^1\Pi_g)$ (Reaction (A4)) is one order of magnitude smaller than $N_2\,(B^3\Pi_g)$ and $N_2\,(C^3\Pi_u)$ states. For the $N_2\,(a^1\Pi_g)$ state, the rate coefficient used in [160] ($2.8 \times 10^{-11}\,\mathrm{cm^3\,s^{-1}}$) was taken from [151] and corresponds to the quenching of the $N_2\,(a'^1\Sigma_u^-)$ state. In [124], the rate coefficient of the quenching of $N_2\,(a^1\Pi_g)$ with O_2 has been measured experimentally and was found high at $4.3 \times 10^{-10}\,\mathrm{cm^3\,s^{-1}}$.

The percentage of singlet excited states $N_2\,(a^1\Pi_g)$ production by electron impact reactions in air calculated with BOLSIG+ is depicted in Fig. 6.2, showing that $N_2\,(a^1\Pi_g)$ is dominant

#	Reaction	k_f [$\mathrm{cm^3\,s^{-1}}$]	Ref
(B1)	$N_2(A_3) + O \longrightarrow NO + N(^2D)$	7×10^{-12}	[32]
(B2)	$N_2(A_3) + O \longrightarrow N_2 + O(^1S)$	3×10^{-11}	[32]
(B3)	$N_2(A_3) + N \longrightarrow N_2 + N$	2×10^{-12}	[32]
(B4)	$N_2(A_3) + N \longrightarrow N_2 + N(^2P)$	$1.725 \times 10^{-9}\ T_g^{-0.66}$	[32]
(B5)	$N_2(A_3) + O_2 \longrightarrow N_2 + 2\,O$	$8.356 \times 10^{-14} \times T_g^{0.55}$	[78]
(B6)	$N_2(A_3) + O_2 \longrightarrow N_2 + O_2(a_1)$	$8.681 \times 10^{-15}\ T_g^{0.55}$	[32]
(B7)	$N_2(A_3) + O_2 \longrightarrow N_2 + O_2(b_1)$	$8.681 \times 10^{-15}\ T_g^{0.55}$	[32]
(B8)	$N_2(A_3) + O_2 \longrightarrow N_2O + O$	$8.681 \times 10^{-15}\ T_g^{0.55}$	[32]
(B9)	$N_2(A_3) + N_2 \longrightarrow 2\,N_2$	3×10^{-16}	[32]
(B10)	$N_2(A_3) + N_2O \longrightarrow N_2 + N + NO$	1×10^{-11}	[32]
(B11)	$N_2(A_3) + NO_2 \longrightarrow N_2 + O + NO$	1×10^{-12}	[32]
(B12)	$N_2(A_3) + N_2(A_3) \longrightarrow N_2 + N_2(C_3)$	$5.453 \times 10^{-4}\ T_g^{-2.64}$	[94]
(B13)	$N_2(A_3) + N_2(A_3) \longrightarrow N_2 + N_2(B_3)$	7.7×10^{-11}	[152]
(B14)	$N_2(B_3) + N_2 \longrightarrow 2\,N_2$	2×10^{-12}	[32]
(B15)	$N_2(B_3) + O_2 \longrightarrow N_2 + 2\,O$	3×10^{-10}	[32]
(B16)	$N_2(C_3) + N_2 \longrightarrow N_2(a_1) + N_2$	1×10^{-11}	[32]
(B17)	$N_2(C_3) + O_2 \longrightarrow N_2 + 2\,O$	$2.492 \times 10^{-11}\ T_g^{0.3}$	[167]
(B18)	$N_2(C_3) + O_2 \longrightarrow N_2 + O + O(^1D)$	$2.818 \times 10^{-11}\ T_g^{0.3}$	[167]
(B19)	$N_2(C_3) + O_2 \longrightarrow N_2 + O + O(^1S)$	$1.084 \times 10^{-12}\ T_g^{0.3}$	[167]
(B20)	$N_2(C_3) + N_2 \longrightarrow N_2(B_3) + N_2$	1×10^{-11}	[157]
(B21)	$N_2(B_3) + N_2 \longrightarrow N_2(A_3) + N_2$	1×10^{-11}	[157]
(B22)	$N_2(a_1) + N_2 \longrightarrow N_2(B_3) + N_2$	2×10^{-13}	[157]
(B23)	$N_2(a_1) + O_2 \longrightarrow N_2 + 2\,O$	4.3×10^{-10}	[124]
(B24)	$N_2(a_1) + NO \longrightarrow N_2 + N + O$	3.6×10^{-10}	[32]
(B25)	$N_2(a_1) + N_2(A_3) \longrightarrow {N_4}^+ + e^-$	5×10^{-11}	[32]
(B26)	$N_2(a_1) + N_2(a_1) \longrightarrow {N_4}^+ + e^-$	2×10^{-10}	[32]

Table 6.4: Reaction rates for collisional quenching of ${N_2}^*$

over $N_2\,(a'^1\Sigma_u^-)$ and $N_2\,(w^1\Delta_u)$ for electric fields higher than 100 Td with more than 50% of the overall production of singlet states. The state $N_2\,(a'^1\Sigma_u^-)$ only represents about 20% of the singlet states produced by the discharge.

The timescale of the reaction ((A4)) is on the order of 3 ns in air at $T = 1500\,\mathrm{K}$ and atmospheric pressure assuming $X_{O_2} = 0.15$ (air already partially dissociated by previous discharges). According to [32], the $N_2\,(a^1\Pi_g) \rightarrow N_2\,(a'^1\Sigma_u^-)$ optical transition occurs at the millisecond timescale, which is much higher than the timescale of the reaction ((A4)). The $N_2\,(a^1\Pi_g)$ collisional quenching timescale of reaction (R4) is also longer by one order of magnitude (20 ns) compared to the O_2 dissociative quenching timescale. Thus, during the first nanoseconds following the pulse, it can be concluded that $N_2(a'^1\Sigma_u^-, a^1\Pi_g, w^1\Delta_u)$ is mainly composed of $N_2\,(a^1\Pi_g)$. When not specified, the rate from [124] for the reaction ((A4)) was employed.

$$N_2\left(a^1\Pi_g\right) + M \longrightarrow N_2\left(a'^1\Sigma_u^-\right) + M, \qquad k = 9 \times 10^{-12}\,\mathrm{cm^3\,s^{-1}} \tag{R4}$$

6.4 Fast gas heating modelling

Usually, the heat release rate of a reaction j is computed using the species internal energy or enthalpy change associated to it:

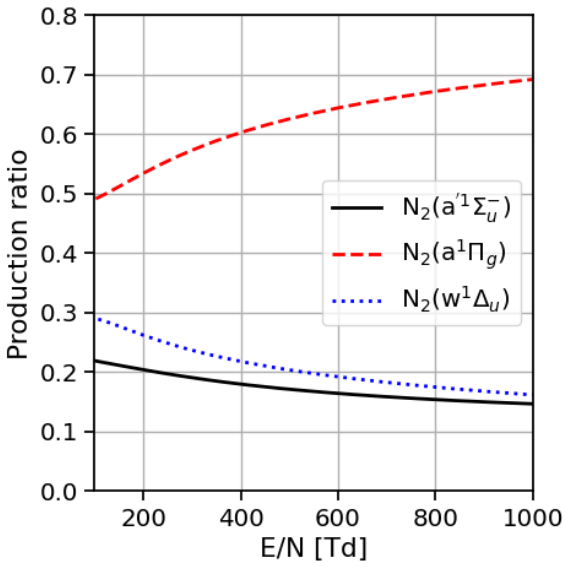

Figure 6.2: Percentage of production rates of singlet excited states of N_2 computed with BOLSIG+ [72].

$$\dot{\omega}_T^j = -\mathcal{Q}_j \Delta u_j = -\mathcal{Q}_j \sum_{k=1}^{N_s} \nu_{kj} u_k \tag{6.6}$$

$$\dot{\omega}_T^j = -\mathcal{Q}_j \Delta h_j = -\mathcal{Q}_j \sum_{k=1}^{N_s} \nu_{kj} h_k \tag{6.7}$$

where $\mathcal{Q}_j$ is the molar production rate of reaction j, ν_{kj} the stoichiometric coefficient of species k in process j, u_k the internal molar energy of species k and h_k the molar enthalpy of species k. The reactions must be split into two sets: the set of reactions $\mathcal{B}$ which corresponds to the electron impact processes relying on the Boltzmann solver and the set of reactions $\mathcal{C}$ which corresponds to the common reactions in the mechanism for which explicit definitions of the rate coefficients are given. For electron impact processes (set of reactions $\mathcal{B}$), it is not possible to use Eq. 6.6 to compute the associated heat release rate because it does not account for the electron energy loss. The Table 6.5 illustrates the different behaviors encountered in electron impact processes. In the first process of Tab. 6.5, the whole energy lost by the electron $\Delta\varepsilon$ serves to excite N_2 into its electronic state $N_2(A_3)$. Consequently, there is no heat released in this process. On the contrary in the second process of Tab. 6.5 the electron loses more energy than necessary to dissociate O_2. This excess of energy is associated with an instantaneous gas heating so that the heat release $\dot{\omega}_T'^j$ follows the rule given by Eq. 6.8 for a process j, in which the energy change is accounting for an electron energy release. A complete description of the electron impact reaction heating energies ΔE for N_2 and O_2 can be found in Tables 6.1 and 6.2.

$$\dot{\omega}_T'^j = \mathcal{Q}_j \Delta E = \mathcal{Q}_j (\Delta\varepsilon_j - \Delta u_j) \tag{6.8}$$

For the other reactions (set of reactions $\mathcal{C}$), part of the energy of the products can be stored into rotational and vibrational modes as suggested by Popov [157, 159] and references therein. To account for this phenomenon, the heat release rate of some reactions is forced to the Fast Gas Heating (FGH, Model 1) values listed in Tab. 6.6 according to the work

#	Process	$\Delta\varepsilon$ [eV]	Δu [eV]	$\Delta E = (\Delta\varepsilon - \Delta u)$ [eV]
1	$e^-(\varepsilon) + N_2 \longrightarrow e^-(\varepsilon - \Delta\varepsilon) + N_2(A)$	6.17	6.17	0
2	$e^-(\varepsilon) + O_2 \longrightarrow e^-(\varepsilon - \Delta\varepsilon) + 2\,O$	6.0	5.16	0.84

Table 6.5: Example of heat release rate of reaction for different electron impact processes.

of [157, 159]. In this table, FGH corresponds to the forced energy release per collision (either observed experimentally or computed using the methodology of [157]) and HRR (Model 2) refers to the use of the conventional definition of the Heat Release of Reaction using the formation enthalpy of the reactants and products. At the end, energy conservation is ensured through a vibrational energy residual ε_{vib} in the products following Eq. (6.9), discussed in more details in Section 6.5.

$$\varepsilon_{\text{vib}} = \text{HRR} - \text{FGH} \tag{6.9}$$

Num	Reaction	Model 1		Model 2
		FGH [eV]	Ref	HRR [eV]
(C1)	$e^- + {N_4}^+ \longrightarrow N_2(v) + N_2(C)$	0	[131]	3.4
(C2)	$N_2(A) + O_2 \longrightarrow N_2(v) + O_2(b_1)$	0	[157]	4.53
(C3)	$N_2(A) + N_2(A) \longrightarrow N_2(v) + N_2(C)$	0.4	[157]	1.3
(C4)	$N_2(A) + N_2(A) \longrightarrow N_2(v) + N_2(B)$	3.5	[157]	4.99
(C5)	$N_2(B) + O_2 \longrightarrow N_2(v) + 2\,O$	1.1	[157, Eq. 6]	2.19
(C6)	$N_2(B) + N_2 \longrightarrow N_2(A) + N_2(v)$	0	[131]	1.18
(C7)	$N_2(a) + N_2 \longrightarrow N_2(B) + N_2(v)$	0	[131]	1.05
(C8)	$N_2(C) + O_2 \longrightarrow N_2(v) + O + O$	5.55	[157, Eq. 6]	5.87
(C9)	$N_2(C) + O_2 \longrightarrow N_2(v) + O + O(^1D)$	3.59	[157, Eq. 6]	3.99
(C10)	$N_2(C) + O_2 \longrightarrow N_2(v) + O + O(^1S)$	1.37	[157, Eq. 6]	1.68
(C11)	$N_2(C) + N_2 \longrightarrow N_2(B) + N_2(v)$	0	[157]	3.68
(C12)	$O(^1D) + O_2 \longrightarrow O + O_2(v)$	0	[157]	1.97
(C13)	$O(^1D) + O_2 \longrightarrow O + O_2(a_1, v)$	0	[157]	0.99
(C14)	$O(^1D) + O_2 \longrightarrow O + O_2(b_1, v)$	0	[157]	0.34
(C15)	$O(^1D) + N_2 \longrightarrow O + N_2(v)$	1.38	[157]	1.97

Table 6.6: Fast Gas Heating (FGH) and conventional Heat Release of Reaction (HRR) for reactions for which they differ.

Finally, three different models for gas heating are tested and referred to as follows. Model 1 considers the forced energy release of the reaction in Tab. 6.6 and the rate from Piper [151] for the reaction ((A4)), Model 2 refers to the use of the conventional HRR with the same rates as in Model 1 and Model 3 is based upon Model 1 with the rate from [124] for the dissociative quenching of O_2 by $N_2\,(a^1\Pi_g)$ as discussed in Section 6.3.

6.5 Vibration modeling and slow gas heating

The fast gas heating produced by a plasma discharge is followed by a slow gas heating corresponding to the relaxation of vibrational states. For the discharges considered in this work ($E/N \geq 100$Td), an overwhelming majority of this energy is stored into vibrational modes of N_2 as shown in 6.1. Thus, both detailed and simplified modeling of $N_2(v)$ are available in the kinetic mechanism, wheareas only a simplified model for $O_2(v)$ is used. In the detailed model VIB. 1,

the electron vibrational excitation cross sections are taken from [112] and [148] for N_2(v=1-8) and from [83] for N_2(v=9-17). The main relaxation processes are vibrational-translational (VT) N_2-O and vibrational-vibrational (VV) N_2-N_2 reactions, and as a first approximation, only those processes have been accounted for in the detailed model:

$$N_2(v) + O \longleftrightarrow N_2(v-1) + O \tag{R5}$$
$$N_2(v) + N_2(w-1) \longleftrightarrow N_2(v-1) + N_2(w) \tag{R6}$$

The vibrational energy of level v, E_v, accounts for anharmonicity effects, using a Morse potential energy expression:

$$\frac{E_v}{hc} = \omega_e\left(v + \frac{1}{2}\right) - \omega_e x_e\left(v + \frac{1}{2}\right)^2 \tag{6.10}$$

where h is the Planck constant, c is the speed of light in vacuum, ω_e is the characteristic vibrational pulsation and $\omega_e x_e$ is the anharmonicity. ω_e and $\omega_e x_e$ are given in units of wavelength and can be found in [32]. The base rate and scaling for both VV and VT relaxations are taken from [70]. The resulting mechanism contains 116 species woth the detailed approach (71 species of the plasma mechanism developed above plus 45 vibrational states N_2(v=1,45)) and 1916 reactions.

The modeling of the vibration kinetics of species k can be simplified by considering the mean vibrational energy e^k_{vib}. The time evolution of e^k_{vib} and its interaction with the gas temperature are given by:

$$\frac{de^k_{\text{vib}}}{dt} = \dot{E}^k_{\text{vib}} - \dot{R}^k_{\text{VT}} \tag{6.11}$$
$$mc_v\frac{\mathrm{d}T}{\mathrm{d}t} = \dot{\omega}_T + \sum_k \dot{R}^k_{\text{VT}} \tag{6.12}$$

In Eq. (6.11), $\dot{E}^k_{\text{vib}}$ corresponds to the vibrational excitation of species k produced by the discharge. Reactions such as (C6) and (C7) do not produce any heating and instead the energy is deposited as molecular vibration in $\dot{E}^{\text{N2}}_{\text{vib}}$. The sink term $\dot{R}^k_{\text{VT}}$ corresponds to the vibrational-translational (VT) relaxation from species k:

$$\dot{R}^k_{\text{VT}} = \frac{e^k_{\text{vib}}}{\tau^k_{\text{VT}}} \qquad \tau^k_{\text{VT}} = \left(\sum_p 1/\tau^{pk}_{\text{VT}}\right) \tag{6.13}$$

where p denotes all colliding partners of the species k. Note that the power source term $\dot{Q}$ of Eq. (5.16) has been expanded as $\dot{Q} = \sum_k \dot{R}^k_{\text{VT}}$.

In the simplified model VIB. 2, the mean vibrational energy of $k = N_2$ is considered with the colliding partners $p = O, N_2$ and the relaxation times τ^{pk}_{VT} are taken from [129].

In both models VIB. 1 and VIB. 2, the relaxation of the vibrational energy of O_2 is modeled using the simplified approach with the colliding partners $p = O, N_2, O_2$ and relaxation times taken from [179]. Note that $O_2(a_1, v)$ and $O_2(b_1, v)$ produced respectively by reactions (C14) and (C15) in Tab. 6.6 are modeled like O_2(v).

Using Model 1 (FGH) for reactions listed in Tab. 6.6 introduces reactions that produce vibrational species at an unknown distribution. It is thus impossible to include them in a detailed model of vibration, and the corresponding vibrational energy residual is relaxed using Eq. (6.13), i.e., following model VIB. 2.

6.6 Building a complete detailed mechanism

The above mentionned reactions in this Chapter only describe the most important processes of the plasma kinetic mechanism and need to be completed by other plasma reactions based on the literature. In addition to the electron impact reactions with N_2 and O_2 described in Section 6.1, the plasma mechanism is accompanied with other cross-sections for electron collisions with neutrals (N_2, $N_2(A^3\Sigma_u^+)$, $N_2(B^3\Pi_g)$, $N_2(C^3\Pi_u)$, $N_2(a^1\Pi_g)$, O_2, Ar, $O_2(a^1\Delta_g)$, $O_2\left(b_1\Sigma_g^+\right)$, CH_4, NO, N_2O, O(^{3}P, ^{1}D, ^{1}S), O_3, N_2(v)) that are taken from various datasets of the LXCat database (see Tab. 6.7), and associated reactions are included in the mechanism. Elastic cross-sections have been included for the $N_2(B_3, C_3, a_1)$ electronic states of N_2, assumed to be the same as for the ground state N_2. The electronically excited triplet states $N_2(B^3\Pi_g)$ - $N_2(B'^3\Sigma_u^-)$ - $N_2(W^3\Delta_u)$ and singlet states $N_2(a^1\Pi_g)$ - $N_2(a'^1\Sigma_u^-)$ - $N_2(w^1\Delta_u)$ are lumped into the $N_2(B^3\Pi_g)$ and $N_2(a^1\Pi_g)$ states respectively.

Electron impact reactions need to be supplemented with electron-ion and heavy species reactions to form a complete kinetic mechanism for plasma discharge. Two main references ([32, Chap. 7-10], [157]) have been chosen to construct the plasma mechanism with which the combustion mechanism will be merged. Argon was also added to the plasma mechanism to prepare its use in plasma-assisted combustion cases. Indeed, Argon is often used as a diluent in plasma-assisted combustion studies [178]. A quite simple plasma chemistry for Ar has been taken from [11] to handle mixture dilution with this noble gas. The detailed plasma mechanism finally contains 71 species and 680 reactions.

Colliding partners	σ
N_2, $N_2(A^3\Sigma_u^+)$, $N_2(B^3\Pi_g)$, $N_2(C^3\Pi_u)$, $N_2(a^1\Pi_g)$, O_2, Ar	Phelps [148]
$O_2(a^1\Delta_g)$, $O_2\left(b_1\Sigma_g^+\right)$	Triniti [188]
CH_4, NO, N_2O	Hayashi [75]
O(^{3}P, ^{1}D, ^{1}S), N(^{4}S, ^{2}D)	IST-Lisbon [112]
O_3	Morgan [134]
N_2(v)	[148, 112, 83]

Table 6.7: Electron impact cross-sections used in this work.

6.7 Ground states reactions in air

A detailed combustion mechanism was added on the top of the plasma mechanism for plasma-assisted combustion application. Two combustion mechanisms have been considered with different levels of complexity: the GRI-3.0 [177] mechanism (53 species, 325 reactions) and the Konnov [106] mechanism (201 species, 2300 reactions). More details on these mechanisms regarding their performances can be found in Section 7.3. We focus here on the species and reactions involving N and O elements as they are essential in plasma-combustion coupling. In

effect, the detailed combustion mechanisms contain a complete description of the long-term behavior of the ground-state species in the air that is mandatory for the discharge afterglow. Moreover, these schemes are validated against experiments contrary to the set of ground-state molecule reactions that can be found in [32].

Some reactions are redundant between the plasma and the combustion mechanism. In the GRI 3.0 mechanism, approximately 40 reactions already exist in the plasma mechanism, while this number is close to 100 in the Konnov mechanism. While some of these reactions use the same rate constants, most do not and a choice must be made.

GRI 3.0 In the case of GRI 3.0 mechanism, it was found that the rate constants of the common reactions have negligible effects on the studied plasma cases. Thus, the rates of GRI 3.0 were kept as they are optimized for combustion applications.

Konnov v0.6 As for the GRI 3.0, the rates of the common reactions involving non-excited species can be taken from either mechanism without significant change in the cases studied in this work. However the Konnov mechanism [106] contains excited species [93], which are $O(^1D)$, $O_2(\Delta)$ and $OH(\Sigma)$ denoted "OX", "O2X" and "OHX" respectively. The reactions involving these species are important for the plasma as they contain part of the discharge energy, and need to be treated carefully. Due to the merging of the singlet states of O_2 in [106], the quenching of $O(^1D)$ by O_2 is described in the original Konnov mechanism by:

$$O(^1D) + O_2 \longrightarrow O + O_2(a_1) \quad k = 2.64 \times 10^{-11} \exp\left(139/RT_g\right) \tag{R7}$$

However our plasma chemistry considers two distinct species $O_2(a_1)$ and $O_2(b_1)$, and the rate coefficients of $O(^1D)$ quenching by O_2 are described more precisely as in Capitelli et al. [32]:

$$O(^1D) + O_2 \longrightarrow O + O_2 \qquad k = 6.4 \times 10^{-12} \exp(133/RT_g) \mathrm{cm}^3\,\mathrm{s}^{-1} \tag{R8}$$

$$O(^1D) + O_2 \longrightarrow O + O_2(a_1) \qquad k = 1 \times 10^{-12}\,\mathrm{cm}^3\,\mathrm{s}^{-1} \tag{R9}$$

$$O(^1D) + O_2 \longrightarrow O + O_2(b_1) \qquad k = 2.6 \times 10^{-11} \exp(133/RT_g) \mathrm{cm}^3\,\mathrm{s}^{-1} \tag{R10}$$

The reaction rate used for reaction (R7) actually corresponds to that of reaction (R10). The underlying assumption is that the $O_2(b_1)$ formed in reaction (R10) is directly quenched to form $O_2(a_1)$. This assumption is relaxed in the merged chemistry as reaction (R7) is replaced by reactions (R8), (R9) and (R10).

Modifications have also been made to ensure correct repartition of the discharge energy: the heat release rate of some plasma reactions was split into a fast gas heating (FGH) and a slow gas heating (SGH) following Eq. (6.9) based on Popov [157]. The three quenching reactions above produce only vibrational energy, *i.e.*, SGH. Likewise the quenching of reaction (R11) is described as in Popov [157] with 30% of energy going into FGH and 70% into vibration. A summary of energy repartition and reaction rates in the merged mechanism can be found in Tab. 6.8.

$$O(^1D) + N_2 \longrightarrow O + N_2(v) \tag{R11}$$

Reaction	FGH [%]	Vibration (SGH) [%]	k_f [$\mathrm{cm^3\,s^{-1}}$]
$O(^1D) + O_2 \longrightarrow O + O_2(v)$	0	100	$6.4 \times 10^{-12} \exp(67/T_g)$
$O(^1D) + O_2 \longrightarrow O + O_2(a_1, v)$	0	100	10^{-12}
$O(^1D) + O_2 \longrightarrow O + O_2(b_1, v)$	0	100	$2.6 \times 10^{-11} \exp(67/T_g)$
$O(^1D) + N_2 \longrightarrow O + N_2(v)$	30	70	7.6×10^{-11}

Table 6.8: Modifications of the Konnov mechanism when merging it with the plasma mechanism. FGH and vibrational excitation are given in terms of percentage of the total energy change of reaction.

6.8 Discharge energy branching from 0D simulations

A plasma discharge can be characterized by its global effects on the gas mixture. To do so, the plasma discharge energy density e_p is defined by:

$$E_\mathrm{p} = \int_{V_p} \left(\int_t \mathbf{j_e} \cdot \mathbf{E} \; dt \right) dV \tag{6.14}$$

where V_p is the discharge volume, $\mathbf{j_e}$ is the electron current density and $\mathbf{E}$ is the electric field. In 0D reactors, the volume integration is straigforward and gives:

$$E_\mathrm{p} = V_p \int_t \mathbf{j_e} \cdot \mathbf{E} \; dt \tag{6.15}$$

Then, the discharge energy is divided into several contributions:

$$E_\mathrm{p} = E_\mathrm{chem} + E_\mathrm{heat} + E_\mathrm{vib} + E_\mathrm{exc} + E_\mathrm{ion} \tag{6.16}$$

where E_chem is the chemical energy, E_heat is the fast gas heating, E_vib is the vibrational energy, E_elec is the excitation energy and E_ion is the ionization energy.

The chemical energy is given by Eq. 6.17 where $\dot{\omega}_k^p$ is the molar production rate and u_k^0 the total molar energy of the ground state of the species k. For an excited species k, the internal molar energy is $u_k = u_k^0 + u_k^*$ where u_k^* corresponds to the excitation energy. The superscript p indicates that only the species produced by plasma reactions (set of reactions denoted $\mathcal{P}$) are considered in the plasma chemical effect.

$$E_\mathrm{chem}(t) = V_p \int_t \left(\sum_{k=1}^{N_s} \dot{\omega}_k^p u_k^0 \right) dt \tag{6.17}$$

The excitation energy E_exc corresponds to the energy of electronically excited species ($N_2{}^*$, $O_2{}^*$, O^*, ...) that are produced during the discharge. This energy is not considered as a chemical effect of the discharge because it is quickly converted to other energy channels and reflects a relatively fast transient plasma energy. This energy can be computed using:

$$E_\mathrm{exc}(t) = V_p \int_t \left(\sum_{k=1}^{N_s} \dot{\omega}_k^p u_k^* \right) dt \tag{6.18}$$

The heating effect of the discharge is computed using Eq. 6.19 where $\Delta u_j = \sum_k \nu_{kj} u_k$ is the reaction energy change per mole with u_k the internal energy of species k and $\dot{\mathcal{Q}}_j$ the molar reaction rate of reaction j. The sum is performed over the set of plasma reactions $\mathcal{P}$:

$$E_{\text{heat}}(t) = -V_p \int_t \left(\sum_{j \in \mathcal{P}} \dot{\mathcal{Q}}_j \Delta u_j \right) dt \tag{6.19}$$

The vibrational energy E_{vib} at a given time t is computed using Eq. 6.20 where e^k_{vib} was previously described in Section 6.5. The sum is performed over the set of vibrationally excited species $\mathcal{V}$ that is restricted to N_2 and O_2 in this work.

$$E_{\text{vib}}(t) = V_p \sum_{k \in \mathcal{V}} e^k_{\text{vib}} \tag{6.20}$$

Finally, the ionization energy E_{ion} is given by Eq. 6.21 where I_k stands for the ionization potential of the species k that is equal to zero for neutral species.

$$E_{\text{ion}}(t) = V_p \int_t \left(\sum_{k=1}^{N_s} \dot{\omega}^p_k I_k \right) dt \tag{6.21}$$

In conventional combustion studies, the chemical energy change is exactely balanced by the heating energy so that:

$$\Delta E_{\text{chem}} = -\Delta E_{\text{heat}} \tag{6.22}$$

where the symbol Δ represents the energy change between two instants (for example $\Delta E_{\text{chem}} = E_{\text{chem}}(t) - E_{\text{chem}}(t - \Delta t)$). In that case, a decrease of the chemical energy leads to gas heating (exothermic reaction) whereas an increase of the chemical energy cools down the mixture (endothermic reaction). The electron impact processes (set of reactions $\mathcal{B}$) can not be fully characterized this way as they can both increase the chemical energy and temperature of the mixture. To better understand the energy distribution in electron impact reactions, the electron impact dissociation of O_2 producing electronically excited atomic oxygen $O(^1D)$ in reaction (R12) is choosen as an example. During this process, about 5.12 eV goes to the chemical energy E_{chem} corresponding to the energy of the process $O_2 \longrightarrow 2\,O$. Simultaneously, about 1.96 eV is transfered to E_{exc} corresponding to the excitation energy of $O(^1D)$ and 1.26 eV serves to heat the gas. We see that in this reaction, both chemical and heat energies can increase due to the external power source term provided by the plasma discharge through the electrons.

$$e^- + O_2 \longrightarrow e^- + O + O(^1D) + 1.26 \text{ eV} \tag{R12}$$

In the heavy species reactions (set of reactions C), the sum of the different energy channels remains unchanged but the repartition is modified. The reaction (R13) gives a good understanding of what appends to the excitation energy. In this reaction, all the electronic excitation energy is converted to E_{chem} (+ 5.12 eV), E_{heat} (+ 5.55 eV) and E_{vib} (+ 0.32 eV).

$$N_2(C_3) + O_2 \longrightarrow N_2(v) + 2\,O + 5.55 \text{ eV} \tag{R13}$$

6.9 Case A: Fast gas heating and atomic oxygen production

Case A corresponds to an experimental setup presented in Rusterholtz et al. [167] and is used here to validate two of the essential aspects of the plasma discharge features in the air: the atomic oxygen production and fast gas heating. NRP discharges are applied in the air in a 4 mm pin-to-pin configuration. The discharges are 10 ns long with an applied voltage of 5.7 kV between the electrodes at a frequency of 10 kHz. The electrodes are located in a parrallel pre-heated air-flow at 1000 K and velocity of 2.6 m s^{-1} as shown in Fig. 6.3. The gas temperature was estimated through measurements of the $N_2(B, C)$ rotational temperature. However, more recent work [186] shows that the rotational distribution of the excited states depends on various kinetic processes, including electronic excitation, collisional quenching and rotational excitation. The authors of [186] have developed a detailed model to account for these processes and enabled to infer the actual gas temperature from the measured rotational distributions of the $N_2(B)$ and $N_2(C)$ states. After multiple pulses, the temperature of the gas just before a pulse is 1500 K with a temperature rise of about 900 K in 20 ns. Optical measurements allow to obtain data on the electrons, nitrogen electronic states ($N_2(B)$, $N_2(C)$) and atomic oxygen densities. At the end of the discharge, around 50% of oxygen is dissociated, and the energy of the discharge is $E_p = 670 \pm 50$ µJ. There is 35% approximately of this energy used for dissociation of O_2 and 21% for gas heating according to the experimental results.

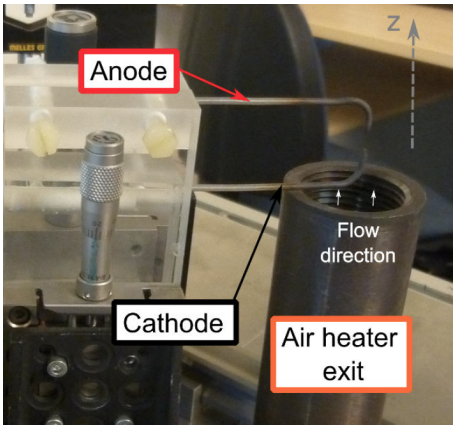

Figure 6.3: Experimental electrodes assembly of the Case A reproduced from [166].

For the CANTERA 0D simulations, the reduced electric field is taken from experimental measurements [167] while the electron density at the center of the discharge is taken from a 1D simulation [158]. The temporal profiles of reduced electric field and electron density are shown in Fig. 6.4. Initially, the mixture composition is N_2:O_2:O:77.4:18.6:4 (molar fractions) accounting for O_2 dissociation from previous discharges that was measured experimentally [167].

6.9.1 Fast gas heating

The NRP discharges of Case A [167] produce fast and intense gas heating during the first tens of nanoseconds. The temperature rise is used to assess the quality of the three models of fast gas heating presented in Section 6.4. In addition to these models, simulation has been performed using the kinetic mechanism of The Ohio State University (TOSU) [8, 197]. Simulation and experimental results are shown in Fig. 6.5, along with previous simulation results of Popov

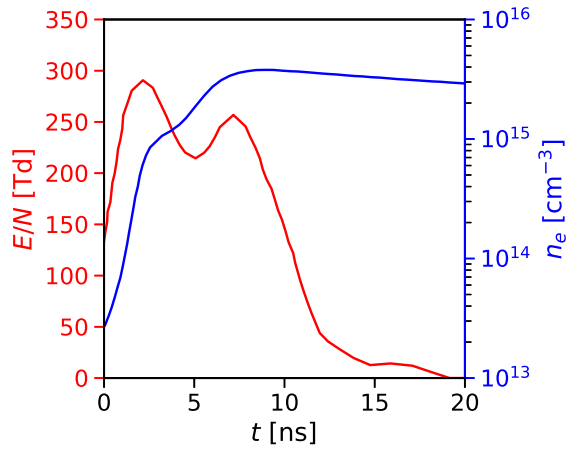

Figure 6.4: Input profiles used in the 0D simulation of the Case A: electron density is taken from [158] and reduced electric field from [167].

[158, 160]. This figure shows only the GRI 3.0 results for readability since similar conclusions were obtained with the Konnov mechanism.

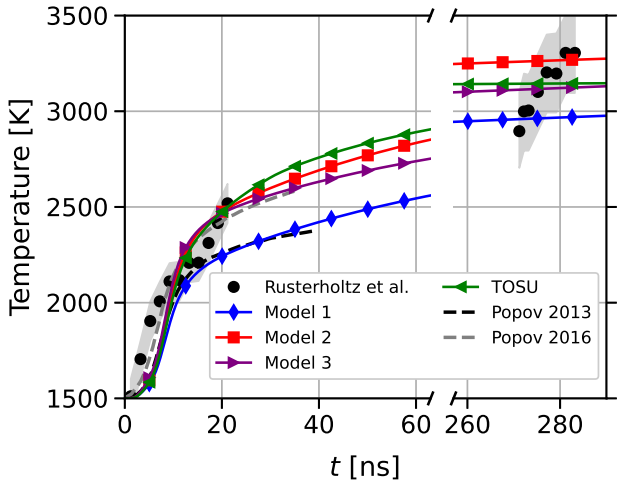

Figure 6.5: Gas temperature time evolution for Case A [167] using the GRI 3.0 with the different fast gas heating models of Section 6.4, and TOSU mechanism against experimental measurements (circle) [167] and reference simulations (dashed: Popov 2013 [158], Popov 2016 [160]). The filled areas correspond to the experimental uncertainties of [167].

In Fig.6.5, while Models 2 and 3 are close, a 300 K temperature difference is observed with Model 1 after 60 ns which corresponds to $\approx 30\%$ of the gas temperature increase. Both Models 2 and 3 are in good agreement with the measurements, hence other measured quantities should be used to differentiate them. The TOSU mechanism yields a gas temperature increase similar to Models 2 and 3. In the work of Popov 2016 [160], the model developed in [158] has been updated to account for quenching reactions of electronically excited nitrogen by atomic oxygen (*i.e.* $N_2^* + O \longrightarrow NO + N$) following the work of [175]. Despite gas temperature prediction improvements, a loss of accuracy on atomic oxygen production induced by this quenching is shown in Section 6.9.2.

To go deeper into the gas heating analysis, Fig. 6.6 shows the contribution of each reaction

to the global heat release defined as:

$$r^j_{\text{heat}} = \frac{\dot{\omega}^j_T}{\dot{\omega}_T} \tag{6.23}$$

During the pulse ($t = 7.5\,\text{ns}$), the dissociative quenching of $N_2{}^*$ by O_2 and electron impact dissociation are the most important processes that release heat as shown in Fig. 6.6a. The $O(^1D)$ quenching by N_2 also contributes to a significant part of the FGH. At the end of the pulse ($t = 15\,\text{ns}$), most of the heat release is produced by the quenching of electronic states (See Fig. 6.6b). As shown in Fig. 6.5, the gas temperature continues to increase during the first instants of the afterglow. Figure 6.6c reveals that most of the heat release at $t = 40\,\text{ns}$ is due to the quenching of electronically excited atoms $O(^1D, {}^1S)$ and $N(^2D)$ as well as $N_2(A_3)$ quenching by O. Note that the reaction $N_2 + O(^1D) \longrightarrow N_2 + O$ still contributes significantly to the heat release in the afterglow. Hence, the choices of its rate coefficient and of the vibrational energy residual in N_2 (See Section 6.4) must be made carefully. Finally, the most important process for gas heating from 0 to 100 ns are shown in Fig. 6.6d. The quenching of $O(^1D)$ by N_2 is the most important process, followed by the quenching of electronically excited nitrogen molecules and electron impact dissociation of oxygen molecules.

Additional information was obtained in the experiment thanks to a secondary reflected pulse at $t = 270\,\text{ns}$ as shown in Fig. 6.5. This pulse was strong enough to efficiently stimulate the C states of N_2 allowing an estimate of its rotational temperature. At the very beginning of this pulse, recent work [186] inferred a gas temperature of $3110\,\text{K} \pm 200\,\text{K}$ from the rotational temperature of $N_2(C_3)$, indicating a significant gas temperature increase of about $600\,\text{K} \pm 200\,\text{K}$ from the end of the first pulse. With 0D simulations, the gas temperature ranges between 2900 and 3300 K depending on the model used, Model 1 staying approximately 200 K lower than the others. However, at a high temperature of about $T = 2500\,\text{K}$, the compression wave formed by the fast gas heating during the first pulse can not be neglected to analyze the results of the second pulse. Indeed, the acoustic timescale τ_a is of the order of 200 ns in a volume of size 225 µm and a speed of sound $a = \sqrt{\gamma R T_g / \bar{W}} \simeq 1000\,\text{m}\,\text{s}^{-1}$. This rapid gas expansion is responsible for gas temperature decrease, which is a sign that gas temperature should be even higher than the one predicted by Models 2 and 3. However, the 0D model is not able to accurately estimate the density change resulting from the compression wave. Hence the reduced electric field can not be computed so that the pulse reflection was not included in our 0D simulation. Therefore the simulated temperature stays flat contrary to the experimental measurements. The gas dynamics effects require 1D or 2D simulations and will be discussed in Chapter 12.

6.9.2 Atomic oxygen production

Radical production is another important characteristic of the discharge studied in the experiment of Case A [167]. The time evolution of $O(^3P)$ density has been measured using Two-Photon Absorption Laser Induced Fluorescence (TALIF) technique during the pulse and the afterglow. The atomic oxygen from CANTERA simulations is displayed in Fig. 6.7 for the different models used. For the same reasons as in the fast gas heating study, only the results for GRI 3.0 mechanism are shown. Models 1 to 3 yield satisfactory results when compared with experimental measurements [167] and Popov's simulation [158]. Model 3 exhibits a slightly higher O production of ~ 8 % than Model 1 and seems to be in better agreement with the experimental results. However, the TOSU mechanism [8] underestimates the atomic oxygen by approximately 30%.

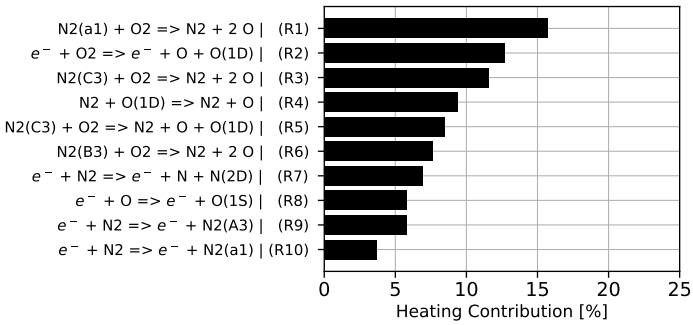

(a) 7.5 ns

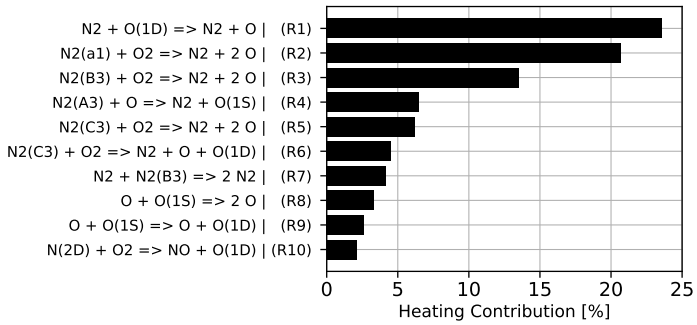

(b) 15 ns

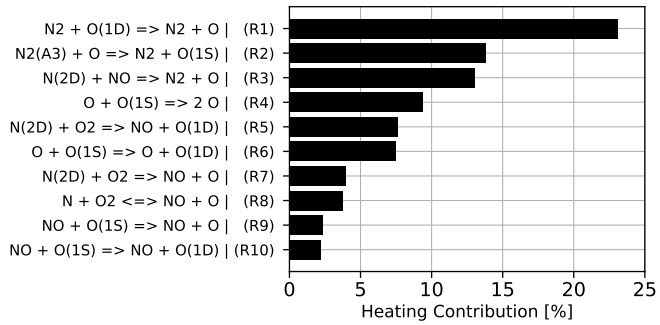

(c) 40 ns

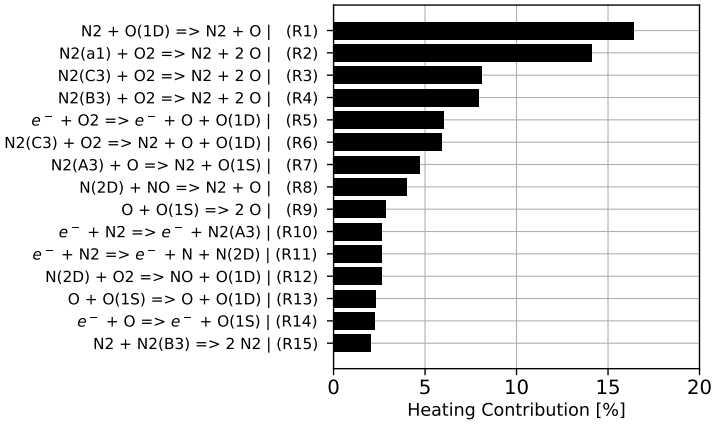

(d) Integrated within [0, 100] ns

Figure 6.6: Heat release contribution of the most important reactions (a) during the pulse, (b) at the end of the pulse, (c) in the afterglow and integrated within the interval [0, 100] ns.

This is attributed to the quenching reaction of $N_2{}^*$ with $O(^3P)$ atoms (Eq. (R14)) which occurs with a very high rate. Indeed, the addition of this reaction in Model 1 leading to Model 4 of Fig. 6.7 strongly disturbs the atomic oxygen production. This observation questions the effectiveness of reaction (R14) in our conditions and is also revealed by the $N_2(B, C)$ decay discussed in Section 6.9.3.

$$N_2{}^* + O(^3P) \longrightarrow NO + N(^2D) \quad k = 3 \times 10^{-10} \mathrm{cm}^3\,\mathrm{s}^{-1} \tag{R14}$$

A closer look at atomic oxygen production is performed in Fig. 6.8. Figure 6.8a shows the most important reactions producing O during the high voltage pulse at a high reduced electric

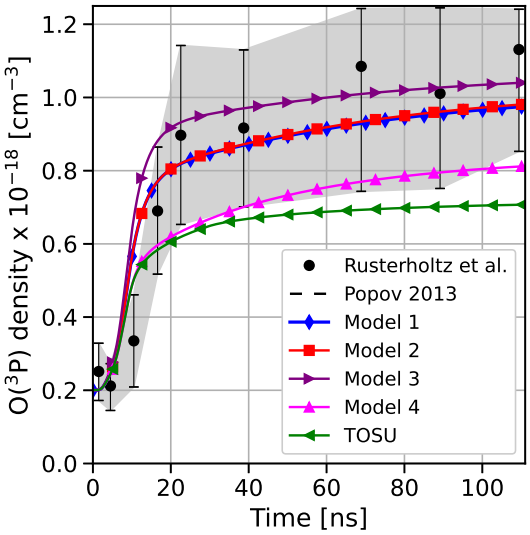

Figure 6.7: Time evolution of atomic oxygen density for Case A [167] using different fast gas heating model against experimental measurements (circles) [167] and reference simulations (dashed line) [158]. The shaded area corresponds to the experimental uncertainties.

field where electron impact dissociation is effective. At the end of the pulse, the quenching of excited nitrogen is the dominant process producing atomic oxygen, as pointed out in Fig. 6.8b. Finally, the molar production rates are integrated within the interval [0-100] ns in Fig. 6.8c to reveal the prominent plasma reactions producing atomic oxygen. As expected, electron impact dissociation and N_2* quenching highly contribute to the dioxygen dissociation.

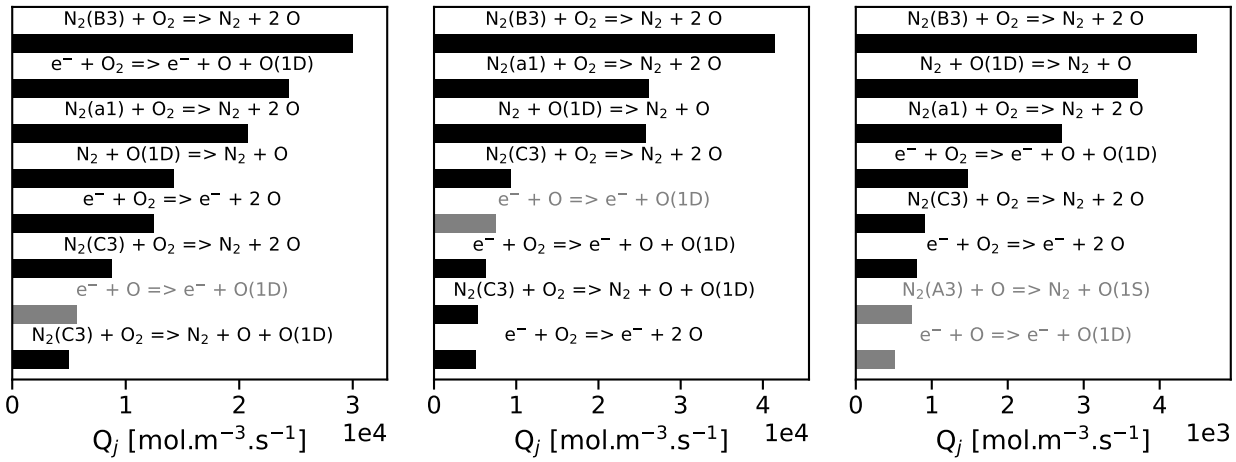

(a) 7 ns (b) 11 ns (c) Integrated [0-100] ns

Figure 6.8: Molar production rate of atomic oxygen (a) during the pulse, (b) at the end of the pulse and (c) integrated on the interval [0, 100] ns. Black bars correspond to $Q_j > 0$ and gray ones correspond to $Q_j \leq 0$.

6.9.3 Production and decay of $N_2(B_3)$ and $N_2(C_3)$

In Shkurenkov et al. [175], the rate of the reaction (R14) was assumed to be close to the gas kinetic rate at a high value of $3 \times 10^{-10}\,\mathrm{cm^3\,s^{-1}}$. This reaction was supposed to explain the NO production in highly dissociated plasma (*i.e.* $X_O > X_{O2}$) in [175]. This reaction was also considered in the recent work of Popov [160] to explain higher gas temperature increase. The Case A experiment produces a highly dissociated plasma with up to 50% of oxygen dissociation. Moreover, electronically excited nitrogen $N_2(B_3)$ and $N_2(C_3)$ densities were measured during the pulse and the first instants of the afterglow up to 40 ns. Hence, Case A is helpful to assess the effectiveness of reaction R14. The results of Model 3, which gives the best results for both fast gas heating and atomic oxygen production, are shown in Fig 6.9a and compared to the experiment. In spite of a factor of five found for the $N_2(C)$ peak as already observed in [158], a good aggrement is found for the time evolution of both $N_2(B)$ and $N_2(C)$. Looking at the results of Model 4 in Fig. 6.9b, a faster decay is observed for both $N_2(B)$ and $N_2(C)$ compared to Model 3. This difference must be attributed to reaction (R14) that is the only difference between the two models. Whereas $N_2(C)$ decay remains acceptable with Model 4, the $N_2(B)$ decay is substantially modified with a density about one order of magnitude lower than Model 3 and experimental results at $t = 20$ ns. It is undeniable that reaction R14 exists, but its rate might be considerably lower than the gas kinetic value assumed in [175]. Regarding the NO production, which motivated the use reaction (R14) in [175], the Model 3 ability to well reproduce it will be verified later in Section. 6.11.

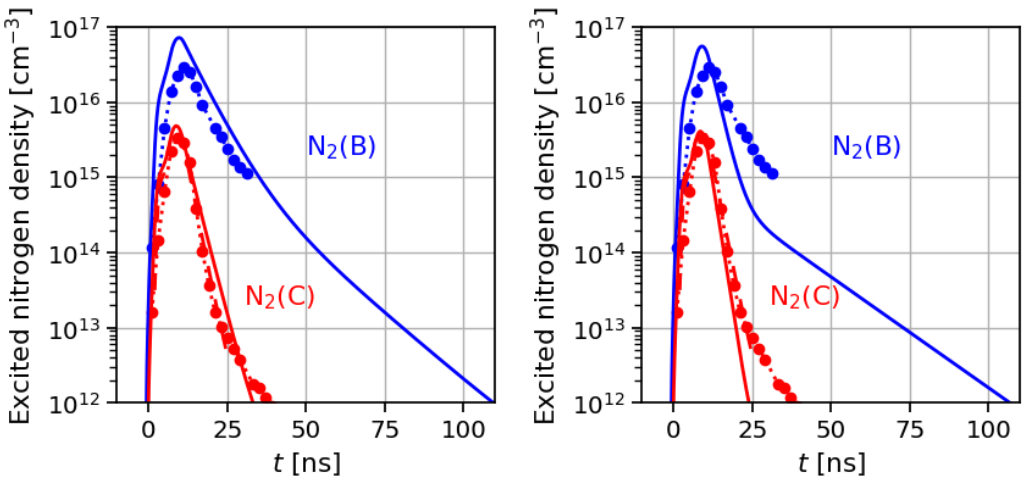

(a) Model 3 (b) Model 4

Figure 6.9: Time evolution of $N_2(B, C)$ density for Case A [167] using fast gas heating models 3 and 4. Simulated $N_2(C)$ density has been divided by 5, as in [158]. Markers correspond to experiments [167] and solid lines to simulations.

6.9.4 Discharge energy branching

The discharge energy branching analysis performed in Section 6.1 only considers the energy transferred from electrons to the heavy molecules. It was shown that in the Case A condition ($E/N \geq 100$ Td), most of the electron energy goes to electronic states of nitrogen. These excited states, as well as other excited or ionized species, quickly release their energy into

heat, chemical and vibrational energy. As discussed in Section 6.8, the discharge energy can be temporally splitted into five diferent channels as shown in Fig. 6.10. As expected, the ionization energy remains low in Case A for which the reduced electric field peak is lower than 300 Td. An important part of the discharge energy goes to the electronic excitation E_{exc} which peaks at 20 ns with approximately 50 % of the discharge energy. This energy is continuously relaxed to other channels and reaches less than 5 % of the discharge energy after 100 ns. The vibrational energy is mainly produced during the high voltage pulse, followed by a plateau representing 20 % of the discharge energy. The vibrational relaxation is a slow process occurring on microsecond timescale, not visible in this simulation, and is studied in more detail in case B (See Section 6.10). The chemical energy sharply increases during the first 25 ns, and then stagnates at ≈ 43 % of the discharge energy. The oxygen molecule dissociation process $O_2 \longrightarrow 2\,O$ almost represents 35 % of the chemical energy. The remaining chemical energy is spent into N_2 dissociation (≈ 5 %) and the production of other chemical components such as NO, O_3, ... Finally, a significant amount of the discharge energy is spent on gas heating, reaching 20 % of the discharge energy at the end of the pulse ($t \approx 25$ ns). Then, the heating energy still increases due to the relaxation of electronically excited molecules and chemical energy conversion to represent approximately 30 % of the discharge energy at 100 ns. The Table 6.9 summarizes the energy fractions that are transferred into the different channels. These values are compared with those of the experiment [167] and the simulation of [158]. An excellent agreement is found for the chemical energy noting that only oxygen dissociation is considered in [167, 158]. Moreover, good agreement is found on the heating energy at $t = 25$ ns. It is worth mentioning that a significant part of the energy is stored into electronic states at $t = 25$ ns which is further relaxed into heat and chemical energies so that values at 25 ns are underestimated.

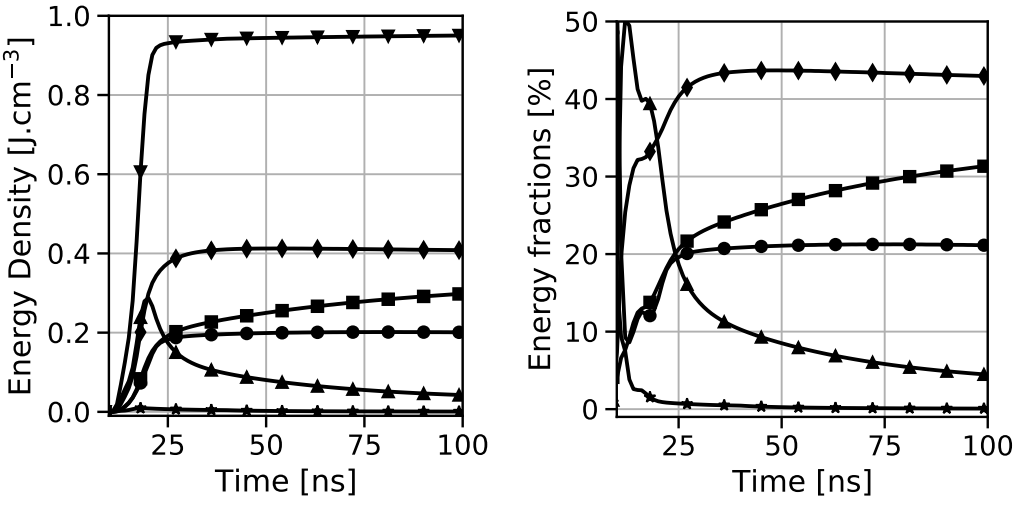

(a) (b)

Figure 6.10: Discharge energy transfer in different channels of the case A using Model 3 (▲ E_{exc}, ● E_{vib}, ■ E_{heat}, ◆ E_{chem}, ★ E_{ion}, ▼ E_{p}): (a) energy density and (b) energy fractions of the total discharge energy.

Source	E_{chem}	E_{heat}	E_{vib}	E_{exc}
This work ($t = 25$ ns)	40 %	21 %	20 %	19 %
This work ($t = 100$ ns)	43 %	31 %	21 %	5 %
Rusterholtz et al. [167]	35 %[a]	20 %[b]	-	-
Popov [158]	35 % [c]	25 %	-	-

Table 6.9: Discharge energy repartition of the case A at $t = 25$ ns and $t = 100$ ns (this work) compared to the results of [167] and [158].

[a] Value taken at $t = 100$ ns
[b] Value taken at $t = 25$ ns
[c] This value is an estimate at $t = 100$ ns and is not given explicitely in [158]

6.10 Case B: Slow gas heating

The experiment used as Case B is presented in Montello et al. [133]. NRP discharges are studied in plane-to-plane and pin-to-pin geometries, and the focus is made on vibration populations of nitrogen. The discharges are either applied in burst mode (40 to 150 pulses) in the plane-to-plane configuration or in a mono-pulse mode in the pin-to-pin configuration. It is found that in these conditions, up to 50% of the discharge energy is stored in nitrogen vibrational modes. The initial temperature and pressure are $T_0 = 300\,\text{K}$ and $P_0 = 100\,\text{Torr}$ respectively. The discharges are approximately 100 ns long. In this work, only the pin-to-pin configuration has been simulated. Images of the electrode configuration, as well as the discharge filament formed by a single pulse discharge, can be observed in Fig 6.11

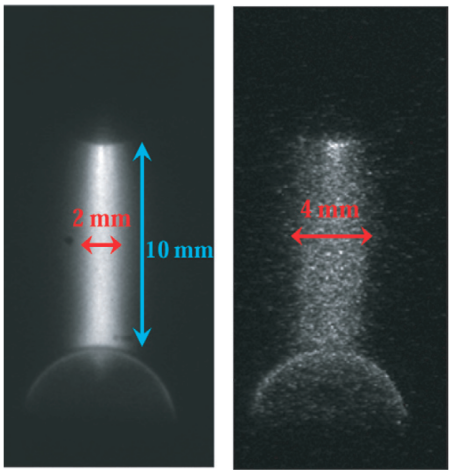

Figure 6.11: Images of a ns pulse filament discharge between two pin-pin electrodes in air at P = 100 Torr retrieved from [133, Fig. 4]: (left) during a single pulse and (right) 30-pulse average 1 µs after the pulse.

Smooth electron density and reduced electric field profiles from [133] (See Fig. 6.12) are imposed in the 0D simulations. During the long plateau between 100 and 175 ns, the intermediate reduced electric field of about 100 Td efficiently excites vibrational states of N_2 that is the dominant discharge energy channel as discussed in Section 6.1.

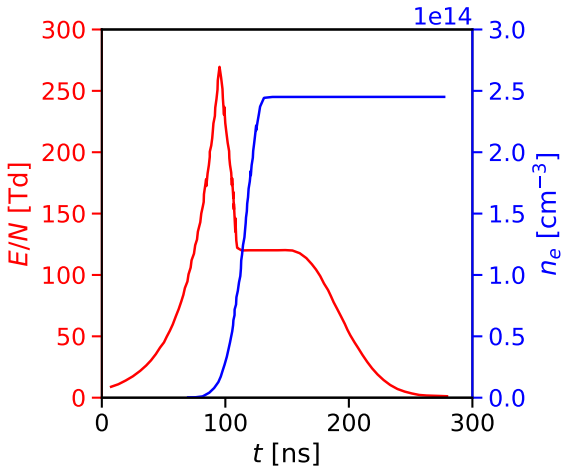

Figure 6.12: Electron density and reduced electric field profiles used as input of our 0D reactor retrieved from [133, Fig. 17]

6.10.1 Slow gas heating

Slow gas heating results from the relaxation of vibrationally excited nitrogen molecules. The detailed simulation using VIB. 1 model (See Section **??**) on the Montello experiment yields good results for the gas temperature (Fig. 6.13a) as well as for the vibrational populations (Fig. 6.13b) over time irrespective of the combustion mechanism. The VV N_2-N_2 and VT N_2-O relaxations are thus the main vibrational relaxation channels in air. The simpler VIB. 2 model shows good agreement with the detailed model for the gas temperature in Fig. 6.13a, validating the model and the relaxation times considered. This approach can drastically reduce the number of species in the mechanism and must be considered as a valuable option for multi-dimensional works. For these reasons, VIB. 2 model is kept for all other calculations.

6.10.2 Active species production

In [133], a kinetic simulation has been performed to estimate the time evolution of the major plasma discharges products. Figure 6.14 compares their results to our simulation using the Konnov-Plasma mechanism. A good agreement is found for atomic oxygen production regarding the ground state species. Regarding nitric oxide production, the profiles are temporally shifted, and our model predicts a sharp increase about one order of magnitude earlier than in simulation of [133]. A good agreement is found for the atomic nitrogen, with the same temporal sequences of production [10^{-8}-10^{-7} s] followed by a plateau [10^{-7}-10^{-5} s] and finally a decay [10^{-5}-10^{-4} s]. However, a high discrepancy is observed for the plateau value during which our mechanism predicts a tenfold lower value than [133]. Moreover, a good agreement is found for $N_2(A_3)$, $N_2(B_3)$ and $N_2(C_3)$ production and decays with only a factor of two between the simulations. Nevertheless, a huge difference is observed for $N_2(a_1)$ which is one order of magnitude higher in the simulations of [133]. The higher rate used in this work for reaction ((A4)) compared to [133] can explain this behavior. To conclude, an overall agreement is observed between our work and [133], but more experimental measurements are required to assess which mechanism is the most predictive. To do so, the next section describes a similar case with experimental measurements of O, N and NO densities.

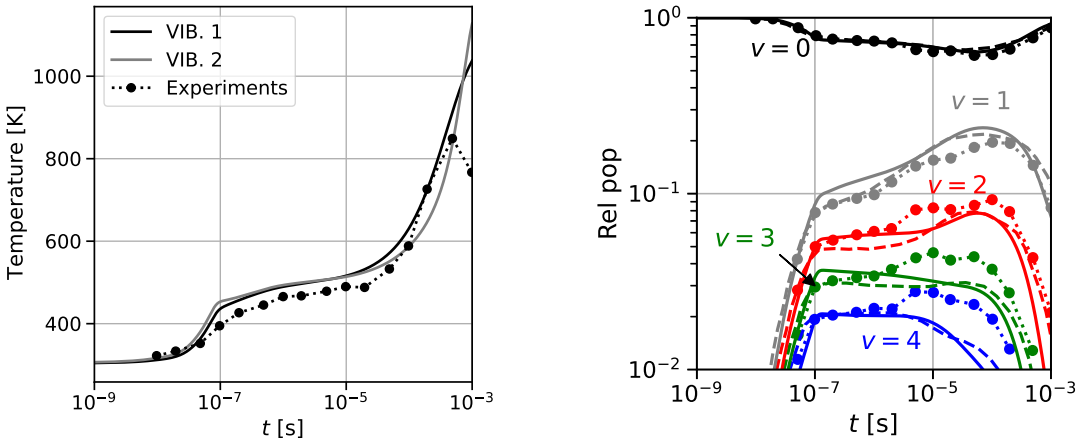

(a) Gas temperature (b) $N_2(v)$

Figure 6.13: Comparison of vibrational model on Case B [133] (a) gas temperature (solid, black and gray for simulation) against experimental measurements (point-dotted); (b) vibrational populations over time, $v = (0, 1, 2, 3, 4)$ correspond respectively to black, grey, red, green, blue for VIB. 2 model (solid), experimental measurements [133](point-dotted) and reference simulation [8] (dashed).

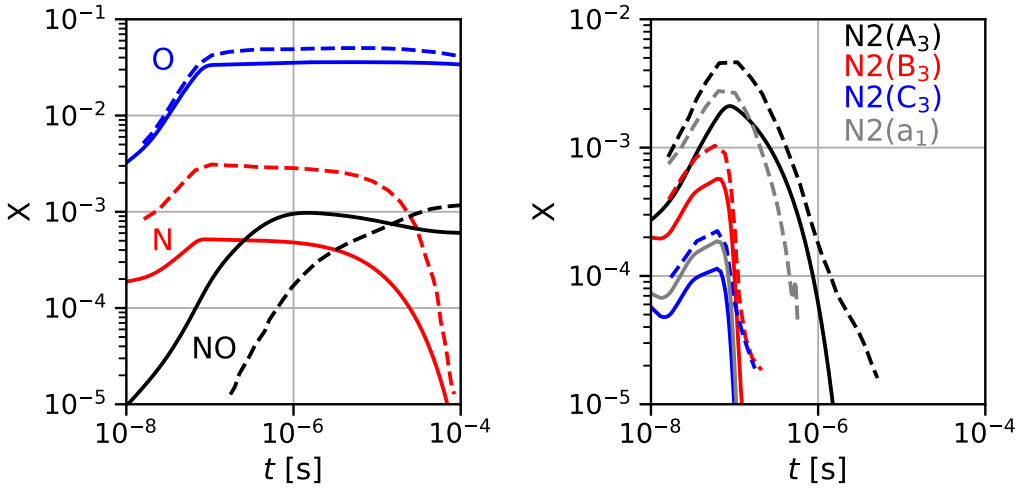

(a) (b)

Figure 6.14: Comparison of species production on Case B [133] (a) major discharge products and (b) electronically excited nitrogen. Solid-lines correspond to this work and dashed-lines are taken from simulations of [133].

6.11 Case C: Production of N and NO

The experiment of Case C is presented in [30] and is very close to the pin-pin experiment of the Case B [133] previously described (300 K - 100 Torr). In addition to what has been measured in case B (i.e. O density, N_2(v) populations, and gas temperature), the time evolution of NO and N has been determined using LIF and TALIF methods respectively, allowing the validation of additional active species production.

This experiment has been studied numerically by Shkurenkov et al. [175], who used a 1D

axial model that also solves the Poisson equation. By doing so, their model can predict the time evolution of reduced electric field E/N and electron density n_e. These two quantities shown in Fig 6.15 are used as input parameters of the 0D model used in this work.

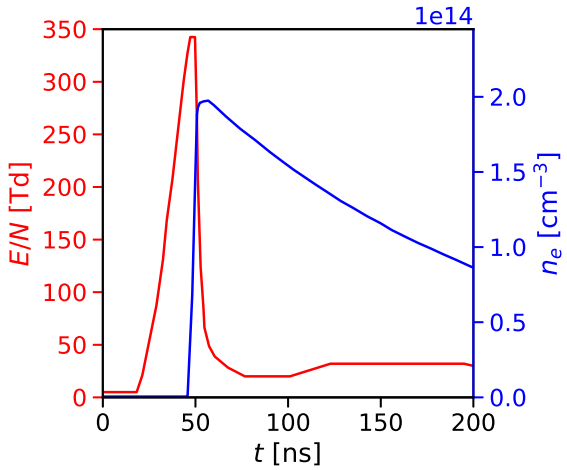

Figure 6.15: Electron density and reduced electric field profiles used as input of our 0D reactor retrieved from [175, Fig. 4b]

6.11.1 Gas temperature

In the experiment of [30], the rotational gas temperature remains low with an increase of about 75 K. In the simulations shown in Fig. 6.16, the fast gas heating occurring during the first 100 ns is responsible for a 50 K increase. The subsequent vibrational energy relaxation, which arises on the microsecond timescale, increases the temperature up to 400 K at 1 ms. As our model does not include any dimensional effect, it can not capture the gas temperature decay after 1 ms that is a consequence of diffusive effects. Moreover, our simulation does not account for the compression wave and its successive expansion which occurred on the acoustic timescale $\tau_a = r_d/a \simeq 3\,\mu s$. Thus, gas cooling observed experimentally around 1 µs is not reproduced by our model. However, our model gives a good estimate of the overall gas temperature increase independently of the combustion mechanism used.

6.11.2 Species production

The discharge used in the experiment of [30] loads a significant amount of energy into vibrational modes of N_2 due to the low reduced electric field after the breakdown. Our model gives a good estimate of the N_2(v=0,4) populations as shown in Fig. 6.17a. Moreover, Fig. 6.17b shows that our detailed model VIB.1. is able to well reproduce the vibrational temperature defined by:

$$T_{\text{vib}}^{01} = \frac{E_1 - E_0}{k_B \ln\left(N_0\right)/N_1} \tag{6.24}$$

where E_0 and E_1 are the vibrational energy of the two first levels, k_B is the Boltzmann constant, N_0 and N_1 are the densities of the two first levels N_2(v=0) and N_2(v=1).

The time evolutions of O, N and NO predicted by our kinetic mechanisms are compared with the experimental results of [30] and kinetic simulation of [175]. An excellent agreement is found

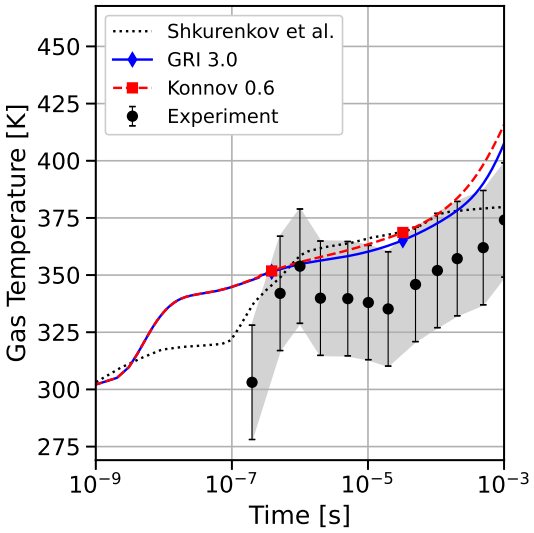

Figure 6.16: Time evolution of gas temperature for case C [30] using GRI 3.0 and Konnov plasma mechanisms against experimental results of [30] and previous kinetic simulation of [175]

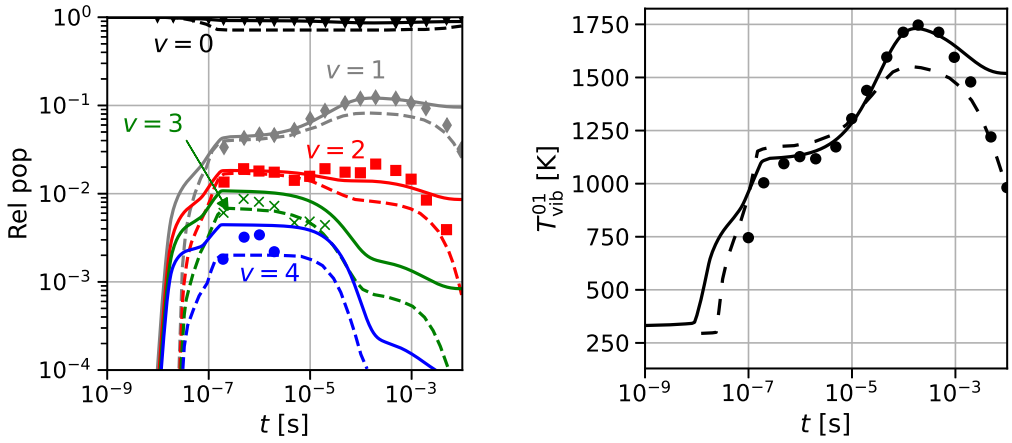

(a) (b)

Figure 6.17: Comparison of the detailed vibrational model VIB. 1 on Case C [30] (a) vibrational populations over time, $v = (0, 1, 2, 3, 4)$ correspond respectively to black, grey, red, green, blue and (b) vibrational temperature: this work (solid lines), experimental measurements [30] (markers) and reference simulation [175] (dashed lines).

for all the species when using our plasma mechanism supplemented by Konnov's mechanism (Figure. 6.18). Both maximum value and species decay are well reproduced. For the chemistry using the GRI 3.0 mechanism, the NO decay is rather too quick while other species decays are satisfying. Interestingly, a good estimate of NO is found by our model without considering the quenching reaction of N_2* by atomic oxygen. In [175], this reaction was claimed to be responsible for an important part of the NO production. The kinetic mechanism of [175] underestimates the NO density when it does not consider this reaction. In our mechanism, the main process of NO formation is explained as follows. First, electron impact dissociation of N_2 mainly occurs through the channel (R15) forming $N(^2D)$ state according to [48].

$$e^- + N_2 \longrightarrow e^- + N + N(^2D) \tag{R15}$$

Then, $N(^2D)$ is quenched by O_2 to form NO according to reactions (R16) and (R17) for which rates are taken from [32, 94].

$$N(^2D) + O_2 \longrightarrow NO + O \quad k = 1.5 \times 10^{-12}\,\mathrm{cm^3\,s^{-1}} \tag{R16}$$

$$N(^2D) + O_2 \longrightarrow NO + O(^1D) \quad k = 6 \times 10^{-12}\,\mathrm{cm^3\,s^{-1}} \tag{R17}$$

Notice that in this work, the Phelps cross-sections are used to evaluate the electron impact reaction rates for nitrogen molecules. Since the NO production depends on $N(^2P)$ in our mechanism, uncertainties on the dissociative cross-section must be evaluated in future work to assess the validity of the chemical paths observed in this work. Indeed, high uncertainties exist on the nitrogen molecule dissociative cross-section, and the one of Phelps is approximately 50% higher than the recommended cross-section in [48] for instance.

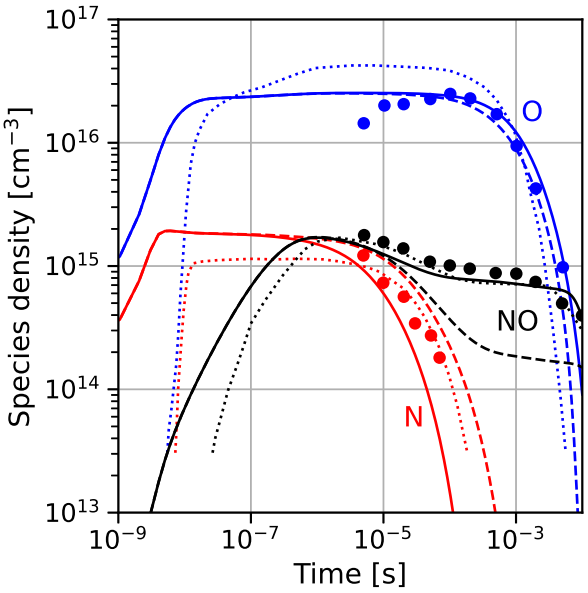

Figure 6.18: Time evolution of species density for case C [30] using GRI 3.0 (dashed) and Konnov (solid) plasma mechanisms against experimental results of [30] (symbols) and previous kinetic simulation of [175] (dotted)

Chapter 7

Toward plasma-assisted combustion: addition of methane

Contents

The kinetic schemes introduced in Chapter 6 are now used to extend the chemistry to methane combustion. The interaction of the plasma with methane is now added to build a suitable mechanism for plasma-assisted combustion of methane-air mixtures.

7.1 Electron impact processes with methane

In a stoichiometric CH_4-air mixture, the methane almost represents 10% (in mole) of the mixture (*i.e.*, $X_{CH_4} \approx 0.1$). Thus, it is essential to take it into account when computing the EEDF of the electrons. To do so, a complete set of cross-sections needs to be selected. In this work, the dataset of Hayashi [75] was chosen as in [51], and the associated reactions are described in Tab. 7.1. It was assumed that the 7.9 eV-excitation (Reactions ((CS3.4))) leads to the methane dissociation as it is almost 3 eV above the CH_4-dissociation threshold.

As previously done in air in Section 6.1, discharge energy branching analysis in a stoichiometric CH_4-air mixture has been performed, and results are plotted in Fig. 7.1. It is observed

#	Process	Reaction	$\Delta\epsilon$ [eV]	ΔE [eV]	Type
(CS3.1)	$CH_4 \longrightarrow CH_4^-$	$e^- + CH_4 \longrightarrow CH_4^-$	0.0	0.00	Attachment
(CS3.2)	$CH_4 \longrightarrow CH_4 \cdot (0.159\,eV)$	$e^- + CH_4 \longrightarrow e^- + CH_4(v_{24})$	0.162	0.00	Vibration
(CS3.3)	$CH_4 \longrightarrow CH_4 \cdot (0.37\,eV)$	$e^- + CH_4 \longrightarrow e^- + CH_4(v_{13})$	0.361	0.00	Vibration
(CS3.4)	$CH_4 \longrightarrow CH_4 \cdot (7.9\,eV)$	$e^- + CH_4 \longrightarrow e^- + CH_3 + H + \Delta E$	7.9	3.35	Dissociation
(CS3.5)	$CH_4 \longrightarrow CH_4^+$	$e^- + CH_4 \longrightarrow 2\,e^- + CH_4^+ + \Delta E$	12.9	0.00	Ionization

Table 7.1: List of processes in the Hayashi database [75] for e^--CH_4 processes and the associated reactions considered in this work. (Vib ≡ Vibrational excitation, Elec≡ Electronic exciation, Diss≡ Dissociation, Ioniz≡Ionization and El+Rot≡Elastic collision + rotational excitation)

that a significant part of the discharge energy is loaded into vibrational modes of CH_4 for reduced electric fields lower than 40 Td. At higher reduced electric fields, the observations made in air (See Sec. 6.1) are not disturbed by the methane addition. The CH_4-dissociation peaks at 400 Td representing 7% of the discharge energy. It should be noted that a reduced electric field of $E/N = 200$ Td is near to the optimum for O_2/CH_4-dissociation and N_2-electronic excitation.

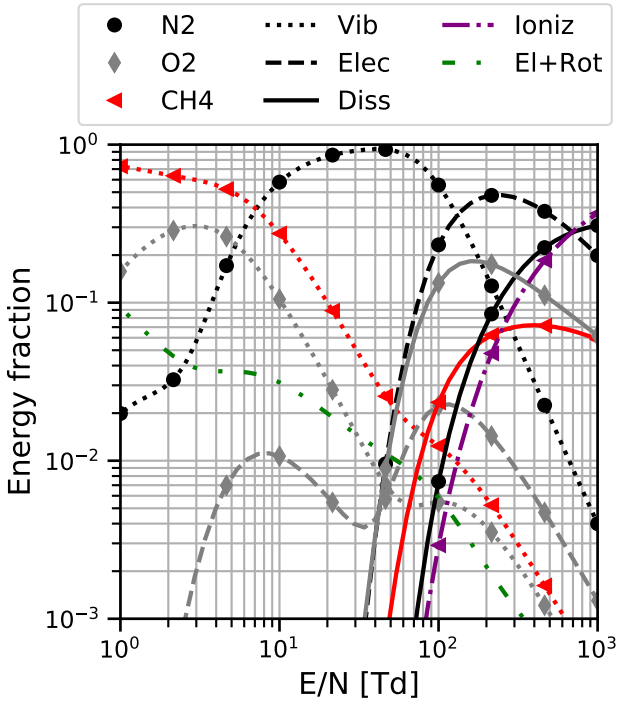

Figure 7.1: Discharge energy branching in stoichiometric methane-air mixture computed using BOLSIG+ [72]

7.2 Other processes

In addition to the electron-impact processes with methane, the plasma-air mechanism must be supplemented by electron-ion recombinations and heavy species reactions to compute plasma-assisted combustion. To do so, a compilation of the reactions from [77, 59, 190] has been done. Table. 7.2 summarizes the most important plasma reactions involving CH_4. As in air, the

quenching of electronically excited nitrogen by CH_4 in reactions (D4) to (D7) can efficiently produce radicals: CH_3 and H. In addition to the radical production, the production of excited atomic oxygen $O(^1D)$ can significantly accelerate methane oxidation without energy activation in reactions (D8) and (D9).

#	Reaction	k_f $[cm^3\,s^{-1}]$	Ref.
	Electron-ion recombination		
(D1)	$e^- + {CH_4}^+ \longrightarrow CH_3 + H$	$1.18 \times 10^{-8}\,(300/T_g)^{0.5}$	[77]
(D2)	$e^- + {CH_4}^+ \longrightarrow CH_2 + 2\,H$	$2.42 \times 10^{-8}\,(300/T_g)^{0.5}$	[77]
(D3)	$e^- + {CH_4}^+ \longrightarrow CH + H_2 + H$	$1.41 \times 10^{-8}\,(300/T_g)^{0.5}$	[77]
	Quenching of excited states		
(D4)	$N_2(A) + CH_4 \longrightarrow N_2 + CH_3 + H$	3.3×10^{-15}	[191]
(D5)	$N_2(B) + CH_4 \longrightarrow N_2 + CH_3 + H$	3×10^{-10}	[191]
(D6)	$N_2(C) + CH_4 \longrightarrow N_2 + CH_3 + H$	5×10^{-10}	[191]
(D7)	$N_2(a) + CH_4 \longrightarrow N_2 + CH_3 + H$	3×10^{-10}	[191]
(D8)	$O(^1D) + CH_4 \longrightarrow CH_3 + OH$	1.89×10^{-10}	[59]
(D9)	$O(^1D) + CH_4 \longrightarrow CH_3O + H$	3.1×10^{-11}	[59]

Table 7.2: Major plasma reactions in CH_4-containing mixture.

7.3 Detailed combustion mechanisms

Two detailed combustion mechanisms (GRI 3.0 and Konnov) were already added to the detailed plasma mechanism in the previous chapter to adequately describe the long-term behavior of the ground state molecules in air. This section highlights the difference between these two kinetic mechanisms regarding their behaviors in flame, characterized with the ignition delay time and the flame speed S_L. Auto-ignition is computed for a stoichiometric mixture with varying the initial temperature, and flame speed is computed with a fresh gas temperature and pressure of 300 K and 1 atmosphere and varying equivalence ratio. Regarding auto-ignition times in Fig. 7.2a, both mechanisms are in good agreement when dealing with standard conditions (CH_4, N_2 and O_2 only). However, the addition of a small amount of atomic oxygen $\Delta Y_O = 1 \times 10^{-3}$, to mimic a plasma chemical effect, reveals a noticeable difference between the two mechanisms. The addition of atomic oxygen reduces the ignition delay time for both mechanisms, but this effect is stronger for the GRI-3.0 mechanism. Concerning flame speeds shown in Fig. 7.2b, a difference of about 10% is observed between the two mechanisms in the lean-to-stoichiometric region for pure CH_4-air mixture. The addition of atomic oxygen leads to a slightly higher flame speed in the stochiometric and stochiometric-rich regions for the GRI-3.0 and Konnov mechanisms respectively. Overall, these preliminary results show that the two mechanisms behave similarly in pure CH_4-air, but their response to plasma discharges can be quite different.

7.4 Case D: Discharge in methane-air without combustion

7.4.1 Case description and numerical setup

The experiment described in [191] contains two planar electrodes in a rectangular geometry that produce NRP discharges in pure air and CH_4-air mixtures at 300 K and 60 Torr. The

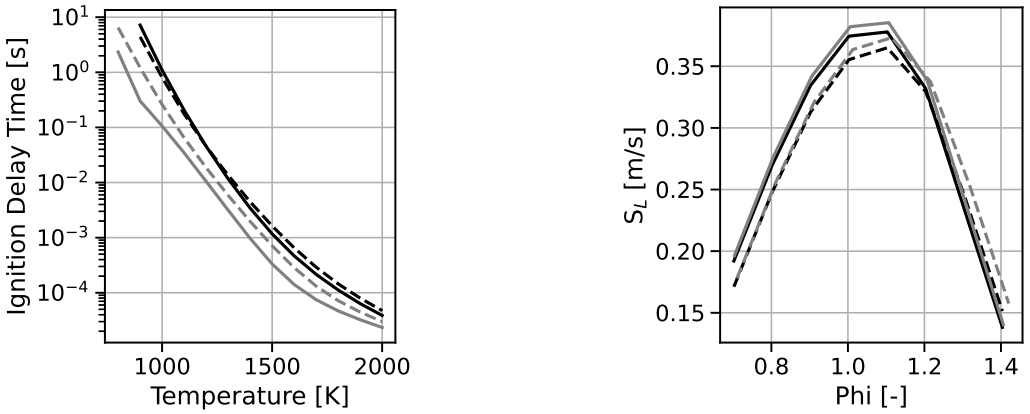

(a) Auto-ignition delay at $\phi = 1$ (b) Flame speed at $T_0 = 300\,\mathrm{K}$, $P_0 = 1$ atm

Figure 7.2: Comparison of the GRI-3.0 (solid lines) and Konnov (dashed lines) mechanisms for pure CH_4-air (black) and with small atomic oxygen addition $\Delta Y_O = 1 \times 10^{-3}$ (gray) to mimic plasma discharge.

pulses are 25 ns long and can be applied in single mode or in burst mode, in which case from 2 to 100 pulses are applied at 100 kHz. However, only the single pulse case was studied in this work. Measurements of atomic oxygen after the discharges are given in [191] as well as simulation results. The objective is to validate the atomic oxygen decay in both air and CH_4-air mixtures. Moreover, the deposited energy is too small to activate combustion processes so that only the kinetic effect of discharge is observed.

The simulations of [191] have been made with a reduced electric field and an electron density which follow a Gaussian profile with $\Delta t_{\mathrm{FWHM}} = 25\,\mathrm{ns}$ as depicted in Fig. 7.3. The reduced electric field peaks at $E/N^{\mathrm{MAX}} = 247$ Td and the electron density at $n_e^{\mathrm{MAX}} = 2.5 \times 10^{11}\,\mathrm{cm}^{-3}$ to match with the peak of atomic oxygen mole fraction in air as done in [191]. These parameters are kept constant for both air and CH_4-air mixtures to focus on the effect of the mixture composition.

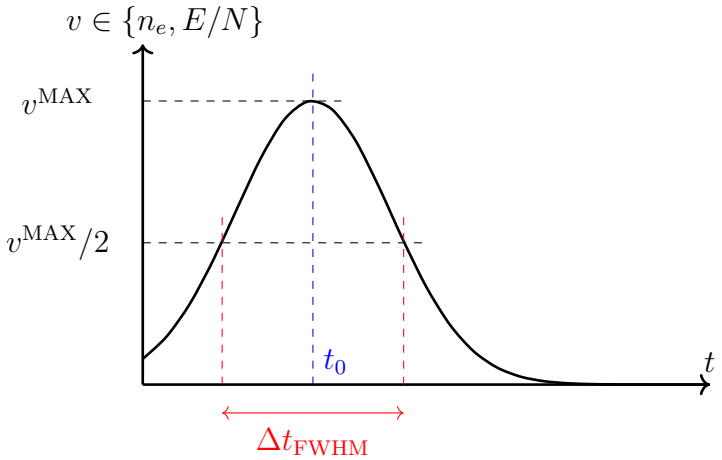

Figure 7.3: Schematic of the electron density and reduced electric field imposed in the Case D

7.4.2 Atomic oxygen decay

The atomic oxygen decay after a discharge in both air and methane-air mixtures has been recorded by Uddi et al. [191]. The Konnov and GRI 3.0 plasma mechanisms using Model 3 (See Section. 6.4) give satisfactory results concerning the rate of decay of atomic oxygen in both cases compared to experimental results and reference simulations as shown in Fig. 7.4.

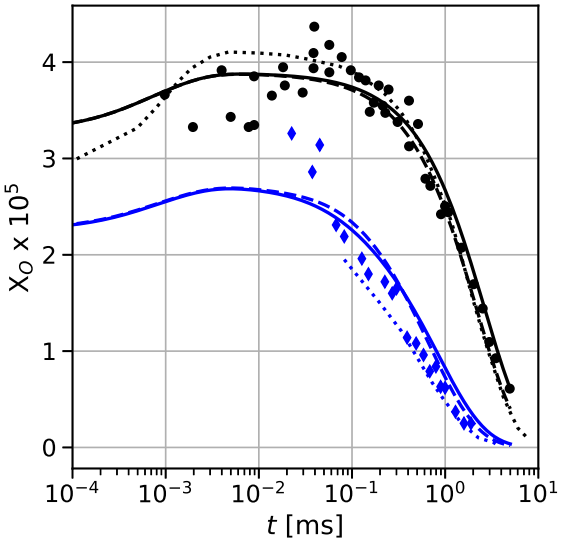

Figure 7.4: Time evolution of atomic oxygen mole fraction for Case D [191] using Model 3 along with GRI 3.0 (solid) or Konnov (dashed) mechanisms. Measurements (markers) [191] and reference simulations (dotted) [191] are also given for comparison. Black and blue colors are respectively used for air and air-methane cases.

In pure air, the difference between the two combustion mechanisms is due to the different rates of O_3 chemistry. Indeed, atomic oxygen is mainly consumed through the three-body recombination reactions with O_2 which form O_3 as shown in Fig. 7.5a. As in Case A of the previous chapter, most of the atomic oxygen production is due to the quenching of N_2* and electron impact dissociation. Thus, the temperature and pressure changes do not significantly affect the species production during the plasma phase. In the CH_4-air mixture, atomic oxygen is consumed in reactions involving carbonated and hydrogenated species. Among them, atomic oxygen strongly reacts with HO_2 and CH_3 as shown in Fig. 7.5b. Moreover, the ozone formation remains an important loss of atomic oxygen. Thus, in both air and CH_4-air mixtures, a significant amount of oxygen is stored into O_3 ($X_{O_3} \simeq 1 \times 10^{-5}$) as shown in Fig. 7.6. As discussed in [180], the ozone molecule has a long lifetime and can significantly affect the flame and ignition characteristics. Hence, it is important to adequately describe the ozone chemistry which is not always detailed in combustion mechanism such as the GRI 3.0 [177]. The impact of ozone on combustion was not investigated in detail in this work, and remains an interesting question to be addressed in the future [180].

7.4.3 Production and decay of other radicals

In addition to the atomic oxygen discussed in the previous section, other radicals such as CH_3, H and OH are produced in the CH_4-air case. Figure 7.7 shows the time evolution of the four main radicals produced in this case. A sharp increase of the radicals occurs during the pulse and

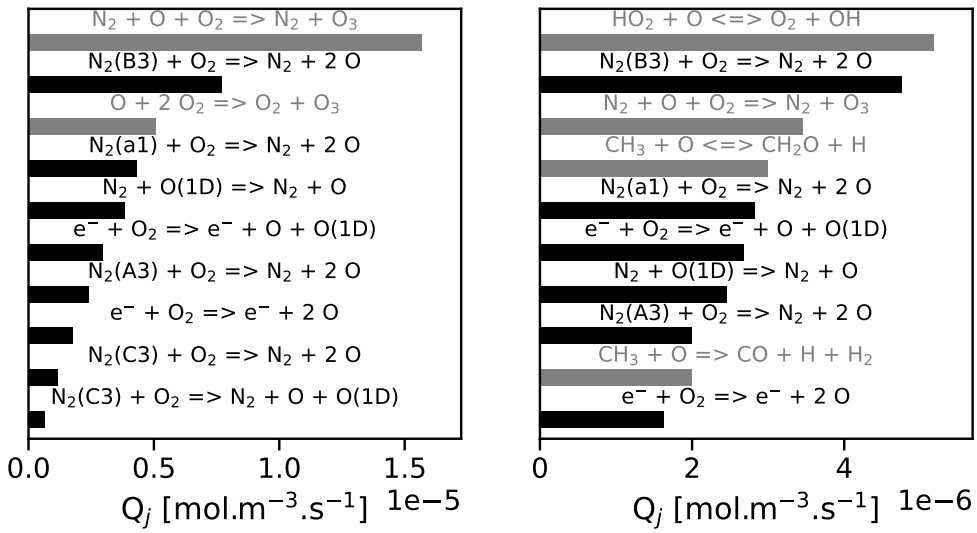

(a) Air (b) CH_4-Air

Figure 7.5: Integrated molar production rate of atomic oxygen O between 0 and 5 ms in (a) air and (b) CH_4-air mixtures. Black bars correspond to $Q_j > 0$ and gray ones correspond to $Q_j \leq 0$.

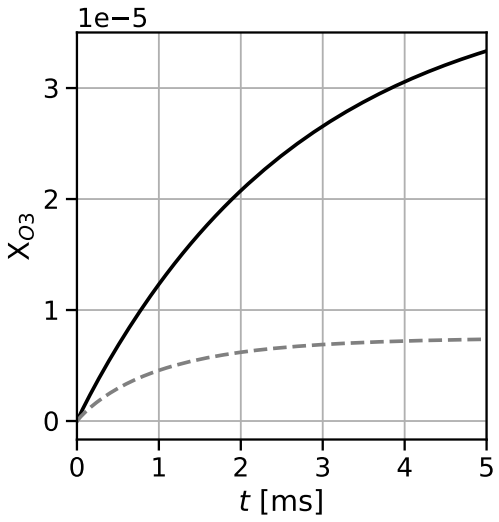

Figure 7.6: Time evolution of O_3 in the Case D: (—) Air and (- - -) CH_4-Air.

the first instants of the afterglow ($t \leq 60$ ns). Then, molar fractions of these radicals remain almost constants until 10 µs. After that time, H and CH_3 are decaying successively around 20 µs and 100 µs. In the same time, OH molar fraction increases within the interval [20, 300] µs. Finally, both O and OH decay in the millisecond timescale.

To better understand the processes that are responsible for radical production and decay, the production and consumption rates of each species are analyzed at $t = 100$ µs in Fig. 7.8. The atomic oxygen is not produced anymore and strongly reacts with CH_3. This is confirmed in Fig. 7.8c where CH_3 is almost entirely consumed through its reaction with O. The decay of atomic hydrogen is due mainly to the three-body reaction with O_2 that forms HO_2. HO_2 was found to be an essential species for the atomic oxygen decay in the previous section and

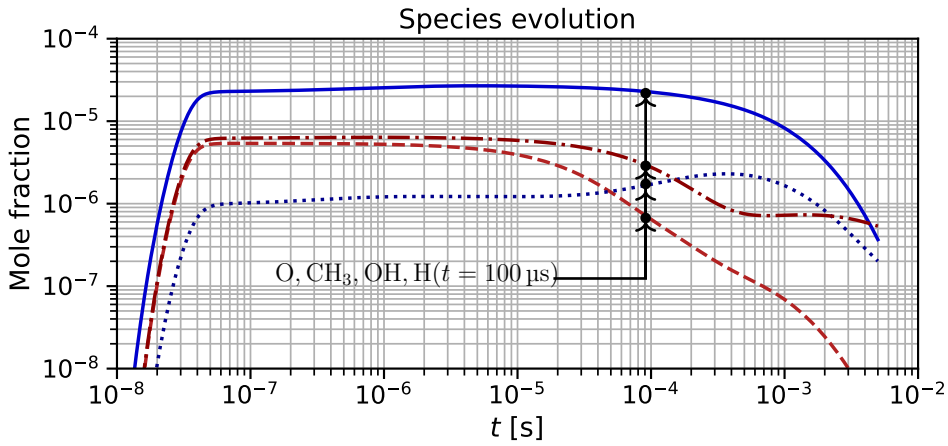

Figure 7.7: Time evolution of main radicals in the CH_4-air Case D using Model 3 along with GRI 3.0 mechanism: (—) O, (- - -) H, (·····) OH and (-···-) CH_3. Black dots correspond to the instants where molar production rates are analyzed.

is also found to be responsible for OH formation (See fig. 7.8d). Moreover, HO_2 is significanly produced within the interval [10, 100] µs as depicted in Fig. 7.9. Thus, a significant part of the HO_2 production is due to chemical reactions involving atomic hydrogen H.

To conclude, the atomic oxygen decay in the CH_4-air case can be explained by the following series of reactions. Firstly, atomic hydrogen is produced during the discharge by the reactions:

$$e^- + CH_4 \longrightarrow e^- + CH_3 + H \tag{R18}$$
$$N_2{}^* + CH_4 \longrightarrow N_2 + CH_3 + H \tag{R19}$$

Then, H particates to the production of HO_2 in a three-body reaction with O_2:

$$H + O_2 + N_2 \longrightarrow HO_2 + N_2 \tag{R20}$$

Finally, HO_2 combines with O to form O_2 and an OH radical:

$$HO_2 + O \longrightarrow O_2 + OH \tag{R21}$$

In addition to that, the three-body recombination of O with O_2, which forms O_3, remains a critical process for the atomic oxygen decay as in pure air.

7.5 Case E: Plasma assisted ignition of methane

7.5.1 Case description and numerical setup

A shock tube setup was used to study ignition using NRP discharges in Starikovskaia et al. [178]. A shock wave is initiated using a broken diaphragm and passes between two electrodes where the discharge is applied. The simulated case, taken from [11], is characterized by an

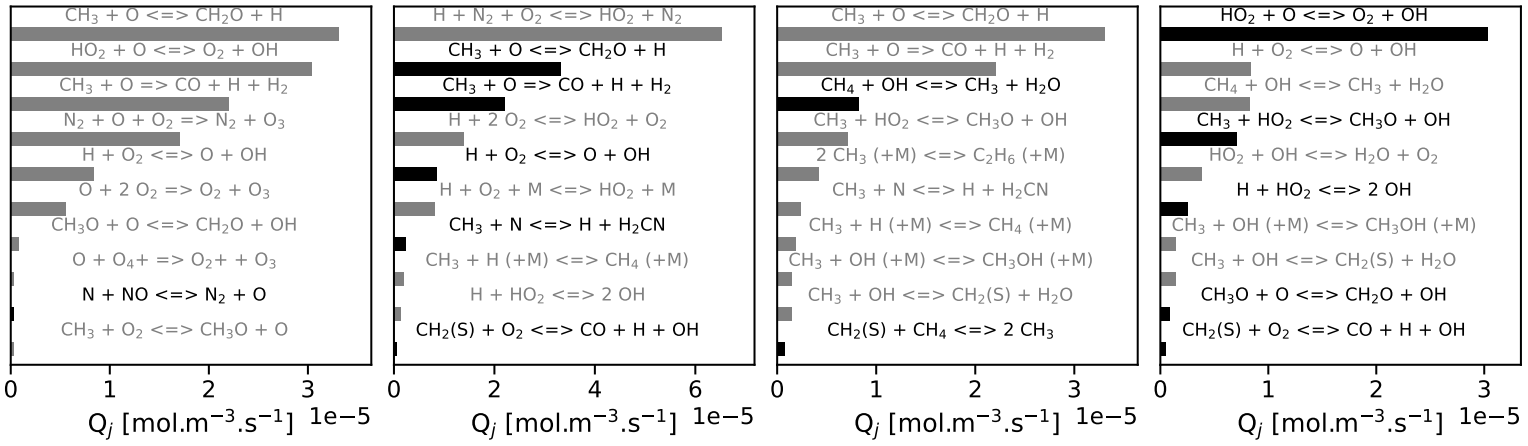

(a) O (b) H (c) CH_3 (d) OH

Figure 7.8: Instantaneous molar production rate of O, H, CH_3 and OH at $t = 100\,\mu s$ of the CH_4-air mixture (Case D) using the GRI 3.0 plasma mechanism. Black bars correspond to $Q_j > 0$ and gray ones correspond to $Q_j \leq 0$.

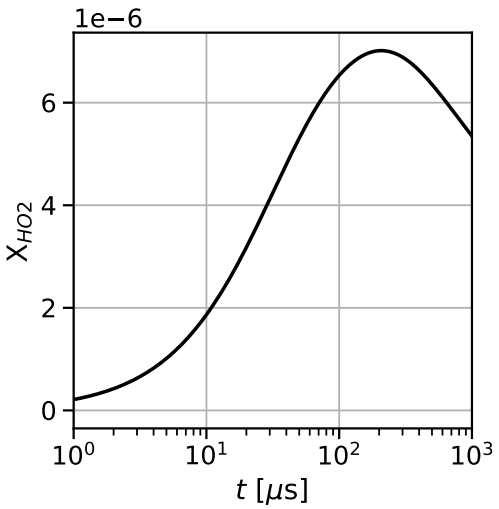

Figure 7.9: Time evolution of HO_2 in CH_4-air mixture (Case D) using the GRI 3.0 plasma mechanism.

initial temperature $T_0 = 1330\,K$, an initial pressure $P_0 = 0.45\,bar$ and an initial composition Ar:N_2:O_2:CH_4-80:15:4:1 (in mole). The electric field is deduced from the electric potential measurements at two different locations. As the discharge is modeled in a 0D framework, it is necessary to impose the electron density profile during the pulses, which is deduced from the discharge energy density e_p used in the simulation of [11] and given by:

$$e_p(t) = \int_0^t e n_e \mu_e \mathbf{E}^2 dt = e_p(t - \Delta t) + \int_{t-\Delta t}^t e n_e \mu_e \mathbf{E}^2 dt \tag{7.1}$$

Assuming that n_e, μ_e and $\mathbf{E}$ are constants during the interval $[t - \Delta t, t]$ we have:

$$n_e(t) = \frac{e_p(t) - e_p(t - \Delta t)}{e \mu_e \mathbf{E}^2 \Delta t} \tag{7.2}$$

The resulting input profiles are shown in Fig. 7.10 for the main pulse (Pulse 1) and the three reflected pulses (Pulses 2, 3 and 4). The data digitalization induces electron density oscillations during the first pulse. However, the electron density remains almost constant during the pulse at a value around $\approx 8 \times 10^{13}\,\mathrm{cm}^{-3}$ which is coherent with the glow discharge observed experimentally. Moreover, a good agreement between our energy density profile and the one measured experimentally is found in Fig. 7.11. There is approximately 50% of the energy that is deposited during pulses 1 and 2. The remaining energy is equally shared between pulses 3 and 4.

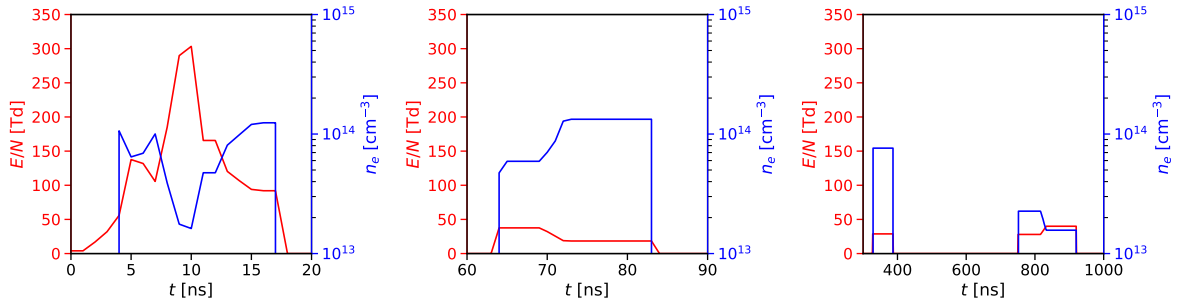

(a) Pulse 1 (b) Pulse 2 (c) Pulses 3 and 4

Figure 7.10: Electron density and reduced electric field imposed imposed in the Case E during (a) the main pulse, (b) the first reflection and (c) the third and fourth reflections.

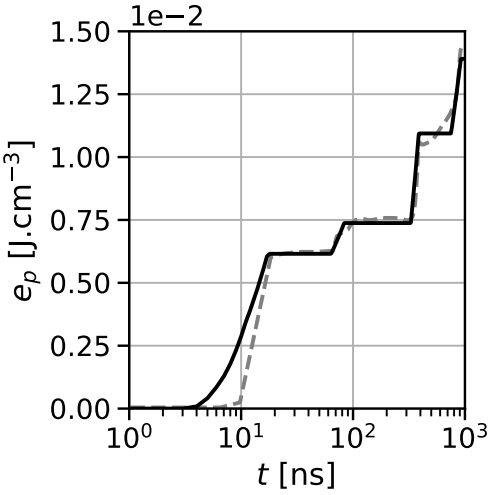

Figure 7.11: Energy density of the case E: (—) Results of our simulations and (- - -) experimental measurement.

7.5.2 Argon mechanism

This case occurs in a mixture highly diluted with argon. Thus, it is essential to include a plasma chemical mechanism for argon to properly describe electron energy transfer to the gas. The simple argon mechanism presented in [11] is used in this work. A full description of the argon sub-mechanism is given in Tab. 7.3. During the discharge, Ar can be either excited into Ar* with electronic excitation energy of 11.5 eV or ionized. Then, Ar^+ can exchange its charge with

N_2, O_2 and CH_4 to form ions that are already considered in our detailed plasma mechanism. The quenching of Ar^* leads to O_2 and CH_4 dissociation as well as the formation of excited $N_2(B_3, C_3)$.

Reaction	k_f $[cm^3\,s^{-1}]$	Ref.
Electron-impact reactions		
$e^- + Ar \longrightarrow e^- + Ar^*$	σ	[148]
$e^- + Ar \longrightarrow 2\,e^- + Ar^+$	σ	[148]
Charge exchange		
$Ar^+ + N_2 \longrightarrow Ar + {N_2}^+$	5×10^{-11}	[132]
$Ar^+ + CH_4 \longrightarrow Ar + {CH_3}^+ + H$	1.1×10^{-9}	[132]
$Ar^+ + CH_4 \longrightarrow Ar + {CH_2}^+ + H_2$	2.3×10^{-10}	[132]
$Ar^+ + O_2 \longrightarrow Ar + {O_2}^+$	1×10^{-10}	[132]
Quenching of excited states		
$Ar^* + O_2 \longrightarrow Ar + 2\,O$	2×10^{-10}	[85]
$Ar^* + CH_4 \longrightarrow Ar + CH_2 + 2\,H$	3.3×10^{-10}	[193]
$Ar^* + CH_4 \longrightarrow Ar + CH + H + H_2$	5.8×10^{-11}	[193]
$Ar^* + CH_4 \longrightarrow Ar + CH_3 + H$	5.8×10^{-11}	[193]
$Ar^* + CH_4 \longrightarrow Ar + CH_2 + H_2$	5.8×10^{-11}	[193]
$Ar^* + N_2 \longrightarrow Ar + N_2(C_3)$	1.5×10^{-11}	[85]
$Ar^* + N_2 \longrightarrow Ar + N_2(B_3)$	1.5×10^{-11}	[85]

Table 7.3: Sub-mechanism for argon in Ar:N_2:O_2:CH_4 mixtures taken from [11].

7.5.3 Plasma-ignition delay time

The discharge used in [178] is characterized by a combination of radical production and fast gas heating promoting the ignition process. The gas heating during the discharge remains relatively low, which leads to a gas temperature increase of about 100 K. The ignition delay time τ_{ig} measured experimentally is compared with the one extracted from the simulation using the same procedure based on the OH mole fraction: τ_{ig} is defined at the intersection of two tangents of the OH density profiles, one at the minimum value and the other at the inflection point during the sharp increase corresponding to the ignition process. This method is described in Fig. 7.12a. The ignition delay times obtained for the different combustion mechanisms are given in Tab. 7.4 and time evolution of the gas temperature is shown in Fig. 7.12b. A very good agreement with the experimental value $\tau_{ig}^{exp} = 376\,\mu s$ [178] is found for the case using the Konnov mechanism. The case using the GRI-3.0 mechanism exhibits a 50% lower ignition time compared to the Konnov mechanism, which is consistent with the preliminary study of ignition delay time performed in Section 7.3. An additional simulation, referred to as "NO FGH", was performed without gas heating during the discharge phase (i.e. $t \leq 1\,\mu s$) as done in [11]. In that case, the ignition delay time increases to 448 µs showing the importance of accounting for the fast gas heating effect during the discharge phase. The plasma-assisted ignition delay time is significantly lower than the auto-ignition delay time, which is found about 20 ms when using the Konnov mechanism.

7.5.4 Kinetics effects

The kinetic effects of the discharge are now analyzed for the Konnov-plasma mechanism, which exhibits the best agreement with ignition delay time as discussed in the previous section. Fig-

τ_{ig}	X_O	X_H	X_{CH3}	Reference
332 µs	2.79×10^{-3}	2.7×10^{-4}	2.47×10^{-4}	[11]
135 µs	3.43×10^{-3}	3.06×10^{-3}	5.94×10^{-4}	GRI 3.0 (This work)
334 µs	3.14×10^{-3}	2.67×10^{-3}	7.26×10^{-4}	Konnov v0.6 (This work)
448 µs	2.92×10^{-3}	2.56×10^{-3}	6.78×10^{-4}	Konnov v0.6 NO FGH (This work)

Table 7.4: Ignition time and maximum values of radical mole fractions.

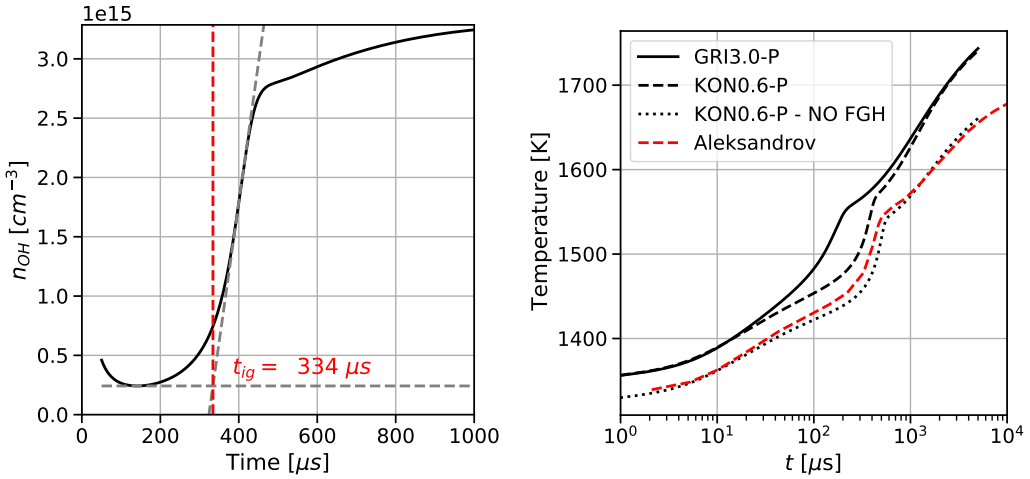

(a) (b)

Figure 7.12: Results of Case E [11] (a) ignition time delay for the simulation using Konnov mechanism and (b) gas temperature.

ure 7.13 shows the dynamics of the main radicals and excited species during the plasma phase for $t \leq 1\,\mu s$. Atomic oxygen is the main radical produced during the plasma phase, 60% being produced during pulses 1 and 2. Interestingly, pulses 3 and 4 are also able to produce atomic oxygen. Despite the low reduced electric field during pulses 3 and 4, they are responsible for 40% of the atomic oxygen production. The effects of the discharges on the three other radicals shown in Fig. 7.13a are less pronounced. For CH_3 and H, a sharp increase is only observed during pulses 1 and 2, while only a minor increase is observed during pulses 3 and 4. The OH density rise is not synchronized with the discharge energy deposition and results from reactions that follow the pulses. During the main pulse, Ar^* and $N_2(B_3)$ are the most important excited species. Almost all the excited species quickly vanish at the end of the first pulse, and the second pulse does not have a significant effect on them. Pulses 3 and 4 mainly produce $N_2(A_3, B_3)$ due to the low electric field during these pulses. Despite the high argon molar fraction, the pulse reflections cannot excite it, and the discharge effects are mainly controlled by the production of excited nitrogen and its subsequent quenching.

At the end of the plasma phase, the atomic oxygen consumption goes hand in hand with a rise of the other radicals, as indicated in Fig. 7.14a. Then within [10-100] µs, almost all the radicals are decaying until a favorable condition for ignition is reached at $t \approx 200\,\mu s$. At that time, H and OH densities are higher than O despite the higher atomic oxygen production during the pulse. In our condition, it seems that the atomic oxygen produced during the plasma phase serves to produce H and OH which in turn trigger the ignition. The ignition can also be observed in Fig 7.14b in which steep variation of the major mixture components are clearly visible around $t = 300\,\mu s$.

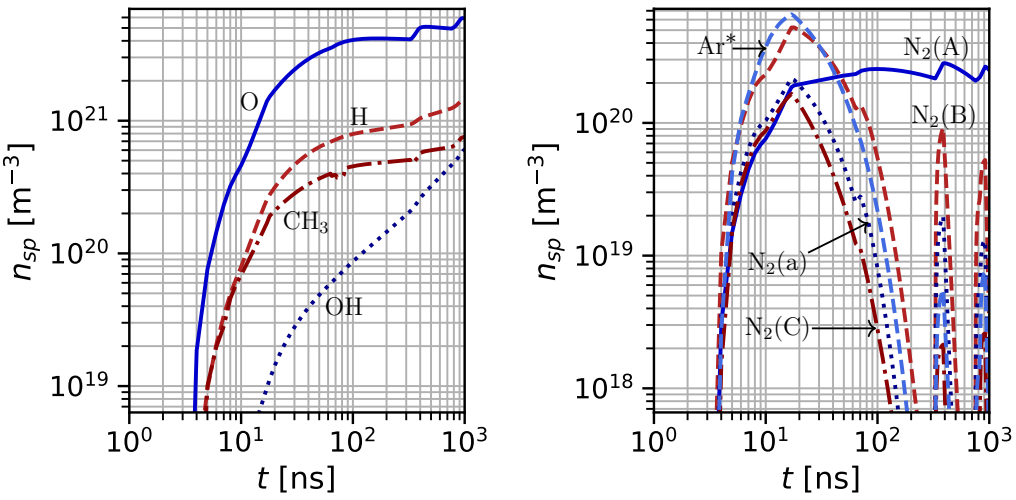

(a) (b)

Figure 7.13: Time evolution of species density in the Case E during the plasma phase [1-1000] ns using the Konnov-plasma mechanism: (a) main radicals and (b) excited species.

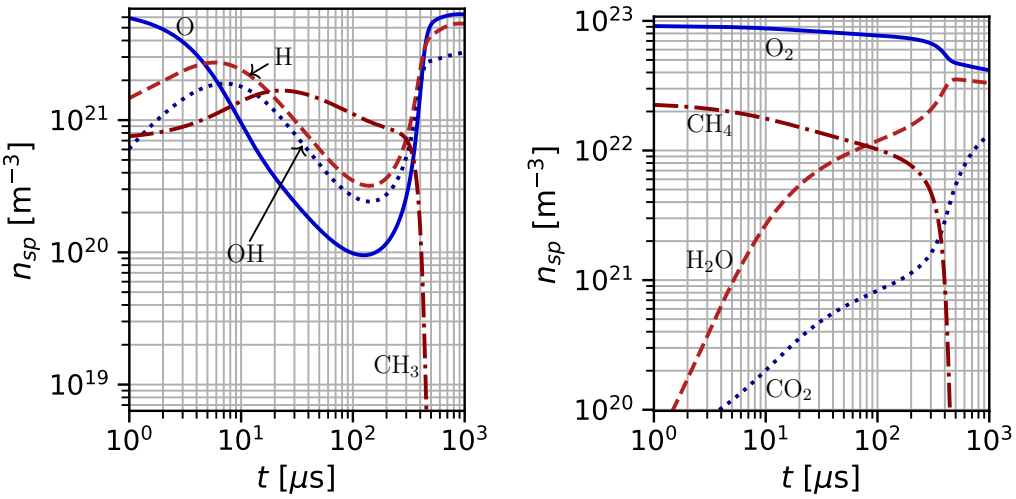

(a) (b)

Figure 7.14: Time evolution of species density in the Case E during the ignition phase [1-1000] μs using the Konnov-plasma mechanism: (a) main radicals and (b) major mixture components.

Chapter 8

Kinetics of plasma discharges in burnt gases

Contents

8.1 Motivation

For ignition applications, the reactive mixture is mainly composed of N_2, O_2 and a hydrocarbon CxHy. Such mixtures have been extensively studied in the past both numerically [8, 11, 51, 190, 59] and experimentally [108, 90, 178]. Chapters 6 and 7 also investigate in details the plasma chemistry in this kind of mixtures. However, plasma-assisted combustion with NRP discharges leads to dicharges in mixtures containing combustion products, which is rarely addressed in the literature. In practical applications such as gas turbines, it is almost unavoidable that the discharge occurs in the burnt gas region as encountered in [169]. Promising results concerning flame stabilization have been observed by Pilla et al. [150] and Lacoste et al. [101] where the discharge is located in a recirculation of burnt gases above a bluff body that comprises burnt gases. The effect of burnt gases composition on the discharge is under investigation experimentally in [46, 47] where the discharges occur both in fresh and burnt gases.

On the numerical side, most studies of PAC with NRP discharges do not or only partially consider the effect of CO_2 and H_2O [16, 51]. If this may be appropriate for when the mixture composition does not differ significantly from the fresh gas composition, it is less adapted to flame stabilization, where the discharge can occur in burnt or partially burnt gases. In that case, the concentrations of CO_2 and H_2O become relatively high and can not be neglected in the chemical mechanism. In [20], a 3D numerical study of plasma-assisted flame stabilization was performed using the phenomenological model of Castela et al. [34], which is based on experimental results in air [167], *i.e.*, in condition for which the model was not validated. To our knowledge, there is no comprehensive chemical mechanism for NRP discharge in burnt gases. The present chapter aims to extend the fuel-air plasma assisted combustion chemical mechanism developed in Chap. 6 and 7 to burnt gases mixtures.

8.2 Mechanism extension to CO_2-H_2O containing mixtures

The base mechanism detailed in the two previous chapters has been supplemented with mechanisms available in the literature for plasma discharge in CO_2 and H_2O. The kinetic mechanism of Kozák and Bogaerts [95] and Wang et al. [195] were considered for the CO_2 compound, while Liu et al. [113] and Wang et al. [195] were used to include H_2O. For both species, special care was necessary to select the proper cross-sections (see Sections 8.2.1 and 8.2.2) and additional reactions were necessary to properly describe the quenching of excited states (see Section 8.2.4).

8.2.1 Electron impact processes with CO_2

Recently, a detailed mechanism for CO_2-containing mixture was proposed by Aerts et al. [9] and then improved for vibrational excitation in [95, 96]. However, these mechanisms do not consider in detail the electronic excitation and direct electron impact dissociation that is dominating in discharges occurring at a high reduced electric field ($>$ 100 Td). Instead, they focus on CO_2 dissociation due to the vibrational excitation. These two CO_2 dissociation mechanisms are well described by Fig. 8.1 and detailed below.

The first one is due to vibrational excitation and is usually referred to as ladder climbing. The second one is the dissociation by direct electron impact. In that case, CO_2 is excited in an electronically unstable state $CO_2{}^*$ (also called pre-dissociated state), which quickly dissociates:

$$e^- + CO_2 \rightarrow e^- + CO_2{}^* \rightarrow e^- + CO + O \tag{8.1}$$

In reality, these two effects may combine, *i.e.*, direct electron impact dissociation of a vibrationally excited state. In that case, the energy necessary for direct electron impact dissociation can be reduced drastically by vibrational excitation. However, these two processes do not occur at the same electron energy. Similarly to N_2, discharge energy branching in pure CO_2 (see Fig. 8.2) reveals that the vibrational excitation is the dominant channel of energy transfer at low reduced electric field ($E/N < 100$ Td) while for $E/N > 100$ Td the electronic excitation and direct dissociation dominate. Around 100 Td, the vibrational excitation takes almost $30 - 40$ % of the energy discharge. For $E/N \geq 100$ Td, which is the case in most NRP discharges, the vibrational excitation is not high enough to promote the electron impact dissociation and could be neglected in the modeling of NRP discharges when $E/N > 100$ Td as discussed in [135, page 9]. In the end, the vibrational excitation of carbon dioxide may be treated in the same manner

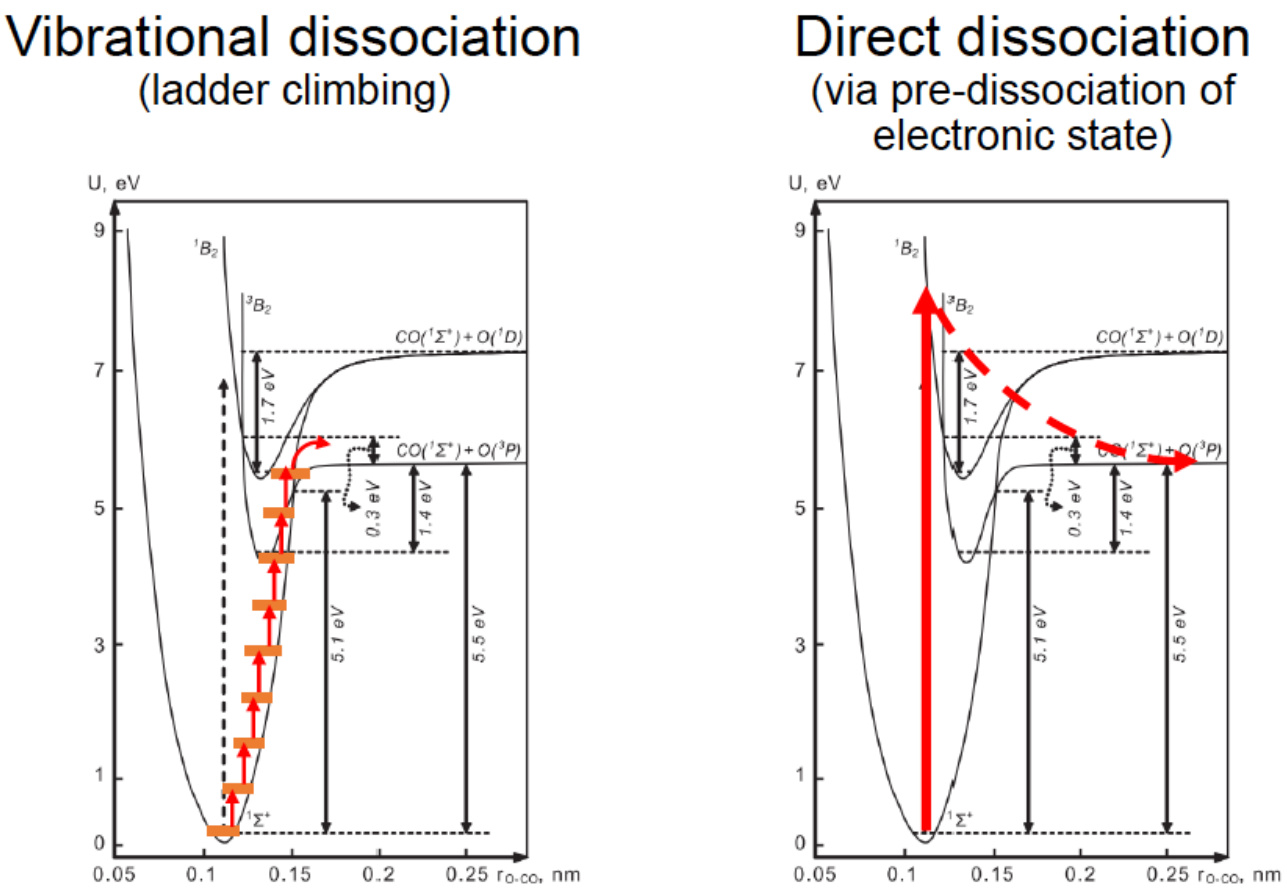

Figure 8.1: Potential energy curves for two CO_2 dissociation mechanism: (left) Ladder-climbing effect (right) dissociative electronic excitation. Red arrows correspond to the internal energy change following a signel collision. The horizontal axis corresponds to the internuclear distance. Reproduced from [144]

as in the vibrational model VIB. 2 of N_2, detailed in Section 6.5, to ensure energy conservation. In that case, $CO_2(v)$ is not considered as a species in the mechanism but is replaced by a mean CO_2 non-equilibrium energy $e_{\text{vib}}^{CO_2}$ which follows Eq. 6.11. The $CO_2(v)$ relaxation times can be found in [32].

The direct electron impact dissociation of CO_2 has been further investigated at IST Lisbon and in the PLASMANT group [68, 25, 69]. According to these studies, the most reliable cross-sections to compute the rate of electron impact CO_2 dissociation are those from Polak and Slovetsky [156] labeled σ_{Polak} in the following. However, these cross-sections can not be used to compute the Electron Energy Distribution Function (EEDF) as they do not form a complete and consistent set of cross-sections. Therefore, the Phelps' cross-sections taken from LxCat [148] were used to compute the EEDF. This set of cross-sections contains two excitation cross-sections at 7 eV and 10.5 eV denoted σ_1 and σ_2 respectively. Both correspond to an indistinguishable lumping of different excitation processes. These two cross-sections have been split into an energy loss process σ_k^{loss} and a dissociative process σ_k^d so that $\sigma_k = \sigma_k^d + \sigma_k^{\text{loss}}$. The dissociation cross-sections σ_k^d must ideally verify:

$$\sigma_{\text{Polak}} = \sigma_1^d + \sigma_2^d \tag{8.2}$$

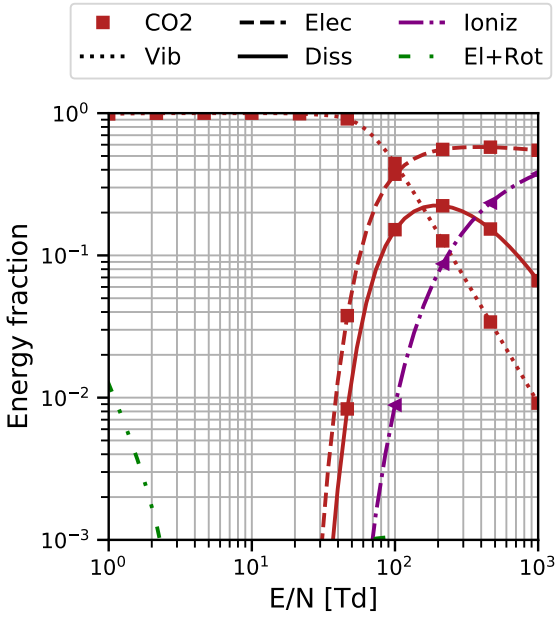

Figure 8.2: Discharge energy branching in pure CO_2 considering the processes detailed in Tab. 8.1 using BOLSIG+ [72]

However, it happens that $\sigma_{\text{Polak}} > \sigma_1 + \sigma_2$ for some energy values. without modifying the cross-section dataset properties. Hence, instead of Eq. 8.2, it is only verified that $\sigma_{\text{Polak}} \leq \sigma_1^d + \sigma_2^d$ by applying:

$$\sigma_1^d = \min(\sigma_1, \sigma_{\text{Polak}})$$
$$\sigma_2^d = \min(\sigma_2, \sigma_{\text{Polak}} - \sigma_1^d)$$

This procedure keeps the EEDF unchanged while introducing new physical information in the cross-sections dataset. The newly defined cross-sections are depicted in Fig. 8.3a. As shown in Fig. 8.3a, the Polak's cross-section can not be fully retrieved in the region of $[10 - 11]$ eV as it exceeds the sum of excitation cross sections $\sigma_1 + \sigma_2$. Thus, it is vital to check that the procedure does not significantly influence the dissociation process rate coefficients. These rate coefficients have been computed using BOLSIG+ [72] and are shown in Fig. 8.3b. There is an excellent agreement between the rates using the original cross-section σ_{Polak} and the extracted cross-sections σ_1^d and σ_2^d with a maximum difference of 6% reached at 90 Td. This difference is much smaller than the uncertainties on electron impact cross sections and validates the procedure. The direct use of Phelps cross-sections as dissociative process would have led to an overestimation of the rate of CO_2 dissociation.

Finally, Table 8.1 summarizes the cross-sections selected for CO_2 as well as the associated reactions. As discussed previously, only a mean energy of CO_2-vibrational excitation is considered so that vibrational levels are not detailed. Electronic excitation is replaced by a heating source term (*i.e.*, assuming an instantaneous relaxation into heat) due to the lack of information about these states and further quenching. Moreover, an energy source term is added to the electron impact dissociation processes as their energy thresholds $\Delta\epsilon$ exceed the dissociation energy of CO_2.

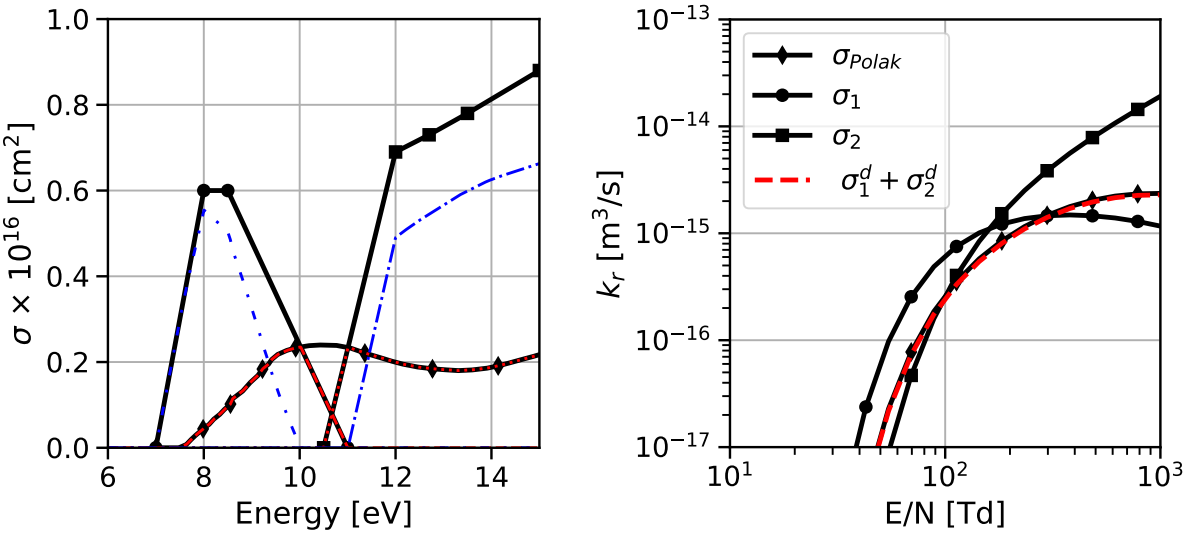

(a) Cross-sections (b) Rate coefficients

Figure 8.3: Electron impact CO_2 dissociation (a) cross sections and (b) corresponding rate coefficients. Legend for the left figure: ● σ_1, ■ σ_2, ◆ σ_{Polak}, (- - -) σ_1^d, (·····) σ_2^d, (- · -) σ_1^{loss}, (-·-·-) σ_2^{loss}.

	Process	Reaction	$\Delta\epsilon$ [eV]	ΔE [eV]	Type
(CS4.1) [a]	$CO_2 \longrightarrow CO + O^-$	$e^- + CO_2 \longrightarrow CO + O^-$	0.0	0.00	Attachment
(CS4.2) [a]	$CO_2 \longrightarrow CO_2(0.083\,\text{eV})$	$e^- + CO_2 \longrightarrow e^- + CO_2(v)$	0.083	0.00	Vibration
(CS4.3) [a]	$CO_2 \longrightarrow CO_2(0.167\,\text{eV})$	$e^- + CO_2 \longrightarrow e^- + CO_2(v)$	0.167	0.00	Vibration
(CS4.4) [a]	$CO_2 \longrightarrow CO_2(0.252\,\text{eV})$	$e^- + CO_2 \longrightarrow e^- + CO_2(v)$	0.252	0.00	Vibration
(CS4.5) [a]	$CO_2 \longrightarrow CO_2(0.291\,\text{eV})$	$e^- + CO_2 \longrightarrow e^- + CO_2(v)$	0.291	0.00	Vibration
(CS4.6) [a]	$CO_2 \longrightarrow CO_2(0.339\,\text{eV})$	$e^- + CO_2 \longrightarrow e^- + CO_2(v)$	0.339	0.00	Vibration
(CS4.7) [a]	$CO_2 \longrightarrow CO_2(0.422\,\text{eV})$	$e^- + CO_2 \longrightarrow e^- + CO_2(v)$	0.422	0.00	Vibration
(CS4.8) [a]	$CO_2 \longrightarrow CO_2(0.505\,\text{eV})$	$e^- + CO_2 \longrightarrow e^- + CO_2(v)$	0.505	0.00	Vibration
(CS4.9) [a]	$CO_2 \longrightarrow CO_2 \cdot (2.5\,\text{eV})$	$e^- + CO_2 \longrightarrow e^- + CO_2 + \Delta E$	2.5	2.5	Dissociation
(CS4.10) [a]	$CO_2 \longrightarrow CO_2 \cdot (3.85\,\text{eV})$	$e^- + CO_2 \longrightarrow e^- + CO_2 + \Delta E$	3.85	3.85	Dissociation
(CS4.11) σ_1^{loss},[b]	$CO_2 \longrightarrow CO_2 \cdot (7\,\text{eVloss})$	$e^- + CO_2 \longrightarrow e^- + CO_2 + \Delta E$	7.0	7.0	Excitation
(CS4.12) σ_1^{d},[b]	$CO_2 \longrightarrow CO_2 \cdot (7\,\text{eVdiss})$	$e^- + CO_2 \longrightarrow e^- + CO + O$	7.0	1.52	Dissociation
(CS4.13) σ_2^{loss},[b]	$CO_2 \longrightarrow CO_2 \cdot (10.5\,\text{eVloss})$	$e^- + CO_2 \longrightarrow e^- + CO_2 + \Delta E$	10.5	10.5	Excitation
(CS4.14) σ_2^{d},[b]	$CO_2 \longrightarrow CO_2 \cdot (10.5\,\text{eVdiss})$	$e^- + CO_2 \longrightarrow e^- + CO + O$	10.5	5.02	Dissociation
(CS4.15) [a]	$CO_2 \longrightarrow CO_2^+$	$e^- + CO_2 \longrightarrow 2\,e^- + CO_2^+$	13.3	0.00	Ionization

Table 8.1: List of processes considered for CO_2 and the associated reactions considered in this work.
[a] [148]
[b] [148] and [156]

8.2.2 H_2O cross-sections

While being one of the most abundant molecules on Earth, electron impact cross-sections of H_2O remain subject to significant uncertainties. An extensive and comprehensive review of these cross-sections has been made in [84], in which recommendations are made for different processes. These cross-sections were used for example in [113, 195]. However, Itkawa's cross-sections do not form a complete and validated database as pointed out in [194]. We also observed a wide discrepancy when using Itikawa's cross-sections as shown in Fig. 8.4a where

the drift-velocity $v_{\text{drift}} = |\mu E|$ is compared to simulations and experiments. Finally, the Triniti dataset [188] has been tested, and a good agreement with previous simulations and experiments was found, as shown in Fig. 8.4b. Thus, Triniti's cross-sections have been employed. A detailed description of the processes contained in this database can be found in Tab. 8.2.

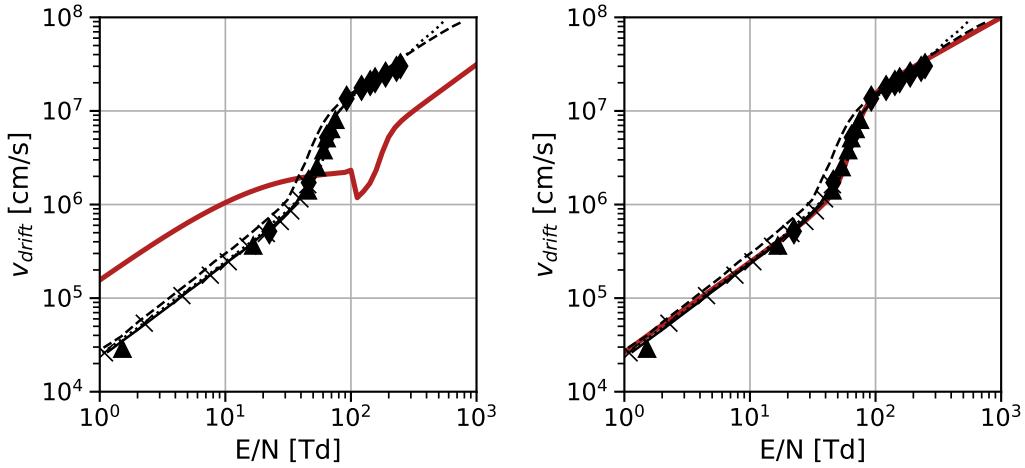

(a) Itikawa (b) Triniti

Figure 8.4: Comparison of the drift-velocity from BOLSIG+ [72] using: (a) Itikawa cross-sections [84] and (b) Triniti database [188] with the simulations of (—) [199], (- - -) [76], (·····) [139] and experiment from ▲ [196], ✕ [118], ◆ [168]

	Process	Reaction	$\Delta\epsilon$ [eV]	ΔE [eV]	Type
(CS5.1)	$H_2O \longrightarrow H_2 + O(-)$	$e^- + H_2O \longrightarrow H_2 + O^-$	0.0	0.0	Attachment
(CS5.2)	$H_2O \longrightarrow OH + H(-)$	$e^- + H_2O \longrightarrow OH + H^-$	0.0	0.0	Attachment
(CS5.3)	$H_2O \longrightarrow H_2O(ROT)$	$e^- + H_2O \longrightarrow e^- + H_2O + \Delta E$	0.04	0.04	Rotational
(CS5.4)	$H_2O \longrightarrow H_2O(010)$	$e^- + H_2O \longrightarrow e^- + H_2O(v)$	0.198	0.0	Vibrational
(CS5.5)	$H_2O \longrightarrow H_2O(101)$	$e^- + H_2O \longrightarrow e^- + H_2O(v)$	0.453	0.0	Vibrational
(CS5.6)	$H_2O \longrightarrow H + OH$	$e^- + H_2O \longrightarrow e^- + H + OH$	7.1	1.93	Dissociation
(CS5.7)	$H_2O \longrightarrow H_2O(^+)$	$e^- + H_2O \longrightarrow 2\,e^- + H_2O^+$	12.61	0.0	Ionization

Table 8.2: List of processes in the Triniti database [188] for H_2O and the associated reactions considered in this work.

As for CO_2, the discharge energy branching analysis has been performed, and results can be found in Fig. 8.5. Almost all the electron energy is transferred to elastic collisions and rotational excitation at low reduced electric fields. However, these energy channels represent less than 5% of the discharge energy for $E/N \geq 100$ Td and are not considered in the kinetic mechanism. Instead, the rotational excitation is modeled by a heating reaction as described in reaction (CS5.3). The vibrational excitation reaches a maximum at $E/N = 60$ above which it sharply decreases. Hence, the simplified vibrational model VIB. 2 (See Section 6.5) is used for vibrational relaxation of the water molecules. Relaxation times are available in Capitelli et al. [32, Table 7.8]. Finally, almost all of the energy is spent into H_2O-dissociation through the reaction (CS5.6).

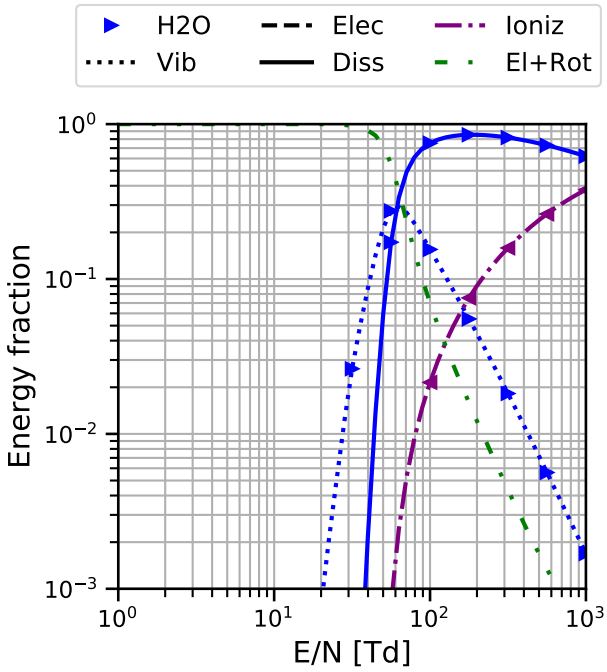

Figure 8.5: Discharge energy branching in pure H_2O considering the processes detailed in Tab. 8.2 using BOLSIG+ [72]

8.2.3 Discharge energy branching in burnt gases

The discharge energy branching is now analyzed in a typical methane-air burnt gases composition taken from a 1D flame simulation. Results are shown in Fig. 8.6. Two equivalence ratio were considered: a lean mixture at $\phi = 0.8$ (CO_2:H_2O:N_2:O_2:8.9:13.7:73.3:3.3 in mole), which is typical of most practical systems, and a stoichiometric mixture for which O_2 is no more present (CO_2:H_2O:N_2:9.5:19:71.5 in mole), both at $T_0 = 300$ K and $P_0 = 1$ atm. Firstly, it must be noted that the overall trends between the two conditions are almost the same. At low reduced electric fields [1-20] Td, the presence of H_2O leads to significant electron energy losses in elastic collisions and rotational excitation. Then within [20-100] Td, most of the energy is spent to excite N_2(v) while the production of CO_2(v) and H_2O(v) almost disapear. For $100 \leq E/N \leq 500$ Td, N_2-electronic states are efficiently produced with a peak value around 50% of the discharge energy. The peak for electron impact dissociation of H_2O, CO_2 and O_2 is also around 200 Td. Finally, at a very high reduced electric field, the ionization and production of atomic nitrogen become predominant.

A comparison of the energy fraction between the lean and stoichiometric cases is given in Tab. 8.3 for the most important channels at 200 Td. The most significant change concerns the H_2O-dissociation which increases by 3% in stoichiometric condition to replace the O_2-dissociation in lean condition.

ϕ	N_2*	CO_2*	N_2-diss	H_2O-diss	CO_2-diss	O_2-diss	N_2(v)	Ion
0.8	50%	4%	7%	12%	2%	3 %	15%	4%
1	50%	5%	7%	15%	2%	-	15%	4%

Table 8.3: Discharge energy branching ratio at 200 Td for lean and stoichiometric burnt gases compositions.

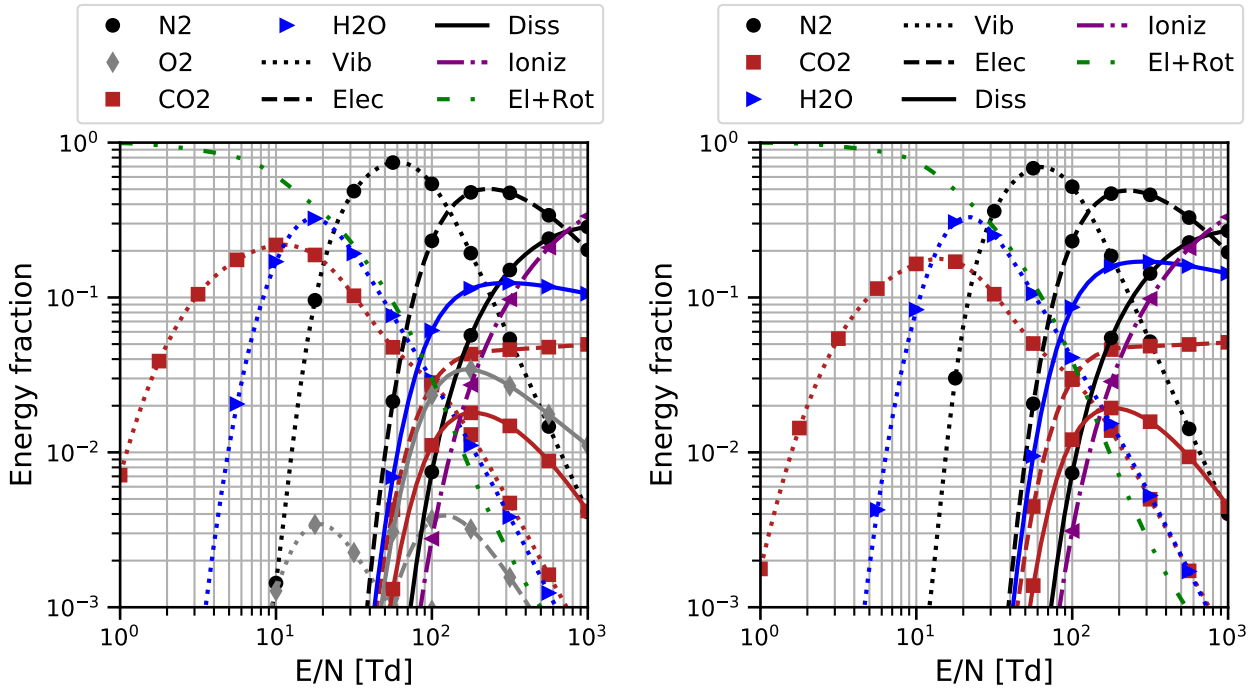

(a) $\phi = 0.8$ (b) $\phi = 1$

Figure 8.6: Discharge energy branching in burnt gases of methane-air flames for (a) lean mixture at $\phi = 0.8$ and (b) a stoichiometric mixture using BOLSIG+ [72]

8.2.4 Quenching of electronically excited species

Most of the time, the studies of CO_2 and H_2O in plasma discharges are limited to the molecules themselves and their fragments. However, for PAC applications, N_2 remains the most abundant species both in fresh and burnt gases. As shown in Section 8.2.3, the electronic excitation of N_2 remains the most important process in which electrons lose their energy for $E/N \gg 100$ Td. Thus, it is important to describe accurately the collisional quenching of $N_2{}^*$ in burnt gases conditions in which two new important colliding partners appear: CO_2 and H_2O.

The the CO_2 chemical mechanisms described previously, the effects of other components of the mixture, such as N_2, are not fully included. An attempt to describe a plasma-based CO_2 conversion by mean of kinetic modeling was done in [195] by taking into account of the presence of H_2O, O_2, N_2 and many other components. Nevertheless, the quenching of electronically excited $N_2{}^*, O^*$ is not complete. The mechanism proposed in [195] includes some quenching reactions that can be summarized as follows:

$$N_2{}^* + CO_2 \longrightarrow \text{Products} \tag{R22}$$

A thorough examination of the literature was carried out to establish the quenching processes of Tab. 8.4 based [195] for the quenching of $N_2{}^*$. The products of the reactions (E3) and (E5) were taken from [31] and [124] respectively. The reaction (E4) was supposed to be reactive (*i.e.*, leading to dissociation) as regards with the high value of the $N_2(C_3)$ excitation energy. Moreover, as discussed in [157], the production of $N_2(A_3)$ by electron impact goes hand in hand with vibrational excitation of this state, legitimating the use of reaction (E2).

#	Reaction	k_f $[\mathrm{cm^3\,s^{-1}}]$	Reference
(E1)	$N_2(A^3) + CO_2 \longrightarrow N_2 + CO_2$	9.9×10^{-15}	[54]
(E2)	$N_2(A^3, v \geq 5) + CO_2 \longrightarrow N_2 + CO + O$	1.54×10^{-12}	[54]
(E3)	$N_2(B^3) + CO_2 \longrightarrow N_2 + CO + O$	2×10^{-10}	[152]
(E4)	$N_2(C^3) + CO_2 \longrightarrow N_2 + CO + O$	3.1×10^{-10}	[10]
(E5)	$N_2(a_1) + CO_2 \longrightarrow N_2 + CO + O$	2.5×10^{-11}	[151]
(E6)	$O(^1D) + CO_2 \longrightarrow O(^3P) + CO_2$	$1.74 \times 10^{-9} T_g^{-0.38} \exp(-484/RT_g)$	[189]
(E7)	$O(^1D) + CO_2 \longrightarrow O_2(a_1) + CO$	$8.64 \times 10^{-12} T_g^{0.39} \exp(221/RT_g)$	[189]
(E8)	$O(^1D) + CO_2 \longrightarrow O_2(b_1) + CO$	$1.65 \times 10^{-12} T_g^{0.22} \exp(-5653/RT_g)$	[189]

Table 8.4: Quenching reactions of N_2* and O* with CO_2

Concerning $O(^1D)$, Wang et al. [195] did not consider quenching with M=CO_2 in the global reaction (R23) but only with M=CO.

$$O(^1D) + M \longrightarrow \text{Products} \tag{R23}$$

It is not obvious from [189] that the products in reaction $CO + O(^1D) \longrightarrow$ Products must be CO_2. In Tully [189, Table I], the possible products of $O(^1D)$ quenching process are given for different quenchers. For CO, only the process $O(^1D) + CO \longrightarrow O(^3P) + CO$ was considered and is kept in our mechanisms. For $O(^1D)$ quenching by CO_2, the following channels were considered:

$$\begin{aligned} O(^1D) + CO_2 &\longrightarrow O(^3P) + CO_2 && \text{(R24)} \\ &\longrightarrow O_2(X) + CO && \text{(R25)} \\ &\longrightarrow O_2(a_1) + CO && \text{(R26)} \\ &\longrightarrow O_2(b_1) + CO && \text{(R27)} \end{aligned}$$

It was found in [189] that the process (R25) is not important compared to the other reactions. The other rates were fitted with an Arrhenius law, and corresponding coefficients can be found in Tab. 8.4.

Unfortunately, much less information was found concerning the quenching reaction of N_2* by H_2O. For example in [151] and [124], the quenching of $N_2(a_1)$ by H_2O was not measured. This is also the case for the $N_2(B_3)$ quenching by H_2O in [152]. Thus, the reaction rates of these two processes were taken from [11] in which they are estimated by similarity with the quenching by O_2. For $N_2(C_3)$, the rate coefficient of the quenching reaction was measured in [10]. The rate coefficient of the process $N_2(A_3, v) + H_2O \longrightarrow$ Products was taken from the review of Herron [78]. Finally, the quenching of $O(^1D)$ by H_2O is well described in the mechanism of [113] which serves as a baseline of our H_2O-plasma mechanism. There are still many uncertainties on these water dissociation processes, and more experimental measurements could help to better understand them. Indeed, it is not sure that H_2O-dissociation leads to the formation of OH + H as assumed in this work. Another possibility would be to consider the process $H_2O \longrightarrow H_2 + O$.

8.3 Case F: MiniPAC burner

There are only a few experimental studies in burnt gases conditions that give quantitative results on the plasma chemical effects of NRP discharges. Among them, the MiniPAC burner from the EM2C and CORIA labs [130] is used to analyze the NRP discharge effects on a premixed methane-air bluff-body stabilized turbulent flame. At an equivalence ratio of 0.8, a pilot flame is attached to the bluff-body (See Fig. 8.7a), and a significant combustion improvement is obtained when activating the plasma discharges as depicted in Fig. 8.7b. As shown in Fig 8.7, the discharges occur in a burnt gases region. Thus it constitutes a suitable case to understand better the fundamental mechanisms of NRP discharges in burnt gases. This case is then used to challenge our mechanism and provide results that could serve as a reference in the future comparisons.

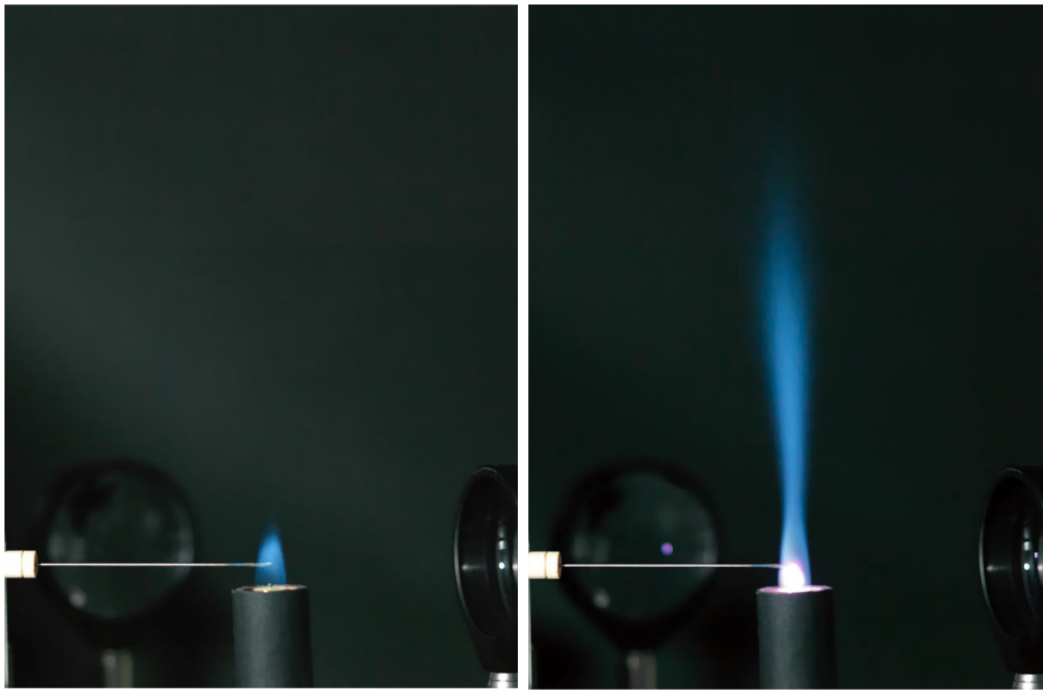

(a) Pilot flame (b) Plasma-assisted flame

Figure 8.7: Picture of the MiniPAC flame at $\phi = 0.8$: (a) without plasma discharge and (b) enhanced by NRP discharges. Reproduced from [130]

8.3.1 Experimental conditions

Most measurements in MiniPAC were done in the steady-state regime after several hundreds of pulses. However, there is no information on the mixture composition in the steady-state regime, so it is impossible to initialize a 0D reactor properly. For that reason, only the first pulse can be simulated for now. This discharge occurs in the stable pilot flame. A numerical simulation of this pilot flame was performed at EM2C using detailed chemistry and gives the mixture composition and temperature at the center of the inter-electrode gap (see Tab.8.5).

Whereas there is a little quantitative experimental data on this specific condition for now, the electrical current and applied voltage have been measured and are given in Fig. 8.8. Regarding the electrical current profile, it seems that the bump before 20 ns is not associated

T [K]	N_2	O_2	O	CH_4	H_2O	CO_2	OH	CO
1930 K	0.733	0.03	6.1×10^{-4}	0	0.137	0.089	3.1×10^{-3}	3.4×10^{-3}

Table 8.5: Local composition at the discharge location and temperature of the Case F taken from a detailed simulation of the pilot flame.

with a conduction current but rather with a displacement current. Thus, it was neglected in our 0D reactor. Moreover, a strange behavior can be observed at 45 ns with a sudden current increase. As the applied voltage reaches small values for $t \geq 45$ ns, the electrical profiles were only considered up to 45 ns and set to zero for later times.

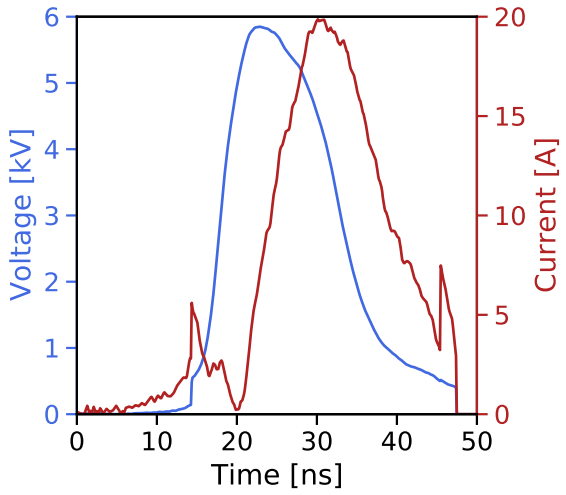

Figure 8.8: Electrical measurements on the first pulse of the MiniPAC experiment (measured by V. Blanchard at EM2C).

As for the previous 0D simulations, we need to impose the reduced electric field and the electron density during the pulse. The reduced electric field was estimated by:

$$\frac{E}{N} = \frac{U}{dN_0} \tag{8.3}$$

where U is the applied voltage, $d = 5\,\text{mm}$ is the inter-electrode gap distance and N_0 is the gas density at 1930 K and 1 atm. The electron density was computed using the current profile that is approximated by:

$$I = en_e\mu_e||\mathbf{E}||S \tag{8.4}$$

where S is the discharge section area estimated from the discharge radius measurement. This discharge radius was estimated to 500 µm using the optical emission of excited nitrogen $N_2(B_3, C_3)$ as in [167]. The electron mobility μ_e was estimated using BOLSIG+ at the conditions given in Tab. 8.5. Finally, temporal profiles of the electron density and the reduced electric field are given in Fig. 8.9a. The electron density was set to a constant value before 20 ns due to the difficulty of estimating the conduction current. This value corresponds to the one computed at 20 ns using the electrical parameters. As shown in Fig. 8.9b, this low value does not lead to an increase of the discharge energy density for $t \leq 20$ ns due to the low discharge power.

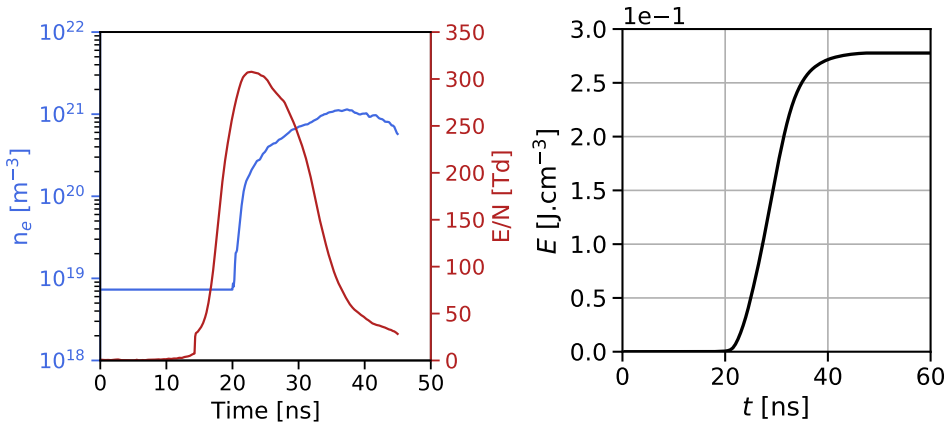

(a) (b)

Figure 8.9: Input parameters for the Case F: (a) Electron density and reduced electric field profiles and (b) discharge energy density evolution.

8.3.2 Fast gas heating

As for the case in air and CH_4-air mixtures, a fast gas heating occurs during the discharge phase [0-100] ns as depicted in Fig. 8.10. To relate this gas heating to the discharge energy, it is possible to approximate the heating energy density e^p_{heat} by:

$$e^p_{\text{heat}} \simeq \rho c_v \Delta T \tag{8.5}$$

where in our case $\rho \approx 0.18\,\text{kg}\,\text{m}^{-3}$, $c_v \approx 1150\,\text{J}\,\text{kg}^{-1}\,\text{K}^{-1}$ and $\Delta T \approx 400\,\text{K}$ leading to $e^p_{\text{heat}} \simeq 1 \times 10^{-1}\,\text{J}\,\text{cm}^{-3}$. According to Fig. 8.9b, it corresponds to $\approx 30\%$ of the discharge energy density. It is important to notice that this value is very close to the value obtained in air (See Sec. 6.9).

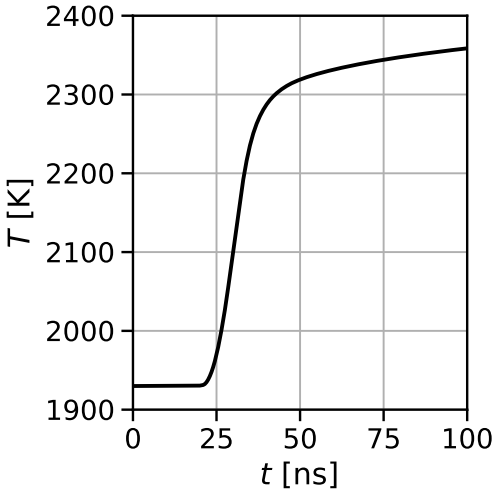

Figure 8.10: Gas temperature time evolution of the Case F during the plasma phase.

To better understand the processes responsible for fast gas heating, the heat release rate of reactions has been integrated within the interval [0, 100] ns. The most important processes releasing heat during this interval are shown in Fig. 8.11. The reactions displayed in Fig. 8.11

cumulate 83% of the gas heating and other processes only contribute individually to less than 1 % of the total heat release. The electron impact collisions are responsible for ≈ 34 % of the fast gas heating. Among them, the electronic excitation of CO_2 (R1) is the most important process for gas heating and corresponds to ≈ 13 % of the FGH. As a reminder, electronic excitation of CO_2 was replaced by a heating source term as detailed in Tab. 8.1. Thus, the reaction (R1) corresponds to a lumping of the processes (CS4.9), (CS4.10), (CS4.11) and (CS4.13) in the Table 8.1. Similarly, the gas heating in reaction (R8) corresponds to the rotational excitation of H_2O which has been replaced by heat. In addition to its chemical effect, electron impact dissociation of H_2O and CO_2 contribute respectively to 8.5 % and 2 % of the gas heating. Other electron impact processes cumulate ≈ 7 % of the gas heating. As in air, quenching of electronically excited N_2* largely contributes to the FGH with a total contribution of ≈ 42 %. Most of this energy is released during the dissociative quenching of $N_2(a_1, C_3, B_3)$ by H_2O (23 %). It is observed that $N_2(A_3)$ is efficiently quenched by atomic hydrogen in reaction (R6) to produce 6 % of the gas heating. The dissociative quenching of CO_2 by N_2* contributes to 7 % of the fast gas heating. Finally, it is important to notice that all the reactions participating in the gas heating involve electrons or excited species, except reaction (R15) and (R19) for which two species in their fundamental state react. As will be discussed in Section 8.3.4, the species involved in these two reactions are produced during the discharge, and some reactions start to consume them to produce heat.

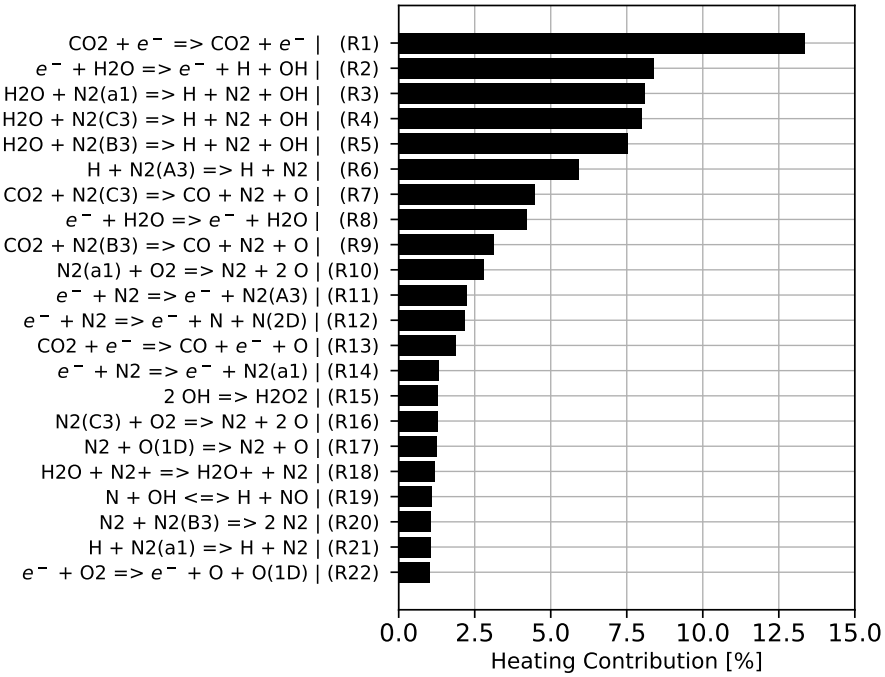

Figure 8.11: Most important reactions for gas heating during the interval [0,100] ns.

8.3.3 Slow gas heating

At the end of the discharge, the gas temperature continues to rise, as shown in Fig. 8.12. Starting from ≈ 2400 K at the end of the plasma decay, the temperature continues to rise until 100 µs to reach a temperature of 3100 K. Using Eq. 8.5, a gas temperature increase of 1200 K approximately corresponds to $2.6 \times 10^{-1}\,\mathrm{J\,cm^{-3}}$. It means that the whole discharge

energy is converted to heat on a long timescale. This energy conversion is mainly due to the combination of hydroxyl radical to form H_2O_2 as shown in Fig. 8.13. However, these results must be taken with caution as they do not include any diffusive phenomena, leading to a possible overestimated gas temperature.

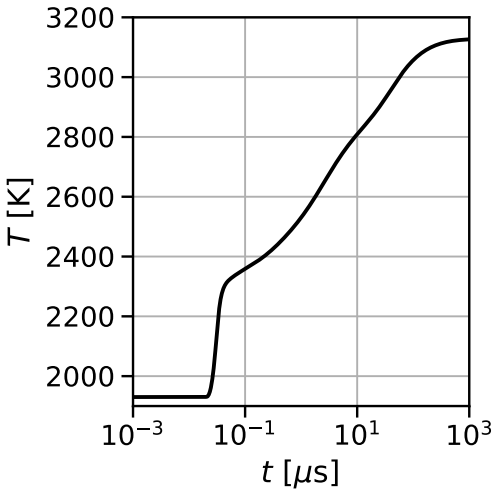

Figure 8.12: Gas temperature time evolution of the Case F during the afterglow.

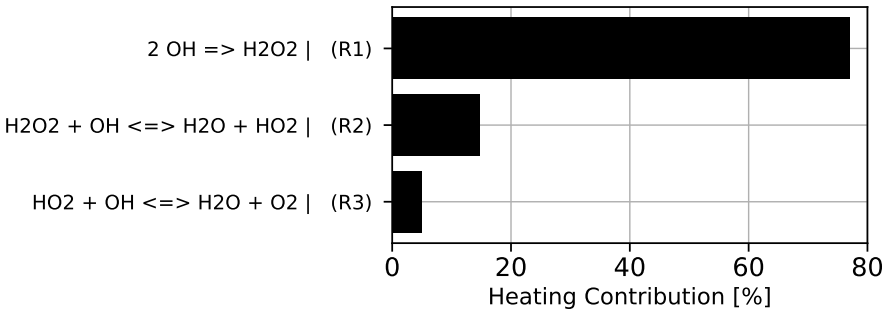

Figure 8.13: Most important reactions for the slow gas heating during the afterglow.

8.3.4 Chemical effects

The species production during the first 100 ns of the simulation has been analyzed to identify the principal chemical effects of the discharge in burnt gases. In addition to the atomic oxygen, H, OH and CO are efficiently produced by the discharge as shown in Fig. 8.14. Their sharp increase is well synchronized with the discharge energy density rise, suggesting that the species production occurs during the discharge. This is in contrast to the OH production in the case E, which was delayed from the other radical production. Indeed, OH can be produced during the electron impact dissociation of H_2O and the quenching of N_2* by H_2O. The atomic hydrogen rise goes hand in hand with the OH production as both are formed during water dissociation. Carbon oxide is almost entirely produced following the CO_2 dissociation, which also forms atomic oxygen. However, atomic oxygen production is approximately 50% higher than the CO production. This extra production of atomic oxygen must be associated with O_2 dissociation, which remains an important process even at low O_2 concentration.

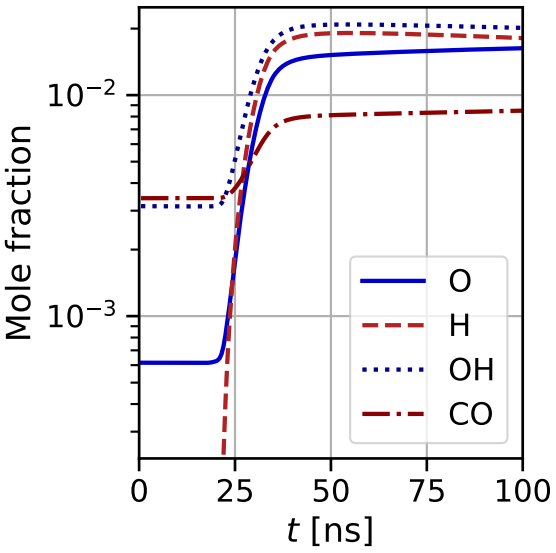

Figure 8.14: Time evolution of the main radicals during the pulse in Case F

In burnt gases, the discharge effects do not to enhance combustion locally but may impact the flame front located at some distance away. For example, the discharge of the MiniPAC experiment occurs at a distance of 5 mm from the flame front. Thus, to have an effect, the radicals and heat produced between the electrodes must be transported to the flame front either by convection or by diffusion processes. These transport processes can take several microseconds to milliseconds, depending on the conditions, during which the radicals have time to react. Figure 8.15 shows the time evolution of the main radicals up to 1 ms. Quickly after the discharge, both H and OH start to decrease while O and CO continue to rise until 500 ns and 10 µs respectively. After 500 ns, O follows the same trend than H which sharply decreases up to 20 µs before reaching a stable value at 1 ms. During the sharp decrease of O and H, OH only looses half of its value before stabilizing around $X_{\mathrm{OH}} = 10^{-2}$. On its side, carbon oxyde smoothly rises until 1 ms to reach $X_{\mathrm{CO}} = 2 \times 10^{-2}$. While the equilibrium molar fractions at 1 ms depend on the temperature, which is overestimated by our 0D model, it seems that O and H radicals react too fastly to be transported to the flame front. Thus, after a few hundreds of microseconds, the chemical effect of the discharge is reduced to an increase of the OH concentration. These conclusions must be verified on a multi-dimensional simulation, including transport phenomena.

8.3.5 Global effects

Sections 8.3.2 and 8.3.4 have evidenced the heating and chemical effects of the discharge. While the heating energy has been estimated to ≈ 32 % of the discharge energy, the chemical energy was not estimated. As for the Case A in Section 6.9.4, the discharge energy has been split into different channels as detailed in Section 6.8. According to Fig. 8.16a, approximately 93 % of the discharge energy can be retrieved a posteriori in the five considered channels. The relative contributions of these channels to the total discharge energy can be found in Fig. 8.16b. The vibrational energy fraction is almost the same as in the Case A in air. The peak value of electronic excitation is around 40%, close to the value in Case A. However, a faster decay is observed, and E_{exc} represents less than 2% of the discharge energy at 100 ns. The heating

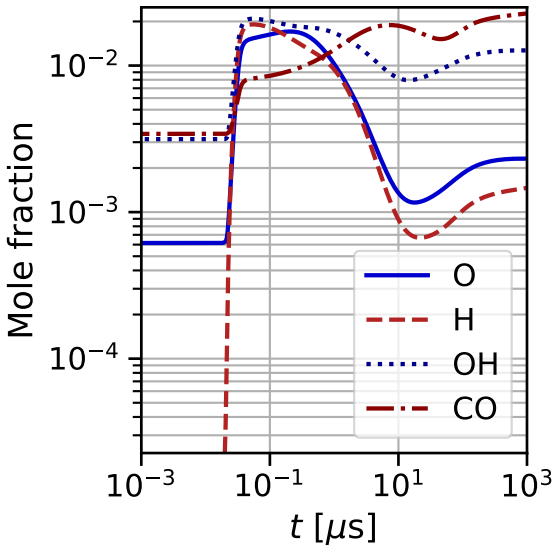

Figure 8.15: Long term evolution of the radicals produced by the discharge in Case F.

energy fraction is almost stable after 40 ns, and its increase from 40 to 100 ns is low compared to the case in air. While not producing the same species, the plasma chemical energy still represents a substantial fraction of the total discharge energy.

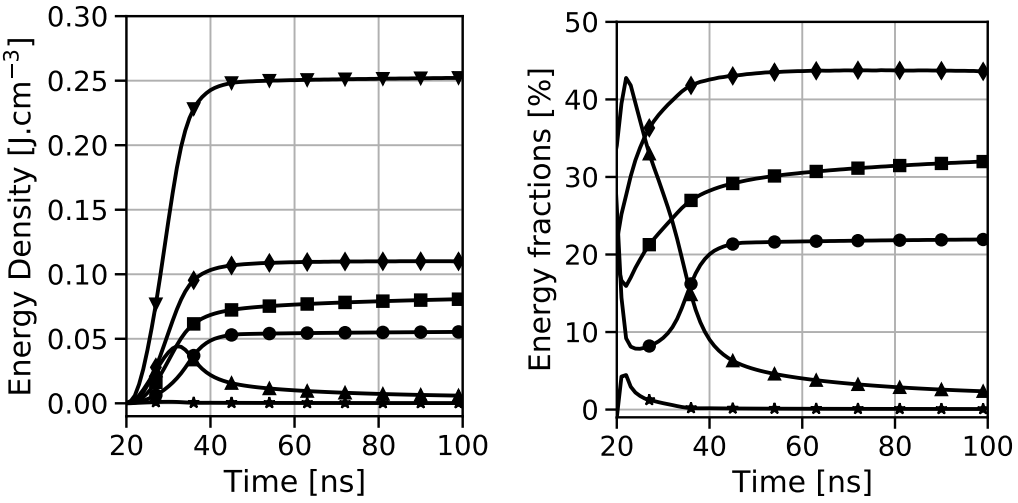

(a) (b)

Figure 8.16: Discharge energy transfer in different channels of the Case F (▲ E_{exc}, ● E_{vib}, ■ E_{heat}, ◆ E_{chem}, ★ E_{ion}, ▼ E_{p}): (a) energy density and (b) energy fractions over the total discharge energy.

Very recently, in [23], the time-resolved temperature rise during the 10th pulse of the Mini-PAC configuration has been measured. Whereas it is not the first pulse that was as simulated in Case F, the fraction of the discharge energy that serves to heat the gas may be compared. During the 10th pulse in [23], the discharge energy deposited is around 1.8 mJ, with around 75% during the main pulse. The remaining 25% are deposited in two or more reflected pulses. According to the discharge radius measurement ($r_d \simeq 0.6\,\text{mm}$), the energy density deposited

during the main pulse is around $2.3 \times 10^{-1}\,\mathrm{J\,cm^{-3}}$. Moreover, the gas temperature increases by 350 K during the first 15 ns, starting from an initial temperature around 2900 K. At this high temperature, the gas density ρ and constant volume heat capacity c_v of the burnt gas mixture are respectively $0.12\,\mathrm{kg\,m^{-3}}$ and $1200\,\mathrm{J\,K^{-1}\,kg^{-1}}$. Using Eq. 8.5, the heat energy density can be estimated to $5 \times 10^{-2}\,\mathrm{J\,cm^{-3}}$, which corresponds to 21.7% of the discharge energy. This value is coherent with our simulation in which $\approx 32\%$ of the discharge energy is converted to heat after 80 ns. Additionally, the simulated heating energy fraction is around 27% at $t = 35$ ns, corresponding to 15 ns in the experiment. Thus, these experimental data allow us to validate our mechanism's fast gas heating estimate. As the vibrational energy of $N_2(v)$ was already validated in Chapter 6 for $N_2(v)$, which is dominant vibrationally excited species in the Case F conditions, we are quite confident on the energy fraction that goes to chemical effects.

8.4 Conclusion

The above analysis highlighted the most important discharge effects on burnt gases. In the Case F, around 42 % of the discharge energy is quickly stored into chemical energy. This energy is mainly due to electron impact dissociation processes:

$$e^- + H_2O \longrightarrow e^- + OH + H \quad \text{(R28)}$$
$$e^- + CO_2 \longrightarrow e^- + CO + O \quad \text{(R29)}$$

Moreover, a significant part of the energy is stored in electronic states of N_2 during the pulse. These excited species can dissociate H_2O and CO2 in the reactions:

$$N_2(B_3, C_3, a_1) + H_2O \longrightarrow N_2 + OH + H \quad \text{(R30)}$$
$$N_2(B_3, C_3, a_1) + O_2 \longrightarrow N_2 + CO + O \quad \text{(R31)}$$

Despite its low concentration, O_2 can be efficiently dissociated by $N_2{}^*$ producing a non-negligible amount of atomic oxygen in lean conditions. Fast and intense gas heating goes hand in hand with the production of radicals and represents $\approx 32\%$ of the energy. Finally, 21 % of the energy is stored into vibrational modes of N_2 that will slowly relax to produce heat.

Some radicals produced during the discharge have a short lifetime. This is the case of O and H which quickly decay after a few microseconds. Then, a significant part of the chemical effect can be observed in the rise of OH on the microsecond to the millisecond timescales.

Chapter 9

Chemistry reduction

Contents

The detailed kinetic mechanism developed in Chapters 6 to 8 contains up to 250 species and 2500 reactions. Hence, it is too costly to include in a multi-dimensional reactive flow simulation. In this chapter, a reduction methodology is presented and applied for plasma discharge in different mixtures. The ARCANE tool [37] is used to perform this reduction with some modifications to account for plasma chemistry. These reduced schemes will be used in Part III to couple the plasma discharges to the gaseous mixture using multi-dimensional simulations.

9.1 Methodology

The reduction methodology used in ARCANE is highly inspired from the developments made in Pepiot [145]. It comprises three procedures allowing each to go deeper in the reduction when the others are limited. Only the Direct Relation Graph with Error Propagation (DRGEP) method

[146] has been used in this work, and the key ideas of the method are given Section 9.1.1. Contrary to [22], the original DRGEP method or ARCANE has been kept unchanged, and only minor plasma-specific features have been applied as detailed in Section. 9.1.2. The chemical lumping [147] and the Quasi Steady State Approximation (QSSA) [119] were not used in this work as they are not directly applicable to plasma mechanisms.

9.1.1 The DRGEP method

To reduce a detailed mechanism, a set of cases on which the reduced scheme must be accurate and a set of target quantities are selected. The cases used for the reduction must be representative of the cases in which the reduced mechanism is intended to be used. The DRGEP method allows to indentify the most important species and reactions for the targets on the cases considered. For now, only the species reduction is applied, but reaction reduction could be done quite easily. To identify the species that could be removed with minimal impact on the targets. To do so, the Direct Interaction Coefficient (DIC) $r_{\mathrm{AB}} \in [0, 1]$ between species A and any species B, is computed as:

$$r_{\mathrm{AB}} = \frac{\left|\sum_{i=1}^{n_R} \nu_{i,\mathrm{A}} \omega_i \delta_{\mathrm{B}}^i\right|}{\max\left(P_{\mathrm{A}}, C_{\mathrm{A}}\right)} \tag{9.1}$$

where $\nu_{i,\mathrm{A}}$ is the stoichiometric coefficient of species A in reaction i, ω_i is the net rate of progress of reaction i, n_R is the number of reactions in the mechanism, δ_{B}^i is the Kronecker symbol equal to one when species B is present in reaction i. P_{A} and C_{A} are the production and consumption rates of the species A given respectively by Eq. 9.2 and Eq. 9.3.

$$P_{\mathrm{A}} = \sum_{i=1}^{n_R} \max\left(0, \nu_{i,\mathrm{A}} \omega_i\right) \tag{9.2}$$

$$C_{\mathrm{A}} = \sum_{i=1}^{n_R} \max\left(0, -\nu_{i,\mathrm{A}} \omega_i\right) \tag{9.3}$$

A high value of r_{AB} indicates that species B significantly contributes to species A production or consumption. For example, $r_{AB} = 1$ if species A is only produced by reactions involving species B. On the other hand, $r_{AB} = 0$ if species A is never involved in reactiond with species B. Then, to account for chained reactions, the DIC coefficient is computed for all the chemical paths p between A and B, and the maximum is kept:

$$R_{\mathrm{AB}} = \max_p \left(\prod_{i=1}^{N-1} r_{S_i S_{i+1}} \right) \tag{9.4}$$

where $S_0 = \mathrm{A}$, $S_N = \mathrm{B}$ and $N \in [1, N_s]$ corresponds to the path length. Indirect links between species A and B are considered using Eq. 9.4 as for example A $\longrightarrow$ C $\longrightarrow$ B.

Notice that it is also possible to use the heat release rate $\dot{\omega}_T$ as a target, instead of a species, to identify species that contribute significantly to the gas temperature change. In that case, the DIC coefficient reads:

$$r_{\dot{\omega}_T B} = \frac{\left|\sum_{i=1}^{n_R} \dot{\omega}_T^j \delta_{\mathrm{B}}^i\right|}{\max\left(\dot{\omega}_T^+, \dot{\omega}_T^-\right)} \tag{9.5}$$

where $\dot{\omega}_T^j$ is the heat release rate of reaction j, $\dot{\omega}_T^+$ and $\dot{\omega}_T^-$ respectively correspond to the exothermic and endothermic heat release rate given by:

$$\dot{\omega}_T^+ = \sum_{i=1}^{n_R} \max\left(0, \dot{\omega}_T^j\right) \tag{9.6}$$

$$\dot{\omega}_T^- = \sum_{i=1}^{n_R} \max\left(0, -\dot{\omega}_T^j\right) \tag{9.7}$$

Finally, the DIC between species A and B is computed at different instants of the reduction cases, and the maximum value is kept. These values are used to sort the species from the most important to the least important. Then the species are removed starting from the one with the lowest DIC. After each removal of a species, all the reduction cases are simulated again to assess the validity of the species removal by comparison with the reference solution of the detailed mechanism. The reduced mechanism is stated valid if all the errors on predefined error quantities are below a given threshold. If it is not the case, the removed species is put back in the mechanism, and the reduction continues with the next species.

9.1.2 Specific features for the reduction of plasma chemistry

A major property to be preserved during the reduction process is the energy transferred from the discharge to the electrons and ultimately to the gas mixture. In the present model, the electron temperature is computed self-consistently with the reduced electric field, gas composition and temperature using an EEDF solver as detailed in Chapter 5. With this approach, the discharge energy transfer to the gas mixture is preserved only if all the cross-sections considered in the EEDF are associated with a reaction in the kinetic mechanism, which strongly limits the reduction. A method to relax this constraint is presented in the following.

While the set of cross-sections used to compute the EEDF is immutable, the associated reactions can be simplified. For instance, the production of an electronically excited state AB^* by electron impact reaction on a species AB can be replaced by an inert heat production process described in reaction (9.8). The underlying assumption is that the quenching of the excited state of a molecule does not change its formula but only transfers its excitation energy into a translational mode. For reaction (9.9), the chemical effect is kept when possible by quenching the excited species B^* in the products, as done previously. In a case for which species B does not exist, the reaction reduces to Eq. (9.8). Applying these rules allows to remove the excited species AB^* and B^* while keeping the total energy transfer to the gas unchanged, thus reducing the mechanism size.

$$e^- + AB \longrightarrow e^- + AB^* \longrightarrow e^- + AB + \text{heat} \tag{9.8}$$

$$e^- + AB \longrightarrow e^- + A + B^* \longrightarrow e^- + A + B + \text{heat} \tag{9.9}$$

9.2 Reduction A: air discharges

This reduction aims to obtain a mechanism for discharges in air at atmospheric pressure and elevated temperature ($\approx 1500\,\mathrm{K}$). These conditions are representative of the Case A described in Section 6.9 that will be simulated in Chapter 12.

9.2.1 Cases, targets and errors

Two cases are used for this reduction. The first one is the Case A presented in Section 6.9 which is very close to the case simulated in Chapter 12. This case allows to assess the ultra-fast gas heating and the O_2 dissociation which occur during the discharge. Naturally, the atomic oxygen and heat release are used as targets to relate the species of the mechanism to the gas heating and atomic oxygen production. At the end of each reduction step (*i.e.* the removal of one species), the errors on the final gas temperature and atomic oxygen density are computed and compared to the solution with the detailed mechanism. For both quantities, an error of 5 % has been accepted.

In the Case A simulation, the time evolution of electron density is imposed. Indeed, a 0D simulation cannot model the ionization phase for a pin-pin configuration, and at least a 1D-radial model must be used to describe the plasma growth. Consequently, electroneutrality must be imposed, and then the growth and decay of charged species are not monitored by Case A. They are crucial in multi-dimensional simulations as they control the discharge propagation [98, 137, 92]. Therefore, a simple reference case without an imposed electron density profile, referred to as Plasma Dynamics, is included to reproduce the net ionization rate and plasma decay phase.

For the Plasma Dynamics case, a 12 ns pulse with constant reduced electric field $E/N = 200$ Td is used to mimic a discharge leading to a peak electron density of $\approx 1 \times 10^{13}\,\mathrm{cm}^{-3}$. The plasma decay is simulated up to 10 µs, which is representative of a 100 kHz repetition frequency of an NRP discharge. These are typical parameters used experimentally for NRP discharges [142, 167, 108] The initial composition is a N_2:O_2:79:21 mixture (in mole) at 1000 K and atmospheric pressure. These conditions are representative of the first pulse in the experiment of [167].

The time evolution of electron and ion densities obtained with the GRI-3.0 plasma mechanism developed in Chapter 7 is shown in Fig. 9.1. An increase of charged species density is observed during the first 12 ns followed by a plasma decay phase. Electron density is considered as the target for DRGEP coefficients and the error on the maximum value of electron density $n_e^{\max}$ and its final value n_e^{end} is systematically checked after the removal of a species.

A summary of the cases, targets and errors quantities for the reduction A can be found in Tab. 9.1.

Cases	Targets	Errors
Case A [167]	O, $\dot{\omega}_T$	T_g^{end} (5%), $n_{\mathrm{O}}^{\mathrm{end}}$ (5%)
Plasma Dynamics	e^-	$n_e^{\max}$ (5%), n_e^{end} (25%)

Table 9.1: Summary of targets and errors used for the reduction A.

9.2.2 Reduced mechanism A

The reduced mechanism contains 26 species detailed in Tab. 9.2 and 312 reactions. It is composed of five species in their ground states responsible for the chemical effect of the discharge. There are 11 excited species in the mechanism, which reflect the discharge potential to excite the molecules. Despite their short lifetime, the description of the excited molecules is crucial to properly model the fast gas heating and chemical effects produced by the discharge. A total of 8 ions remain in the reduced chemistry. Most of the positive ions are necessary to describe the

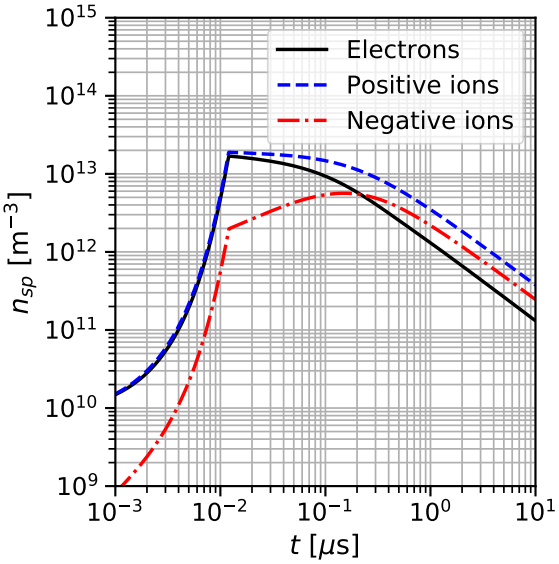

Figure 9.1: Time evolution of electron and ion density for the Plasma Dynamics case used in the reduction A, using the detailed mechanism.

plasma growth during the pulse, as shown in Fig. 9.2. However, N_4^+ only plays the role of an intermediate ion: it rises at the end of the pulse before a very sharp decay to reach negligible density after $\approx$ 100 ns. While not being produced during the pulse, a substantial part of the positive charges is stored into NO^+ at the end of the pulse. Finally, three negative ions are necessary to model the plasma decay properly. Among them, O_2^- is the most important species and represents $\approx$ 90% of the negative ions at $t = 10$ µs.

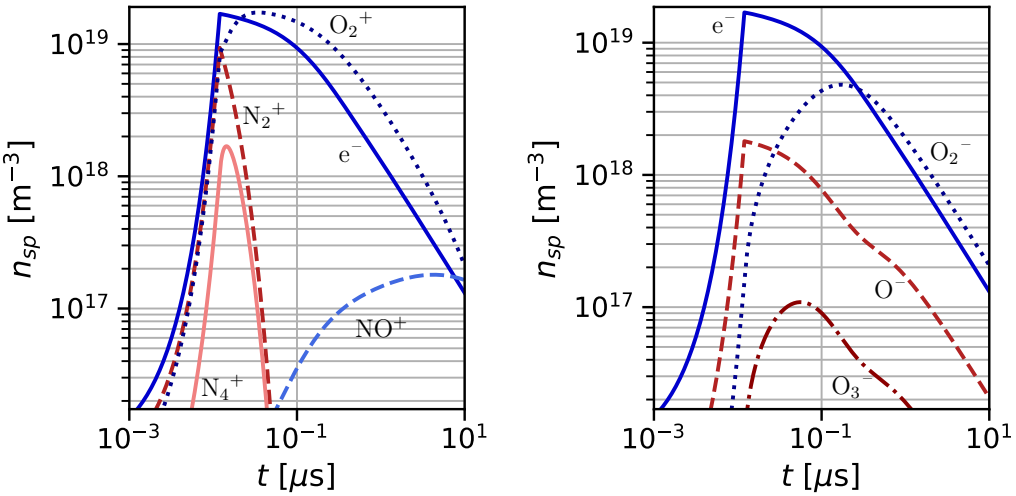

(a) (b)

Figure 9.2: Dynamics of (a) the positive and (b) negative ions in the Plasma Dynamics case of the reduction A, obtained with the reduced chemitry.

Ground states
O, O_2, N_2, N, NO, O_3
Charged species
N_2^+, O_2^+, O^+, NO^+, N_4^+, e^-, O^-, O_2^-, O_3^-
Excited species
$N_2(A_3)$, $N_2(B_3)$, $N_2(C_3)$, $N_2(a_1)$, $O_2(a_1)$, $O_2(b_1)$, $O_2(A_3)$ $O(^1D)$, $O(^1S)$, $N(^2D)$, $N(^2P)$

Table 9.2: Summary of species in the reduced mechanism of the reduction A.

9.3 Reduction B: plasma-assisted ignition

9.3.1 Cases, targets and errors

This reduction aims to be used in a multi-dimensional plasma-assisted ignition simulation. Therefore, the test cases on which the reduction process is based must represent the various phenomena occurring in this type of simulation. The chosen set of reduction cases is detailed in the following, and a summary can be found in Tab. 9.3.

Plasma cases are selected to validate the reduced mechanism fast gas heating and radical production. The discharge described in [167] (Case A) highlights these two effects in air while Case D of [191] allows to validate radical production in a CH_4 containing mixture. In both cases, the atomic oxygen concentration is targeted, and the final atomic oxygen density error is checked. Due to the important gas heating, the heat release rate is also targeted in [167] and the error on the final gas temperature is also assessed.

Canonical combustion cases and targets (CO, $\dot{\omega}_T$) are chosen following [37]: a 0D isochoric reactor with an initial temperature of 1000 K and a 1D flame with a fresh gas temperature of 300 K. Both combustion cases are performed for stoichiometric CH_4-air mixtures at atmospheric pressure. The error on auto-ignition delay time τ_{ig} is checked on the 0D case while the laminar flame speed S_L and maximum temperature $T_g^{\max}$ are assessed on the 1D flame case.

Finally, the plasma-combustion coupling is assessed on a single pulse plasma-assisted ignition (Case E) taken from Starikovskaia et al. [178], Aleksandrov et al. [11]. For this 0D plasma-assisted ignition case, the targets are: O, CO and $\dot{\omega}_T$. The error on the ignition delay time τ_{ig} is used to validate the reduced mechanism.

In all the plasma cases used for this reduction (Cases A, D and E), the time evolution of the electron density is imposed. Consequently, electroneutrality must be imposed and then the growth and decay of charged species are not monitored by the plasma cases. As for the reduction in Air (See Section 9.2), a simple reference test case without an imposed electron density profile is included in reduction B (Plasma Dynamics case). The discharge parameters of this case are the same for reduction in Air: a 12 ns pulse with constant reduced electric field $E/N = 200$ Td followed by a 10 µs plasma decay. The initial mixture is a stoichiometric methane-air mixture at 1000 K and atmospheric pressure. The targets and errors are the same as for the Plasma Dynamics case in air.

9.3.2 Reduced mechanism B

The reduction was performed starting from the GRI 3.0 mechanism updated with our plasma mechanism using the simplified vibrational model VIB. 2 (See Section 6.5), resulting in a

Cases	Targets	Errors
Case A [167]	O, $\dot{\omega}_T$	T_g^{end} (10%), $n_{\text{O}}^{\text{end}}$ (10%)
Case D [191]	O	$n_{\text{O}}^{\text{end}}$ (10%)
Case E [11]	O, CO, $\dot{\omega}_T$	τ_{ig}(10%)
Plasma Dynamics	e^-	$n_e^{\max}$ (5%), n_e^{end} (25%)
Auto-ignition	CO, $\dot{\omega}_T$	τ_{ig}(5%)
1D flame	CO, $\dot{\omega}_T$	s_L(5%), $T_g^{\max}$(1%)

Table 9.3: Summary of targets and errors used for the reduction B.

detailed mechanism composed of 100 species and 950 reactions. The reduction performed with ARCANE led to a mechanism made of 47 species and 429 reactions. Species included in the reduced mechanism are listed in Tab. 9.4: 28 species come from the GRI 3.0 mechanism while 19 species are kept from the plasma mechanism. The number of ions are the same as in the reduction A from which N_4^+, O^+ and O_3^- have been replaced by CH_4^+, CH_3^+ and Ar^+. In spite of the higher number of cases considered in this reduction compared to reduction A, the reduced mechanism only contains 9 excited species. This must be explained by the higher tolerance in Case A and the fact that the other cases consider error quantities at a time much longer than the excited species lifetime. Indeed, the electronically excited species have time to relax their energy when looking at quantities at $t \gg 1$ µs. In that case, the simplifications discussed in Sec. 9.1.2 are valid and can be applied to some excited species. In particular, $N(^2P)$, $O_2(b_1)$ and $O_2(A_3)$ have been treated this way.

Ground states
$O, O_2, H, OH, H_2, HO_2, H_2O_2, CH, CO, CH_2, HCO, CH_2(S)$ $CH_3, CH_2O, CH_4, CO_2, CH_3O, CH_3OH, C_2H_4, C_2H_5, C_2H_6$ $H_2O, N_2, Ar, N, NO, NO_2, H_2CN, O_3$
Charged species
$e^-, N_2^+, O_2^+, CH_4^+, CH_3^+, Ar^+, NO^+, O^-, O_2^-$
Excited species
$N_2(A_3), N_2(B_3), N_2(a_1), N_2(C_3), N(^2D), O_2(a_1), O(^1D), O(^1S), Ar^*$

Table 9.4: Summary of species in the reduced mechanism of the reduction B starting from the GRI 3.0-plasma mechanism.

The same reduction was also performed starting with the detailed Konnov-plasma mechanism, containing 264 species and 2860 reactions. The mechanism size has been reduced by a factor of five, leading to a reduced mechanism containing 49 species shown in Tab. 9.5 and 498 reactions. The charged and excited species are almost identical to the GRI-plasma reduction in which $O_2(b_1)$ has been discarded. Whereas other species replace some grounded species, only one additional species is necessary to reduce the Konnov-plasma mechanism.

Another reduction considering only 0D auto-ignition and 1D flame cases (i.e. without plasma cases) was also performed for comparison. In that case, five other species of the GRI 3.0 mechanism (CH, CH_3OH, N, NO_2 and H_2CN) are removed. This highlights the importance of new chemical paths in plasma-assisted combustion and validates the reduction strategy including both plasma and combustion chemistries.

The reduction procedure adopted here keeps the effective electron temperature almost unchanged, as shown in Fig. 9.3a, contrary to what has been observed in [22]. This is a consequence

Ground states
$O, O_2, H, OH, H_2, HO_2, H_2O_2, CO, CH_2, HCO, SCH_2$ $CH_3, CH_2O, CH_4, CO_2, CH_3O, CH_3OH, C_2H_4, C_2H_5, C_2H_6$ $H_2O, N_2, Ar, N, NO, NO_2, C_2H_2, CH_3O_2, IC_4H_3, O_3$
Charged species
$e^-, N_2^+, O_2^+, CH_4^+, CH_3^+, Ar^+, NO^+, O^-, O_2^-$
Excited species
$N_2(A_3), N_2(B_3), N_2(a_1), N_2(C_3), N(^2D), O_2(a_1), O_2(b_1), O(^1D), O(^1S), Ar^*$

Table 9.5: Summary of species in the reduced mechanism of the reduction B starting from the Konnov-plasma mechanism.

of the use of an EEDF solver within the plasma reactors in our simulations. As pointed out previously, it must be verified that the energy transferred from electrons to heavy molecules is preserved during the reduction. In Figure 9.3b, the total energy has been split into chemical, heating, vibrational and excitation channels detailed in Sec. 6.8 to precisely identify the potential changes caused by the reduction. While chemical and vibrational energies remain unchanged, the heating energy slightly increases to compensate for a decrease in the excitation energy. This is a consequence of the procedure described by reactions (9.8) and (9.9). Finally, the total energy transferred from the electrons to the gas in the Case A [167] is well reproduced by the reduced mechanism with a final error lower than 0.2%.

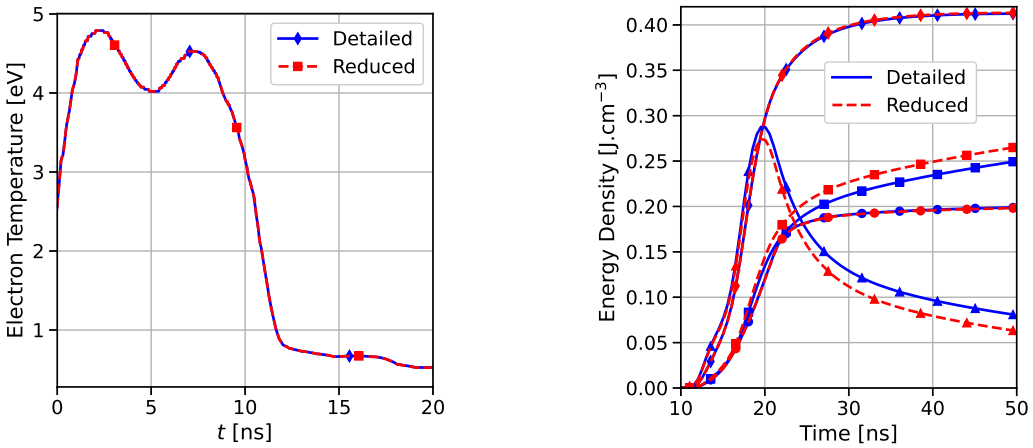

(a) (b)

Figure 9.3: Comparison of the detailed and reduced mechanisms on (a) the effective temperature of the electrons (Case A) and (b) the discharge energy transfer in different channels (Case A) (▲ Electronic, ● Vibration, ■ Heat, ◆ Chemical).

A comparison of the reduced and detailed mechanisms on the combustion features is shown in Fig. 9.4. The error on the auto-ignition delay time remains lower than 5% on a large range of temperature [800-2000] K and equivalence ratio [0.5-1.5] as shown in Fig. 9.4a. Despite the use of stoichiometric conditions in the auto-ignition test cases during the reduction, an excellent agreement is found for lean and rich mixtures. Satisfying results are also obtained for the laminar flame speed in a wide range of equivalence ratios [0.6-1.4] as demonstrated in Fig. 9.4b.

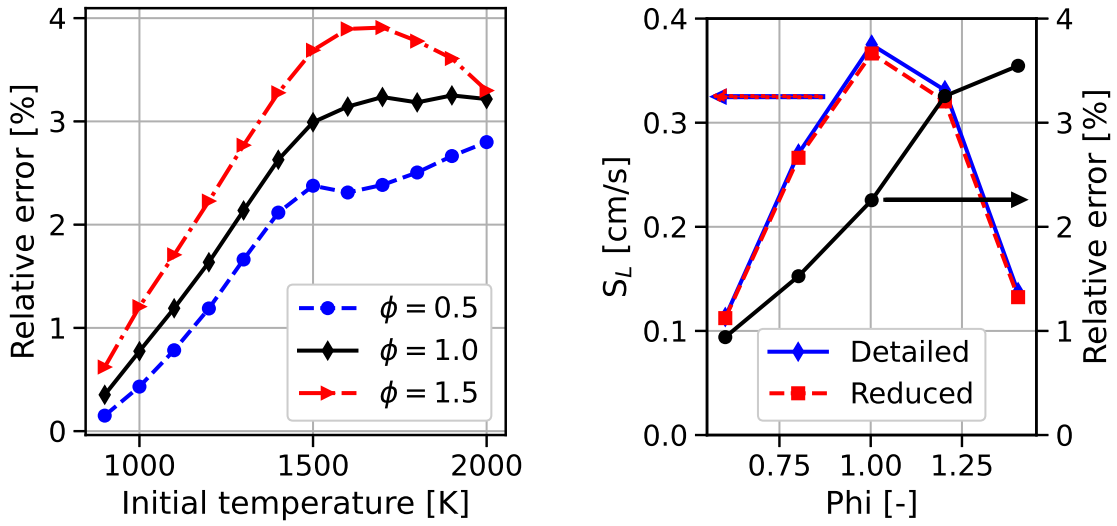

(a) Auto-ignition

(b) 1D Flame

Figure 9.4: Comparison of detailed and reduced mechanisms: (a) auto-ignition time (relative error) and (b) laminar flame speed (value and relative error).

9.3.3 Application of the reduced mechanism to Plasma-Assisted Ignition cases

The reduced mechanism has been evaluated outside of the reduction conditions. An energy density of $8 \times 10^6\,\mathrm{J\,m^{-3}}$ is deposited in a single pulse at a constant reduced electric field between 150 and 300 Td to ignite a mixture initially at $T_g = 300\,\mathrm{K}$, $P = 1$ atm and equivalence ratio $\phi = 1$. Simulations have been performed in a CH_4-air mixture with 80% argon dilution. The argon diluted case differs significantly from the Case E by its lower temperature and higher equivalence ratio. The CH_4-air case operates in a mixture that was not ignited in the reduction cases and is used here to highlight the effects of argon dilution. The ignition delay times for detailed and reduced mechanisms, along with relative errors, are depicted in Fig. 9.5. In the argon diluted case shown in Fig. 9.5a, the error on the ignition delay time remains lower than 10% for a large range of reduced electric field. This error is particularly low from 150 to 200 Td where most of the reduction cases operate. For a higher reduced electric field, it is observed that the ignition delay time increases. This can be explained by the change in dominant electron-impact reactions from electronic excitation to ionization. While electronically excited species can efficiently produce radicals, ionized species mostly recombine, resulting in gas heating. The formation of active radicals is more efficient to ignite a mixture than heat deposition leading to shorter ignition delay times. The reduced mechanism is less accurate in the CH_4-air mixture as depicted in Fig. 9.5b, highlighting the noticeable importance of argon dilution on plasma-assisted ignition behavior. Indeed, when argon is the dominant mixture component, most of the electron energy is transferred to Ar^*, Ar^+ which then transfer their energy to the other molecules. However, in CH_4-air mixture, electron energy transfer is more complex as a wide variety of processes exist (i.e. vibrational excitation and different electronic states of N_2). In Fig. 9.5b, the minimum ignition delay time is around 200 Td, which corresponds to the case where electronic excitation and electron impact dissociation are at their maximums, as it was shown in Fig. 6.1. The slower ignition observed around 150 Td and 300 Td, respectively due

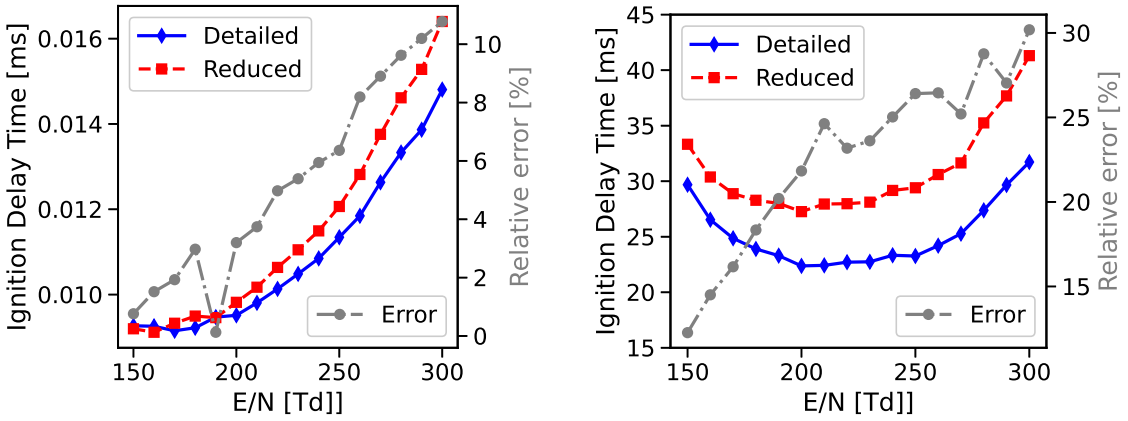

(a) Ar:N_2:O_2:CH_4-80:14.3:3.8:0.19 (b) N_2:O_2:CH_4-71.5:19:9.5

Figure 9.5: Comparison of detailed and GRI-Plasma reduced mechanisms on plasma-assisted ignition delay times at various reduced electric fields for (a) argon dilluted mixture and (b) CH_4-air mixture.

to an increase of vibrational and ionization energies, illustrates the efficiency of the electronic excitation and electron impact dissociation.

9.4 Reduction C: Reduced mechanism for NRP discharges in burnt gases

9.4.1 Reduction cases

More simplified cases are now considered for reduction C to identify the species which must be kept for discharges in burnt gases. To preserve the plasma-combustion intereaction of the mechanism, a plasma-assisted ignition case (PAI) is considered. A lean CH_4-air mixture ($\phi = 0.8$) at T=300 K and P=1 atm is ignited using a single plasma discharge in which a high reduced electric field of 200 Td is imposed within [0-4.5] ns. This pulse deposits an energy density of $\approx 1\,\mathrm{J\,cm^{-3}}$ which ignites the mixture after $\approx 2\,\mathrm{ms}$ as shown in Fig. 9.6a. The DRGEP targets are O, CO and $\dot{\omega}_T$ and the ignition delay time τ_{ig} is used for the error.

Then a discharge in burnt gases using the initial conditions of Case F (CH_4-air, $\phi = 0.8$, 1930 K) is used to assess the validity of the reduced mechanism in burnt gases conditions. A 20 ns-long pulse at constant E/N=200 Td allows to deposit an energy density of $0.19\,\mathrm{J\,cm^{-3}}$. Then the discharge afterglow is simulated up to 100 ns. The DRGEP targets are O and $\dot{\omega}_T$ while maximum values of O, OH, H and T_g are used for the errors. These four last quantites are shown in Figs. 9.6b and 9.6c.

Finally, two Plasma Dynamics cases (See Section 9.2.1) are considered to assess both plasma growth and decay. Two initial conditions were considered for this reduction: a lean methane-air mixture (FG case) and burnt gases conditions (BG case).

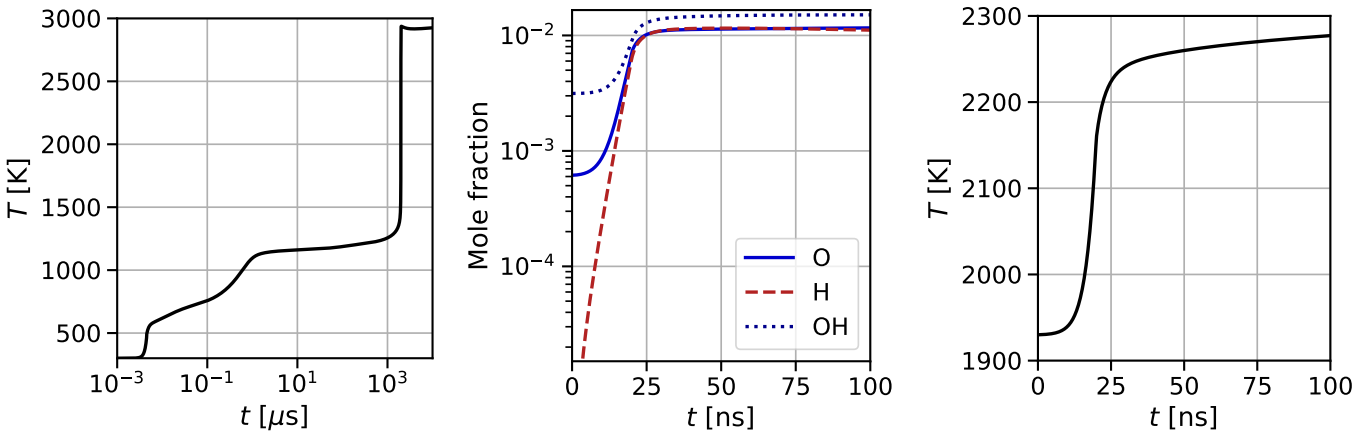

(a) PAI (b) Burnt gases species (c) Burnt gases temperature

Figure 9.6: Main features of the reduction cases used in Reduction C: (a) Gas temperature of the plasma-assisted ignition case, (b) main species in the burnt gases case and (c) gas temperature in the burnt gases case.

Cases	Targets	Errors
Plasma-Assisted Ignition (PAI)	O, $\dot{\omega}_T$	$\tau_{\text{ig}}(5\%)$
Burnt Gases (BG)	O, $\dot{\omega}_T$	$n_{\text{O}}^{\text{max}}$ (10%), $n_{\text{O}}^{\text{max}}$ (10%), $n_{\text{O}}^{\text{max}}$ (10%)
Plasma Dynamics FG	e^-	n_e^{max} (5%), n_e^{end} (25%)
Plasma Dynamics BG	e^-	n_e^{max} (5%), n_e^{end} (25%)

Table 9.6: Summary of targets and errors used for the reduction C.

9.4.2 Reduced mechanism and discussion

The reduced mechanism is composed of 53 species given in Tab. 9.7 and 573 reactions. Most of the ground state species are identical to the reduction B. Three ground states species are missing in Reduction C compared to Reduction B: CH_2, CH_3OH and O_3. On the other hand, CH_2CHO is kept in the reduced mechanism C. The ozone removal in reduction C is due to the lack of cases targeting the long-term behavior of the atomic oxygen. However, it might be possible that ozone is not important in the conditions considered in this reduction. The nine excited species are very similar to those in the reductions A and B. Thus, the excited states required in fresh and burnt gases are almost the same, and they do not increase the size of the reduced mechanism. However, the number of charged species (17 species) is surprisingly high in the reduction C. Some complicated paths between ions seem to operate and must be studied in more detail.

9.5 Conclusion and perpectives

In this chapter, an automatic procedure to reduce plasma chemical mechanisms with an accuracy control has been used successfully employed. It allow to reduce a detailed chemical mechanism on conditions for which it is intended to be used. Three reductions have were performed for typical conditions encountered in the Chapters 6, 7 and 8. However, new reduced mechanisms could be easily generated on other conditions if necessary for a specific purpose.

Ground states
$O, O_2, OH, H, H_2, HO_2, H_2O_2, CH, CO, HCO, CH_2(S), CH_3, CH_2O$ $CH_4, CO_2, CH_3O, C_2H_3, C_2H_4, C_2H_5, C_2H_6, H_2O, N_2, N, NO, NO_2$ H_2CN, CH_2CHO
Charged species
$e^-, {N_2}^+, {O_2}^+, O^+, N^+, {CH_4}^+, {N_4}^+, {O_4}^+, H^+, {H_2O}^+, {CO_2}^+, {H_3O}^+, {CH_5}^+$ $O-, {O_2}-, OH-, H^-$
Excited species
$N_2(A_3), N_2(B_3), N_2(a_1), N_2(C_3), N(2\,D), N(2\,P), O_2(a_1), O(1\,D), H(n=2)$

Table 9.7: Summary of species in the reduced mechanism of the reduction C starting from the GRI 3.0-plasma mechanism.

Another route would be to reduce the number of ions. In the reduction performed in this chapter, it was difficult to reduce this number and at least eight ions were necessary. In particular, 17 charged species were kept in the reduction C, representing one-third of the species in the reduced mechanism. Some of these ions, such as ${N_4}^+$ in the reduction A, do not have noticeable effects on the gas mixture and disappear at the end of the afterglow. Lumping algorithms could help to remove these ions. Moreover, the idea of a global coefficient for ionization, recombination and attachment processes could help to reduce even more the number of the ions until the ultimate goal of one positive and one negative ions as in the chemistry of Morrow and Lowke [136].

Chapter 10

Phenomenological model

Contents

The chemical mechanism reduction discussed in the previous chapter is a precious tool to perform detailed simulations of the plasma-combustion coupling. However, its use in multi-dimensional simulations (either 2D or 3D) still relies on the full computation of the plasma phase, which involves transporting the charged species, solving the Poisson equation, and respecting the plasma time-steps. While these simulations are fundamental to go deeper into the understanding of plasma-assisted combustion, industrial applications require reduced models, which can give results for an acceptable CPU cost. Indeed, it is already very challenging to perform these industrial simulations even for conventional reactive flow without plasma. Thus, a simplified plasma model must be used as a valuable preliminary stage before going into detailed models. In this chapter, a phenomenological model is proposed based on the model developed in [34]. The baseline model of [34] is first presented in Section 10.1. Then, the model is improved in Section 10.2 thanks to the knowledges gained in Chapters 6, 7 and 8.

10.1 The model of Castela

10.1.1 Governing equations

In place of a detailed description of the plasma discharge, which would lead to a high CPU cost, a phenomenological model has been proposed by Castela et al. [34]. In this model, the impact of the discharge on the mixture is decomposed into three effects which are namely the fast gas heating ($\dot{E}^p_{\text{heat}}$), the chemical effect ($\dot{E}^p_{\text{chem}}$) and a slow gas heating due to the relaxation of the vibrationally excited N_2 ($\dot{E}^p_{\text{vib}}$). The discharge power is decomposed into three contributions:

$$\dot{E}^p = \dot{E}^p_{\text{chem}} + \dot{E}^p_{\text{heat}} + \dot{E}^p_{\text{vib}} \tag{10.1}$$

The Navier-Stokes equations with additional plasma source terms then yield:

$$\frac{\partial \rho}{\partial t} + \frac{\partial (\rho u_i)}{\partial x_i} = 0 \tag{10.2}$$

$$\frac{\partial (\rho u_j)}{\partial t} + \frac{\partial (\rho u_i u_j)}{\partial x_i} = -\frac{\partial p}{\partial x_j} + \frac{\partial \tau_{ij}}{\partial x_i} \tag{10.3}$$

$$\frac{\partial (\rho e)}{\partial t} + \frac{\partial (\rho u_i e)}{\partial x_i} = -\frac{\partial q_i}{\partial x_i} + \frac{\partial (\sigma_{ij} u_i)}{\partial x_i} + \dot{E}^p_{\text{chem}} + \dot{E}^p_{\text{heat}} + \dot{R}^p_{VT} \tag{10.4}$$

$$\frac{\partial (\rho Y_k)}{\partial t} + \frac{\partial (\rho u_i Y_k)}{\partial x_i} = -\frac{\partial (\rho V_{k,i} Y_k)}{\partial x_i} + W_k \dot{\omega}^c_k + W_k \dot{\omega}^p_k \tag{10.5}$$

where $\dot{\omega}^p_k$ corresponds to the molar production rate from the plasma discharge, $\dot{\omega}^c_k$ the molar production rate from a conventional combustion mechanism, $\dot{R}^p_{VT}$ corresponds to the vibrational-translational relaxation of N_2, τ_{ij} is the stress tensor, $\sigma_{ij} = \tau_{ij} - p\delta_{ij}$, $V_{k,i}$ is the diffusion velocity of species k in the mixture and e is the total energy density per mass unit (kinetic + sensible + chemical). As the typical timescale of vibrational-translational relaxation is much higher than the discharge duration, it is necessary to store it into a vibrational energy density e_{vib} which can be transported and relaxed according to:

$$\frac{\partial (\rho e_{\text{vib}})}{\partial t} + \frac{\partial (\rho u_i e_{\text{vib}})}{\partial x_i} = \frac{\partial}{\partial x_i}\left(\rho \mathcal{D}_{N_2} \frac{\partial e_{\text{vib}}}{\partial x_i}\right) + \dot{E}^p_{\text{vib}} - \dot{R}^p_{VT} \tag{10.6}$$

where $\mathcal{D}_{N_2}$ is the diffusion coefficient of N_2 into the mixture, $\dot{E}^p_{\text{vib}}$ is the vibrational energy production term computed from plasma chemistry and $\dot{R}^p_{VT}$ is the vibrational to translational relaxation modeled using the Landau-Teller harmonic oscillator approach as expressed in Eq. 10.7. Relaxation times τ^k_{VT} are computed using experimental coefficients from [129] for N_2, O_2, O. The exchange term between the vibrational energy equation and mixture energy equation then reads:

$$\dot{R}^p_{VT} = \rho \frac{e_{\text{vib}} - e^{\text{eq}}_{\text{vib}}(T)}{\tau_{VT}} \ , \ \tau_{VT} = \left(\sum_k \frac{1}{\tau^k_{VT}}\right)^{-1} \tag{10.7}$$

where

$$e^{\text{eq}}_{\text{vib}}(T) = \frac{r\Theta_1}{e^{\Theta_1/T} - 1} \tag{10.8}$$

is the equilibrium energy of vibrational population of N_2 assuming a harmonic oscillator model with the characteristic vibrational temperature $\Theta_1 = 3386$ K and $r = R/W_{N_2}$.

10.1.2 Model closure

In order to close the model it is necessary to determine the fraction of discharge energy going into $\dot{E}^p_{\text{chem}}$, $\dot{E}^p_{\text{heat}}$ and $\dot{E}^p_{\text{vib}}$. This repartition depends on different parameters such as the gas temperature, the pressure and the mixture composition (T, P, X_i). Other parameters such as the pulse shape or the geometry of the electrodes can also play a role. By only considering the parameters (T, P, X_i), the fraction of the discharge energy going into $\dot{E}^p_{\text{chem}}$ and $\dot{E}^p_{\text{heat}}$ can be written as follows:

$$\dot{E}^p_{\text{heat}} = g_{\text{heat}}\Big(X_{k=1,\dots,N_{sp}}, T, P\Big)\,\dot{E}^p \tag{10.9}$$

$$\dot{E}^p_{\text{chem}} = g_{\text{chem}}\Big(X_{k=1,\dots,N_{sp}}, T, P\Big)\,\dot{E}^p \tag{10.10}$$

where g_{heat} and g_{chem} are the fractions of the discharge energy transferred into sensible and chemical energy, respectively. The chemical energy source term should compensate for the change in sensible energy due to the production of neutral species from the plasma discharge:

$$\dot{E}^p_{\text{chem}} = \sum_k e_k W_k \dot{w}^p_k \tag{10.11}$$

A fraction of the discharge power can be associated with each species following:

$$e_k W_k \dot{w}^p_k = g^k_{\text{chem}} \dot{E}^p \tag{10.12}$$

and consequently:

$$g_{\text{chem}} = \sum_k g^k_{\text{chem}}. \tag{10.13}$$

The production rate of the k^{th} species during the pulse is given by :

$$\dot{w}^p_k = g^k_{\text{chem}} \frac{\dot{E}^p}{e_k W_k} \tag{10.14}$$

Finally the model states that the rest of the energy, that is not transferred into $\dot{E}^p_{\text{chem}}$ and $\dot{E}^p_{\text{heat}}$, goes into vibration:

$$\dot{E}^p_{\text{vib}} = [1 - (g_{\text{heat}} + g_{\text{chem}})]\dot{E}^p \tag{10.15}$$

It is supposed that fast gas heating and chemical effect are mainly due to the dissociation of O_2 in electron impact reaction of quenching of electronically excited N_2. Following the experiments from [167] and simulations made by [158] about 35 ± 5 % of the discharge energy goes into O_2 dissociation and 20 ± 5 % into ultra fast gas heating. These values are valid in the condition of [167] in which the discharges are applied in a partially dissociated air (N_2:O_2:O:77.4:18.6:4 in mole) and heated at 1500 K. According to the model, the remaining discharge energy is stored in vibrational modes of nitrogen molecules. It represents approximately 45 % of the discharge energy. It is assumed that the chemical source term is only due to the dissociation of O_2 and scaled with $Y_{O_2}/Y^f_{O_2}$ where $Y^f_{O_2}$ is the oxygen molecule mass fraction in the fresh gas. This scaling has been introduced to handle discharges occurring in regions where the oxygen molecules have been (partially) consumed (for example in burnt gas). The fraction of energy η going to O_2 dissociation is taken equal to 35% following the results in [167]. $\dot{E}^p_{\text{chem}}$ writes finally:

$$\dot{E}^p_{\text{chem}} = \eta \frac{Y_{O2}}{Y^f_{O2}} \left(1 - \frac{e_{O_2}}{e_O}\right) \dot{E}^p \tag{10.16}$$

To retrieve the energy available for ultra-fast gas heating, another assumption is made: the sum of $\dot{E}^p_{\text{heat}}$ and $\dot{E}^p_{\text{chem}}$ is equal to the energy fraction $\alpha \simeq 0.55$ which is transferred to the electronic states of N_2. As a consequence, the chemical energy decrease due to the Y_{O_2} scaling is replaced by heat, so that case we have:

$$\dot{E}^p_{\text{heat}} + \dot{E}^p_{\text{chem}} = \alpha \dot{E}^p \tag{10.17}$$

As mentioned previously, the vibrational energy is assumed to be the remaining energy and the three energy channels finally read:

$$\dot{E}^p_{\text{chem}} = \eta \frac{Y_{O2}}{Y^f_{O2}} \left(1 - \frac{e_{O_2}}{e_O}\right) \dot{E}^p \tag{10.18}$$

$$\dot{E}^p_{\text{heat}} = \left[\alpha - \eta \frac{Y_{O2}}{Y^f_{O2}} \left(1 - \frac{e_{O_2}}{e_O}\right)\right] \dot{E}^p \tag{10.19}$$

$$\dot{E}^p_{\text{vib}} = (1 - \alpha) \dot{E}^p \tag{10.20}$$

10.1.3 Model parameters

Two parameters have been introduced in 10.1.2: the coefficient η which gives the maximum fraction of energy that can be transferred into oxygen dissociation, and the coefficient α, which corresponds to the sum of chemical effect and the fast gas heating. As a reminder these two parameters are taken constant with $\eta = 0.35$ and $\alpha = 0.55$ in Castela et al. [34]. These values were determined experimentally by Rusterholtz et al. [167] and numerically by Popov [158]. They rely on the results in Fig. 10.1 reproduced here for convenience.

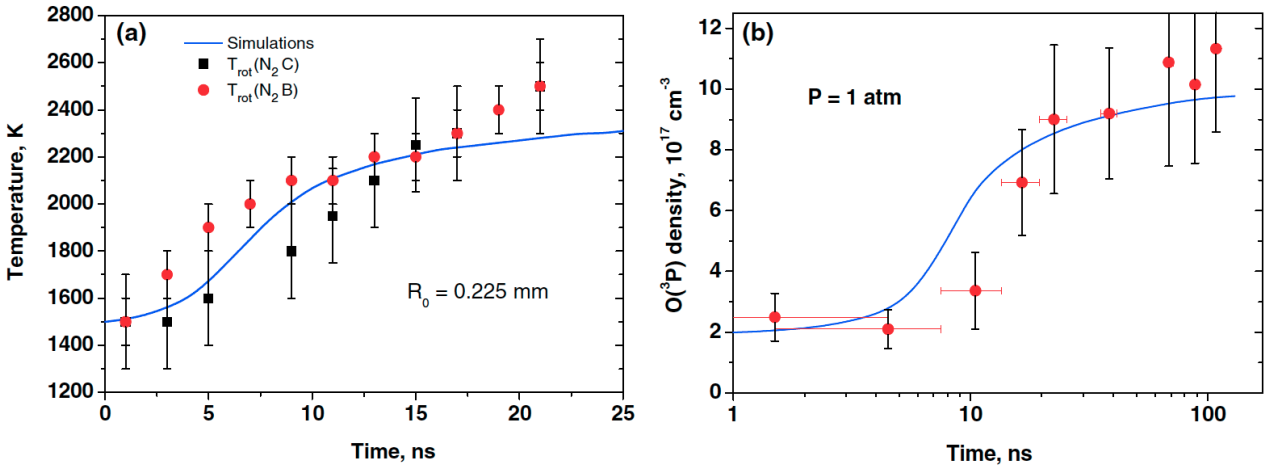

Figure 10.1: Temporal evolution of (a) the temperature and (b) the ground state atomic oxygen density reproduced from [167]. Markers correspond to the experiment of [167] and solid lines correspond to the simulation in [158].

10.1.3.1 Chemical effect

Experimentally the increase of atomic oxygen density was found to be $9 \times 10^{17}\,\mathrm{cm}^{-3}$ at $t = 100\,\mathrm{ns}$ (see Fig. 10.1(right)). The energy spent on O_2 dissociation can be estimated by :

$$\varepsilon_{\mathrm{O_2}}^{\mathrm{diss}} = \frac{n_O^{\mathrm{exp}}}{N_a} V \frac{\varepsilon_d}{2} = 235\,\mu\mathrm{J} \tag{10.21}$$

where N_a is the Avogadro number, V is the experimental discharge volume (diameter of $450\,\mu\mathrm{m}$ and gap distance of $4\,\mathrm{mm}$) and $\varepsilon_d \approx 497\,\mathrm{kJ\,mol}^{-1}$ the dissociation energy for one mole of O_2. Compared to the electrical energy of the discharge ($670\,\mu\mathrm{J}$), it corresponds to a fraction of 35%. From Popov's simulation, atomic oxygen density is slightly lower ($\Delta n_{\mathrm{O}} = 8 \times 10^{17}\,\mathrm{cm}^{-3}$) and approximately corresponds to 31% of the discharge energy. In our simulations performed in Section 6.9, this fraction was also around 35% so that our detailed chemistry is in good agreement with the Castela's parameters for the O_2 dissociation in this particular condition.

10.1.3.2 Fast gas heating

The energy of the discharge spent on the fast gas heating $\varepsilon_{\mathrm{heat}}$ is estimated a posteriori by considering the temperature change. Assuming that the temperature change is only due to the plasma discharge, the discharge heat energy can be approximated by:

$$\varepsilon_{\mathrm{heat}} = \rho c_v \Delta T \times V \tag{10.22}$$

In the experimental conditions of [167], the initial composition in the discharge axis is dominated by $\mathrm{O_2}, \mathrm{N_2}, \mathrm{O}$ components with $X_{\mathrm{O}} = 0.041$, $X_{\mathrm{O_2}} = 0.186$ and $X_{\mathrm{N_2}} = 0.773$. At a temperature $T_0 = 1500\,\mathrm{K}$ and pressure $P_0 = 1\,\mathrm{bar}$, the initial mass density of the mixture is approximately $\rho_0 = 0.22\,\mathrm{kg\,m}^{-3}$. Experimentally the temperature increase is estimated to be $\Delta T = 1000\,\mathrm{K}$ at $t = 20\,\mathrm{ns}$. The constant volume heat capacity c_v only varies from $930\,\mathrm{J\,K}^{-1}\,\mathrm{kg}^{-1}$ to $980\,\mathrm{J\,K}^{-1}\,\mathrm{kg}^{-1}$ between 1500 K and 2500 K. Using the value at 2500 K, the value of 21% given in [167] for the heat energy fraction is retrieved. In the simulation of [158], this fraction is around 18% at $t = 25$ ns. More recently in [160], an update of the kinetic mechanism has led to an energy fraction of $\approx 24\%$ at $t = 35$ ns. In our simulation (see Section 6.9.4), we evaluated this ratio to 21% and 31% at respectively 25 ns and 100 ns. Thus our simulation predicts a substantial gas heating between 25 and 100 nanoseconds.

10.1.4 Effect of the combustion mechanism

In addition to the chemical source term $\dot{\omega}_k^p$ that is due to the plasma model, a combustion mechanism must be used to complete the description of the plasma-assisted combustion chemistry. However, some reactions involving ground states particles present in the combustion mechanism are already considered during the evaluation of the constants of the Castela model. If these reactions are included in a simulation using the Castela model, their effects are then double-counted during the discharge phase (*i.e.*, in the simulation and in the model parameters). As an example in the GRI 3.0 mechanism, the three-body recombination of atomic oxygen is represented by the following reaction:

$$2\,\mathrm{O} + \mathrm{M} \longleftrightarrow \mathrm{O_2} + \mathrm{M} \tag{10.23}$$

with a forward reaction rate $k_f = 1.2 \times 10^{17}\ \mathrm{T}^{-1}\mathrm{cm}^6\,\mathrm{mol}^{-1}\,\mathrm{s}^{-1}$. To give an upper estimate of the temperature change due to this reaction, the gas temperature is set to T=1500 K. At

standard pressure, the particle density of the gas N_0 is equal to $4.8 \times 10^{18}\,\mathrm{cm}^{-3}$. The atomic oxygen density is taken to be $1 \times 10^{18}\,\mathrm{cm}^{-3}$ which is close to the maximal value reached experimentally. The energy released per mole of O_2 produced is $\epsilon_{\mathrm{recomb}}^{\mathrm{O_2}} = 497\,\mathrm{kJ}$. Then, the variation rate of temperature due to reaction Eq. 10.23 is given by:

$$\frac{dT}{dt} = \frac{k_f[\mathrm{O}]^2[\mathrm{M}]\epsilon_{\mathrm{recomb}}^{\mathrm{O_2}}}{\rho c_v} \simeq 4.3 \times 10^7\,\mathrm{K\,s}^{-1} \tag{10.24}$$

where $\rho = 0.22\,\mathrm{kg\,m}^{-3}$ and $c_v = 930\,\mathrm{J\,K}^{-1}\,\mathrm{kg}^{-1}$ for a N_2:O_2:O=0.77:0.19:0.04 mixture (in mole) at T=1500 K and standard pressure. During the time interval considered for the analysis (i.e $t \in [0, 100]$ns), the temperature change is around 4 K. This value is low regarding the total temperature change $\Delta T = 1000\,\mathrm{K}$ (0.5%), but could increase with the number of reactions that are double-counted. Moreover, this value could be much higher in reactive mixtures for which radicals produced by the discharge quickly react. The example presented above has motivated us only to consider the set of plasma reactions $\mathcal{P}$ (*i.e.*, those which are not in the combustion mechanism), as already discussed in Sec. 6.9.4), in the discharge heat energy computation and in the plasma species production rates. More details concerning the separation of plasma and combustion reactions are given in Section 10.3.2.

10.1.5 Limits of the model

The Castela's model was developed based on plasma discharges in air. In these conditions, most of the discharge effects result in gas heating, O_2 dissociation and vibrational excitation. However, the model is intended to be used for reactive mixtures. When studying the plasma-assisted ignition with this model in [34], the discharge operates in a fresh gas mixture that can contain almost 10% of methane at $\phi = 1$. In that case, the model omits the CH_4 dissociation resulting from the quenching of $N_2{}^*$ as shown in Chapter 7. In [21, 20], the model was used to study the stabilization of turbulent methane-air flame using NRP discharges. In these two last studies, the discharges occur in a region filled with a vitiated mixture in which H_2O and CO_2 are two important chemical components. In these conditions, the oxygen molecule mass fraction tends to zero that leads to $\dot{E}^p_{\mathrm{chem}} \to 0$ in the model according to Eq. 10.18. This behavior conflicts with the results in Chapter 8 which have shown an important chemical effect of the plasma discharge in burnt gases. In the following, the Castela's model is extended to a wide range of conditions encountered in typical laminar premixed flame based on the knowledge gained during the development of the detailed plasma kinetic mechanism.

10.2 Extension of the model to discharges in CH4/air mixtures

10.2.1 Model formulation

As in the original model, the discharge energy is divided into chemical, heat and vibrational energies:

$$\dot{E}^p = \dot{E}^p_{\mathrm{chem}} + \dot{E}^p_{\mathrm{heat}} + \dot{E}^p_{\mathrm{vib}} \tag{10.25}$$

The chemical energy is now divided into several global processes $j \in [1, P]$ allowing to consider the wide variety of chemical processes occurring during the discharge. Thus, the

chemical energy of the discharge reads:

$$\dot{E}^p_{\text{chem}} = \sum_{j=1}^{P} \alpha_j \dot{E}^p = \alpha_{\text{chem}} \dot{E}^p \tag{10.26}$$

where α_j is the discharge energy fraction which contributes to the process j and $\alpha_{\text{chem}} = \sum_j \alpha_j$. In Section 10.1, only the dioxygen dissociation process $O_2 \longrightarrow 2\,O$ was considered. This is called a global process as it does not physically exist but reflects the effects of different elementary reactions:

$$e^- + O_2 \rightarrow e^- + 2\,O \tag{10.27}$$
$$N_2(A_3, B_3, C_3, a_1) + O_2 \rightarrow N_2 + 2\,O \tag{10.28}$$

From the results of Chapters 6, 7 and 8, the most important global processes are detailed in Tab. 10.1. The model now contains 12 species that must be considered in the combustion mechanism. The three first processes correspond to the dominant processes in N_2:O_2 mixtures. Whereas it is straightforward to understand the links between the physical and global processes of processes 1 and 2, the third one is a bit different. Indeed, the atom balance is modified between the physical and the global reactions of the third process. This is to avoid double counting the atomic oxygen production, which is already considered in the first process. The reaction is first written in terms of ground state molecules that are initially present in the mixture:

$$N(^2D) + O_2 \longrightarrow NO + O \quad \Rightarrow \quad N_2 + 2\,O_2 \longrightarrow 2\,NO + 2\,O \tag{10.29}$$

and then decomposed as:

$$O_2 + N_2 \rightarrow 2\,NO \tag{10.30}$$
$$O_2 \rightarrow 2\,O \tag{10.31}$$

so that the atomic oxygen production in the initial reaction is accounted for in the first global process. The processes 4 to 6 can be understood quite easily and reflect the additions of CH_4, CO_2 and H_2O. Finally, the 7th process reproduces the high chemical reactivity of $O(^1D)$ and CH_4.

Finally, the plasma chemical source term of species k, $\dot{\omega}^p_k$, can be rewritten as:

$$\dot{\omega}^p_k = \sum_{j=1}^{P} \nu_{kj} \mathcal{Q}_j \tag{10.32}$$

where ν_{kj} is the stoichiometric coefficient of the species k in the global process j and $\mathcal{Q}_j$ is the molar production rate of the process j given by:

$$\mathcal{Q}_j = \alpha_j \frac{\dot{E}^p}{\Delta e_j} \tag{10.33}$$

Finally, we define α_{heat} and α_{vib} as the proportions of the discharge energy that are transferred respectively to the fast gas heating and the vibrational excitation. Thus the model can be summarized by:

$$\dot{E}^p_{\text{chem}} = \sum_{j=1}^{P} \alpha_j \dot{E}^p \tag{10.34}$$

$$\dot{E}^p_{\text{heat}} = \alpha_{\text{heat}} \dot{E}^p \tag{10.35}$$

$$\dot{E}^p_{\text{vib}} = \alpha_{\text{vib}} \dot{E}^p \tag{10.36}$$

that verifies:

$$\sum_{j=1}^{P} \alpha_j + \alpha_{\text{heat}} + \alpha_{\text{vib}} = 1 \tag{10.37}$$

#	Dominant physical process	Global process	Δe_j [kJ/mol]
1	$e^- + O_2 \longrightarrow e^- + 2\,O$ $N_2(A_3, B_3, C_3, a_1) + O_2 \longrightarrow N_2 + 2\,O$	$O_2 \longrightarrow 2\,O$	498.3
2	$e^- + N_2 \longrightarrow e^- + N + N(^2D)$	$N_2 \longrightarrow 2\,N$	945.4
3	$N(^2D) + O_2 \longrightarrow NO + O$	$O_2 + N_2 \longrightarrow 2\,NO$	182.5
4	$e^- + CH_4 \longrightarrow e^- + CH_3 + H$ $N_2(A_3, B_3, C_3, a_1) + CH_4 \longrightarrow N_2 + CH_3 + H$	$CH_4 \longrightarrow CH_3 + H$	439.5
5	$e^- + CO_2 \longrightarrow e^- + CO + O$ $N_2(A_3, B_3, C_3, a_1) + CO_2 \longrightarrow N_2 + CO + O$	$CO_2 \longrightarrow CO + O$	532.1
6	$e^- + H_2O \longrightarrow e^- + OH + H$ $N_2(A_3, B_3, C_3, a_1) + H_2O \longrightarrow N_2 + OH + H$	$H_2O \longrightarrow OH + H$	499.2
7	$CH_4 + O(^1D) \longrightarrow CH_3 + OH$	$CH_4 + \frac{1}{2}\,O_2 \longrightarrow CH_3 + OH$	257.5

Table 10.1: Description of the global processes considered in the improved phenomenological model. Δe_j corresponds to the internal energy change of the global process.

10.2.2 Link with the parameters of the Castela Model

The parameters of the new model can be easily determined to retrieve the properties of the Castela model. As already mentioned, only the oxygen molecule dissociation must be considered, and the associated coefficient writes:

$$\alpha_1 = \eta \frac{Y_{O_2}}{Y^f_{O_2}} \tag{10.38}$$

where $\eta = 0.35$ is the Castela parameter for the chemical effect. Moreover, the heat energy and vibrational energy fractions read respectively $\alpha_{\text{heat}} = \alpha - \alpha_1$ and $\alpha_{\text{vib}} = (1 - \alpha)$ with $\alpha = 0.55$ from Section 10.1. The reduction of our model to the Castela model will be useful for comparison purposes.

10.2.3 Model parameters

In this work, the model parameters $(\alpha_j, \alpha_{\text{heat}}, \alpha_{\text{vib}})$ are determined from 0D simulations using the detailed mechanism previously developed. The plasma chemical source terms $\dot{\omega}^p_k$ and global process production rates are related by:

$$\dot{\omega}^{\mathbf{p}} = \mathbf{A}\mathcal{Q} \tag{10.39}$$

where $\dot{\omega}^{\mathbf{p}} = (\dot{\omega}^p_1, \cdots, \dot{\omega}^p_{N_s})$ is the molar species production rate vector due to the plasma discharge, $\mathbf{A}$ is the matrix of the stoichiometric coefficients and $\mathcal{Q} = (\mathcal{Q}_1, \cdots, \mathcal{Q}_P)$ is the molar production rates vector of the global processes considered in the model. The molar production rate $\dot{\omega}_k$ of species k is known in the 0D simulations and divided into the combustion and plasma contributions $\dot{\omega}^c$ and $\dot{\omega}^p$:

$$\dot{\omega}_k = \sum_{j\in\mathcal{C}} \dot{\omega}_{k,j} + \sum_{j\in\mathcal{C}} \dot{\omega}_{k,j} = \dot{\omega}^c_k + \dot{\omega}^p_k \tag{10.40}$$

where $\mathcal{C}$ is the set of combustion reactions and $\mathcal{P}$ is the set of plasma reactions. As we are only interested in the global effect of the discharge and not its temporal evolution, the mean value of $\dot{\omega}^p_k$ is used in the following:

$$\bar{\dot{\omega}}^p_k(t) = \frac{1}{t}\int_0^t \dot{\omega}^p_k dt \tag{10.41}$$

The objective is to determine $\mathcal{Q}_j$ based on $\bar{\dot{\omega}}^p_k$ that is known in the simulation. Unfortunately, the matrix $\mathbf{A}$ is not invertible in most of the cases as usually the number of species differs from the number of processes. However, when considering the processes given in Tab. 10.1, the following $\mathcal{Q}_j$ verify Eq. 10.39:

$$\mathcal{Q}_1 = \frac{1}{2}\bar{\dot{\omega}}^p_{\mathrm{O}} + \frac{1}{2}\bar{\dot{\omega}}^p_{\mathrm{CO_2}} \tag{10.42}$$
$$\mathcal{Q}_2 = \frac{1}{2}\bar{\dot{\omega}}^p_{\mathrm{N}} \tag{10.43}$$
$$\mathcal{Q}_3 = \frac{1}{2}\bar{\dot{\omega}}^p_{\mathrm{NO}} \tag{10.44}$$
$$\mathcal{Q}_4 = -\bar{\dot{\omega}}^p_{\mathrm{CH_4}} - \bar{\dot{\omega}}^p_{\mathrm{OH}} - \bar{\dot{\omega}}^p_{\mathrm{H_2O}} \tag{10.45}$$
$$\mathcal{Q}_5 = -\bar{\dot{\omega}}^p_{\mathrm{CO_2}} \tag{10.46}$$
$$\mathcal{Q}_6 = -\bar{\dot{\omega}}^p_{\mathrm{H_2O}} \tag{10.47}$$
$$\mathcal{Q}_7 = \bar{\dot{\omega}}^p_{\mathrm{OH}} + \bar{\dot{\omega}}^p_{\mathrm{H_2O}} \tag{10.48}$$

Finally, the α_j coefficients are determined using:

$$\alpha_j = \mathcal{Q}_j \frac{\Delta e_j}{\dot{E}^p} \tag{10.49}$$

The fast gas heating and vibrational energy contributions are obtained as detailed in Section 6.8:

$$\dot{E}^p_{\mathrm{heat}} = \frac{1}{T_p}\int_0^{T_p} \left(\sum_{j\in\mathcal{P}} \dot{\mathcal{Q}}_j \Delta u_j\right) dt \quad \Rightarrow \quad \alpha_{\mathrm{heat}} = \frac{\dot{E}^p_{\mathrm{heat}}}{\dot{E}^p} \tag{10.50}$$

$$\dot{E}^p_{\mathrm{vib}} = \sum_k e^k_{\mathrm{vib}}(t = T_p) \quad \Rightarrow \quad \alpha_{\mathrm{vib}} = \frac{\dot{E}^p_{\mathrm{vib}}}{\dot{E}^p} \tag{10.51}$$

where T_p is the pulse duration in the model.

10.3 Model parameters for a CH_4-air flame

This section aims to provide suitable parameters for the phenomenological model described in Section 10.2 for discharges applied in a CH_4-air mixture.

10.3.1 Operating conditions

The model's parameters mainly depend on the mixture composition characterized by the molar fractions $X_{k\in[1,N_s]}$ and the gas temperature T_g. Thus, the realizable states of the mixture is a $\mathbb{R}^{N_s+1}$ space on which it is inconceivable to tabulate the model parameters. However, in the case of a 1D laminar premixed flame, it is possible to map all the accessed physical regions with only one variable c, called progress variable, which varies from 0 in the fresh gases to 1 in the burnt gases. In this work, we defined this progress variable as:

$$c = \frac{Y_{CO} + Y_{CO_2}}{Y^b_{CO} + Y^b_{CO_2}} \tag{10.52}$$

where the superscript b stands for values in burnt gases region. Another progress variable definition, based on the gas temperature, is also possible. However, it seems that CO and CO_2 mass fractions are less affected by the plasma discharge than gas temperature. In the following, all the model parameters are tabulated against the progress variable c (*i.e* with one coordinate). The main mixture components and the gas temperature versus the progress variable are shown in Figs. 10.2 and 10.3 for a lean and a stoichiometric 1D premixed flames. In both cases, a sharp increase of the H_2O and CO_2 mass fractions is observed at low c values. For the lean flame, oxygen molecules remain non-negligible and are comparable to CO_2 molar fraction at $c = 1$. Moreover, a temperature difference of ≈ 300 K is observed in the burnt gases between the two flames. These two cases are selected here to illustrate the range of mixture equivalence ratios for which NRP discharges are used.

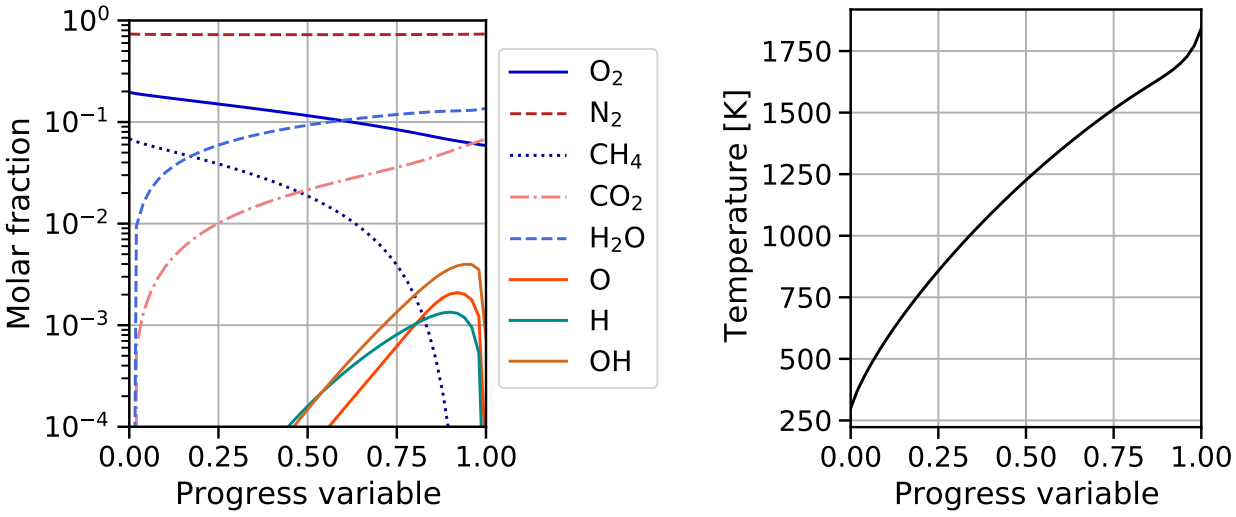

(a) Composition

(b) Temperature

Figure 10.2: Mixture composition and gas temperature evolution versus the progress variable c for a 1D premixed flame at $\phi = 0.7$, $T_0 = 300$ K, $P_0 = 1$ atm using the GRI 3.0 mechanism in CANTERA.

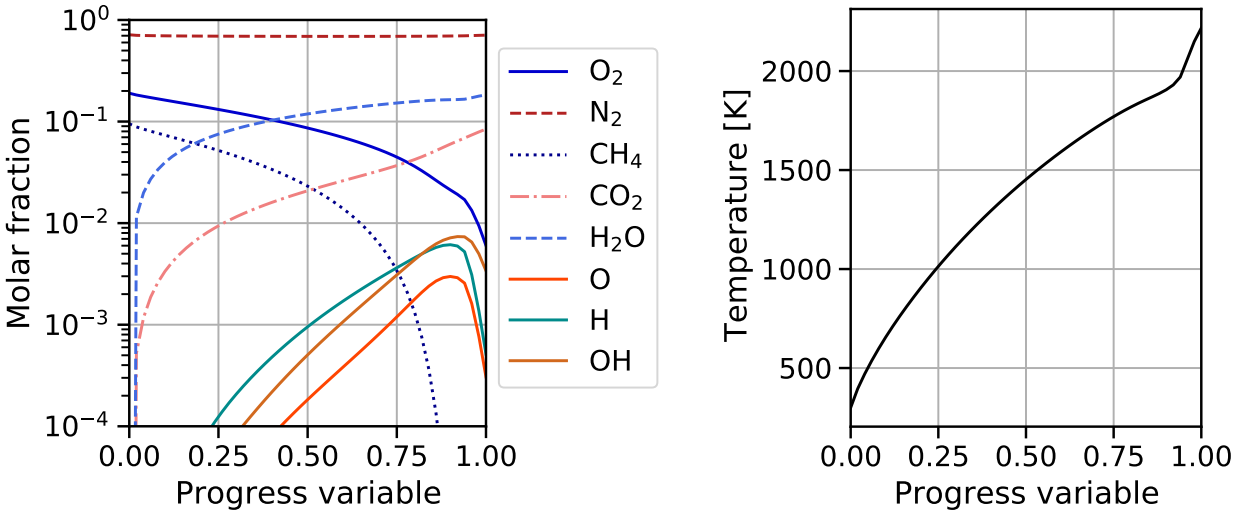

(a) Composition

(b) Temperature

Figure 10.3: Mixture composition and gas temperature evolution versus the progress variable c for a 1D premixed flame at $\phi = 1$, $T_0 = 300$ K, $P_0 = 1$ atm using the GRI 3.0 mechanism in CANTERA.

10.3.2 Model parameters computation

The model parameters are now computed for the two flames presented in Section 10.3.1. We used 51 samples points i as initial compositions and temperature of a 0D plasma reactor corresponding to the progress variable $c_i = i/50,\ i \in 0, 50$. A single pulse is then applied on each reactor at a constant reduced electric field of 200 Td that is representative of NRP discharge application. The discharge energy density deposited is fixed at $e_0^p = 1 \times 10^5\,\mathrm{J\,m^{-3}}$ in the fresh gas (*i.e.* at $T_0 = 300$ K) and then scales with the temperature as in Eq. 10.53. This scaling keeps the energy deposited per particle constant so that gas heating and particle production are close in all the cases.

$$e^p(T) = e_0^p \frac{T_0}{T} \tag{10.53}$$

The detailed mechanism developed for burnt gases, which contains all the developments made for air and CH_4-air mixtures, is used for all the simulations. First of all, it is necessary to highlight the need for the species production rate splitting done in Eq. 10.40. For that, the O and CH_3 particle density production ω_k due to plasma and combustion reactions are shown in Fig. 10.4 for the case $c = 0$ of the lean flame. Whereas for O an overwhelming part of the density change is due to plasma processes, CH_3 is quickly consumed by combustion reactions in a few tens of nanoseconds. Thus, considering $\dot{\omega}_k^{c+p}$ in the model would underestimate the CH_3 production during the plasma discharge.

The heat energy splitting between combustion and plasma processes is also important, as shown in Fig. 10.5. All the heating energy is directly connected to the plasma effect during the first ten nanoseconds. However, at $t = 50$ ns, the combustion reactions produce a non-negligible amount of heat corresponding to $\approx 15\%$ of the total gas heating. The heating energy e_{heat}^c must not be considered in the plasma model as it will already result from the combustion mechanism used on the top of the plasma model on the final simulation.

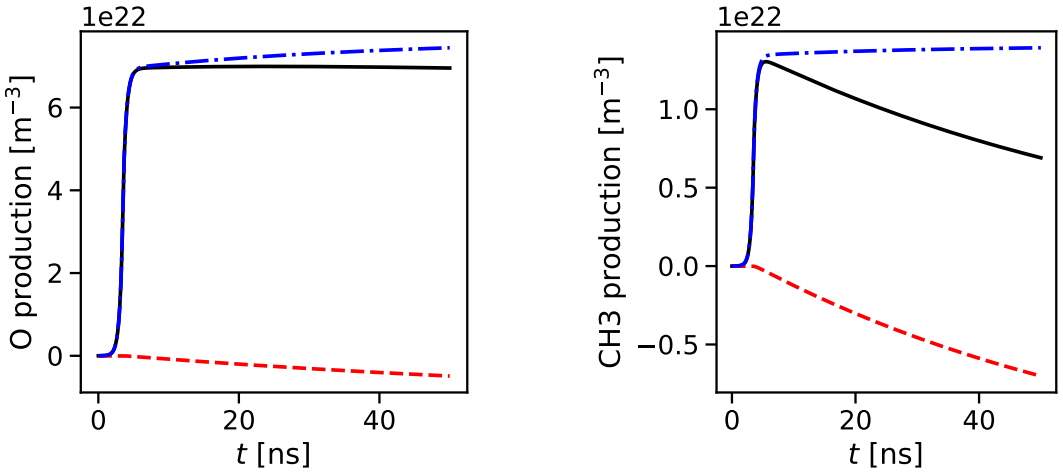

(a) O (b) CH_3

Figure 10.4: Time evolution of the (a) O and (b) CH_3 particle density productions ω_k from the plasma reactions ω_k^p (Blue Dash-dotted), the combustion reactions ω_k^c (Red Dashed) and the sum of the two contributions ω_k^{c+p} (Black Solid) following a single discharge in fresh gases ($\phi = 0.7$, $c = 0$).

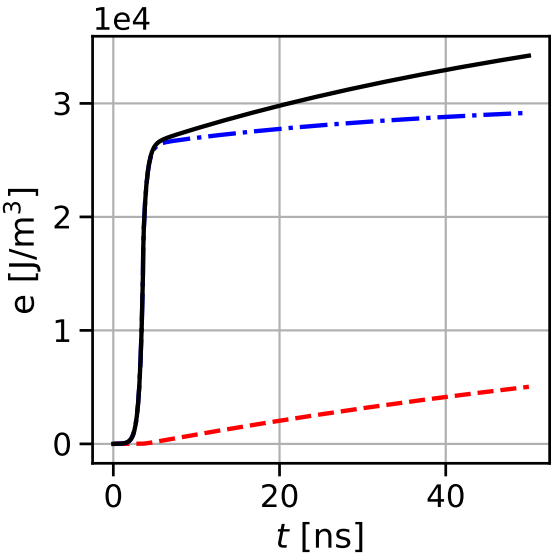

Figure 10.5: Time evolution of the heat energy density from the plasma reactions e_{heat}^p (Blue Dash-dotted), the combustion reactions e_{heat}^c (Red Dashed) and the sum of the two contributions e_{heat}^{c+p} (Black Solid) following a single discharge in fresh gases ($\phi = 0.7$, $c = 0$).

The model parameters are now detailed only for the lean case as similar observations apply for the stoichiometric flame. Three cases are described: the discharge in fresh gases at $c = 0$

(Case 1), an intermediate condition at $c = 0.3$ (Case 2) and in the burnt gases at $c = 1$ (Case 3). From the $\mathcal{Q}_j$ expressions given by Eqs 10.42 to 10.48, the instantaneous species k production can be computed and compared to the the detailed simulation. This is done for the 12 species of the model in Figs 10.6, 10.7 and 10.8 respectively for the Cases 1, 2 and 3.

In Case 1 (Fig. 10.6), we can first exclude CO_2, H_2O, and CO from the discussion as they are minor species of the mixture. It is observed in the simulation that CO is consumed by the plasma reaction whereas H_2O and CO_2 are produced. This behavior is not possible with the irreversible processes considered in our plasma model. Actually, these species are consumed or produced during fast reactions involving ions. For example H_2O is first the product of a combustion reaction and then is ionized to form H_2O^+ in charge exchange processes $A^+ + H_2O \longrightarrow A + H_2O^+$ which recombine with electron to finally form a water molecule from a plasma process $e^- + H_2O^+ \longrightarrow e^+ + H_2O$. However, this degree of accuracy is not expected for our model, and that is why their productions are forced to zero in the model. A large part of the discharge chemical effect lies in the production of atomic oxygen. In fresh gases conditions, atomic oxygen is mainly produced in process 1 ($O_2 \longrightarrow 2\,O$), which can well reproduce the simulation results. The oxygen molecules are also consumed in process 3 ($O_2 + N_2 \longrightarrow 2\,NO$), allowing to have a good prediction of nitric oxide. The NO formation is linked to atomic nitrogen formation, which has an opposite trend. Finally, the CH_4 consumtion is well reproduced by process 4 ($CH_4 \longrightarrow CH_3 + H$) and 7 ($CH_4 + 0.5\,O_2 \longrightarrow CH_3 + OH$) which respectively represent ≈ 80 and $\approx 20\%$ of the CH_4 consumption. To conclude on the Case 1, the plasma production and consumption of the main mixture components can be well reproduced by the seven processes considered in our phenomenological model (*i.e.* the black curves are superimposed on the gray dashed ones). Only a $\approx 5\%$ discrepancy is observed for CH_3 and H that is acceptable as CH_4 dissociation only represent $\approx 10\%$ of the discharge energy (*i.e.* the error made on the total discharge energy is approximately 0.5%).

In the Case 2 (Fig. 10.7), water molecules start to contribute significantly to the mixture composition. The molar fractions of the five most important species are: $X_{N_2} = 6.91 \times 10^{-1}$, $X_{O_2} = 1.15 \times 10^{-1}$, $X_{CH_4} = 4.07 \times 10^{-2}$, $X_{H_2O} = 9.25 \times 10^{-2}$ and $X_{CO_2} = 1.33 \times 10^{-2}$. In that case, all the species evolutions almost fit with the detailed simulation results. In addition to the process 7 already active in Case 1, the 6th process $H_2O \longrightarrow OH + H$ significantly contributes now to the OH and H production.

Finally in Case 3 (Fig. 10.8), the CH_4 and CH_3 molecules are negligble in the mixture composition and their plasma production cannot be well predicted by our model. Indeed, the processes selected in our model are not active under these conditions. However, this can be considered acceptable as the production of these species is very low. Regarding all the other species, an excellent agreement is found between the model and the detailed simulation excepted a $\approx 10\%$ error on H production.

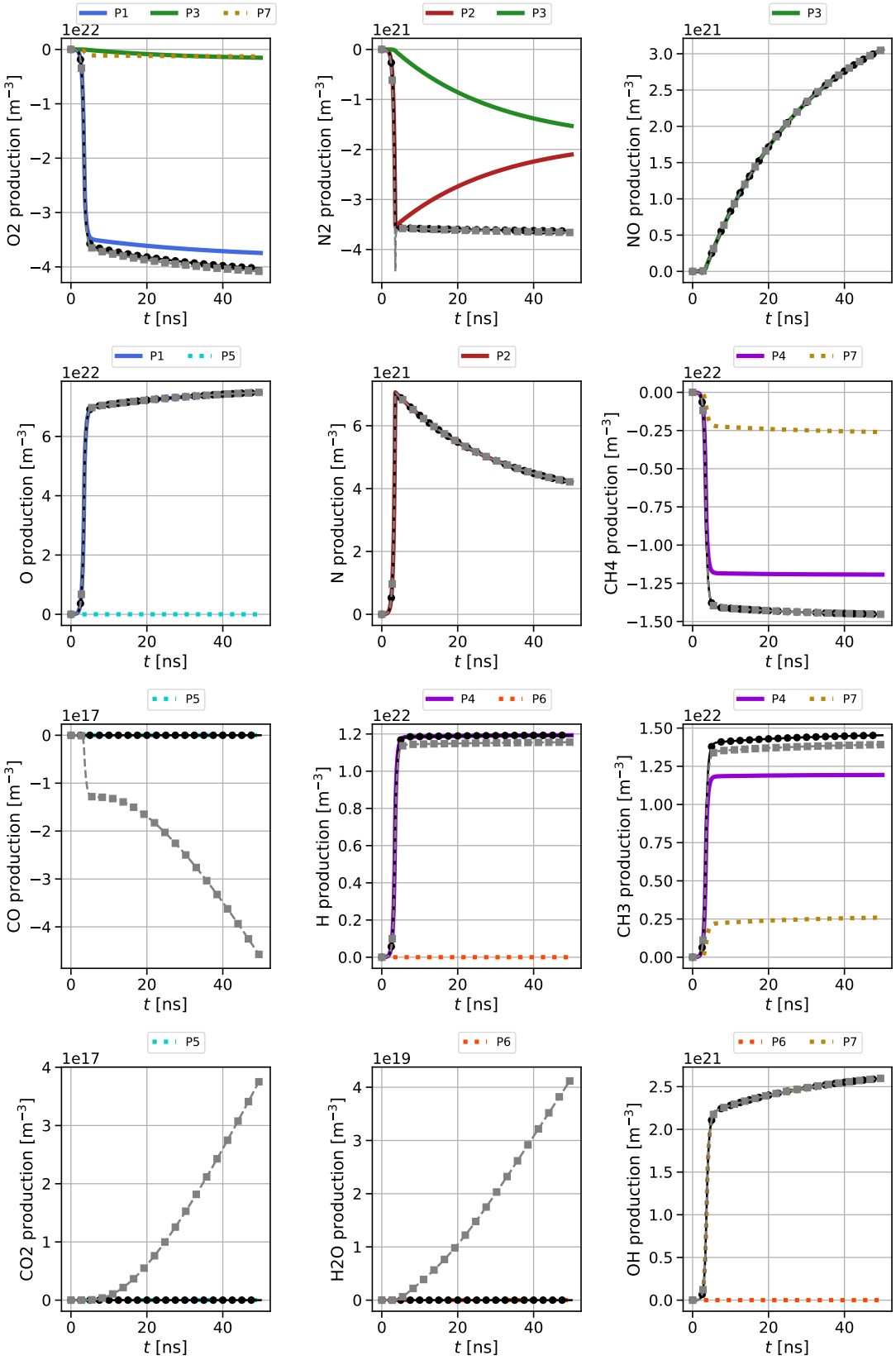

Figure 10.6: Comparison of the species production predicted by improved model (Black Solid) with the results of the detailed simulation (Gray Dashed) for the lean flame $\phi = 0.7$ at $\mathbf{c} = \mathbf{0}$. Colored curves correspond to the production of each global process of the improved model (see Tab. 10.1) with process number in the legend.

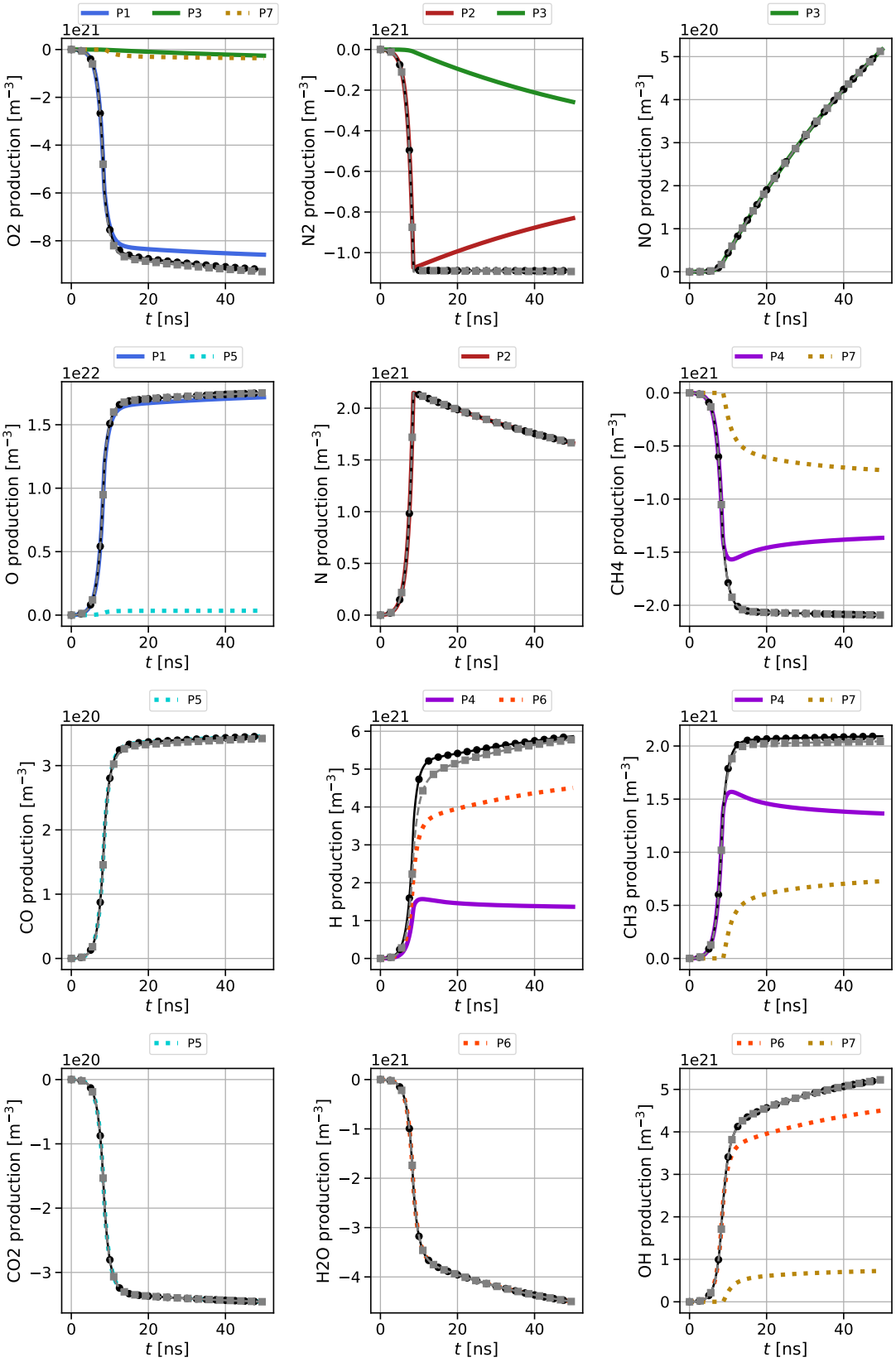

Figure 10.7: Comparison of the species production predicted by improved model (Black Solid) with the results of the detailed simulation (Gray Dashed) for the lean flame $\phi = 0.7$ at $\mathbf{c} = \mathbf{0.3}$. Colored curves correspond to the production of each global process of the improved model (see Tab. 10.1) with process number in the legend.

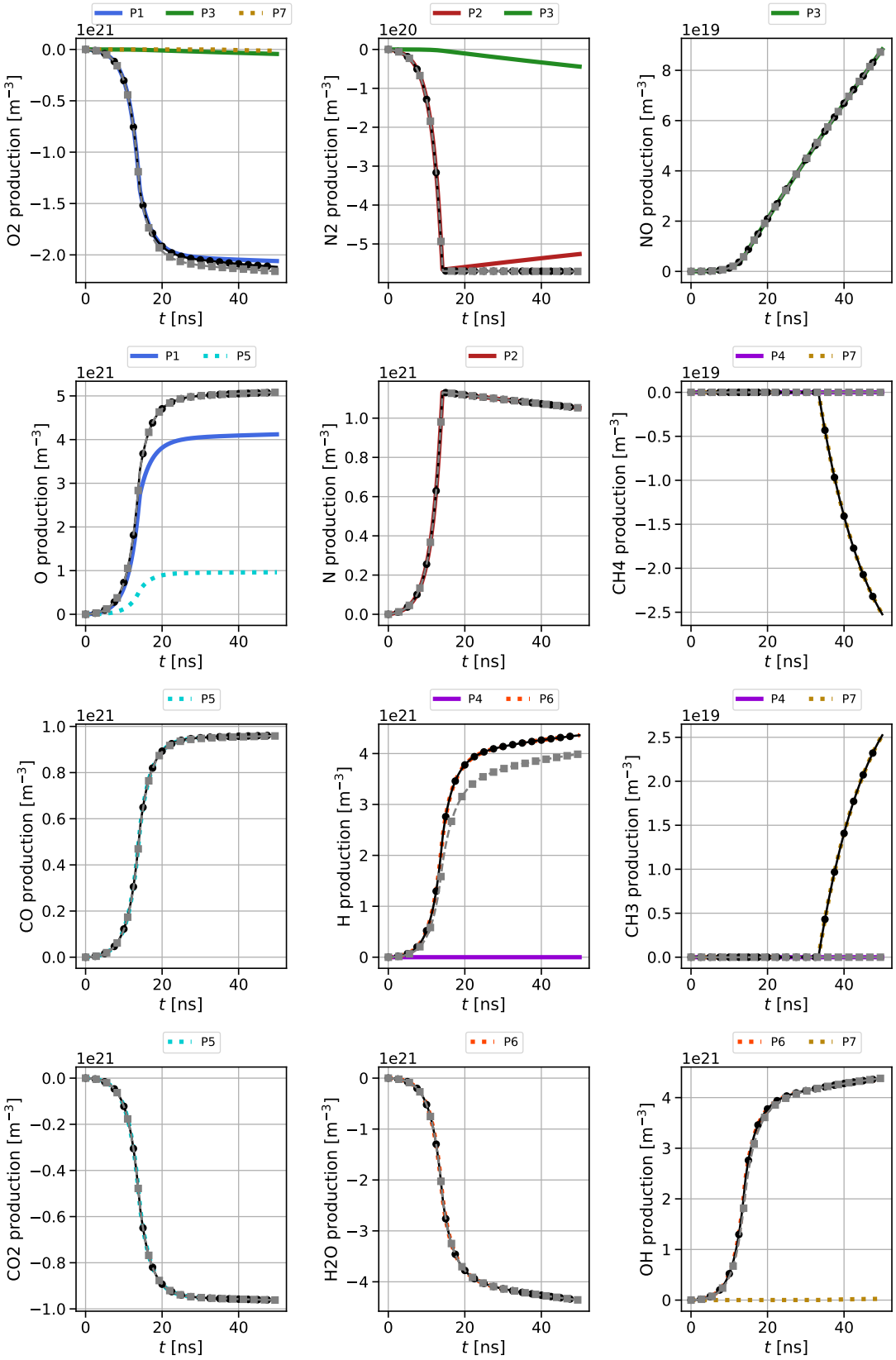

Figure 10.8: Comparison of the species production predicted by improved model (Black Solid) with the results of the detailed simulation (Gray Dashed) for the lean flame $\phi = 0.7$ at $\mathbf{c} = \mathbf{1}$. Colored curves correspond to the production of each global process of the improved model (see Tab. 10.1) with process number in the legend.

The species productions presented above are now used to determine the model parameters α_j. The production rate $\mathcal{Q}_j$ of each global process j are determined at $t = 50$ ns. Then, the fraction of energy spent on each process is computed using Eq. 10.54. The heat and vibrational energy contributions are computed using respectively Eq. 10.50 and Eq. 10.51. All the model parameters are shown in Fig. 10.9 for the lean and stoichiometric cases.

$$\alpha_j = \mathcal{Q}_j \frac{\Delta e_j}{\dot{E}^p} \tag{10.54}$$

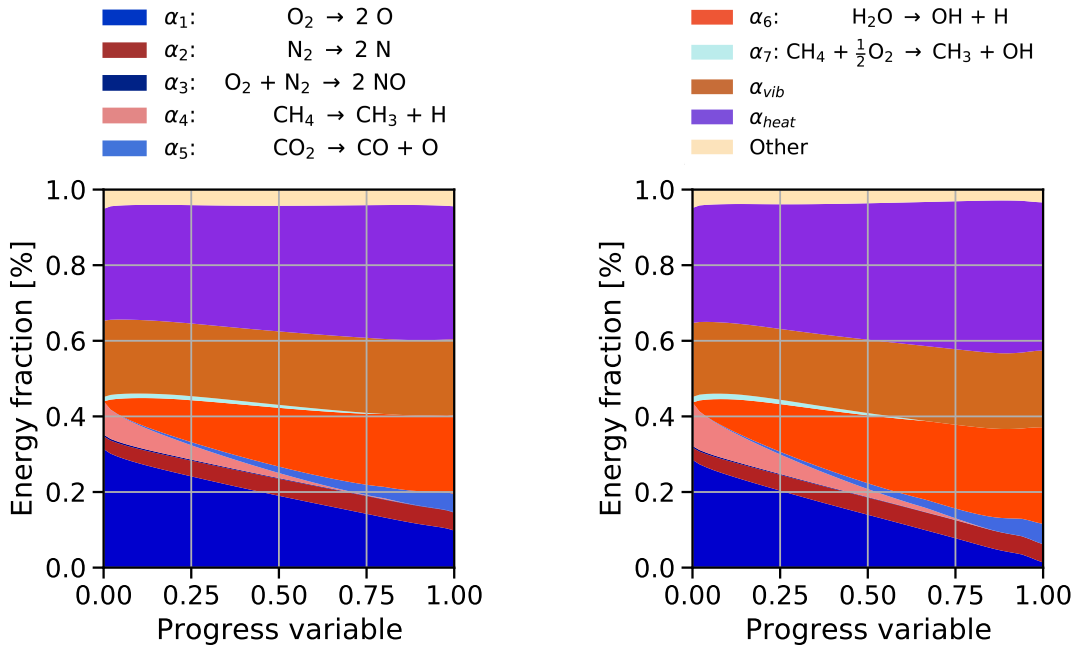

(a) $\phi = 0.7$ (b) $\phi = 1$

Figure 10.9: Energy repartition of the improved phenomenological model for a lean mixture (a) and a stoichiometric mixture (b).

In both cases, the chemical energy of the discharge is around 45% in the fresh and then decreases with c. The decrease of chemical energy is a bit more pronounced in the stoichiometric case for which α_{chem} is lower than 0.4 at $c = 1$. In fresh gases, most of the chemical energy is spent into O_2 dissociation ($\approx$ 75% of the chemical energy), and the remaining energy is shared between N_2 and CH_4 dissociation processes. Moreover, atomic oxygen production in O_2 dissociation almost linearly decreases with c. For the stoichiometric flame, this process becomes negligible in the burnt gases as all the oxygen molecules are consumed, whereas for the lean flame it still corresponds to 10% of the discharge energy. In both flames, the water molecule concentration sharply increases with c. Its dissociation becomes an important chemical process in the discharge and represents up to 25% of the discharge energy at $c = 1$. Whereas CO_2 is also an important component in the burnt gases region, it only corresponds to 5% of the discharge energy. The NO production is almost negligible in terms of energy contribution to total discharge energy. However, we have decided to keep it into the model for application in which NOx are targeted. Regarding the other contributions, the vibrational energy fraction is almost stable in all the cases corresponding to $\approx$ 20% of the discharge energy. For its part, the discharge heat energy slightly increases with c. In the lean case, α_{heat} varies from 0.3 to 0.35, whereas it varies from 0.3 to 0.4 in the stoichiometric flame. Thus, more energy is spent

on chemical processes in lean burnt gases than in stoichiometric burnt gases. Finally, around 5% of the energy is still stored into other contributions dominated by the electronic excitation, which was not fully relaxed at $t = 50$ ns. As it is not expected to include excited species in the combustion mechanism, the total excitation energy could be converted to heat, assuming no chemical effect during their quenching.

10.3.3 Temporal and spatial profiles

In the previous Section, we have determined the fractions of energy transferred into the different channels considered. It is now necessary to specify how this energy is temporally and spatially deposited. In the model, the discharges are applied at a given frequency f and pulse duration T_p to provide an energy E^p. In addition, we define $t^* = t \mod (1/f)$ as the time from the beginning of the current pulse. Then, a temporally constant discharge power $\dot{E}^p$ is applied within the interval $t^* \in [0, 1/f]$. The spatial profile is given by any space function $\mathcal{F}(x, y, z)$ satisfying:

$$\int_V \mathcal{F} dV = 1 \tag{10.55}$$

Finally, the spatio-temporal discharge energy power reads:

$$\dot{E}^p(x, y, z, t) = \begin{cases} \frac{E^p}{T_p}\mathcal{F}(x, y, x) & \text{if } t^* \in [0, 1/f] \\ 0 & \text{otherwize.} \end{cases}$$

10.4 Conclusion and perspectives

In this chapter, an extension of the phenomenological model presented in [34] has been developed in the light of the knowledge acquired during the development of the detailed mechanism. The use of 7 processes extends the model's validity to a whole range of conditions encountered in a flame. In addition, the discharge energy fractions attributed to the ultrafast heating and the vibrational excitation have been re-evaluated. In contrast to the initial model, a smaller part of the discharge energy contributes to the vibrational excitation for typical discharge conditions at 200 Td. This energy difference is divided into the chemical and the heat energies, which are higher than in the original model.

Due to lack of time, it was not possible to use this model on a multi-dimensional simulation. However, the structure of the model has been implemented in the code AVIP with the coefficients of the original model. These developments have been used in the Chapter 13 to deposite all the energy as heat corresponding to $\eta = 0$ and $\alpha = 1$ in Sec. 10.2.2.

Part III

Multi-dimensional simulations of Plasma-Assisted Combustion

Chapter 11

Coupling strategy for detailed plasma-assisted combustion simulations

Contents

11.1 Governing equations

The reactive Navier-Stokes equations supplemented by vibrational power source terms are used to describe the evolution of a compressible flow with chemical reactions:

$$\frac{\partial \rho Y_k}{\partial t} + \nabla \cdot (\rho Y_k(\mathbf{u} + \mathbf{V_k})) = \dot{\omega}_k \tag{11.1}$$

$$\frac{\partial \rho \mathbf{u}}{\partial t} + \nabla \cdot (\rho \mathbf{u}\mathbf{u} + p\mathbf{I}) = \nabla \cdot \boldsymbol{\tau} \tag{11.2}$$

$$\frac{\partial \rho E}{\partial t} + \nabla \cdot ((\rho E + p)\mathbf{u}) = \nabla \cdot (\boldsymbol{\tau} \cdot \mathbf{u} - \mathbf{q}) + \dot{\omega}_T + \dot{R}_{\mathrm{VT}} \tag{11.3}$$

where ρ is the mass density, $\mathbf{u}$ the gaseous velocity, E the total non-chemical energy, p the scalar pressure, Y_k the mass fraction of species k, $\boldsymbol{\tau}$ the viscous stress tensor, $\mathbf{q}$ the heat flux vector, $\mathbf{V_k}$ the diffusion velocity of species k into the mixture (see Section 11.2), $\dot{\omega}_k$ the species k mass production rate and $\dot{R}_{\mathrm{VT}}$ a power source term corresponding to the relaxation of the vibrational energy into translational energy detailed in Section 11.3. The heat flux vector $\mathbf{q}$ is decomposed into a conductive term and another term due to species diffusion:

$$\mathbf{q} = -\lambda \nabla T + \rho \sum_{k=1}^{N} h_k Y_k \mathbf{V_k} \tag{11.4}$$

where λ is the thermal conductivity and h_k is the species k enthalpy. Note here that the mixture mass density ρ represents all the neutral species, including excited atoms and molecules.

All the charged species are transported following the drift diffusion approximation detailed in Chapter 3 which reads for each species k:

$$\frac{\partial \rho_k}{\partial t} + \nabla \cdot (\rho_k \mu_k \mathbf{E} - D_k \nabla \rho_k + \mathbf{u}) = \dot{\omega}_k \tag{11.5}$$

where ρ_k is the charged species density, $\mathbf{E}$ the electric field, μ_k the mobility coefficient, D_k the diffusion coefficient and $\dot{\omega}_k$ the species k mass production rate. The ions are assumed to be in thermal equilibrium at the gas temperature T_g. All the ions mobilities and diffusion coefficients are taken from [136] considering global coefficients for positive and negative ions. Since the electrons are far from equilibrium during the high voltage pulse, it is necessary to compute the electron energy distribution function (EEDF) to retrieve their temperature and swarm parameters. More details is given in Section 11.5.

The electric field is derived from the Poisson equation:

$$\nabla^2 \phi = -\frac{1}{\epsilon_0} \sum_k e q_k n_k \quad \text{with} \quad \mathbf{E} = -\nabla \phi \tag{11.6}$$

where ϕ is the electric potential and q_k is the species k charge.

In the set of equations Eqs. 11.1-11.6, all the coupling between the plasma discharge and the combustion is contained in the chemical source terms $\dot{\omega}_k$ and the heat release rate $\dot{\omega}_T$. In this work, the electro-hydrodynamic effect of the discharge on the flow has been neglected.

11.2 Species diffusion

In AVBP, the species diffusion velocity relies on the widely used Hirshfelder and Curtis approximation [81] which reads:

$$\mathbf{V_k} = -D_k \frac{\nabla X_k}{X_k} \quad \text{with} \quad D_k = \frac{1 - Y_k}{\sum_{j \neq k} X_j / D_{jk}} \tag{11.7}$$

where D_{jk} is the binary mass diffusion coefficient of the species j into the species k. Thus D_k is like an effective diffusion coefficient of the species k in the rest of the mixture. This expression of the diffusion velocity does not ensure mass conservation and must be complemented by a correction velocity $\mathbf{V_c}$ that writes [155]:

$$\mathbf{V_c} = \sum_{k=1}^{N} D_k \frac{W_k}{\bar{W}} \nabla X_k \tag{11.8}$$

Going back to the species conservation equations, it gives:

$$\frac{\partial \rho Y_k}{\partial t} + \nabla \cdot (\rho Y_k (\mathbf{u} + V_c)) = \nabla \cdot \left(\rho D_k \frac{W_k}{\bar{W}} \nabla X_k \right) + \dot{\omega}_k \tag{11.9}$$

In many combustion applications, the diffusion coefficients D_k can be simplified by considering a constant Lewis number Le_k for each species k that is defined by:

$$\mathrm{Le}_k = \frac{D_{\mathrm{th}}}{D_k} \tag{11.10}$$

where $D_{\text{th}} = \lambda/\rho c_p$ is the mixture heat diffusivity that is linked to the kinematic viscosity $\nu = \mu/\rho$ through the Prandtl number of the mixture:

$$\text{Pr} = \frac{\nu}{D_{\text{th}}} \tag{11.11}$$

In practice in AVBP, the dynamic viscosity μ is assumed to only depend on the temperature following a Sutherland law:

$$\frac{\mu}{\mu_0} = \left(\frac{T}{T_0}\right)^{3/2} \frac{T_0 + S}{T + S} \tag{11.12}$$

where μ_0 is a reference viscosity at a reference temperature T_0 and S is an adjustable parameter allowing to fit the dynamic viscosity on an appropriate range of temperatures. A simpler power law can also be used:

$$\frac{\mu}{\mu_0} = \left(\frac{T}{T_0}\right)^{n} \tag{11.13}$$

with a temperature dependence given in terms of the exponent n. In both cases, these parameters are optimized by ARCANE [37] to fit the viscosity encountered in a one-dimensional flame. It is expected that the dynamic viscosity does not vary much in most of the combustible mixture in which N_2 remains the main component both in fresh and burnt gases regions. Finally, from the Prandtl number of the mixture and the Schmidt numbers of each species, it is possible to compute the species diffusion coefficients D_k and the thermal conductivity λ. It is assumed that the Lewis numbers of the excited species are identical to their associated ground state molecules as a first approximation.

11.3 Vibrational energy

The vibration of nitrogen plays an essential role in plasma-assisted combustion, even at high reduced electric fields, as it can store up to 50% of the discharge energy as discussed previously in Section 6.1. Detailed modeling of vibration is too costly, and a global out-of-equilibrium vibrational energy model is considered here as done in [158, 34] and validated in Section 6.10. The governing equation for the non-equilibrium vibrational energy e_{vib} reads:

$$\frac{\partial \rho e_{\text{vib}}}{\partial t} + \nabla \cdot (\rho e_{\text{vib}} \mathbf{u}) = \nabla \cdot (\rho \mathcal{D}_{N_2} \nabla e_{\text{vib}}) + \dot{E}^p_{\text{vib}} - \dot{R}_{VT} \tag{11.14}$$

where $\mathcal{D}_{N_2}$ is the diffusion coefficient of N_2 into the mixture, $\dot{E}^p_{\text{vib}}$ is the vibrational energy production term computed from the electron-impact processes and $\dot{R}_{VT}$ is the vibrational to translational relaxation modeled using the Landau-Teller harmonic oscillator approach. The relaxation term $\dot{R}_{VT}$ is computed using Eq. 11.15 in which the relaxation times τ^k_{VT} are computed using experimental coefficients from Capitelli et al. [32] for H_2O, CO_2 and Millikan and White [129] for N_2, O_2, O. This relaxation term appears in the gaseous mixture's energy Eq. 11.3, which helps to heat the gas slowly.

$$\dot{R}_{VT} = \rho \frac{e_{\text{vib}}}{\tau_{VT}} \tag{11.15}$$

$$\tau_{VT} = \left(\sum_k \frac{1}{\tau^k_{VT}}\right)^{-1} \tag{11.16}$$

11.4 Numerics

In Chapters 12 and 13, the Navier-Stokes equations as well as the non-equilibrium vibrational energy equation are integrated with the HLLC-MUSCL scheme developed in [43, 42] to handle the possible shocks produced by the discharges. The limited Law-Wendroff scheme detailed in Section 3.3.3.3 is used for to integrate the drift-diffusion equation in all the simulations performed in Chapters 12 and 13. This scheme was prefered to the ISG and FOU scheme as it was found to be the more stable on triangular meshes according to the streamer simulations performed in Chapter 4. Finally, the Poisson equation is discretized using the finite volume vertex-centered formulation described in Section 3.4.1, and the resulting linear system is solved using the PETSc library [17].

11.5 Electron parameters

The electrons are far from equilibrium during the high voltage pulse due to the strong electric field with $T_e \gg T_g$. The electrons parameters such as their temperature, mobility, diffusion coefficient and electron impact rate coefficients rely on the Electron Energy Distribution Function (EEDF) F_0, which must be computed. In theory, the EEDF depends on a huge set of variables including the reduced electric field E/N, the mixture composition X_k, the gas temperature T and the ionization degree n_e/N. These parameters can vary a lot within the computational domain and should be computed at each node and each iteration, which is not feasible. Thus, a tabulation strategy has been adopted in AVIP to reduce the computational cost of the EEDF. The lookup table is a $\mathbb{R}^{N_s+3}$ space, with N_s the number of species, on which it is too costly to build a table. To overcome this issue, only the reduced electric field, which is the most important EEDF parameter, is considered on the table and the other parameters are simplified. First, the ionization degree is assumed to be null (*i.e*, $n_e/N \ll 1$), which is acceptable when this ratio does not exceed $10^{-4} - 10^{-3}$. Then the mixture composition and the gas temperature are taken constant using a volume average of the variables in the discharge volume V_p described in Fig. 11.1. The tabulation is finally built at the beginning of the simulation and updated at the same frequency as the pulse repetition, *i.e.*, before each new pulse.

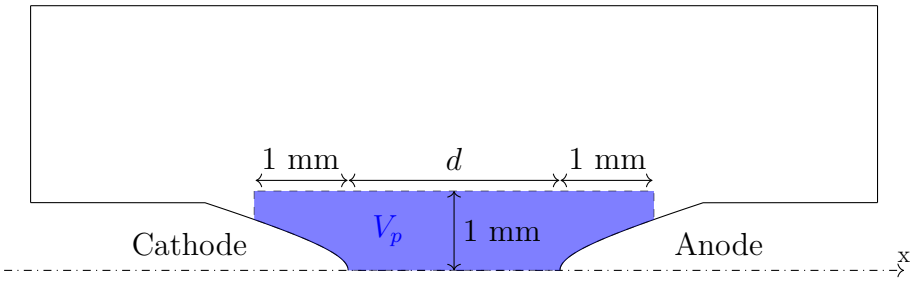

Figure 11.1: Sketch of the discharge volume V_p

11.6 Modeling strategy

The modeling of plasma-assisted combustion is very challenging due to the large variety of timescales and characteristic lengths encountered. Indeed, the plasma discharge itself occurs within a few nanoseconds with typical timesteps on the order of 1×10^{-12} s, which is driven

by the Fourier constraint during the discharge propagation. Moreover, the simulations must describe accurately the very small plasma structures of a few micrometers. On the other hand, combustion processes are microseconds to milliseconds long with a typical size of tens to hundreds of micrometers. To speedup the computation, the simulation of one pulse period (*i.e.* the pulse and the interpulse) is decomposed into three phases as shown in Fig. 11.2. The first one is the discharge propagation followed by the formation of a conducting channel and is computed on a fine mesh M1 with $\Delta x \leq 5\,\mu\text{m}$. The electric field $\mathbf{E}_{\text{POISSON}}$ is resolved self-consistently with the charged species during this phase using the Poisson equation. However, as mentioned in Section 3.6.1, the dielectric time step can become very constraining when the electrical current increases. At the same time, the plasma is nearly uniform and only expands radially. Thus to reduce to CPU cost of the simulation, an automatic switch to the spark model detailed in Section 3.6.1 is performed when the dielectric time step becomes lower than $5 \times 10^{-14}\,\text{s}$. The choices of this time step threshold, as well as the model validity, have been assessed by performing simulations without the help of the spark model. These tests were performed in cases representative of the NRP-spark discharges that are simulated in Chapter 12. No significant impact of the model was observed during these verifications. Finally, when the applied voltage reaches negligible values, the simulation is stopped, and the last solution is interpolated on a coarser mesh M2 with $\Delta x \geq 15\,\mu\text{m}$. Then, the interpulse period is simulated using the ambipolar model as detailed in Section. 3.6.2. At the end of this period (*i.e.*, $\mod(t, T_p) = 0$), the last solution of the interpulse is interpolated on the mesh M1, and the procedure can be repeated.

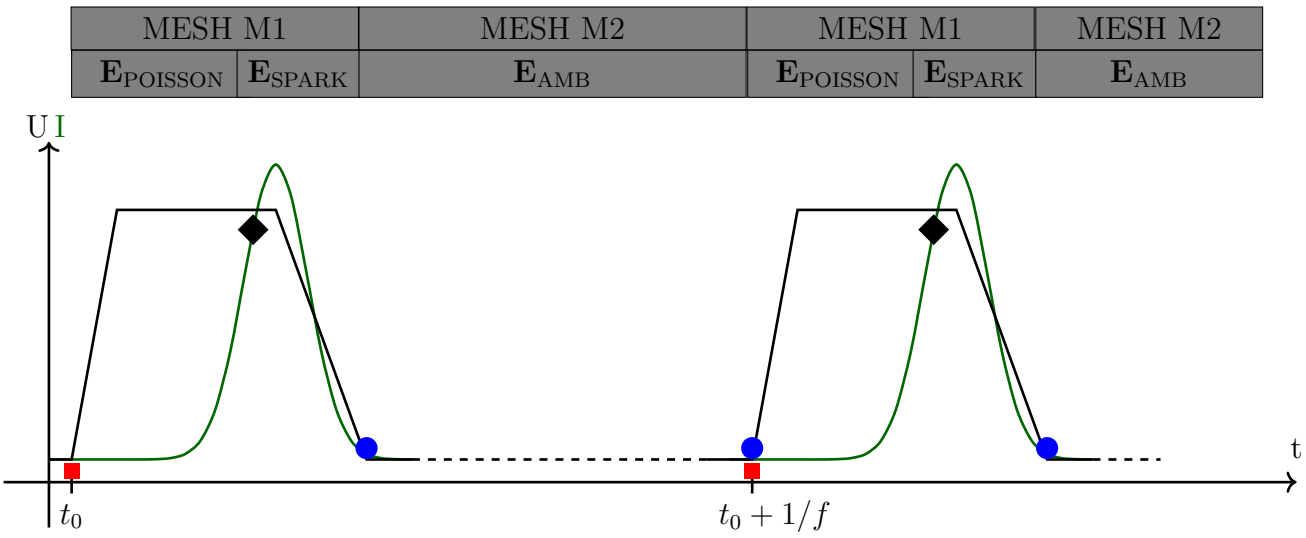

Figure 11.2: Modeling strategy employed to simulate multiple NRP discharges in AVIP. ■ EEDF computation, ● interpolation procedure between meshes M1 and M2 and ◆ switch to the spark model for the electric field.

11.7 Calculation of the discharge energy

Some quantities defined for 0D simulations are slightly adapted for multi-dimensionnal simulations. The discharge energy E^p now needs to be integrated over the discharge volume V_p and

reads

$$E^p(t) = \int_{V_p} e^p(t) dV \tag{11.17}$$

where e^p is the local discharge energy density given by:

$$e^p(t) = \int_0^t \mathbf{j_e} \cdot \mathbf{E} dt \tag{11.18}$$

where $\mathbf{j_e}$ is the electron current density. The vibrational energy at time t is given by a volume integration of the mean vibrational energy density:

$$E^p_{\text{vib}}(t) = \int_{V_p} e_{\text{vib}} dV \tag{11.19}$$

The heating energy of the discharge is computed using Eq. 11.20 which considers the global heat release $\dot{\omega}_T$. Thus, as a first approximation, the heat produced by the plasma is not separated from the neutral reactions as it was done in the 0D reactors. The discharge volume V_p is therefore limited to a small region around the discharge to reduce the effect of neutral reactions far from the discharge. Usually, this volume is a cylinder with a radius of 1 mm and a length that incorporates 1 mm of both the anode and the cathode as depicted in Fig. 11.1.

$$E^p_{\text{heat}}(t) = \int_0^t \left(\int_{V_p} \dot{\omega}_T dV \right) dt \tag{11.20}$$

Chapter 12

Detailed simulation of NRP spark discharge in Air

Contents

12.1 Case description

This chapter aims to extend the work made on the experiment of Rusterholtz et al. [167] in Section 6.9 within a 0D framework to a multi-dimensional framework. The detailed multi-dimensional simulation of NRP discharges in the air is a mandatory step toward the detailed simulation of plasma-assisted combustion simulation since it allows to validate two important

phenomena, the fast gas heating and the radical production, independently of the combustion. However, performing such a comparison of multi-dimensional simulations with experiments is a difficult task and, to the best of my knowledge, was only performed using 0D and 1D simulations. For example in the 1D-radial simulation of Popov [158], the imposed electric field is adjusted to fit the electrical current of the experiment. In the 0D simulation performed in this work, both the electron density and the electric field have to be imposed. This comparison is challenging for a 2D-cylindrical code, as only the voltage waveform is used as an input of the model and several assumptions have to be made concerning the initial mixture field (composition and temperature), the initial plasma density and the electrode radius.

12.1.1 Numerical setup

The experimental setup consists of two pin electrodes separated by 4 mm which are placed in a pre-heated atmospheric airflow at 1000 K. The flow is directed from the cathode to the anode at a velocity $U_0 = 2.6\,\mathrm{m\,s^{-1}}$ as indicated in Fig. 12.1. High voltage 10 ns-long pulses are applied at a pulse repetition frequency of 10 kHz and an amplitude of ≈ 5.7 kV. In the steady-state regime, the gas temperature is stabilized at 1500 K in the center of the inter-electrode gap.

The geometry used in this work is presented in Fig. 12.1. All the simulations are performed in 2D-cylindrical coordinates. This simplification is made possible thanks to the electrode geometry and the laminar flow. Two hyperbolic electrodes with a curvature radius of 200 µm, separated by 4 mm, are used to approximate the real shape of the electrodes. These electrodes are extended with a cylinder of 1 mm radius as in the experiment. The inlet velocity profile is taken from a preliminary simulation performed with an extended cathode to obtain a converged solution of the boundary layer. The initial conditions are detailed in Section 12.1.2.

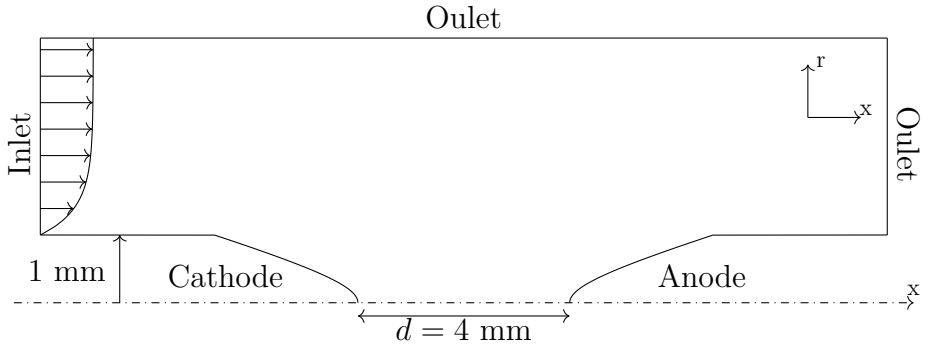

Figure 12.1: Sketch of the geometry used for the multi-dimensional simulations of NRP dicharges in air representing the experiment of [167]

The HLLC-MUSCL scheme recently developed in AVIP [43, 42] is used for the Navier-Stokes equations to handle the shocks produced by the NRP-Spark discharges. A two-stage Runke-Kutta is used for the time integration of the Navier-Stokes equations. An adiabatic non-slipping wall boundary condition is used for the mixture to close the fluxes at the electrode boundary, thus neglecting heat conduction through them. Non-reflecting NSCBC [154] boundary conditions are applied on the left patch (Inlet) and the top/right patches (Outlet). The drift-diffusion equations used for the charged species transport are solved using the Limited Lax-Wendroff scheme, which gave the best results in the streamer simulations performed in

Chapter 4. All the drift-diffusion boundary conditions are treated with a Neumann closure assuming $\nabla n = 0$ (*i.e.* no diffusive flux). A zero Neumann boundary condition is applied for the Poisson equation on the axis as well as for the left, top and right patches. A time-varying but spatially constant Dirichlet boundary condition at potential $V_A(t)$ is used for the anode. The imposed time signal $V_A(t)$ is extracted from experimental data given in [167]. The cathode is grounded (*i.e.*, $V_C = 0$). A summary of all the boundary conditions is given in Tab. 12.1.

	Cathode	Anode	Axis	Left	Top	Right
Poisson	$V_C = 0$	$V_A(t) \geq 0$	$\nabla\phi = 0$	$\nabla\phi = 0$	$\nabla\phi = 0$	$\nabla\phi = 0$
Drift-diffusion	Neumann	Neumann	Symmetry	Outlet	Outlet	Outlet
Navier-Stokes	Wall no-slip	Wall no-slip	Symmetry	Inlet	Outlet	Outlet

Table 12.1: Boundary conditions used for the multi-dimensional simulation of NRP discharges in air.

Finally, two different meshes M1 and M2 have been used for the high voltage pulse phase and the interpulse period respectively as explained in Section 11.6. A caracteristic cell size of $\Delta x_1 = 3\,\mu\text{m}$ is used in mesh M1 in the inter-electrode gap up to $r = 0.5\,\text{mm}$ (Zone 1). Then the mesh is coarsened to reach a cell size of $\Delta x_2 = 6\,\mu\text{m}$ at $r = 1$ mm (Zone 2). Beyond that, a cell size of 0.1 mm is used. The same zones are used for the mesh M2 but with $\Delta x_1 = 15\,\mu\text{m}$ and $\Delta x_2 = 30\,\mu\text{m}$. The meshes M1 and M2 contain respectively 8×10^5 and 2×10^5 nodes. The use of mesh M2 allows to speedup the computation by a factor of ≈ 100 during the interpulse period where the viscous effect are limiting for the time-step (x 4 for the reduction of cells in the mesh, x 25 for the Fourier constraint which scales as $1/\Delta x^2$).

12.1.2 Initial conditions

The measurements made in Rusterholtz et al. [167] are performed in the steady-state regime of the NRP-spark discharges. The number of pulses required to reach the NRP-Spark regime could be important and has been investigated in [142] in similar conditions. In this study, two electrodes separated by 5 mm in a 1000 K airflow were used to produce spark discharges. In this condition, the applied voltage must be set to 7 kV to get a reduced electric field around 190 Td. It was shown in [142, Figure 2] that more than 200 pulses must be applied to reach the spark regime at a frequency of 20 kHz, and up to 400 pulses are required at 6.5kV. Similarly in the conditions of [167] considered here, several hundreds of pulses may be required to reach the spark regime. Thus, we first deciced to focus on the steady state regime in Section 12.2 for which initial conditions are detailed in Section 12.1.2.1. In a second step in Section 12.3, we will try to perform a simulation of the transient regime starting from the initial conditions detailed in Section 12.1.2.2.

12.1.2.1 Initial conditions for the steady state simulations

The initial conditions for the steady-state simulation are based on the measurements made in [167]. We know that in the steady-state regime, at the beginning of the pulse, the gas temperature and the atomic oxygen mole fraction are respectively $T = 1500$ K and $X_O = 0.04$ at the center of the inter-electrode gap. Moreover, the discharge occurs in a pre-ionized region thanks to a memory effect of the previous discharges. Ideally, this simulation would require the knowledge of the initial temperature $T(x, r)$ and electron density $n_e(x, r)$. For all the steady-state

simulations, a uniform mixture composition has been used with N_2:O_2:O : 77.4:18.6:4 (in mole).

It has been shown in the experiment that the effect of the previous discharges is limited to the inter-electrode gap. The discharge radius has been estimated to 225 µm in the experiment using the radial profiles of the $N_2(B, C)$ states. Much more uncertainties are present on the radial temperature profile, but it is reasonable to assume that it follows the $N_2(B, C)$ profiles. Indeed, the fast gas heating is mainly due to the quenching of these states. The electron density must follow the same radial profile as $N_2(B, C)$ originate from electron impact collisions. As in Popov [158], it is possible to assumed that the electron density follows a radial gaussian profile that reads:

$$n_e(r) = n_{e0} + \Delta n_e \exp\left(-\frac{r^2}{\sigma_r^2}\right) \tag{12.1}$$

In that case, the densities of the positive ions are adjusted to ensure a neutral solution. Similarly, the gas temperature profile can also follow a gaussian profile that reads:

$$T(r) = T_0 + \Delta T \exp\left(-\frac{r^2}{\sigma_r^2}\right) \tag{12.2}$$

The discharge radius measured experimentally corresponds to the FWHM of the $N_2(B, C)$ signal. In Eqs 12.1 and 12.2, σ_r is linked to the FWHM by $\sigma_r = \text{FWHM}/\sqrt{2\ln(2)}$ which is equal to 190 µm at the end of the pulse. However, both the electron density and the gas temperature diffuse during the interpulse. For a 1D diffusion problem governed by

$$\frac{\partial u}{\partial t} = \nu \frac{\partial^2 u}{\partial x^2} \tag{12.3}$$

$$u(x, 0) = u_0 \exp\left(-\frac{x^2}{\sigma^2}\right) \tag{12.4}$$

the analytical solution reads [42]:

$$u(x, t) = \frac{u_0 \sigma}{\sqrt{\sigma^2 + 4\nu t}} \exp\left(-\frac{x^2}{\sigma^2 + 4\nu t}\right) \tag{12.5}$$

An important feature of this solution is the variance increase with time. During the interpulse, the charge species almost diffuse as the positive ions [140, 184] with a diffusion coefficient $D_p \simeq 1 \times 10^{-4}\,\mathrm{m^2\,s^{-1}}$. Thus at the end of the interpulse ($t = 1 \times 10^{-4}$ s) σ can be estimated to 275 µm. Concerning the temperature, the thermal diffusitivy in air at 1000 K is around $1.68 \times 10^{-4}\,\mathrm{m^2\,s^{-1}}$, leading to $\sigma \simeq 322$ µm. To conclude, these values are both close to the 300 µm used for the initial conditions in Popov [158]. Hence, the value of 300 µm is retained in this work.

In the end, different initial combinations detailed in Tab. 12.2 have been investigated. In Case A, both the gas temperature and the electron density are taken uniform at their value on the axis prior to the pulse. This uniform case is uses here to illustrate the effects of the temperature and electron density spatial profiles. In Case B, the gaussian profile given in Eq. 12.2 is used for the temperature whereas the electron density is uniform. Contrary to Case B, Case C assumes a uniform gas temperature and uses Eq. 12.1 to initialize the electron density

profile. Finally, in Case D, both the gas temperature and the electron density are initialized with respectively Eq. 12.1 and Eq. 12.2.

	Temperature			Plasma density		
	T_0 [K]	ΔT [K]	σ_r [μm]	n_{e0} [m^{-3}]	Δn_{e0} [m^{-3}]	σ_r [μm]
Case A	1500	0	-	10^{15-17}	0	-
Case B	1000	500	300	10^{15-17}	0	-
Case C	1500	0	-	10^{15}	10^{17}	300
Case D	1000	500	300	10^{15}	10^{17}	300

Table 12.2: Initial conditions used for the steady state simulations.

12.1.2.2 Initial conditions for the transient simulations

The initial conditions of the transient simulations performed in Section 12.3 do not have significant uncertainties as their are well defined experimentally. The gas temperature is uniform at $T = 1000\ K$ and the mixture is representative of air (*i.e.*, N_2:O_2 : 79:21). The pre-ionization level is not known, but must be low before any plasma actuation. To minimic the photionization effect, an initial uniform plasma density of 10^{14}m^{-3} has been used.

12.1.3 Reduced chemistry

The simulation is performed using the chemistry reduced in Section. 9.2. There are 11 species transported with the Navier-Stokes equations and 9 ions transported in the drift-diffusion framework. Before going to the experimental case, we first compare the reduced chemistry to the simple chemistry of Morrow and Lowke [136] introduced in Section. 4.2.2. Only the discharge propagation is compared since the chemistry of [136] does not describe the plasma decay phase. While the electron coefficients are fitted to experiment in [136], they are provided by BOLSIG+ in our reduced chemistry. This difference is now investigated.

12.1.3.1 Electron properties

A critical property of the electron parameters is the breakdown electric field at which ionization frequency reaches the attachment frequency. Above the breakdown field, a discharge can propagate. Figure 12.2a compares the ionization and attachment frequencies of the reduced chemistry with the one of Morrow and Lowke [136]. In the reduced chemistry, the breakdown field is around 117 Td which is $\approx$ 10 % higher than in Morrow and Lowke [136]. Thus, the electric field threshold to propagate a discharge is slightly higher when using BOLSIG+ to compute the electron parameters. At a high reduced electric field ($E/N \approx 1000$ Td), the ionization frequency of the reduced chemistry is approximately 50% larger than in [136]. These high values of E/N can occur in the streamer head during its propagation. Thus, the streamer propagation using the reduced chemistry might be more difficult numerically compared to the one with the coefficient from [136]. First, an increase in the ionization frequency leads to a decrease of the associated timescale $\tau_\alpha = 1/\nu_\alpha$. Second, the characteristic length scale of charge separation (α^{-1}) in the streamer head is smaller with the coefficients from BOLSIG+ compared with those computed with the coefficient from Morrow and Lowke [136] as shown in Fig. 12.2b.

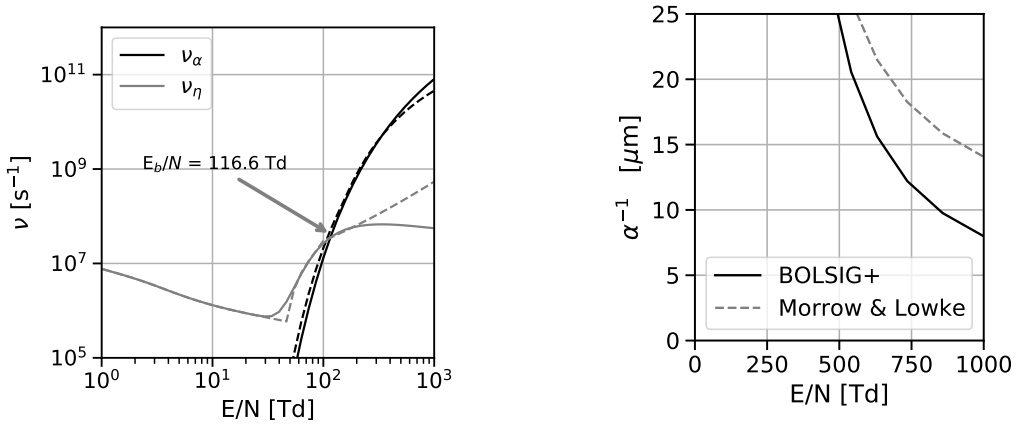

(a) (b)

Figure 12.2: (a) Ionization and attachment frequencies ν_α and ν_η at 1000 K of the reduced chemistry using BOLSIG+ (solid lines) and using the coefficients of Morrow and Lowke [136] (dashes lines) and (b) charge separation length scale in the streamer based on the coeffieicnets using BOLSIG+ and Morrow and Lowke [136].

12.1.3.2 Discharge propagation

The discharge propagation using the data from Morrow and Lowke [136] and our reduced chemistry is compared in Fig. 12.3. An initial atmospheric pressure mixture is considered at 1500 K and the initial uniform composition described in Section 12.1.2. A high background plasma density of $1 \times 10^{15}\,\mathrm{m}^{-3}$ is used to mimic the effect of the plasma channel formed during the previous discharges. These conditions corresponds to the Case A described in Section 12.1.2.1. The positive streamer starts to propagate at $t = 6$ ns while the negative streamer has already traveled 0.75 mm at that time. The two chemistries lead to similar negative streamer propagation in terms of shape and velocity. Whereas the shape of the positive streamer looks similar with both chemistries, its propagation velocity is greater with the reduced chemistry. This is primarily due to the higher ionization frequency in the head of the positive streamer for the reduced chemistry. This difference only arises for the positive streamer because the electric field in the streamer head is higher than for the negative streamer, as shown in Fig. 12.4, where the reduced electric field peaks at ≈ 1000 Td in the positive streamer head. Indeed, the difference between the two chemistries for the ionization frequency increases with the reduced electric field, as discussed in Section 12.1.3.1. To conclude, the simple chemistry proposed by Morrow and Lowke [136] is suitable for preliminary studies. Still, it can lead to substantial differences compared to chemistries in which the EEDF is solved consistently using BOLSIG+ (i.e. by considering the initial composition and temperature). It is worth noting that no oscillation or numerical branching occur in the simulation, thanks to the small cell size used ($\Delta x_1 \leq \alpha^{-1}/2$).

12.2 Single pulse in the steady state regime

As discussed in Section 12.1.2, it can take several hundreds of pulses to reach the steady-state regime during which the measurements are performed in [167]. Thus, this section considers initial conditions close to the real ones at the beginning of a pulse in the steady-state regime.

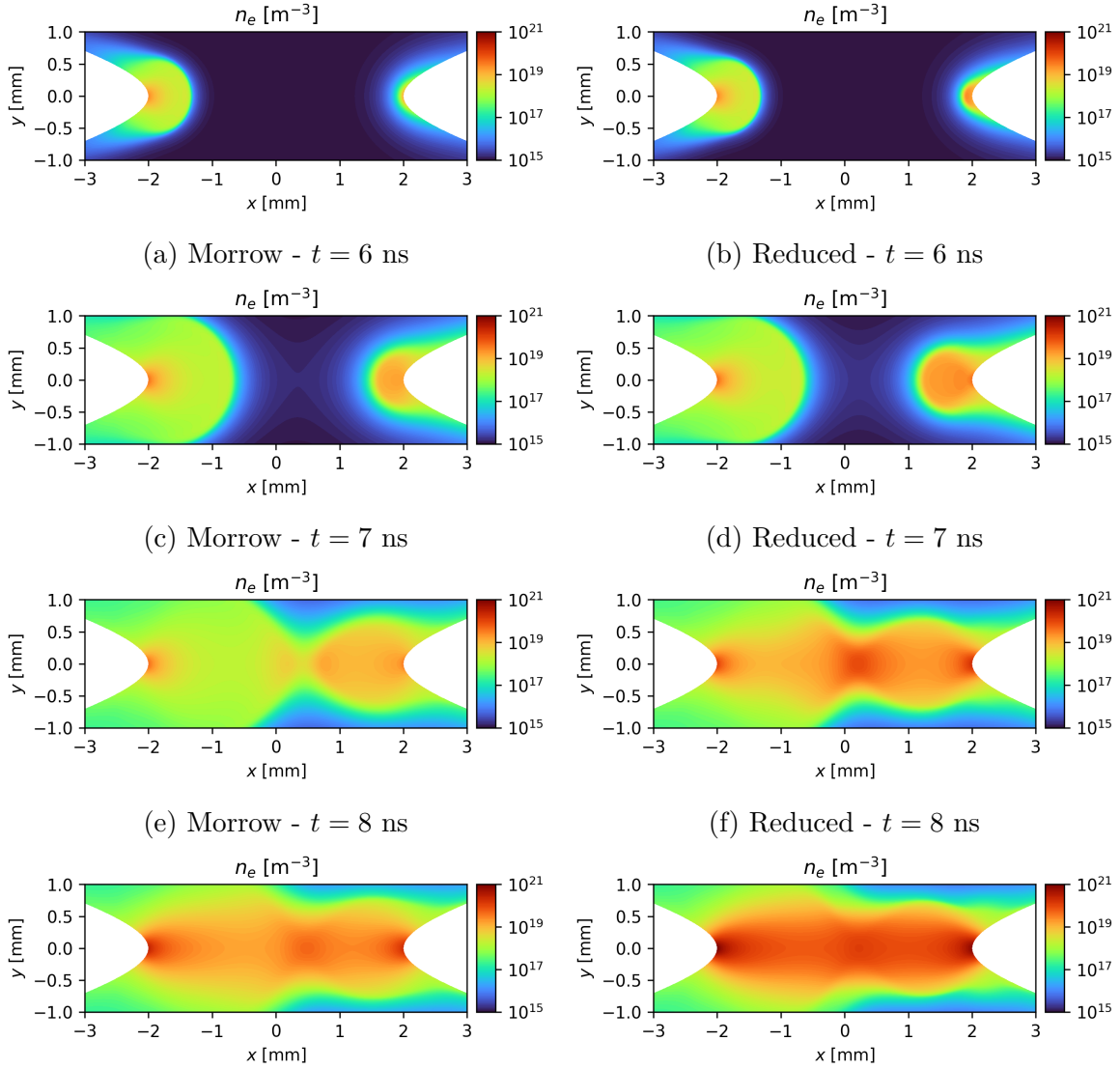

(a) Morrow - $t = 6$ ns

(b) Reduced - $t = 6$ ns

(c) Morrow - $t = 7$ ns

(d) Reduced - $t = 7$ ns

(e) Morrow - $t = 8$ ns

(f) Reduced - $t = 8$ ns

(g) Morrow - $t = 9$ ns

(h) Reduced - $t = 9$ ns

Figure 12.3: Discharge propagation comparison using (left) the analytical coefficients from Morrow and Lowke [136] and (right) using the reduced chemistry in which BOLSIG+ is used to solve the EEDF. Initial conditions of Case A, $n_{e0} = 1 \times 10^{15}\,\mathrm{m}^{-3}$.

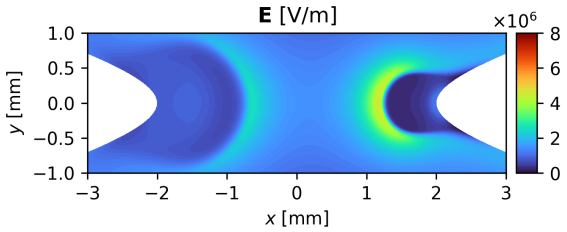

Figure 12.4: Norm of the electric field during the discharge propagation using the reduced chemistry at t=7ns. Initial conditions of Case A, $n_{e0} = 1 \times 10^{15}\,\mathrm{m}^{-3}$.

12.2.1 Case A: Uniform backgrounds

We first consider an uniform background temperature field at 1500 K corresponding to the value measured on the axis at the beginning of the discharge in the steady-state regime. However, the electron density is not well known at the beginning of the pulse. Indeed, the method used in [167] to determine the electron density is only applicable when the discharge starts to dissociate the water vapor present in the laboratory air. Two methods have been used to estimate the initial electron density. The first method is based on the work of [49]: a high background density of $1 \times 10^{15}\,\mathrm{m}^{-3}$ is considered as a lower limit that mimics at least the photoionization effect. This case is referred to as Case A.1 in this section. In the second method, thanks to the work of [160], the electron density on the axis at $t = 40\,\mu\mathrm{s}$ can be estimated to $8 \times 10^{17}\,\mathrm{m}^{-3}$. Hence for the second initial value considered in Case A.2, it is reasonable to consider an electron density of $1 \times 10^{17}\,\mathrm{m}^{-3}$ at $t = 100\,\mu\mathrm{s} = 1/f$ which account for both diffusion and chemical processes. A comparison of the discharge propagation for the two considered conditions is shown in Fig. 12.5. An increase of the background electron density leads to a very diffuse discharge.

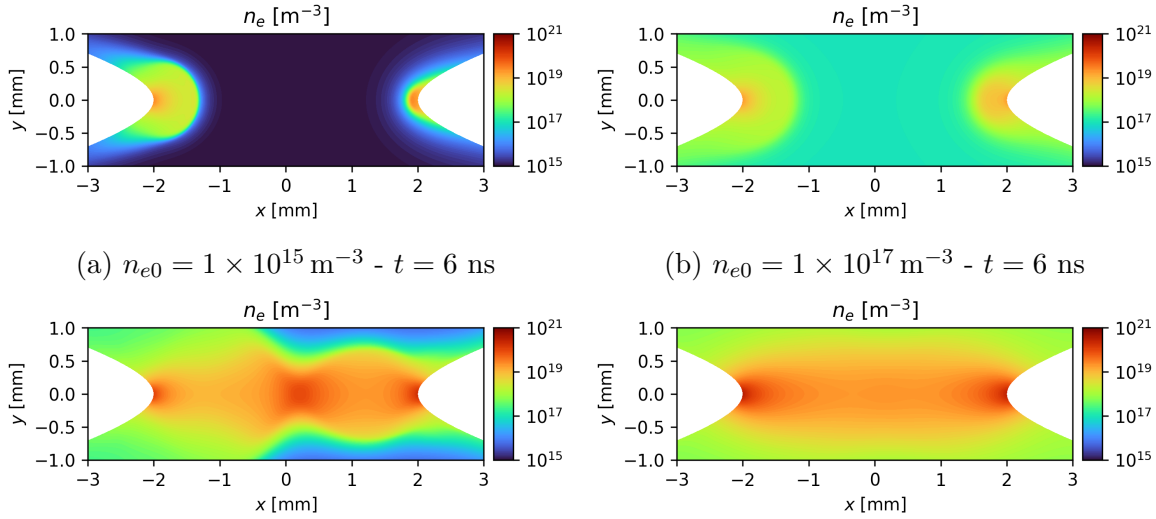

(a) $n_{e0} = 1 \times 10^{15}\,\mathrm{m}^{-3}$ - $t = 6$ ns

(b) $n_{e0} = 1 \times 10^{17}\,\mathrm{m}^{-3}$ - $t = 6$ ns

(c) $n_{e0} = 1 \times 10^{15}\,\mathrm{m}^{-3}$ - $t = 8$ ns

(d) $n_{e0} = 1 \times 10^{17}\,\mathrm{m}^{-3}$ - $t = 8$ ns

Figure 12.5: Effect of the initial electron density on the discharge propagation for a uniform initial solution: (left) Case A.1 and (right) Case A.2.

Whereas 0.81 mJ and 1.06 mJ are respectively deposited in Case A.1 and Case A.2, the gas temperature does not follow the experimental trend as shown in Fig. 12.6 where only Case A.1 is shown (Case A.2 exhibits very similar profiles). After 100 µs, the gas temperature only increases by 500 K in both cases, corresponding to half the experimental heating. The same trend is observed in Fig. 12.6b for the atomic oxygen production, which is underestimated by a factor of two on the discharge axis. This result is correlated to the wider discharge in the simulations compared to the experiment. At $t = 9$ ns, the radial profile of $N_2(B_3)$ has been measured experimentally and is used to estimate the discharge radius. The $N_2(B_3)$ radial profile of Case A.1 is shown in Fig. 12.6c and reveals a FWHM of 319 µm. The FWHM increases to 352 µm in Case A.2. Consequently, the discharge energy density[1] is around $0.63 \times 10^6\,\mathrm{J\,m}^{-3}$ and $0.68 \times 10^6\,\mathrm{J\,m}^{-3}$ in Case A.1 and Case A.2 respectively, that is lower than the experiental value of $1.05 \times 10^6\,\mathrm{J\,m}^{-3}$ despite the higher discharge energy in the simulations. However, the

[1]The energy density e^p is estimated by $e^p = E^p/(\pi\ \mathrm{FWHM}^2\ d)$

energy fractions converted to heat and vibration are coherent with the study performed in Section 6.9 and respectively correspond to 203 µJ (25% of the discharge energy) and 188 µJ (23% of the discharge energy) for the Case A.1 at $t = 100$ ns. Thus, the main features of the plasma chemistry are well reproduced by the reduced mechanism on a multi-dimensional simulation.

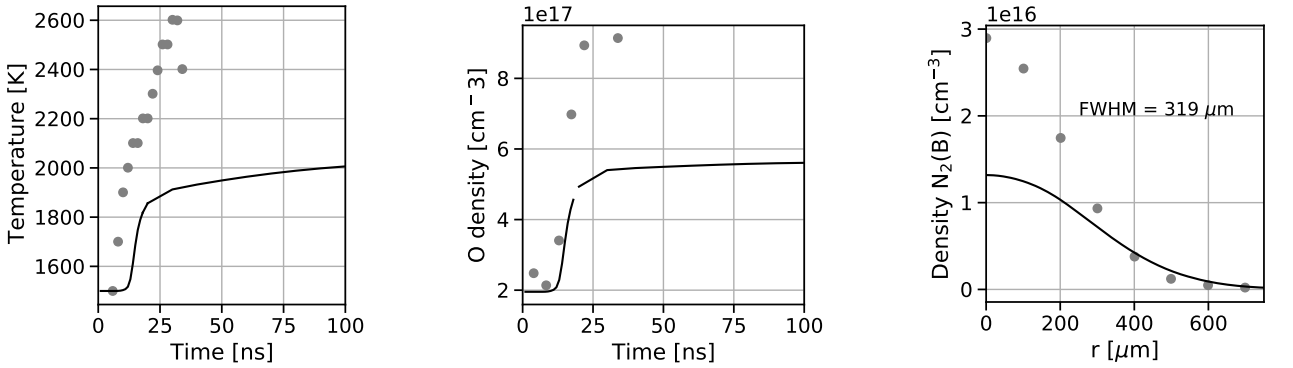

(a) Gas temperature (b) Atomic oxygen production (c) $N_2(B_3)$ radial profile

Figure 12.6: Case A.1 comparison between simulation and experiental measurements for (a) the gas temperature (b) the atomic oxygen production and (c) $N_2(B_3)$ radial profile at $x = 0$ and $t = 9$ ns in the experiment and 14 ns in the simulation. Solid lines correspond to simulation, symbols are the experimental results [167].

12.2.2 Case B: Temperature profile

When using an uniform temperature and electron density fields, the discharge is wider than in the experiment. One reason for that could be the radial temperature profile. Indeed, the discharge can propagate more easily in a hot environment due to the higher reduced electric field and will therefore concentrate on the axis. To verify this intuition, a simulation is performed with a gaussian temperature profile in the radial direction corresponding the the initial conditions of Case B detailed in Tab. 12.2. The uniform pre-ionization level is set to $1 \times 10^{15}\,\mathrm{m}^{-3}$. Results of the discharge propagation is shown in Fig. 12.7. The negative streamer moves at almost the same velocity that in Case A. However, it propagates less diffusely, and the high plasma density region is even narrower than in the positive streamer at $t = 9$ ns. The positive streamer is also more concentrated on the axis and moves a bit faster than in Case A.1 of Section 12.2.1.

More quantitatively, the gas temperature and atomic oxygen dynamics on the axis exhibit a good agreement with the experimental measurements as shown in Figs. 12.8a and 12.8b. However, it is not enough to look only at these two quantities. Indeed, the discharge radius is underestimated by a factor two as indicated in Fig.12.8c. The same goes true for the discharge energy which is only about 210 µJ leading to an energy density $e^p \simeq 1.4 \times 10^6\,\mathrm{J\,m}^{-3}$. This value is even higher than in the experiment and reflects the discharge contraction on the axis. Moreover, the electrical current computed in the plane ($x = 0$, r, θ) and plotted in Fig. 12.8d is also smaller than in the experiment. As shown in Section 12.2.1, a higher initial electron density leads to a larger discharge. The influence of this parameter has been evaluated in another simulation with the same temperature profile and a uniform initial electron density of $1 \times 10^{17}\,\mathrm{m}^{-3}$. No significant changes were observed: the discharge energy increases to 250 µJ

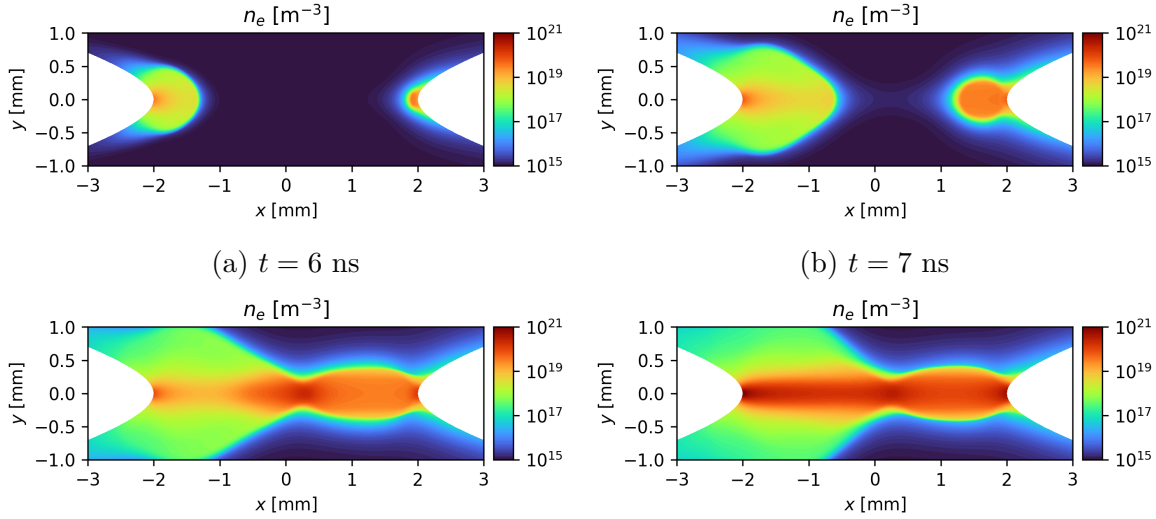

(a) $t = 6$ ns (b) $t = 7$ ns

(c) $t = 8$ ns (d) $t = 9$ ns

Figure 12.7: Discharge propagation using the radial temperature profile of Case B and uniform background electron density of $1 \times 10^{15}\,\mathrm{m}^{-3}$.

and the FWHM is around 100 µm. Contrary to what has been observed in Casen A (see Section 12.1.2), an increase of the electron density does not lead to a rise in the discharge radius. Moreover, the initial electron density change has only a small influence on the results.

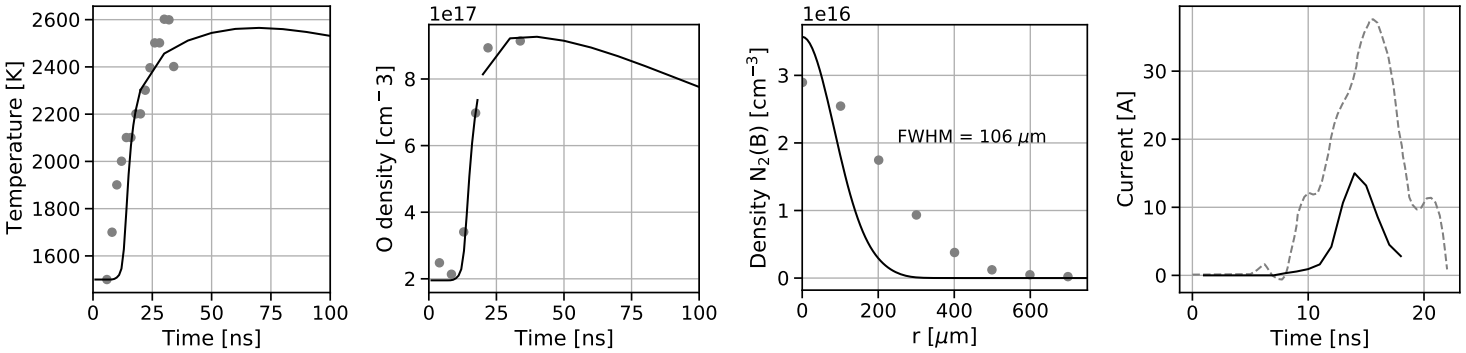

(a) Gas temperature (b) O production (c) $N_2(B_3)$ radial profile (d) Electrical current

Figure 12.8: Comparison of Case B simulation ($1 \times 10^{15}\,\mathrm{m}^{-3}$) to the experimental measurements with (a) the gas temperature (b) the atomic oxygen production, (c) $N_2(B_3)$ radial profile at $x = 0$ and $t = 9$ ns in the experiment and 14 ns in the simulation. and (d) the electrical current. Solid lines correspond to simulation, symbols are the experimental results [167].

12.2.3 Case C: Charged species profiles

The non-uniformity of the electron density at the beginning of the pulse is now investigated. Indeed, the high electron density from the previous pulses must be higher close to the axis compared to its value at some distance from the axis. Thus, the electron density is initialized with a gaussian profile in the radial direction as detailed in Tab. 12.2, Case C. The temperature is supposed to be uniform at 1500 K. In this case, the positive streamer moves significantly

faster than in the cases studied in Sections 12.2.1 and 12.2.2, as shown in Fig. 12.9, at a velocity $\geq 1\,\mathrm{mm\,ns^{-1}}$. Moreover, the positive streamer propagation occurs at an almost constant radius. After the positive and negative streamers connection, the plasma channel radius is lower than in Case A but larger than in Case B. Moreover, the discharge radius is slightly lower than the initial imposed profile and is very close to the experimental one, as depicted in Fig. 12.10c. In this case, the energy of the discharge is around 1.05 mJ corresponding to an energy density of $\approx 1.3 \times 10^6\,\mathrm{J\,m^{-3}}$ that is only 25% higher than in the experiment. Despite the good agreements on the gas temperature and atomic oxygen production shown in Figs. 12.10a and 12.10b, the gas temperature rise is still a bit underestimated despite the higher discharge energy density compared to the experiment. The results concerning the temperature and atomic oxygen production are very close to those obtained in [158] who used the same initial condition in a 1D-radial simulation. This will be further investigated in Section 12.2.5 by adding a spatial profile of temperature. Concerning the electrical current shown in Fig. 12.10d, it is overestimated in the simulation by a factor of two with a current peak of 80 A.

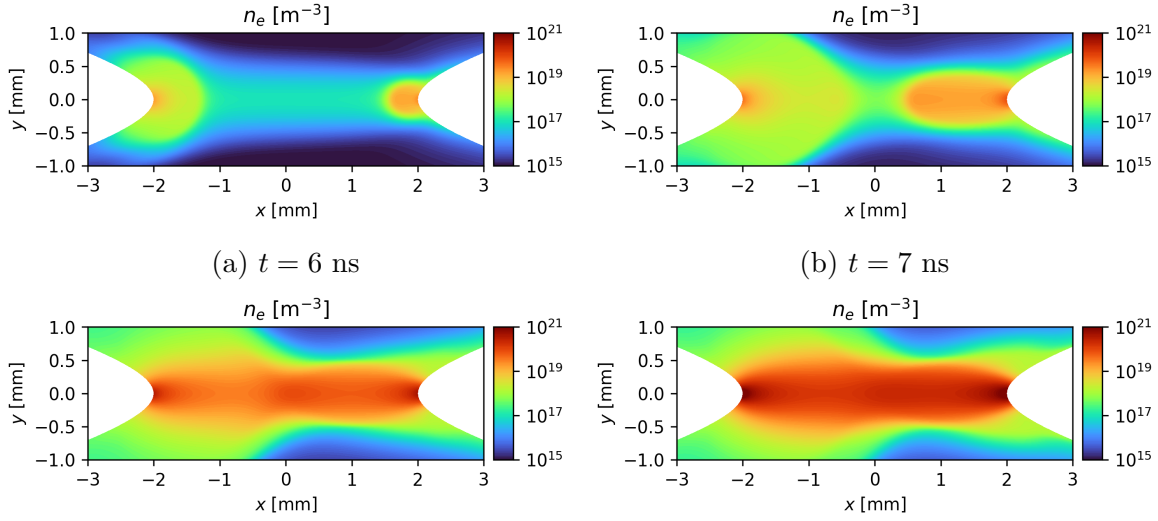

(a) $t = 6$ ns (b) $t = 7$ ns

(c) $t = 8$ ns (d) $t = 9$ ns

Figure 12.9: Discharge propagation in the Case C.

12.2.4 Case D: Charged species and temperature profiles

The initial radial profiles of gas temperature and electron density have been investigated individually in Sections 12.2.2 (Case B) and 12.2.3 (Case C) respectively. It has been observed that imposing a radial gas temperature profile (Case B) can lead to an impressive contraction of streamers leading to a very small discharge radius. The use of a radial electron density profile (Case C) also permits to lowered the discharge radius compared to a uniform density (Case A). However, the plasma radius change is less pronounced in Case C (density profile) than in Case B (temperature profile). These two profiles are now combined to analyze which one is the most important for the discharge features, corresponding to Case D in Tab. 12.2. The discharge propagation is shown in Fig. 12.11. At $t = 9$ ns, the plasma channel is growing almost uniformly in the axial direction, and the discharge radius is almost axially constant. Moreover, the discharge radius is smaller than in all the previous cases studied with $r_d = 93\,\mu\mathrm{m}$ as shown in Fig. 12.12c. The constriction effects observed with the radial profiles of electron density and

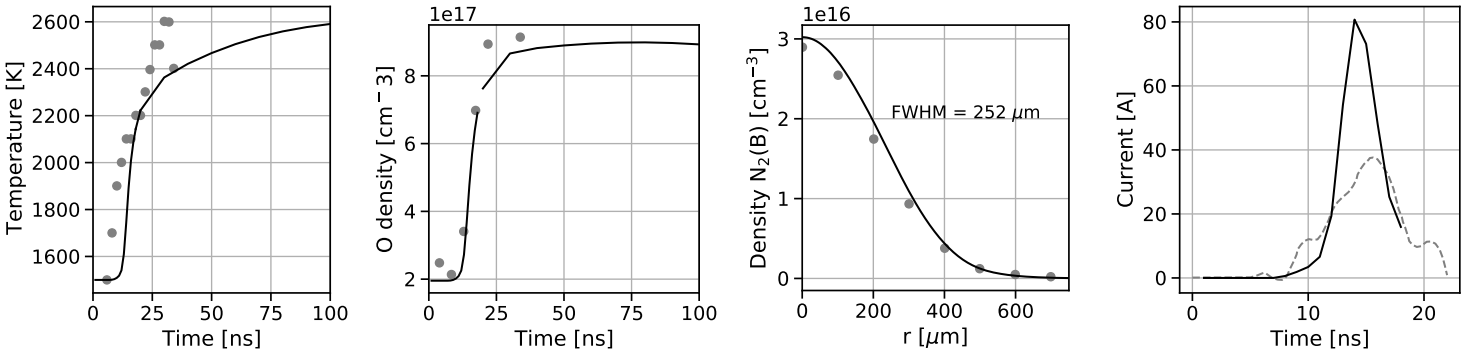

(a) Gas temperature (b) O production (c) $N_2(B_3)$ radial profile (d) Electrical current

Figure 12.10: Comparison of Case C simulation to the experimental measurements with (a) the gas temperature (b) the atomic oxygen production, (c) $N_2(B_3)$ radial profile at $x = 0$ and $t = 9$ ns in the experiment and 14 ns in the simulation. and (d) the electrical current. Solid lines correspond to simulation, symbols are the experimental results [167].

gas temperature are cumulated. This very small discharge radius leads to an overprediction of the gas temperature and atomic oxygen density on the axis despite the small discharge energy around 300 µJ. This is due to the high energy density of the discharge $e^p \simeq 2.75 \times 10^6\,\mathrm{J\,m^{-3}}$. In close connection with the energy underestimation, the electrical current is almost two times lower than in the experiment as shown in Fig. 12.12d. Unfortunately, there is no experimental or numerical data allowing to adjust the temperature and electron density shapes. A first answer will be given in Section 12.3 when multiple pulses are applied.

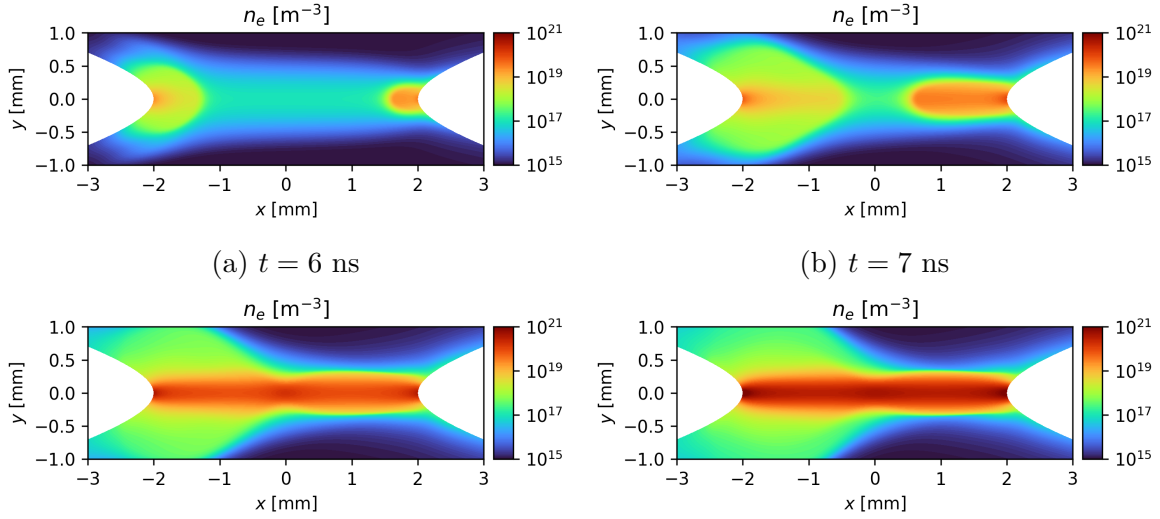

(a) $t = 6$ ns (b) $t = 7$ ns

(c) $t = 8$ ns (d) $t = 9$ ns

Figure 12.11: Discharge propagation in the Case D.

12.2.5 2D temperature and pressure maps

Two very different gas dynamics were observed when testing the different initial conditions (Casees A to D). Figure 12.13 shows the temperature and pressure fields at $t = 200$ ns resulting

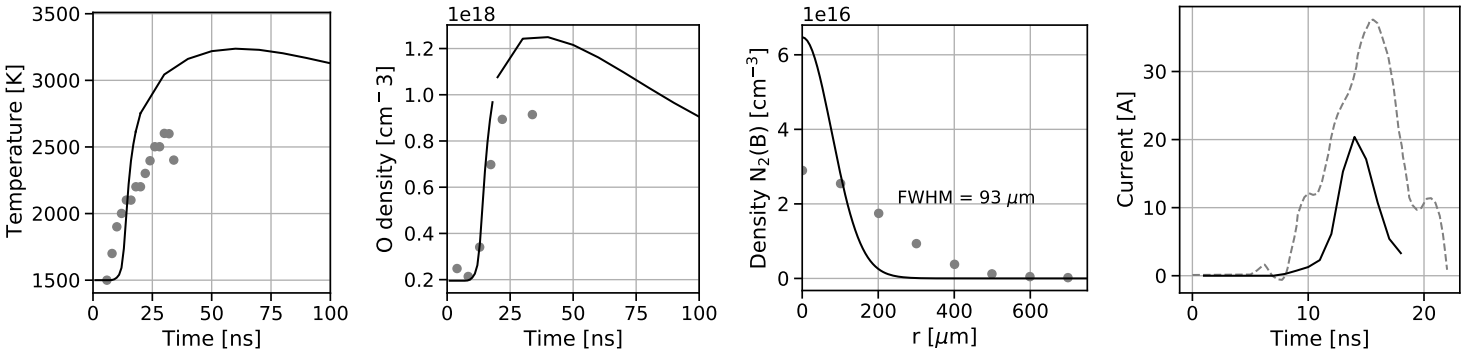

(a) Gas temperature (b) O production (c) $N_2(B_3)$ radial profile (d) Electrical current

Figure 12.12: Comparison of Case D simulation to the experimental measurements with (a) the gas temperature (b) the atomic oxygen production, (c) $N_2(B_3)$ radial profile at $x = 0$ and $t = 9$ ns in the experiment and 14 ns in the simulation. and (d) the electrical current. Solid lines correspond to simulation, symbols are the experimental results [167].

from the previous simulations. For the homogeneous initial conditions (Case A), the temperature field is marked by two hot spots at the electrode tips, as shown in Fig. 12.13a. At the middle of the inter-electrode gap, the gas temperature only increases by 500 K to reach $\approx$ 2000 K. This temperature pattern is accompanied by the formation of two spherical pressure waves around the electrodes depicted in Fig. 12.13b. When adding a radial profile on the electron density (Case C), the same temperature and pressure patterns are observed (see Figs. 12.13e and 12.13f). Hence, the initial electron density profile does not significantly affect the shape of the spatial discharge energy distribution, but the discharge energy density increases. Now looking at the temperature profile effects in Figs. 12.13c and 12.13d (Case B), the heated channel is much smaller in the radial direction compared to Case A and C with homogeneous initial temperature. Moreover, the gas heating is almost axially invariant in Case B with only two small hot spots at the electrode extremities. The resulting pressure wave expands directly in a cylindrical shape with a constant pressure peak along the axial direction. These two patterns are also observed in Case D for which both n_e and T_g are initialized with a gaussian shape. Since the simulation seems to be very sensitive to the initial temperature profile, it is important to have an idea of its shape when dealing with NRP-spark discharge for which the previous discharges can significantly heat the inter-electrode area.

12.2.6 Secondary pulse

Thanks to a secondary pulse, the gas temperature has been measured at $t = 270\,\text{ns}$ as indicated in Fig. 12.14. This important measurement allows to observe a slow but continuous gas temperature increase between the end of the primary pulse and the beginning of the secondary pulse. Indeed, the gas temperature increases by 400 K between 20 ns and 270 ns corresponding to a heating rate of $1.6\,\text{K}\,\text{ns}^{-1}$.

In the 0D study performed in Section 6.9, it was impossible to include the secondary pulse due to the lack of information on the gas dynamics between the primary and secondary pulses. Thus, the multi-dimensional simulations performed in this chapter could help to investigate the secondary pulse. To do so, the simulations made in Sections 12.2.2 (Case B - Radial T_g profile), 12.2.3 (Case C - Radial n_e profile) and 12.2.4 (Case D - Radial n_e and T_g profiles) are

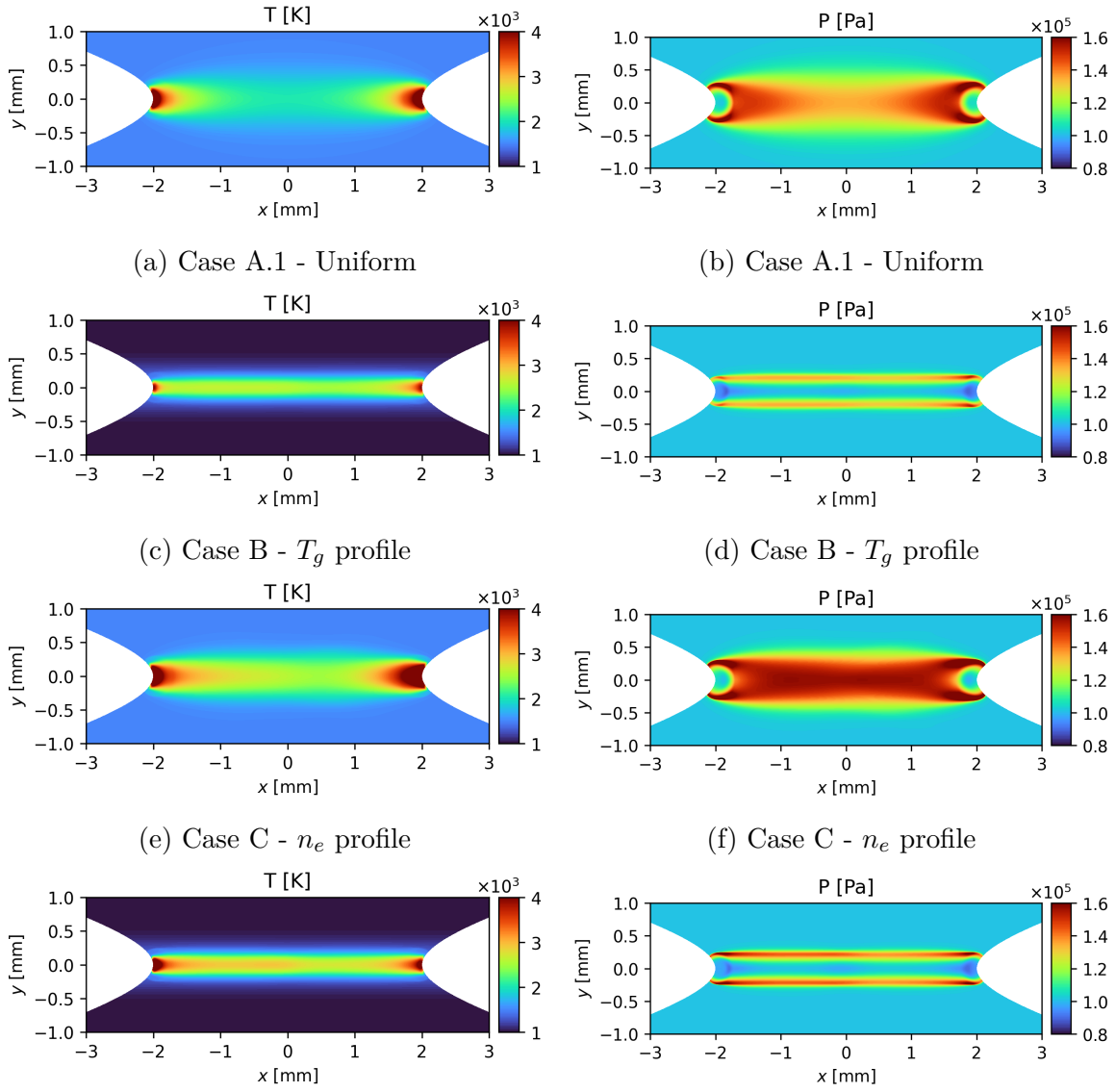

(a) Case A.1 - Uniform

(b) Case A.1 - Uniform

(c) Case B - T_g profile

(d) Case B - T_g profile

(e) Case C - n_e profile

(f) Case C - n_e profile

(g) Case D - n_e and T_g profiles

(h) Case D - n_e and T_g profiles

Figure 12.13: 2D maps of temperature and pressure at 200 ns for the different initial conditions considered.

continued up to 270 ns and the resulting gas temperature dynamics are shown in Fig. 12.15. In Case A shown in Fig. 12.15a, the gas temperature on the axis quickly decreases due to the pressure wave expansion. This strong pressure wave is formed due to the high energy density of the discharge close to the axis. In this case, the maximum temperature reached is much lower than the value measured at 270 ns. The temperature decrease due to the gas expansion is less pronounced in the case considering an electron density profile (Fig. 12.15b). Indeed, the temperature continues to increase up to $\approx$ 150 ns before gradually decreasing. However, the gas temperature is 400 K lower than the experiment at 270 ns. Finally in Case D (see Fig. 12.15c), the gas temperature increases to 3250 K at 50 ns before gradually decreasing because of the pressure wave expansion. Then, it increases again but slowly at 200 ns to reach a value comparable to the experimental measurement at 270 ns.

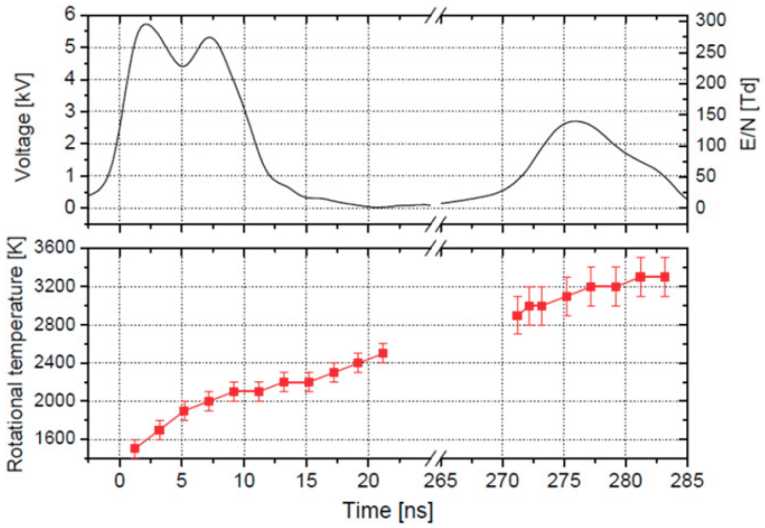

Figure 12.14: Primary and secondary pulses synchronized with the rotational temperature of $N_2(C_3)$ [Reproduced from [167]].

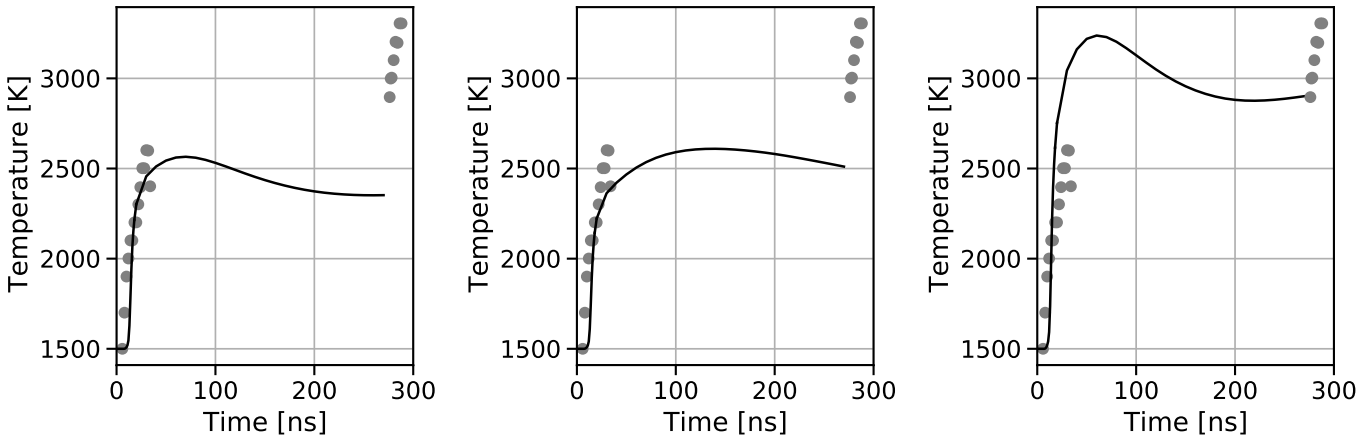

(a) Case B - T_g gaussian (b) Case C - n_e gaussian (c) Case D - T_g and n_e gaussians

Figure 12.15: Evolution of the temperature up to the secondary pulse at $t = 270$ ns considering different options for the initial conditions.

Despite the differences compared to the experiments observed in Section 12.2.4 for the case represented in Fig. 12.15c, the secondary pulse shown in Fig. 12.14 has been applied to evaluate its impact. A good agreement is found for the gas temperature increase during the secondary pulse as shown in Fig. 12.16. It is worth noting that no discharge propagation occurs during the secondary pulse and the plasma density increases almost uniformly in the axial direction, as shown in Fig. 12.17.

12.2.7 Partial conclusions

The steady-state regime experimentally studied in [167] has been investigated in a multi-dimensional framework. Different initial conditions have been considered to mimic the effects of the previous discharges (*i.e.* a gas heating and charged species residuals). It has been observed

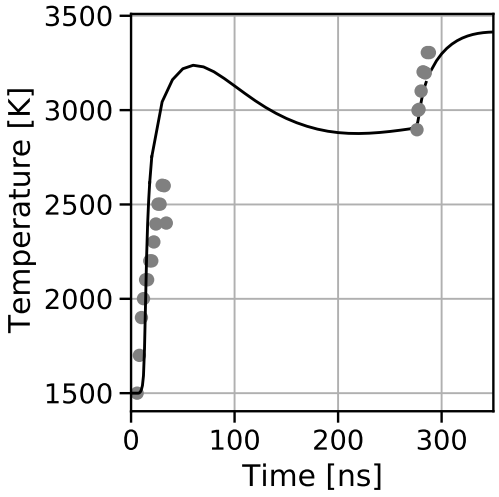

Figure 12.16: Gas temperature evolution including the secondary pulse using both temperature and electron density profile at $t = 0$.

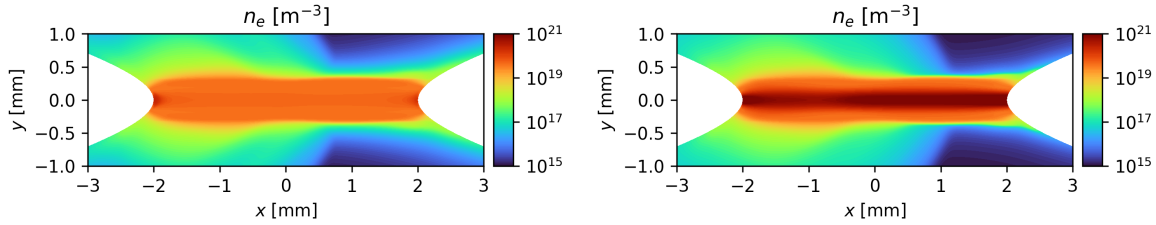

(a) $t = 271$ ns (b) $t = 277$ ns

Figure 12.17: 2D maps of the electron density at (a) the beginning of the secondary pulse and (b) the peak value of voltage.

that the choice of the initial conditions strongly influences the discharge radius. In particular, imposing a radial temperature profile leads to a discharge constriction on the axis, which significantly reduces the discharge radius. This observation is accompanied by an axially homogeneous gas heating and the emergence of a cylindrical pressure wave. On the other hand, using a homogeneous initial temperature produces a larger discharge than with a radial profile. The simulated discharge radius considering a homogeneous initial temperature are closer to the experimental measurements. Moreover, adding a Gaussian profile on the charged species density increases the discharge energy density, and good comparisons have been noticed. A summary of the results obtained in Cases A to D can be found in Tab. 12.3. It seems possible to improve these results with a better knowledge of the initial temperature field, which significantly influences the results. Finally, the model has proven its capacity to properly distribute the discharge energy into heating and vibrational energies. Indeed, it was found in Section 12.2.1 that 25% of the discharge energy is spent to heat the gas and 23% is stored into vibrational energy. These values are close to those obtained in the 0D study made in Section 6.9.

	Case A	Case B	Case C	Case D	Experiment
E_p [mJ]	0.81	0.21	1.05	0.3	0.67
$T^{\max}$ [K]	2000	2550	2600	3200	[2600 - 3000]
$n_O^{\max}$ [m^{-3}]	5.5×10^{23}	9.5×10^{23}	9×10^{23}	1.25×10^{24}	1.1×10^{24}
Radius [μm]	319	106	252	93	[225 - 265]
$I^{\max}$ [A]	60	15	80	20	40

Table 12.3: Summary of the results obtained in Cases A to D in the steady-state simulations of the experiment from Rusterholtz et al. [167]

12.3 Transient regime using multiple-pulses

The study performed in Section 12.2 has revealed the influence of the initial conditions on the discharge propagation in steady state conditions. In this section, the transient phase of the experiment has been simulated starting from an initial mixture at 1000 K and a background plasma density of $1 \times 10^{15}\,m^3$ to mimic photoionization. To apply tens of plasma discharges, it is necessary to consider the flow around the electrodes since it is responsible for a convective energy loss. The steady-state flow before plasma actuation is first studied in Section 12.3.1. Then in Section 12.3.2, around 100 pulses are applied using the experimental voltage profile, which peaks at a maximum of 5.7 kV. A 6.2 kV-voltage is finally investigated in Section 12.3.3 to account for the pulse-to-pulse variation (+10%) of the voltage and a potential secondary pulse, which could increase the discharge energy. These simulations are performed using the modeling strategy described in Section 11.6.

12.3.1 Flow field

It is essential to account for the flow around the electrodes to simulate several discharges. Indeed, this flow influences the discharge regime as discussed in [166]. The airflow could remove a part of the hot channel formed during the high voltage pulse and replace it with ambient air. For example with the flow rate used in [167] corresponding to a velocity of $2.6\,m\,s^{-1}$, one gaseous particle is traveling $\approx 250\,\mu m$ during an interpulse period. Thus, the mixture is entirely refreshed after ≈ 15 pulses, which is much lower than the number of pulses required to reach the steady-state spark regime.

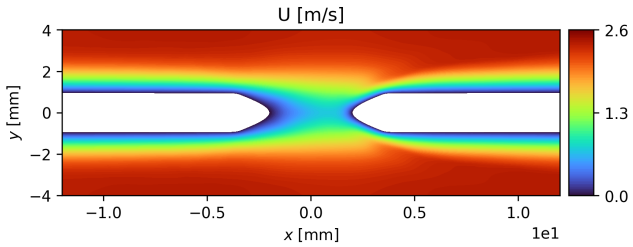

Figure 12.18: Flow field before the plasma actuation for the conditions of Rusterholtz et al. [167] ($2.6\,m\,s^{-1}$)

12.3.2 5.7 kV case

In this section, the experimental pulse given in [167] is applied at a 10 kHz frequency until a steady-state regime is reached. The effects of the repetitive pulses on the discharge pattern are first investigated. Maps of electron density at the end of the pulse are shown in Fig. 12.19. The first pulse, without any pre-ionized channel, is quite different from the others. However, there is no significant change between the second pulse and the following ones. Only the background electron density far from the axis increases a little bit to reach a steady-state regime after ten pulses. This qualitative observation is highlighted in Fig. 12.20a, where the discharge radius is defined as the FWHM of $N_2(B_3)$ at $t = 18$ ns. A sharp increase is first observed between the first and second pulses. Then, the discharge radius slowly decreases to reach a steady-state after approximately 20 pulses. At the same time, the gas temperature at the beginning of the discharge only increases by 12 K after 100 pulses. The gas temperature also reaches a stationary state after ≈ 80 pulses. As discussed previously, the gas temperature and electron density radius at the beginning of the pulse are very important as they can significantly influence the discharge pattern. The FWHM of the gas temperature and the electron density are shown in Fig. 12.20b. For the electron density, the radius follows the same trend as for $N_2(B_3)$ but with a higher value which stabilizes at 775 µm. However, the temperature channel radius drastically decreases between the first and second pulse. Then it continuously increases to reach a stationary value of 550 µm. In these conditions, the plasma and heated channels do not have the same radius, the former being 1.4 times higher than the latter.

As shown previously, the gas temperature increase during the first hundred pulses is very low and does not exceed 15 K. Indeed, the discharge energy remains very low in the conditions studied, as shown in Fig. 12.21 and only a glow discharge is observed. The steady-state regime observed indicates that the energy loss due to the convection and diffusion processes must approximately correspond to 5 µJ per pulse period (*i.e.* the energy deposited by the discharge).

The flow also affects the temperature field in Fig. 12.22a which reveals an asymmetry between the cathode and anode sides. Indeed, ambient air at 1000 K enters the cathode region between each pulse, leading to a cooling effect. On the other side, the air flowing toward the anode area has been heated by the discharge. Thus, energy accumulates in this region. In addition to the cooling effect, the gas flow transports the discharge energy upstream (*i.e.*, to the right) and is clearly visible at $t = 11$ ms. This phenomenon could be used to provide chemical or heating energy to a flame located upstream of the discharge area as shown in Figs. 12.22a and 12.22b.

By applying the 5.7 kV pulse of [167], only a stationary glow discharge was observed and no glow-to-spark transition occurred. This observation could be explained by the uncertainties on the voltage profile measured experimentally which must be imposed in the simulation:

- Pulse to pulse variations (±10%)
- The voltage measurement made in [167] has been performed in the spark regime (steady state). What about the voltage waveform during the transient phase?
- Possible secondary pulse has been ignored for now in the 5.7 kV transient simulation.

In the next section, the voltage profile has been rescaled to have a peak of 6.2 kV, corresponding to a 10% increase, in order to increase the discharge energy.

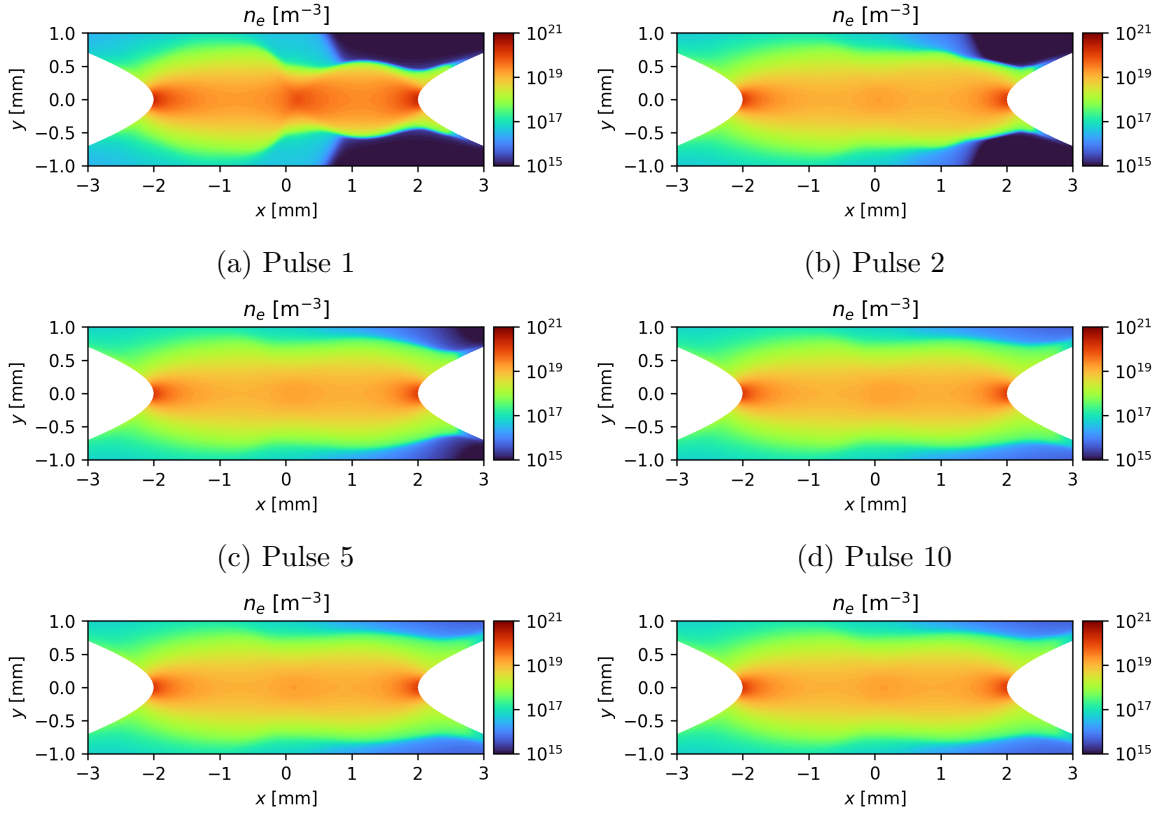

(a) Pulse 1

(b) Pulse 2

(c) Pulse 5

(d) Pulse 10

(e) Pulse 50

(f) Pulse 100

Figure 12.19: 2D maps of the electron density at the end of different pulses in the 5.7 kV pulsed simulation.

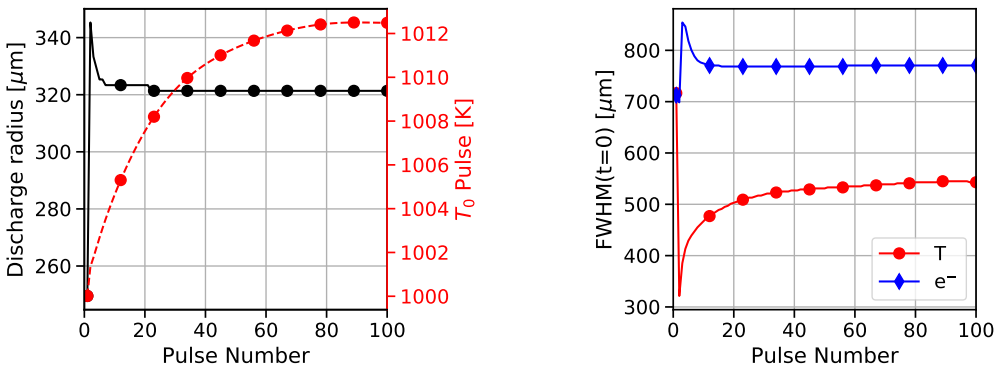

(a)

(b)

Figure 12.20: Time evolution of (a) the discharge radius and gas temperature at the beginning of each pulse and (b) FWHM of electron density and gas temperature for the 5.7 kV pulsed simulation.

12.3.3 6.2 kV case

In this section, the applied voltage has the same shape as in the experiment, but is rescaled to reach a maximum of 6.2 kV. In order to decompose the analysis, the discharge energy is first investigated to get a first idea of the discharge regimes that occur in the simulation. The

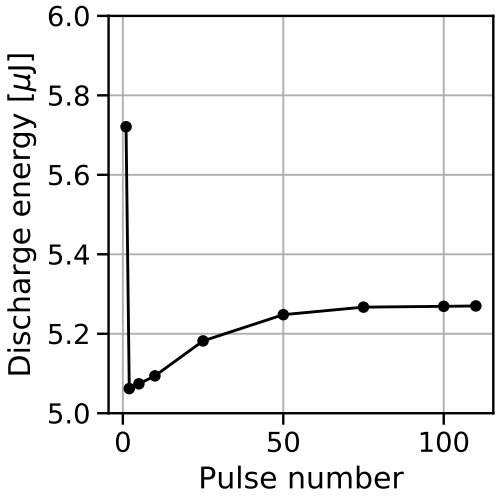

Figure 12.21: Discharge energy in the 5.7 kV pulsed simulation.

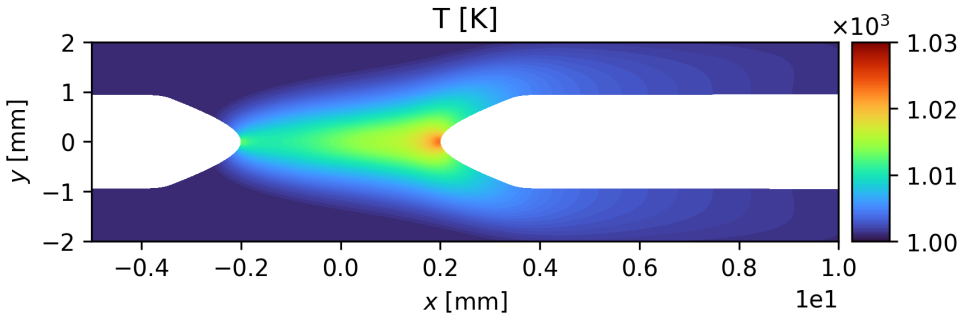

(a)

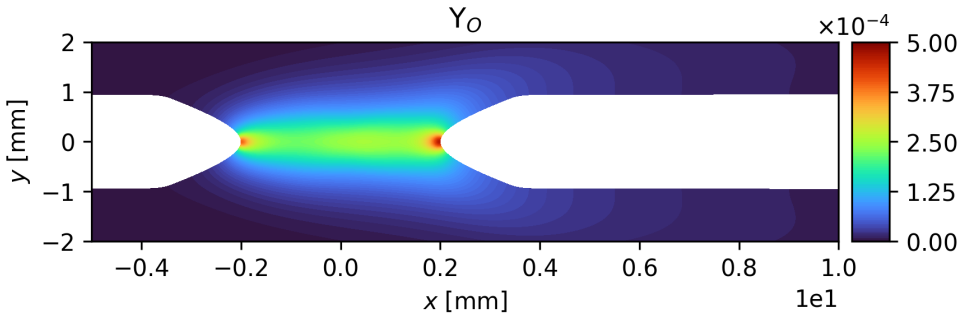

(b)

Figure 12.22: Gas temperature and atomic oxygen fields at the end of the 110$^{\text{th}}$ pulse ($t = 11$ ms) in the 5.7 kV pulsed simulation.

discharge energy is relatively low during the first pulses and corresponds to a weak glow discharge as in the previous 5.7kV-simulation. The increase of the applied voltage allows tripling the value of the discharge energy, which then grows linearly up to the 300$^{\text{th}}$ pulse. Then, the discharge energy starts to accelerate exponentially, as depicted in Fig.12.23b. A clear transition from glow to spark discharge is observed between the pulses 370 and 377, where an exponential growth of the discharge energy and gas temperature occur. Notice that the 378$^{\text{th}}$ pulse has led

to a discharge energy of 8 mJ, leading to an unphysical solution that will be discussed later. The glow to spark transition can also be observed in Fig. 12.23c showing the time evolution of the gas temperature at the middle of the gap. The gas temperature increase remains below 200 K up to the 370$^{\text{th}}$ and then drastically increases, indicating the change of discharge regime.

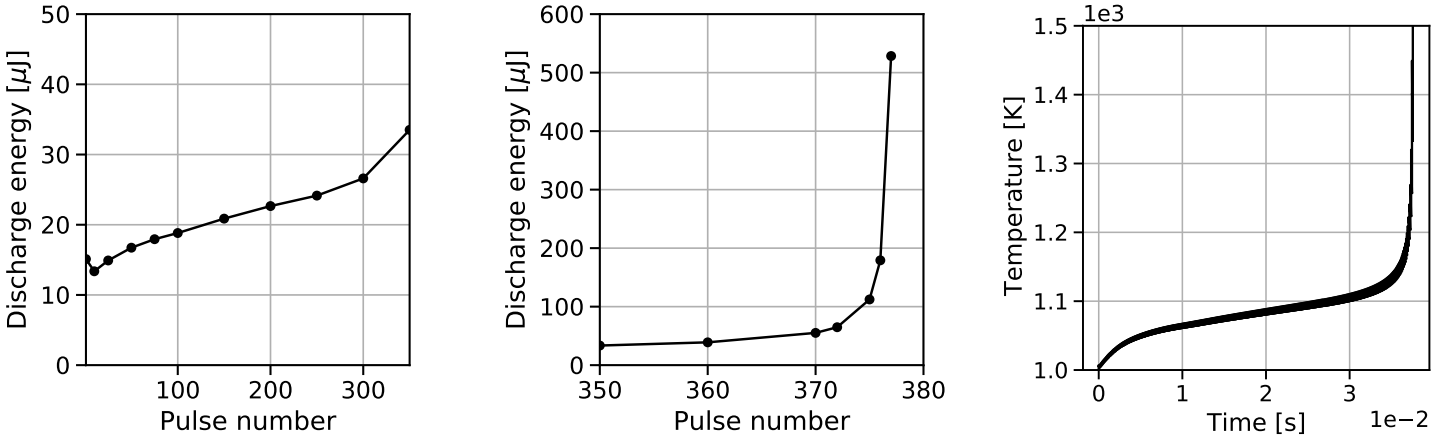

(a) (b) (c)

Figure 12.23: Results of the 6.2 kV pulsed simulation: (a,b) discharge energy of the pulses and (c) gas temperature at the middle of the gap.

The time evolution of the discharge diameter has been computed from the simulation in Fig. 12.24a. During the glow regime, the discharge radius slowly decreases with a value around 275 µm. At the same time, the thermal radius at the beginning of the pulse is almost constant between pulses 50 and 350, as shown in Fig. 12.24b. The discharge radius decrease dring this phase is mainly due to the decrease of the radial electron profile at the beginning of the pulse since the radius of the gas temperature profile is almost constant. Contrary to what has been observed in the 5.7 kV simulation, the FWHM of the temperature profile is lower than the one of the electron profile. Further investigation must be done to understand the physical origin of this change.

The discharge energy of the 377$^{\text{th}}$ ($\simeq 520\,\mu\text{J}$) pulse is only 20% lower than the experimental one ($\simeq 670\,\mu\text{J}$). Thus, it is interesting to focus the analysis on it. The time evolution of the gas temperature, the pressure, the atomic oxygen density and the electron density at the center of the gap during the pulse and its afterglow are shown in Fig. 12.25. Both the gas temperature and the atomic oxygen density are slightly lower than in the experiment at the beginning of the pulse as shown in Fig. 12.25 ($T(t=0) \simeq 1350$ K and $n_O(t=0) = 1.25\times10^{23}\,\text{m}^{-3}$ at he beginning of the 377th pulse, $T(t=0) \simeq 1500$ K and $n_O(t=0) = 2\times10^{23}\,\text{m}^{-3}$ at the beginning of the pulse in the experiment). During the first 100 ns, the gas temperature increases by ≈ 800 K, which is somewhat lower than in the experiment (≥ 1000 K). There are two reasons for that: the initial gas density and discharge energy are respectively higher and lower than in the experiment. The higher gas density requires approximately 10% more energy to heat the same fluid volume than for an atmospheric gas at 1500 K. The atomic oxygen density increases by $\approx 7\times10^{23}\,\text{m}^{-3}$, which is comparable to the $\approx 9\times10^{23}\,\text{m}^{-3}$ observed experimentally. Both the gas temperature and the atomic oxygen density quickly decrease after 100 ns, in close relation with the pressure drop observed in Fig. 12.25b. A fraction of

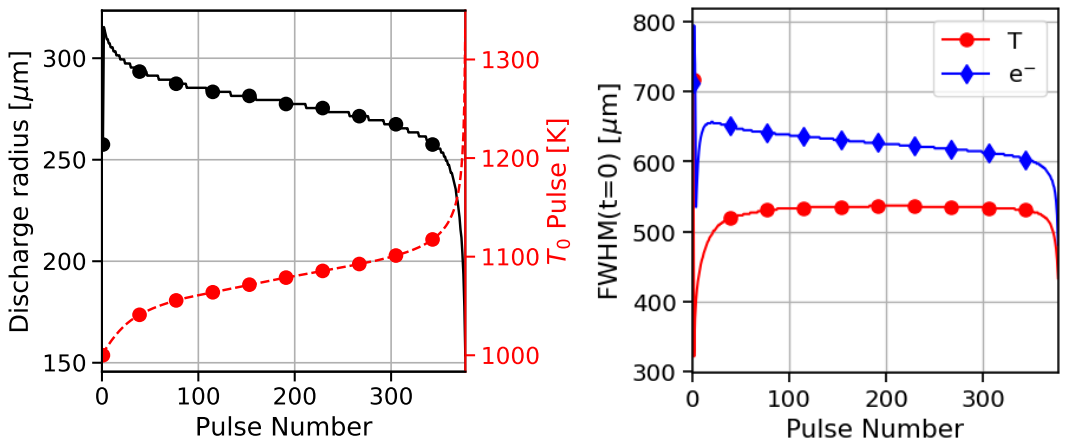

(a) (b)

Figure 12.24: Time evolution of (a) the discharge radius and gas temperature at the beginning of each pulse and (b) FWHM of electron density and gas temperature for the 6.2 kV pulsed simulation.

the discharge energy leaves the discharge channel in the expanding acoustic wave. In less than 1 µs, the pressure reaches the atmospheric value and the gas temperature starts to rise again due to slower processes, including the vibrational to translational energy relaxation, which occurs in the microsecond timescale due to the high centration of atomic oxygen. Then for $t \geq 10$ µs, the diffusive effects start to become important and both the gas temperature and the atomic oxygen density decrease until the end of the interpulse period. At the beginning of the next pulse ($t = 100$ µs), the atomic oxygen is almost at the experimental steady-state value. Moreover, the electron density is identical to the one at the beginning of the pulse. However, the gas temperature at the end of the interpulse is too high compared to the experiment. As a consequence, the next pulse will occur at a higher reduced electric field which is the reason why an intense spark discharge is observed during the 378^{th} pulse. An underestimation of the energy losses during the interpulse period must be further investigated. Indeed, only the convective and diffusive losses are considered for now, and conduction through the electrodes is neglected for instance. Moreover, the numerical scheme used for Euler fluxes is diffusive and can be responsible for convective loss underestimation.

As the energy deposited in the last discharge becomes significant, hydrodynamic effects play an important role in the evolution of the hot kernel between two successive pulses. The flow generated by the pressure wave expansion is responsible for a cooling effect at the electrode tips, as already observed in [35, 56, 130]. A picture of the flow 10 µs after the beginning of the 377^{th} pulse is shown in Fig. 12.26. The axial velocity exhibits a high value close to the electrode tips responsible for fresh gas entrance. Notice that these local high velocities are much higher than the background velocity field and become the dominant convective process in the inter-electrode gap. These hydrodynamic effects are clearly visible in the hot kernel dynamics in Fig. 12.27. At the end of the pulse, two hot kernels are attached to the electrode extremities. Then the fresh gas entrance pushes these two hot spots toward the gap's center. At $t = 10$ µs, the gas temperature peaks are not attached anymore to the electrodes and have been convected by ≈ 250 µm toward to center. Then, the heated channel mostly diffuses in the radial direction as evidenced by the temperature field at 50 µs in Fig. 12.27c.

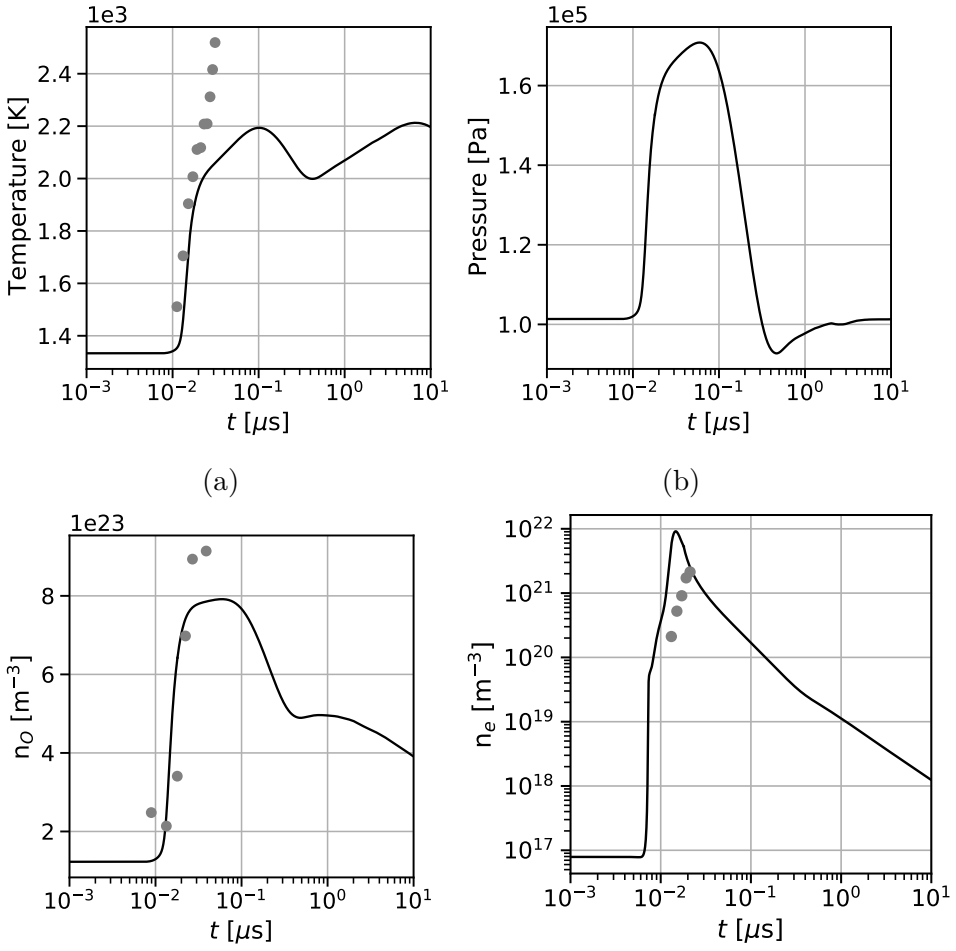

Figure 12.25: Time evolution of (a) the gas temperature, (b) the gas pressure, (c) the atomic oxygen density and (d) the electron density during the 377$^{\text{th}}$ pulse of the 6.2 kV pulsed simulation. Solid lines correspond to simulation, circles correspond to experiment [167].

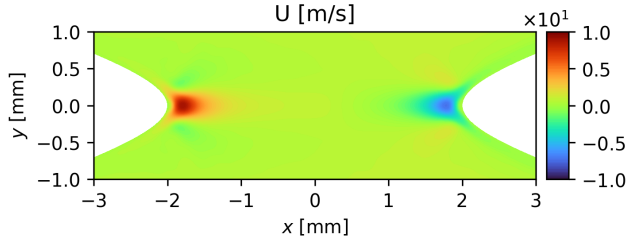

Figure 12.26: Axial velocity field 10 µs after the 377th pulse

12.3.4 One word about CPU cost

In Section 12.3.3, we have been able to simulate more than 300 pulses thanks to the numerical strategy described in Section 11.6. However, it still necessitates around 10^5 CPUh for the whole simulation bearing in mind that the simulation is performed in a 2D domain. In detail, the low energy discharges only require around 200 CPUh while 310 CPUh was spent for the last

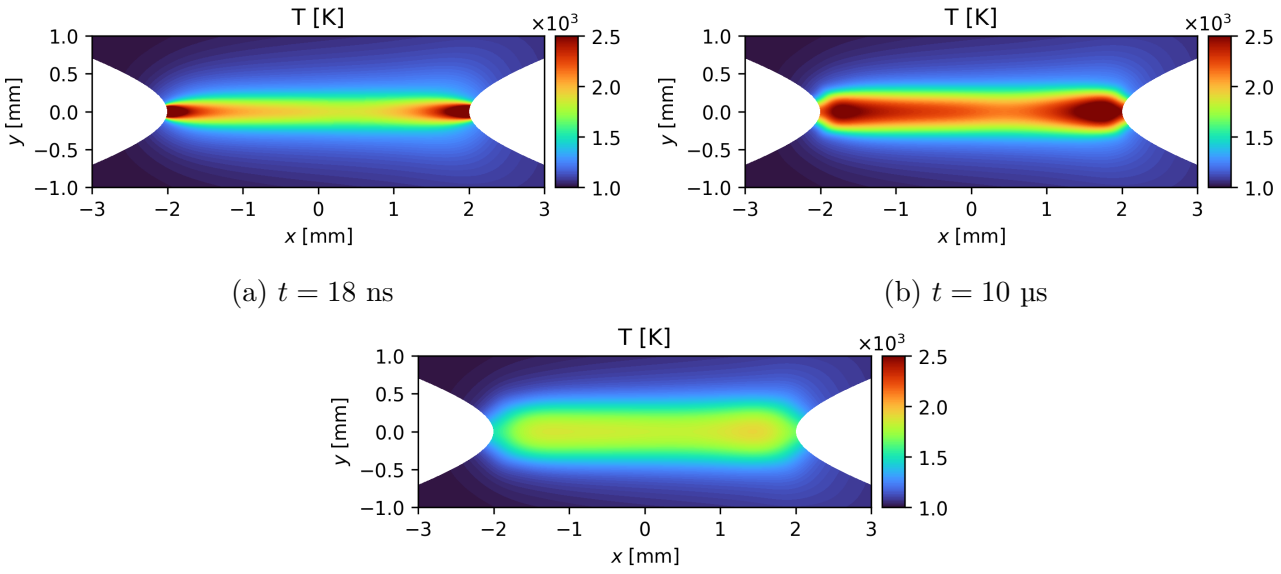

(a) $t = 18$ ns

(b) $t = 10$ µs

(c) $t = 50$ µs

Figure 12.27: 2D maps of the gas temperature at different instants of the 377^{th} pulse.

spark discharge. However, the most expensive discharges were those in-between glow and spark regimes. For example, 400 CPUh were required for the 360^{th} pulse. In these discharges, the spark model is not activated and all the pulse phase is modeled by solving the Poisson equation and accounting for the dielectric time-step. Moreover, the cost of the interpulse period increases pulse after pulse due to the temperature rise leading to higher diffusion coefficients (i.e. the resulting Fourier time-step decreases). Without mesh coarsening during the interpulse, this simulation would have required more than 6×10^5 CPUh just by considering the Fourier time-step constraint. A summary of the CPU cost for one pulse is given in Tab. 12.4

#	Pulse phase	Interpulse phase	Total
1	140 (70%)	60 (30%)	200
360	310 (77%)	90 (23%)	400
377	170 (55%)	140 (45%)	310

Table 12.4: Details of the CPUh required for different pulses.

12.4 Conclusion

In this chapter, detailed multi-dimensional simulations of NRP discharges in air have been performed on the experimental conditions of [167] by coupling AVIP to AVBP. First, simulations have been carried out in steady state regime. It has been observed in Section 12.2 that the simulation is highly sensitive to the initial conditions. In particular, the radial gas temperature profile is responsible for an important reduction of the discharge diameter, while this effect was less pronounced when only using a radial profile for the electron density. Moreover, the structure of the pressure wave that follows the discharge is also highly affected by a radial temperature profile. To overcome these uncertainties, multiple discharges were applied in Sections 12.3.2 and 12.3.3 starting from uniform temperature and electron density fields. In the 5.7 kV case,

a stable glow regime has been observed without any sign of transition to spark regime. In the 6.2 kV case, the glow to spark regime transition has been observed by applying hundreds of pulses. However, we were not able to stabilize a steady-state spark regime. Indeed, the last simulated pulse exhibited a conductive current around 500 A, which is not physically possible in the conditions studied. This is due to the positive feedback loop described in Fig. 12.28 encountered when the energy deposited by the discharge is not lost due to convection and diffusion processes at the end of the interpulse period. In that case, the gas temperature at the beginning of the pulse i is higher than at the beginning of the pulse $i-1$, leading to a decrease of the gas number density N and thus an increase of the reduced electric field E/N for a fixed imposed voltage. In the end, the discharge energy increases, leading to a higher gas temperature and the loop continues. In reality, the plasma conductive channel is placed in an electrical circuit not modeled in AVIP. Electrical circuit models could help to prevent the current rise to unphysical values. This strategy has been successfully employed in [184] using a BNC cable theory and must be investigated in future work.

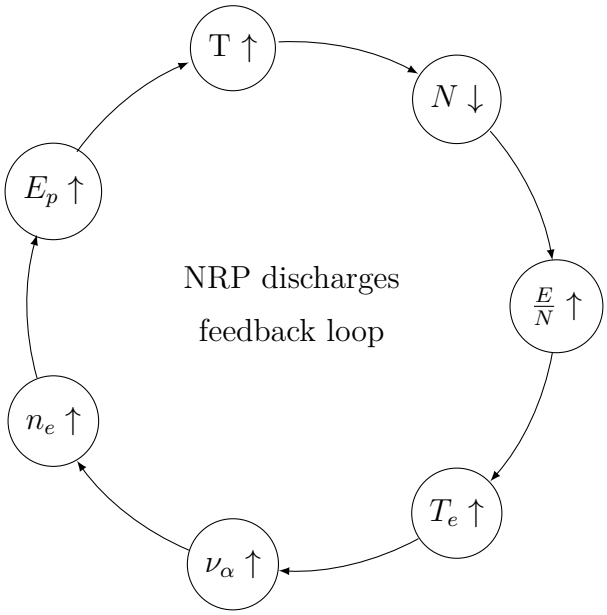

Figure 12.28: Positive feedback loop of NRP discharges.

Chapter 13

Plasma-assisted ignition

Contents

This chapter is based on a paper submitted to the 39th International Symposium on Combustion entitled "*Investigation of the impact of NRP discharge frequency on the ignition of a lean methane-air mixture using fully coupled plasma-combustion numerical simulations*". The two-way coupled plasma-combustion numerical model detailed in Chapter 11 is used to describe the plasma, the combustion and their interactions with a similar level of accuracy, in terms of spatial and temporal discretizations, to simulate the ignition of a lean methane-air mixture using both single and multiple discharges.

In Section 13.1 the considered 2D axisymmetric pin-pin electrode configuration is presented. Then in Section 13.2, the ignition using a single pulse (SP) and multiple pulses (MP) are studied to better understand their physical effects and their differences. First in Section 13.2.1, the ignition following a single plasma discharge is studied in detail from nanosecond to microsecond time scales. This single pulse is compared with a conventional heat deposition in order to emphasize the chemical effects of the plasma discharge. Then in Section 13.2.2, the Pulse Repetition Frequency (PRF) is varied from 10 to 100 kHz to investigate its effects on discharge properties and ignition. The objective of this work is to investigate the benefits of plasma discharges compared with heat deposition as well as to understand in which conditions multiple pulses are more efficient than a single discharge.

13.1 Configuration and numerical setup

A pin-pin electrode geometry is chosen as in [49, 184]. Multiple NRP discharges are simulated in a methane-air mixture at an equivalence ratio of 0.8 and an initial temperature of 600 K. The equivalence ratio considered here is representative of a lean burner such as the MiniPAC

experiment [130]. The hyperbolic-shaped electrodes both have a 200 µm-curvature radius and are separated by a 4 mm gap. The voltage profile is shown in Fig. 13.1 where an initial rise of 1 ns followed by a constant plateau of 8 kV are imposed. This corresponds to a mean reduced electric field of 160 Td in the gap between electrodes at the initial temperature. The discharge energy E^p and energy density e^p are defined by Eqs. 11.17 and 11.18. In order to control the discharge energy deposition, the voltage is switched off at t_{off} when the discharge energy E^p reaches a targeted value E_d.

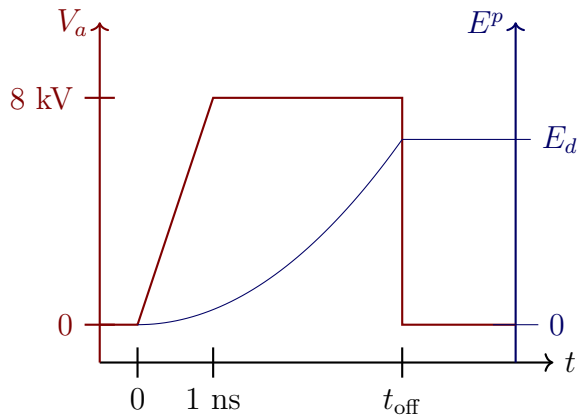

Figure 13.1: Temporal evolution of the discharge energy.

A sketch of the geometry is represented in Fig. 13.2. An unstructured mesh composed of triangular elements is used to discretize the 2D numerical domain. Two mesh refinements are used for the different phases of the computation as much finer cells are required during the voltage pulse compared to the inter-pulse period. The characteristic size of the mesh elements in the different zones are given in Fig. 13.1. With this discretization, a minimum of 15 points inside the thermal flame thickness is ensured for both meshes, thus justifying the DNS approach for the reactive mixture. The domain is extended up to 10 cm from the discharge channel to evacuate properly the pressure wave generated by the discharge. Three probes displayed in Fig. 13.2 are used to monitore the time evolution of the variables at important location which are given in Tab. 13.2.

	Pulse	Interpulse
Δx_{fine}	3 µm	15 µm
Δx_{medium}	10 µm	30 µm
Δx_{coarse}	250 µm	250 µm
Number of nodes	6.9×10^5	8.5×10^4

Table 13.1: Pulse and inter-pulse mesh properties, see Fig. 13.2 for location of mesh zones.

	1	2	3
x [mm]	0	0	1.75
r [mm]	0	1	0

Table 13.2: Locations of the three probes displayed in Fig. 13.2.

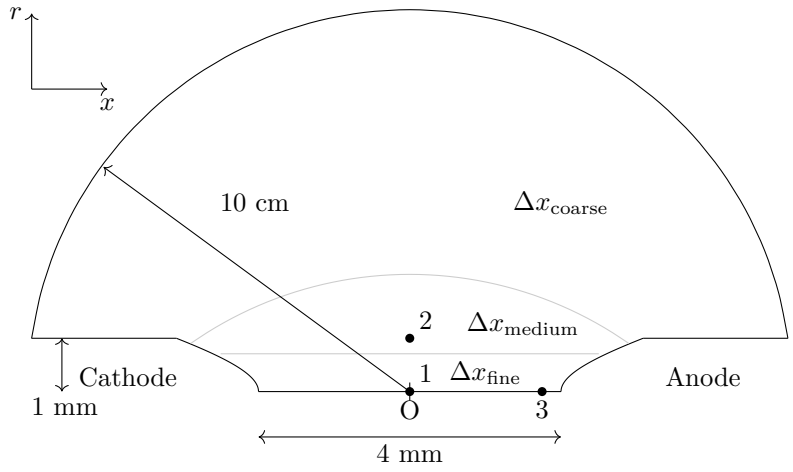

Figure 13.2: Sketch of the 2D axisymmetric geometry with mesh sizes and probes.

13.1.1 Boundary conditions

For the drift-diffusion equations, Neumann boundary conditions are applied on the electrode surfaces as in [49, 184], while an outlet is imposed on the far-field boundary and a symmetry condition is applied on the cylindrical axis.

A zero Neumann boundary condition is applied for the Poisson equation on the axis and the far-field. A time-varying but spatially constant Dirichlet boundary condition at potential V_a is used for the anode. The time signal $V_a(t)$ imposed is shown in Fig. 13.1. The cathode is grounded ($V_c = 0$).

Finally, for the Navier-Stokes equations, adiabatic non-slipping walls are considered on the electrodes, thus neglecting heat conduction through them. A non-reflecting NSCBC [154] boundary condition is applied on the far-field boundary. As for the remaining axis boundary, a symmetry is applied.

13.1.2 Chemistry

The reduced mechanism developed in Section 9.3 is used here. It includes 44 species and 410 reactions based on the GRI 3.0-Plasma mechanism developed in Chapters **??** and 7. In addition to its validity for plasma discharge cases, the reduced mechanism is also able to reproduce correctly conventional auto-ignition delay times of methane-air mixtures in a large range of temperatures $[800 - 2000]$ K and equivalence ratios [0.5-1.5] as well as laminar flame speeds in a large range of equivalence ratios [0.6-1.4].

13.2 Results

13.2.1 Single-pulse ignition

The capacity of non-equilibrium discharges to ignite a reactive mixture is first studied using a single pulse. The discharge energy E^p was varied from 200 µJ to 800 µJ and it was found that the minimum energy necessary to ignite the mixture using a single pulse is around $E_{\text{SP}}^{\text{min}} = 500\,\mu\text{J}$. The 500 µJ-SP discharge is thus investigated in this section.

Two-dimensional fields of electron density and discharge energy density at different instants obtained with this single-pulse can be found in Fig. 13.3. During the first nanoseconds, both positive and negative streamers are propagating towards the center and no significant energy is transmitted to the electrons yet as shown in Figs. 13.3a and 13.3b at 3 ns. Both streamers eventually connect to create a discharge channel around 4 ns. After connection, the electron density in the discharge channel increases significantly as does the discharge energy density which are shown at the cut-off time $t_{\text{off}} = 14.7$ ns with a peak ionization degree of 10^{-3}. The discharge density is strongly peaked close to the electrodes inducing a significant amount of heat and radicals as shown in Fig. 13.4. Close to the electrode tips, the atomic oxygen mass fraction reaches values close to 0.1, indicating that almost half of the oxygen molecules are dissociated. These radicals, produced by the non-equilibrium discharge, are assumed to enhance combustion in several studies [34, 88].

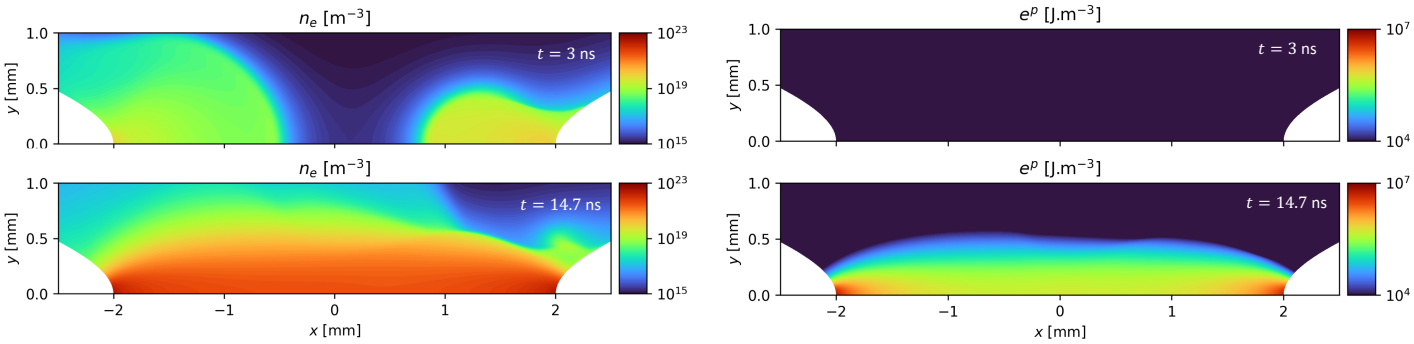

(a) Electron density

(b) Discharge energy density

Figure 13.3: Two-dimensional fields for the single-pulse discharge at different instants.

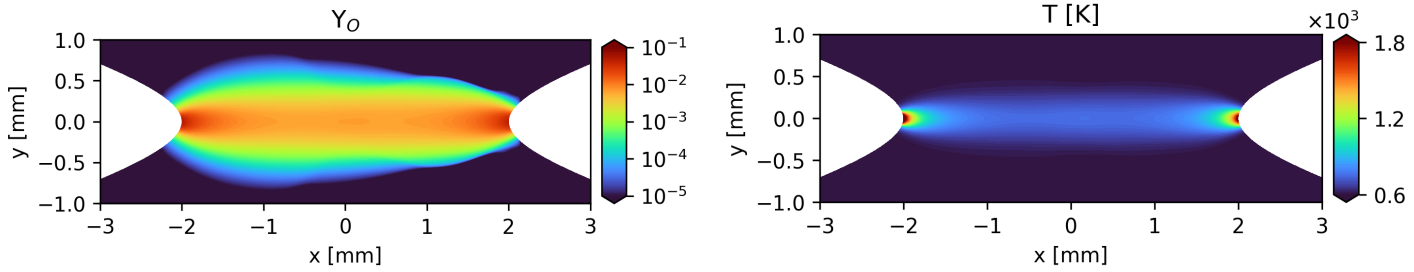

(a)

(b)

Figure 13.4: 2D maps of (a) the atomic oxygen mass fraction and (b) the gas temperature at the end of the 500 µJ-SP case ($t = t_{\text{off}} = 14.7$ ns).

To assess the importance of the chemical enhancement, the same ignition configuration with only energy deposition is also computed and referred to as the *heat deposit* (HD) case in which all the energy is assumed to be converted to heat using the same chemistry. An energy of $E_{\text{HD}} = 500$ µJ is deposited in the form of an energy source term within $\tau_{\text{HD}} = 20$ ns which is representative of the energy deposition duration in the 500 µJ-SP case. The spatial distribution of the energy deposition is taken from the normalized discharge energy density $\mathcal{F}(x, r) = e^p(x, r, t_{\text{off}})/E^p(t_{\text{off}})$ of the 500 µJ-SP case so that the constant power source term, deposited during $[0, \tau_{\text{HD}}]$, reads

$$\dot{Q}_{\mathrm{HD}}(x,r) = \frac{E_{\mathrm{HD}}}{\tau_{\mathrm{HD}}}\mathcal{F}(x,r) \tag{13.1}$$

For $E_{\mathrm{HD}} = 500\,\mu\mathrm{J}$, the mixture does not ignite (Fig. 13.8 left) while for the same energy using a plasma discharge it does (Fig. 13.8 middle). We need to increase the energy to $E_{\mathrm{HD}}^{\mathrm{min}} = 600\,\mu\mathrm{J}$ to observe ignition using only a heat deposit. The 600 µJ-HD and 500 µJ-SP ignitions are compared in Fig. 13.5 where selected species at probe 3, close to the anode, are shown. Radicals O, OH and H are produced directly by the plasma discharge in tens of nanoseconds in the SP case (blue curve), whereas it results from the temperature increase in the HD case (red curve) so that their peak value is lower and occurs later. These radicals accelerate the ignition as the consumption of fuel and oxidizer starts earlier for the SP case compared to the HD case, as shown in the right part of Fig. 13.5.

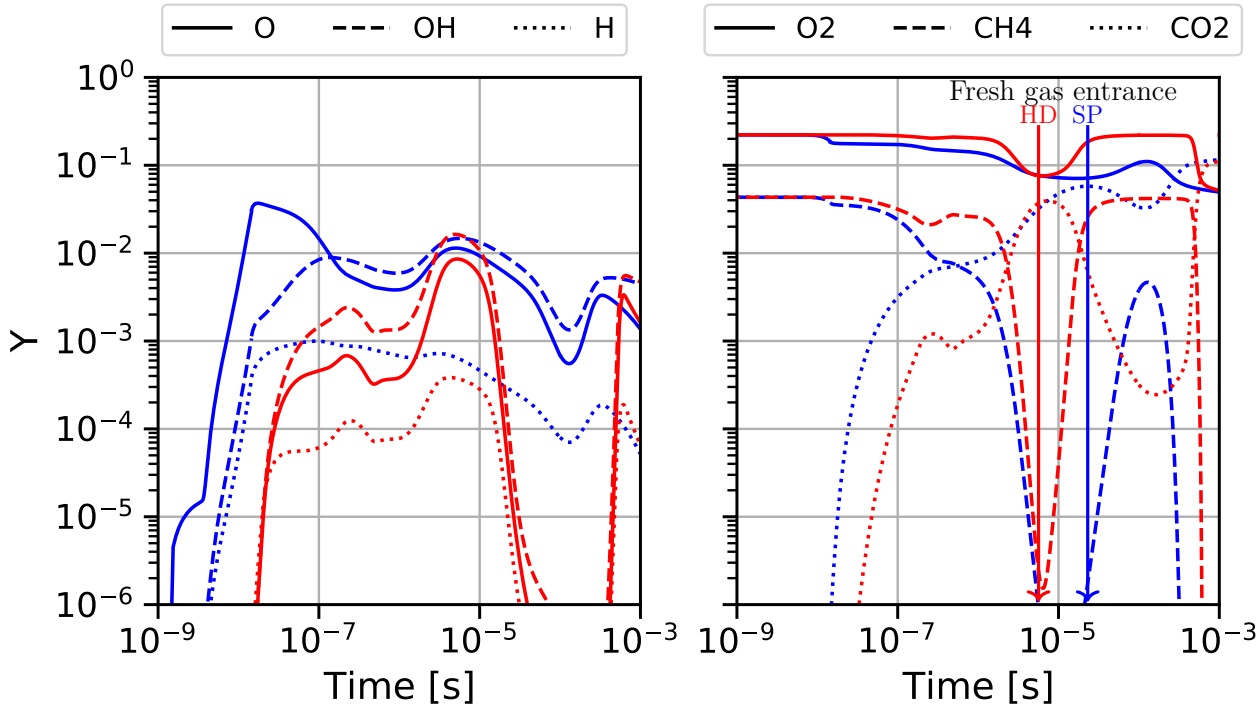

Figure 13.5: Time evolution of selected species mass fractions in a single-pulse discharge with $E_{\mathrm{SP}} = 500\,\mu\mathrm{J}$ (blue), and in the heat deposit case with $E_{\mathrm{HD}} = 600\,\mu\mathrm{J}$ (red) at probe 3. The ends of the pulse and heat deposition are around $2 \times 10^{-8}\,\mathrm{s}$. Vertical arrows on the right figure indicate the instant when fresh gas fills the probe 3 area.

Shortly after the end of the pulse, two strong shocks are formed at the electrode tips as shown in Fig. 13.6 and move outward in a cylindrical shape after merging at $\approx 3\,\mu\mathrm{s}$. The expanding pressure wave contains part of the discharge energy which is then no more available for ignition. However the associated acoustic energy e_a defined in Eq. (13.2) is about 15 µJ for the SP case which represents less than 2% of the discharge energy. In the 500 µJ-HD case, a stronger shock wave is formed with a higher acoustic energy loss of about 35 µJ ($\approx 7\%$ of the discharge energy).

$$e_{\mathrm{a}} = \frac{1}{2}\rho_0 \mathbf{u}_1^2 + \frac{1}{2}\frac{P_1^2}{\rho_0 c_0^2} \tag{13.2}$$

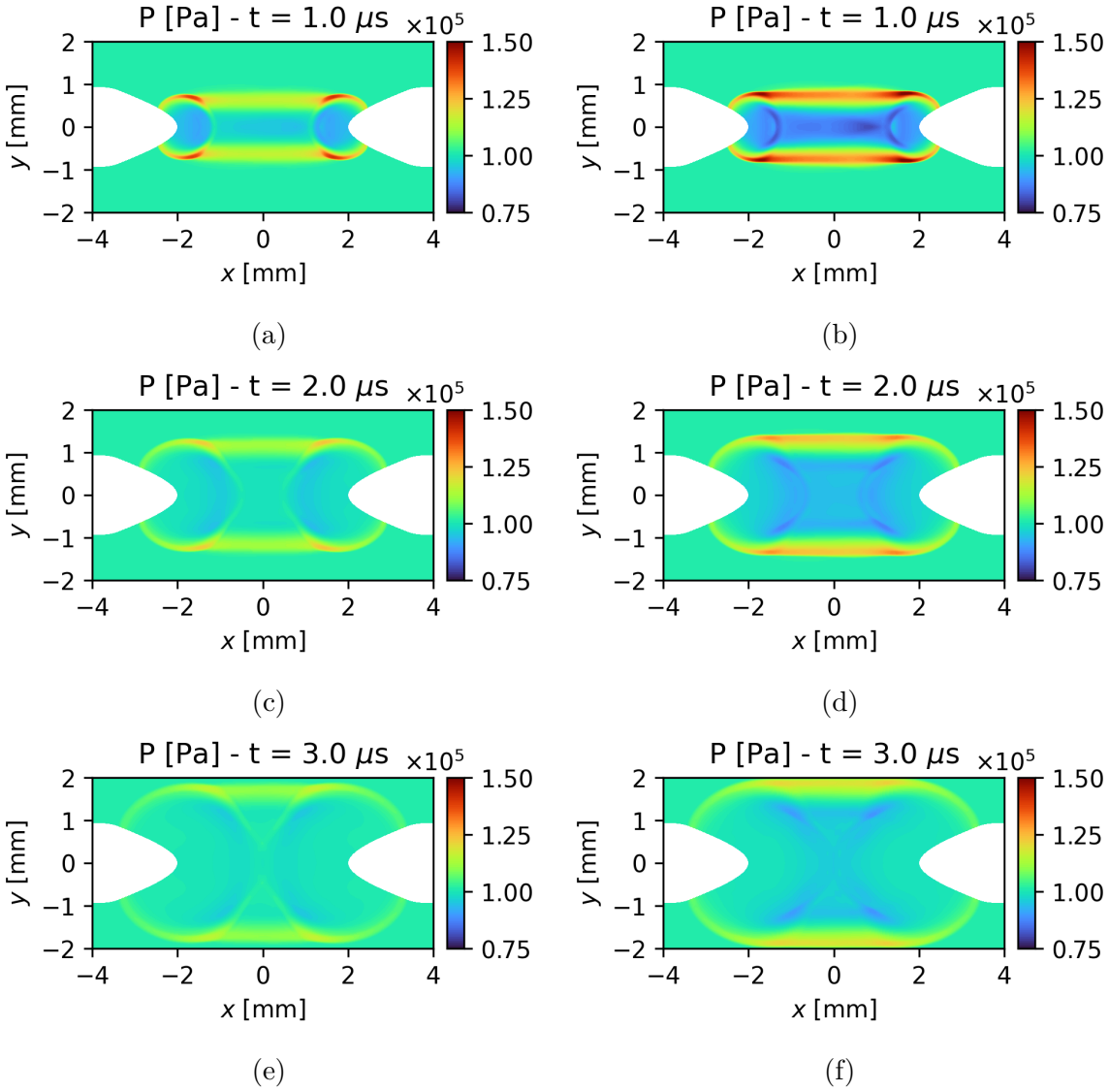

Figure 13.6: Pressure field at different instants for the 500 µJ-SP case (left) and 500 µJ-HD case (right)

A more important consequence of this shock wave is the induced flow close to the electrodes illustrated by Fig. 13.7. The two red spots in Fig. 13.7a correspond to the ignition kernels and the arrows indicate direction of the flow which moves alongside the electrodes towards the center of the gap and leaves it in a radial upward motion. This gaseous flow has two effects: the initial flame kernels are convected towards the center of the inter-electrode gap and the regions around the electrode tips are cooled down. The gaseous flow effects can be seen in Fig. 13.5 around $t \simeq 2 \times 10^{-5}$ s s for the SP case where both O_2 and CH_4 mass fractions increase close to the anode due the entry of fresh gases. A stronger shock in the 600 µJ-HD case fills the anode tip area (probe 3) with fresh gases earlier than the SP case at $t \simeq 5 \times 10^{-6}$ s and ignition occurs later compared to the SP case even with a 20% energy increase.

According to [38], a critical flame radius r_c, above which ignition is ensured, can be estimated under the unity Lewis number assumption as

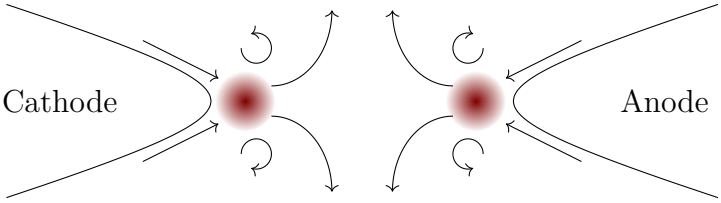

(a) Sketch of the flow around the ignition kernels (in red).

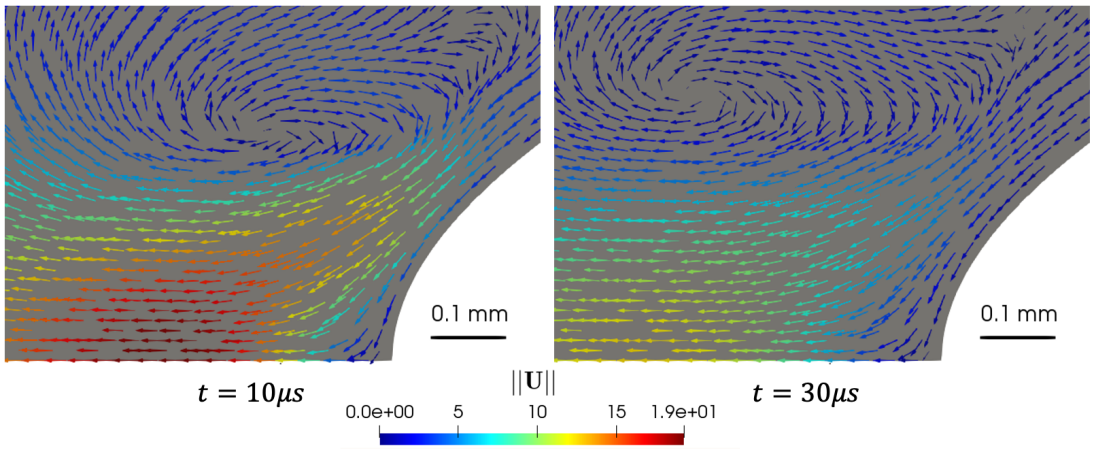

(b) Velocity vector field close to the anode tip

Figure 13.7: Flow around the ignition kernels.

$$r_c = \frac{\lambda(T_{\text{ad}})}{C_p(T_{\text{ad}})\ \rho(T_f)\ S_L^0} \tag{13.3}$$

where T_{ad} is the adiabatic flame temperature, T_f the fresh gas temperature, λ the heat conductivity, C_p the heat capacity at constant pressure and S_L^0 the laminar flame speed. In the present conditions for methane-air combustion at $\phi = 0.8$ ($T_f = 600\,\text{K}$, $T_{\text{ad}} = 2200\,\text{K}$, $S_L^0 = 1.05\,\text{m}\,\text{s}^{-1}$) we have $r_c = 150\,\mu\text{m}$.

5 µs after the end of the pulse, for both the 500 µJ-HD and SP cases, two hot spots are formed at the electrode tips as shown in the first line of Fig. 13.8. At 140 µs, two isolated spherical kernels are formed in the SP case with an approximate radius of 400 µm. Thus, it is very likely that the flame kernels will continue to grow and expand, which is confirmed by the subsequent snapshots of Fig. 13.8 (middle column) as the flame kernels merge and start to expand radially.

On the other hand, as stated at the beginning of the section, the 500 µJ-HD case does not ignite as shown by the left column of Fig. 13.8 due to the stronger shock-wave and recirculation. Increasing the deposited energy to 600 µJ allows *one* flame kernel, at the anode, to grow and travel towards the center of the inter-electrode zone as shown in Fig. 13.9. The volume of the hot kernel formed at the cathode, visible in Figs. 13.9b and 13.9d, does not exceed the critical radius $r_c = 150\,\mu\text{m}$ introduced previously. At $t = 20\,\mu\text{s}$, the radius of the hot kernel is estimated to 140 µm based on the distance between the two heat release peaks along the axis. Then, the kernel radius decreases to reach a value of 100 µm at $t = 30\,\mu\text{s}$. To obtain a growing kernel comparable to that of the plasma discharge case, the deposited energy must be increased to 700 µJ, *i.e.*, 40% more than the plasma discharge.

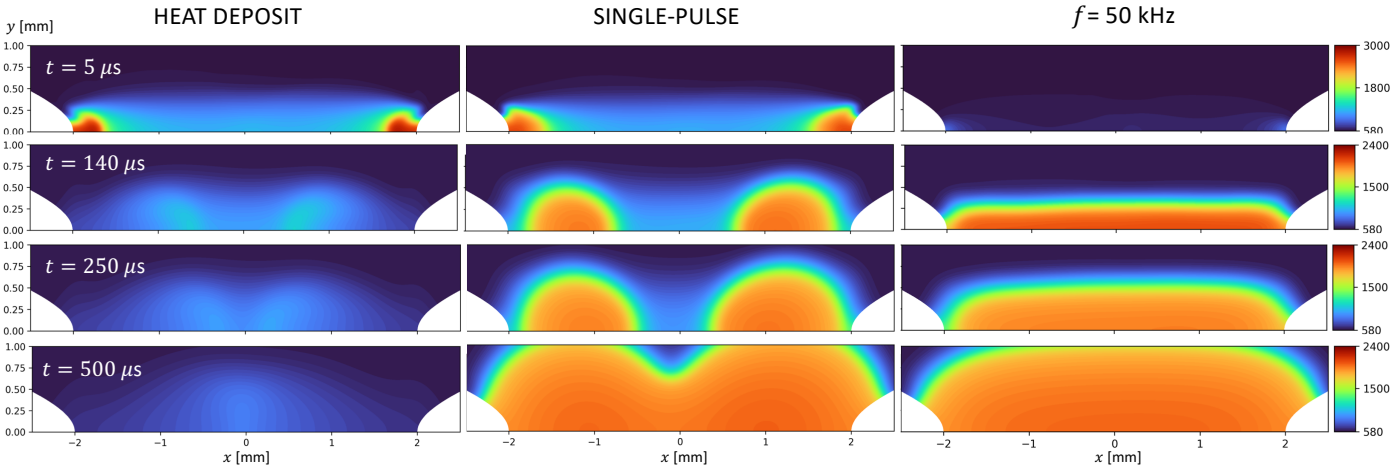

Figure 13.8: Temperature fields in Kelvin at different instants for the HD, SP and 50 kHz-MP cases with an energy deposition of 500, 500 and 350 µJ respectively. Seven pulses are applied for the 50 kHz-MP case (left column): one pulse was applied at 5 µs, seven pulses were applied at 140 µs and later times.

13.2.2 Multi-pulse effect

Multiple discharges at various frequencies are now investigated to ignite the methane-air mixture. The energy per pulse is decreased tenfold compared to the single-pulse at $E_p = 50\,\mu\text{J}$ and the frequency is varied from 10 kHz to 100 kHz.

To evaluate the impact of the pulse frequency on ignition, the gas temperature signal at probe 2 is used to define the ignition delay time. Probe 2, located 1 mm above the axis, is not directly reached by the plasma discharges and thus may be used to indicate the possible passage of a growing flame kernel. For all the studied frequencies f, 20 pulses were applied in order to deposit a total energy of 1 mJ. After each burst of $N_p \in [1, 20]$ pulses, an additional simulation was continued without further discharges up to 1 ms. Figure 13.11a shows the time evolution of the gas temperature at probe 1 for the first 8 pulses. At the end of each pulse, the gas temperature evolution without further plasma discharges (grey-lines) shows that 6 pulses are necessary to initiate a flame kernel close to the axis. This initial kernel is able to self-propagate to a radius of 1 mm, far from the plasma discharge region, as indicated by the temperature signal at probe 2 in Fig. 13.11b. It mean that a burst of low-energy discharges is able to ignite the mixture with a total energy of only $E_{\text{MP}}^{\text{min}} = 6 \times 50 = 300\,\mu\text{J}$, i.e., 40% lower than the minimum energy required for ignition with a single pulse discharge as seen in Section 13.2.1.

Increasing further the number of pulses then leads to faster ignition, until an asymptotic limit is reached after ≈7-9 pulses as shown in Fig. 13.11b. This behavior was observed for all frequencies in the range of [20-100] kHz as shown in Fig. 13.12 where the ignition delay time is defined at probe 2 by Eq. (13.4) where ΔT is arbitrarily set to 1000 K.

$$\tau_{\text{ig}} = \min(t \mid T(t) \geq T_0 + \Delta T) \tag{13.4}$$

Note that for the 25 kHz case, the minimum energy required for ignition is equivalent to that of the SP-ignition, thus limiting the benefit of MP discharges. For lower frequencies (i.e.,

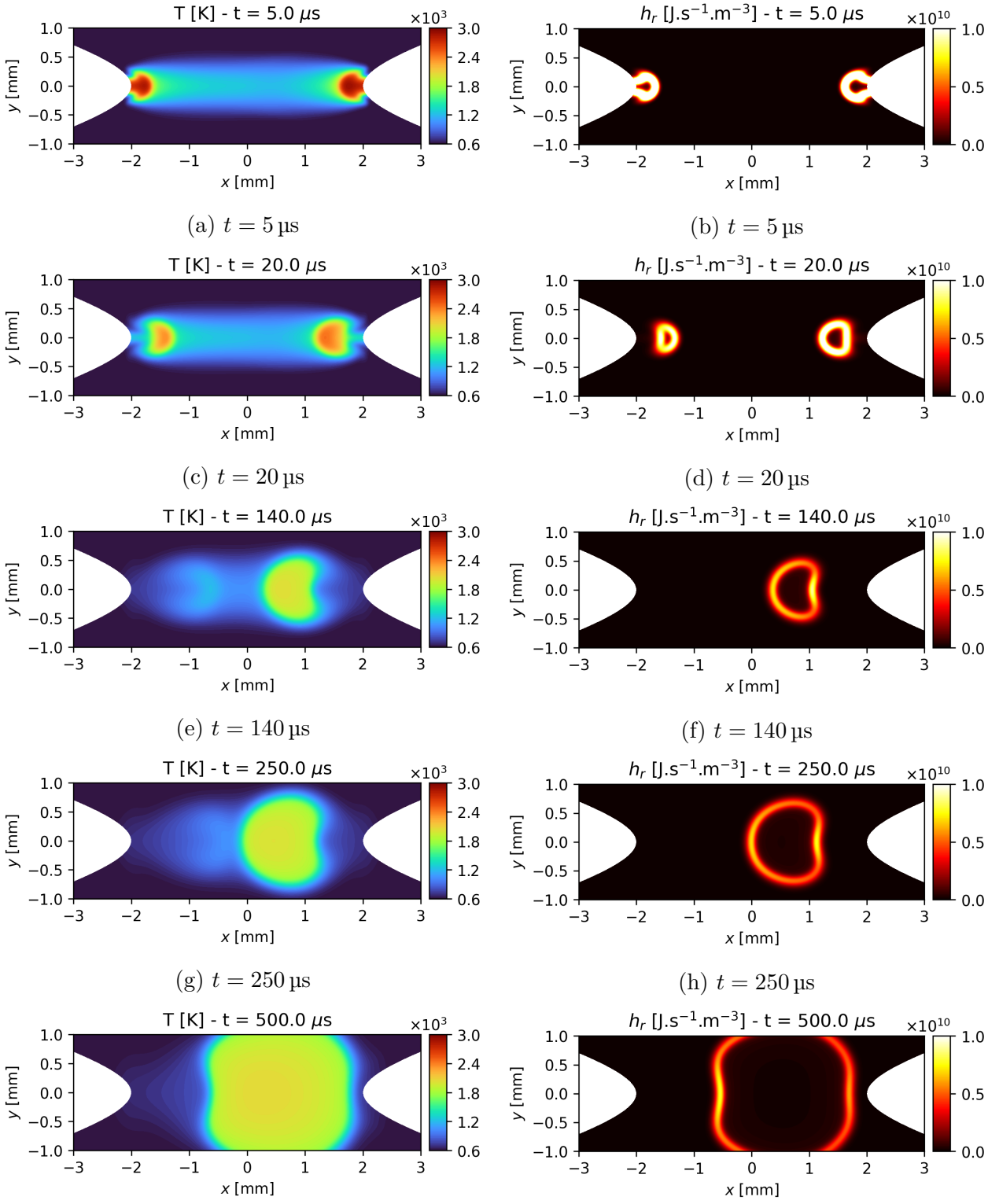

(a) $t = 5\,\mu s$ (b) $t = 5\,\mu s$

(c) $t = 20\,\mu s$ (d) $t = 20\,\mu s$

(e) $t = 140\,\mu s$ (f) $t = 140\,\mu s$

(g) $t = 250\,\mu s$ (h) $t = 250\,\mu s$

(i) $t = 500\,\mu s$ (j) $t = 500\,\mu s$

Figure 13.9: Ignition sequence of the 600 µJ-HD case.

$f \leq 25\,\text{kHz}$), a detrimental effect is even observed as the 20 kHz case requires a total energy of 750 µJ for a successful ignition.

Moreover, it was observed that for frequencies lower than 15 kHz, no ignition event occurs

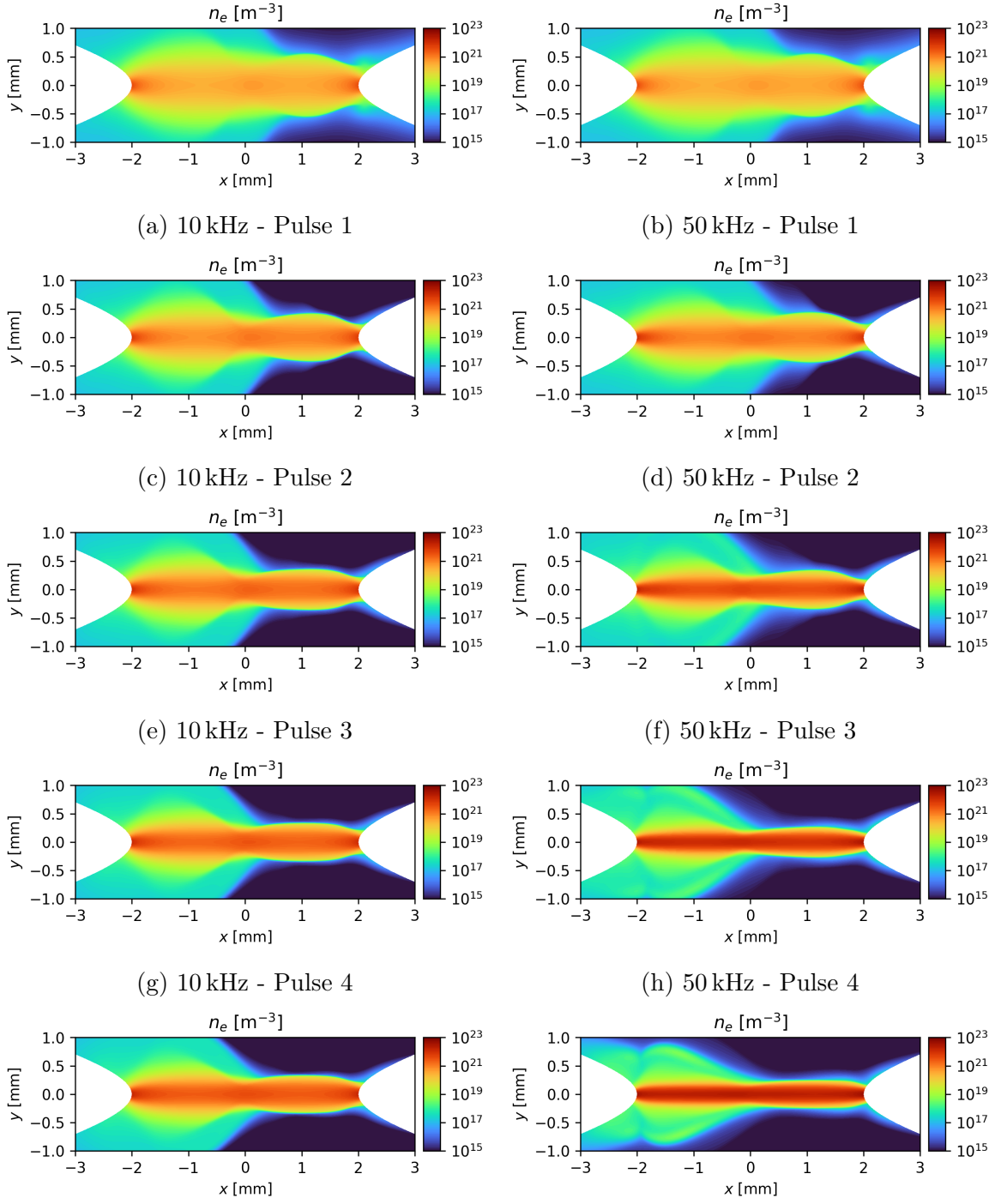

(a) 10 kHz - Pulse 1

(b) 50 kHz - Pulse 1

(c) 10 kHz - Pulse 2

(d) 50 kHz - Pulse 2

(e) 10 kHz - Pulse 3

(f) 50 kHz - Pulse 3

(g) 10 kHz - Pulse 4

(h) 50 kHz - Pulse 4

(i) 10 kHz - Pulse 5

(j) 50 kHz - Pulse 5

Figure 13.10: Electron density at the end of the pulses 1 to 5 for different frequencies: $f = 10\,\text{kHz}$ (left) and $f = 50\,\text{kHz}$ (right).

before 1 ms. Indeed, at low frequency, the cumulative effects of the successive discharges are gradually lost mostly due to the diffusion of temperature and species during the inter-pulse period. Conversely at high frequency, each discharge takes advantage of the previous one and concentrates on the axis as illustrated in Fig. 13.10. The discharge radius, defined with the Full-Width at Half Maximum of the $N_2(B_3)$ peak as in [167], is used to illustrate the cumulative

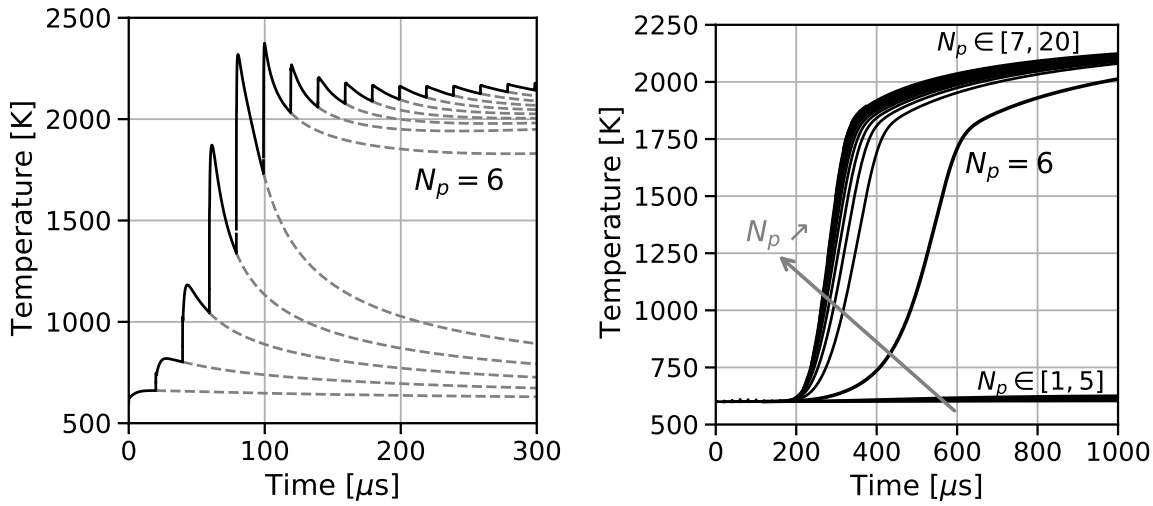

(a) Probe 1

(b) Probe 2

Figure 13.11: Gas temperature evolution at $f = 50\,\text{kHz}$-MP case in (a) the plasma region (probe 1) and (b) at 1mm height (probe 2).

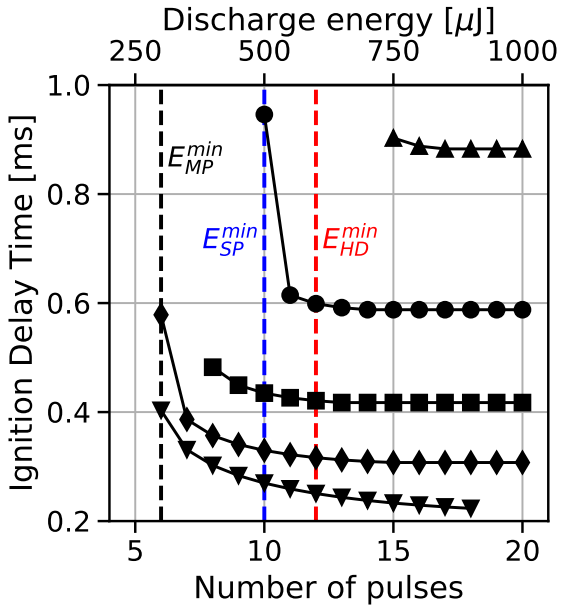

Figure 13.12: Ignition delay time depending on the number of pulses at various frequencies: ▲ 20 kHz ● 25 kHz ■ 33 kHz ◆ 50 kHz ▼ 100 kHz. The corresponding total discharge energy is indicated on the top axis of the figure. $E_{\text{HD}}^{\text{min}}$, $E_{\text{SP}}^{\text{min}}$ and $E_{\text{MP}}^{\text{min}}$ correspond respectively to the minimum energy ignition of the HD, SP and MP cases.

effect of the discharges. Figure 13.13 shows the discharge radius for the 10 and 50 kHz cases at the end of each pulse, together with the gas temperature just before the pulse at the center of the inter-electrode gap. At 10 kHz, the discharge radius first decreases to 125 µm before slowly increasing at the same rate as the gas temperature. Indeed, electron and ion diffusion coefficients are increasing with temperature leading to a wider discharge propagation and stronger diffusion of the plasma channel during the inter-pulse. At 50 kHz, a sharp decrease of the discharge

radius is observed during the first four pulses allowing to concentrate the energy on the axis. For the same amount of energy deposited, smaller volumes lead to higher gas temperatures and radical production allowing to trigger favourable conditions for flame kernel initiation. In the same time, the gas temperature increases drastically and marks the early stage of flame kernel formation. Then, as for the 10 kHz case, the discharge radius increases with temperature and the discharges lead to smaller temperature increase, as was observed for the 7th and later pulses in Fig. 13.11a.

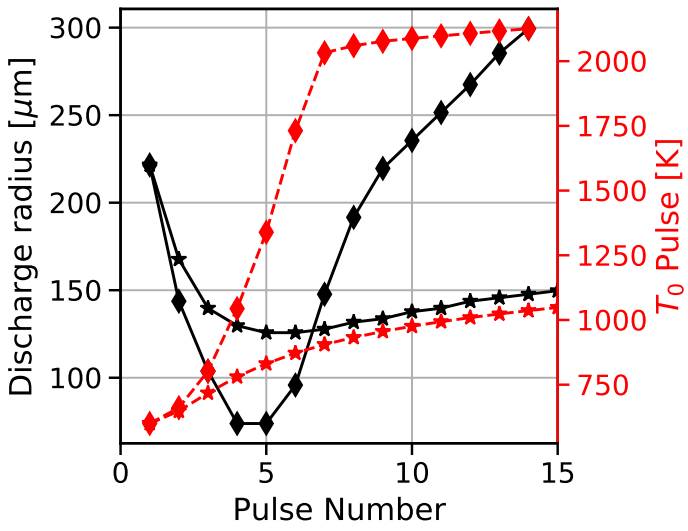

Figure 13.13: Evolution of discharge radius and local gas temperature preceding each pulse (probe 1) at two different frequencies: ★ 10 kHz ◆ 50 kHz

In addition to the efficient ignition of repetitive pulses, the mixture is ignited more homogeneously than the single pulse ignition. The 50 kHz-case is considered to illustrate this behavior. The pressure waves formed by the NRP discharges are much smaller than with the single pulse, primarily due to the pulse energy reduction as shown in Fig. 13.14. The pressure wave resulting from the first pulse, shown in Fig. 13.14a, exhibits a very similar pattern to the single-pulse case with two spherical waves at the electrode tips. However, after several pulses, the pressure wave directly expands with a cylindrical shape, as shown in Fig. 13.14c. This is a consequence of the homogeneous heating produced by the NRP discharges, as shown in Fig. 13.15. From pulses 1 to 3, much more energy is deposited at the electrode extremities than in the center of the gap that agrees well with the pressure wave shapes discussed previously. Then during the fifth pulse, homogeneous heating is observed in Fig. 13.15e. Contrary to what has been observed in the SP case, there is no significant hydrodynamic cooling effect at the electrode tips in Fig. 13.15f. This is primarily due to the lower pulse energy deposition in the MP cases compared with the SP case. Moreover, the more homogeneous energy deposition in the MP cases allows to mitigate the hot spots close to the anode, leading to a cylindrical pressure wave instead of two spherical ones. This behavior was also observed in Chapter 12 when the gas temperature between the electrodes exhibits a radial profile. The reduction of the hydrodynamic cooling effect is responsible for the more efficient ignition observed using multiple discharges compared to the SP ignition.

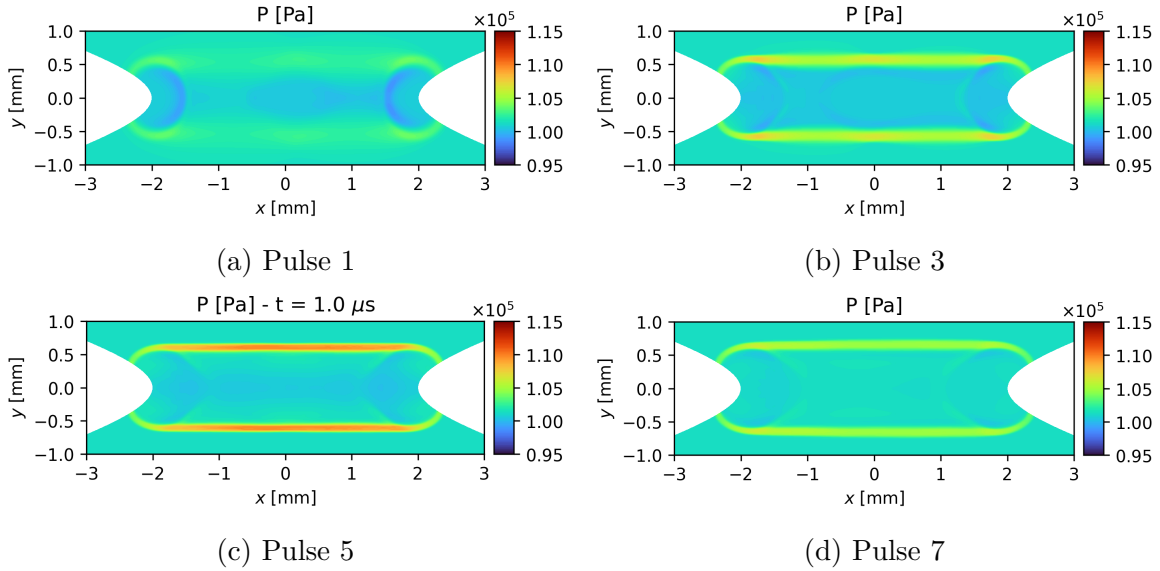

(a) Pulse 1

(b) Pulse 3

(c) Pulse 5

(d) Pulse 7

Figure 13.14: Pressure fields at 1 µs from the beginning of different pulses for the 50 kHz-case.

13.3 Conclusions

Ignition of a lean methane air-mixture has been carried out using the coupled AVIP-AVBP codes with a reduced plasma-assisted combustion chemistry in a pin-pin configuration. Fully coupled plasma and combustion simulations have allowed to investigate the interaction between the plasma discharge and the reacting flow.

Using a single-pulse discharge of 500 µJ, the formation of two ignition kernels were observed at the end of the discharge close to the electrode tips. Along these two kernels a strong shock wave was formed inducing a recirculation of fresh gases into the inter-electrode gap and pushing the two kernels towards the center of the gap. The two kernels eventually merge to form a stable single kernel propagating radially outwards. The chemical effect of the discharge has been highlighted by simulating a similar discharge with energy deposited only as an energy source term. For the same amount of deposited energy of 500 µJ, no ignition was observed as the kernels were quenched by the fresh gases recirculation induced by a stronger shock-wave.

The single pulse discharge ignition was then compared with low-energy (50 µJ), multiple pulses, applied at various frequencies from 10 to 100 kHz. At low frequency, the created spots of temperature have sufficient time to diffuse and below 15 kHz, no ignition is observed. Increasing the frequency above 25 kHz has a beneficial effect on ignition exploiting the synergetic effect of the discharges: the ignition delay time decreases and the minimum energy needed for successful ignition decreases. Indeed at high frequency, the plasma channel does not have time to diffuse significantly and narrower discharges can be produced, thus focusing both heating and radical production on the axis. This shows the benefits of applying smaller energy pulses repetitively as they are able to ignite faster and in a more stable way combustible mixtures.

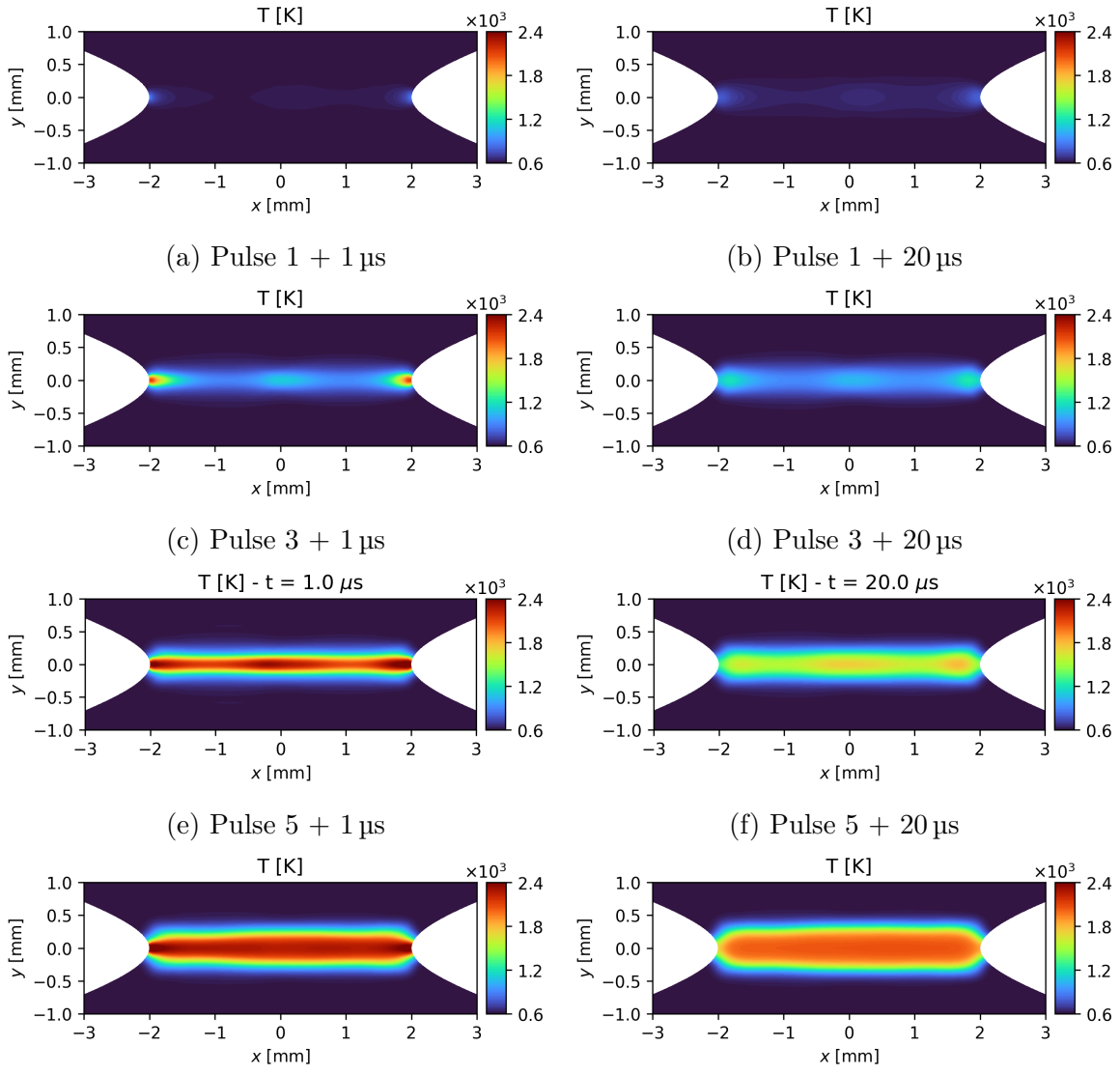

(a) Pulse 1 + 1 µs

(b) Pulse 1 + 20 µs

(c) Pulse 3 + 1 µs

(d) Pulse 3 + 20 µs

(e) Pulse 5 + 1 µs

(f) Pulse 5 + 20 µs

(g) Pulse 7 + 1 µs

(h) Pulse 7 + 20 µs

Figure 13.15: Temperature field at 1 µs and 20 µs from the beginning of different pulses for the 50 kHz-case.

Conclusion

In this work, detailed numerical simulations of Nanosecond Repetitively Pulsed discharges have been performed in air and methane-air mixtures at atmospheric pressure. To carry out these simulations, three main steps were necessary. First, a low-temperature plasma code, AVIP, has been developed based on the structure of the existing AVBP reactive flow solver, in order to simulate the discharge formation. Second, a detailed study of the plasma-combustion chemistry has been performed to couple the plasma discharges to the neutral reactive flow. Third, the AVIP code has been coupled to AVBP to evaluate the impact of NRP discharges in the two aforementioned mixtures.

AVIP handles the necessary features to simulate low-temperature plasma at atmospheric pressure. The drift-diffusion equation has been used to transport the charged species, which are coupled together consistently through the Poisson equation. The main difficulty encountered in the AVIP development was the use of fully unstructured grids. Indeed, most streamer codes are based on structured meshes, or at least quadrangular elements, which allow the development of numerical schemes with good accuracy. In this work, the use of triangular elements was a necessity in order to take into account the geometry of the targeted configurations. To handle the strong gradients present in the streamer simulations, robust and accurate schemes had to be used. Two numerical schemes were mainly studied: the Limited Lax-Wendroff (LLW) and the Improved Scharfetter-Gummel (ISG) schemes. A simple First Order Upwind scheme was also tested for comparison. These schemes were developed in a Finite-Volume Vertex-Centered formulation, which differs from the Finite-Volume Cell-Vertex formulation in AVBP, in order to easily adapt the numerical schemes to cylindrical coordinates. After having validated the schemes in canonical cases, AVIP has been challenged against six other low-temperature plasma codes in the case of discharge propagation between two planar electrodes. Good results were obtained with AVIP on unstructured triangular meshes using the LLW scheme. Moreover, AVIP has demonstrated satisfactory computational performance, placing our code in second place in the benchmark in terms of computational cost. Then, the capability to handle realistic electrode geometries has been investigated by performing atmospheric pressure streamer simulations between two hyperbolic electrodes at 300 K and 1000 K, which is representative of the conditions where NRP discharges are used. Satisfactory results were obtained with the LLW scheme at both temperatures while encouraging results were observed with the ISG scheme on the non-topological mesh. Finally, some criteria on the cell size have been determined by performing a mesh convergence on the hyperbolic electrodes. In particular, it has been observed that the inverse of the first Townsend coefficient gives a good indication of the required mesh size to avoid numerical oscillation or branching.

To couple the detailed plasma simulation to the reactive gaseous mixture, suitable chemistry which includes the plasma effects on the gas, and vice versa, must be used. This chemistry must be validated in cases close to the conditions on which it is intended to be used. In this

work, a new detailed plasma-combustion chemistry has been developed. The detailed kinetic mechanism has been validated using the Cantera solver, on which zero-dimensional plasma reactors have been implemented. These reactors are based on conventional isochoric and isobaric reactors available in Cantera, on which an EEDF solver has been added to compute the electron parameters and electron impact collision rates. The mechanism validation has focused on three aspects of the chemistry: fast gas heating, slow gas heating due to vibrational energy relaxation and radical production. The mechanism has been first validated in air, by challenging it with 3 experiments that have monitored several quantities, including the fast and slow increase of the temperature, the production of key neutral species O, N and NO and the vibrational kinetics. These, the air mechanism has been updated to account for methane addition. The mechanism has been successfully validated by comparison with two experiments. First, a discharge in a methane-air mixture has been used to validate the atomic oxygen decay. Second, a plasma-assisted ignition (PAI) case of an argon diluted methane-air mixture has been investigated. Our mechanism was able to give a satisfactory evaluation of the ignition delay time with around 10% difference compared with the experimental value. In the purpose of using those mechanisms in multi-dimensional simulations, chemical reduction is necessary. Using the ARCANE code co-developed at CERFACS and Cornell University with a DRGEP reduction algorithm, the number of species has been reduced by a factor of 2, yielding a 47-species, 429-reactions reduced mechanism from the GRI-3.0 plasma mechanism. The chemistry reduction strategy has allowed to perform reliable plasma-combustion multi-dimensional simulations in the last part of this work.

Two conditions have been investigated using fully coupled multi-dimensional simulations of the plasma discharge and the gaseous mixture. To to do, the low-temperature plasma code AVIP has been coupled to the combustion code AVBP. NRP-spark discharges in air have been first investigated by comparing the simulation results with experimental measurements in a pin-pin configuration. As a first step, the steady state NRP-spark regime was targeted. A significant influence of the initial conditions was observed in this case. In particular, the presence of a pre-heated channel has shown an impressive effect on the discharge radius and the pattern of the pressure wave induced by the discharge. The initial plasma density profile mostly influences the discharge propagation speed with a small discharge radius decrease. In order to overcome the uncertainties on the initial conditions during the steady state, multiple discharges were simulated starting from the physical conditions prior to the plasma actuation. When applying the 5.7 kV pulse, a steady state glow discharge regime has been obtained after ≈ 100 pulses. By increasing the applied voltage du 6.2 kV, a glow to spark transition was observed after ≈ 370 pulses. While not being able to stabilize the NRP-spark regime due to the lack of an electrical circuit model, the last simulated discharge gives some satisfying results compared with the experiment. Finally, the ignition of a lean methane-air mixture has been carried out in a pin-pin configuration. This study has focused on three energy deposition: using a single plasma discharge (SP), a conventional head deposition (HD) and multiple low-energy pulses applied at various frequencies (MP). It has been observed that for a given energy, the SP energy deposition is more efficient than the HD one. This is primarily due to the chemical effect of the plasma discharge which is not present in the HD case. Moreover, the benefits of applying multiple low-energy pulses at a high frequency have been demonstrated. Above a frequency threshold (≈ 30 kHz in our study), the synergetic effects of NRP discharges were found efficient to ignite the mixture. In particular, the existing pre-ionized and pre-heating channels between the electrodes allow easier discharge propagation and lead to more homogeneous energy depo-

sition which enhances the ignition compared to the SP case. The minimum energy necessary to ignite the mixture decreases with increasing frequency and at the highest studied frequency (100 kHz), ignition has been achieved with 30% less energy than with a single-pulse discharge. In this work, using coupled plasma-combustion models has proved very efficient to investigate open questions about the impact of plasma chemistry and the interaction of the plasma with a gaseous mixture. The coupled model may now be applied to more complex configurations to predict the impact of NRP discharges on flames.

The use of fully coupled plasma-assisted combustion simulations is still limited due to the prohibitive cost of such simulations. To overcome this issue, a phenomenological model of plasma discharges has been investigated in this work. An extension of the Castela model has been proposed based on our work on plasma chemistry. The extended phenomenological model is applicable both in fresh and burnt gas conditions based on the detailed study of plasma discharges in such mixture using 0D simulations. The implementation of this model in AVBP is an ongoing task and will be tested in the future in both academic and industrial burners.

Bibliography

[1] World Energy Outlook 2021 from the International Energy Agency, 2022. URL https://www.iea.org/reports/world-energy-outlook-2021. 1, 2, 3, 4

[2] ZEROe Aribus project, 2022. URL https://www.airbus.com/en/innovation/zero-emission/hydrogen/zeroe. 2

[3] Green Electrical Control of COmbustion (GECCO) project, 2022. URL https://anr.fr/Project-ANR-17-CE06-0019. 13

[4] The Intergovernmental Panel on Climate Change, 2022. URL https://www.ipcc.ch/. 2, 3

[5] JET Fuel SCREENing (JETSCREEN) project, 2022. URL https://ec.europa.eu/inea/en/horizon-2020/projects/h2020-transport/aviation/jetscreen. 2

[6] Plasma ASsisTEd Combustion (PASTEC) project, 2022. URL https://anr.fr/Project-ANR-16-CE22-0005. 13

[7] Simulation and Control of Renewable COmbustion (SCIROCCO) project, 2022. URL https://cerfacs.fr/scirocco/. 2

[8] I. V. Adamovich, T. Li, and W. R. Lempert. Kinetic mechanism of molecular energy transfer and chemical reactions in low-temperature air-fuel plasmas. *Philos. T. R. Soc. A*, 373(2048):20140336, Aug. 2015. 9, 11, 13, 91, 100, 102, 109, 127

[9] R. Aerts, T. Martens, and A. Bogaerts. Influence of vibrational states on CO_2 splitting by dielectric barrier discharges. *The Journal of Physical Chemistry C*, 116(44):23257–23273, Oct. 2012. doi: 10.1021/jp307525t. URL https://doi.org/10.1021/jp307525t. 128

[10] F. Albugues, A. Birot, D. Blanc, H. Brunet, J. Galy, P. Millet, and J. L. Teyssier. Destruction of the levels c3 (v'=0, v'=1) of nitrogen by O_2, CO2, CH4, and h2o. *The Journal of Chemical Physics*, 61(7):2695–2699, Oct. 1974. doi: 10.1063/1.1682401. URL https://doi.org/10.1063/1.1682401. 135

[11] N. L. Aleksandrov, S. V. Kindysheva, E. N. Kukaev, S. M. Starikovskaya, and A. Y. Starikovskii. Simulation of the ignition of a methane-air mixture by a high-voltage nanosecond discharge. *Plasma Phys. Rep.*, 35(10):867–882, Oct. 2009. 10, 11, 13, 96, 121, 122, 123, 124, 125, 127, 135, 150, 151

[12] C. P. Arroyo, J. Dombard, F. Duchaine, L. Gicquel, B. Martin, N. Odier, and G. Staffelbach. Towards the large-eddy simulation of a full engine: Integration of a 360 azimuthal

degrees fan, compressor and combustion chamber. part i: Methodology and initialisation. *Journal of the Global Power and Propulsion Society*, (May):1–16, May 2021. doi: 10.33737/jgpps/133115. URL https://doi.org/10.33737/jgpps/133115. 29

[13] V. Auffray. *Etude comparative de schemas numeriques pour la modelisation de phenomenes diffusifs sur maillages multielements.* PhD thesis, 2007. INP Toulouse. 44, 46

[14] E. Bach, J. Kariuki, J. R. Dawson, E. Mastorakos, and H. joerg Bauer. Spark ignition of single bluff-body premixed flames and annular combustors. In *51st AIAA Aerospace Sciences Meeting including the New Horizons Forum and Aerospace Exposition*. American Institute of Aeronautics and Astronautics, Jan. 2013. doi: 10.2514/6.2013-1182. URL https://doi.org/10.2514/6.2013-1182. 17

[15] B. Bagheri, J. Teunissen, U. Ebert, M. M. Becker, S. Chen, O. Ducasse, O. Eichwald, D. Loffhagen, A. Luque, D. Mihailova, J. M. Plewa, J. van Dijk, and M. Yousfi. Comparison of six simulation codes for positive streamers in air. *Plasma Sources Sci. Technol.*, 27(9):095002, Sept. 2018. 24, 27, 53, 54, 55, 56, 58, 59, 60, 61, 62, 63, 65

[16] M. S. Bak, H. Do, M. G. Mungal, and M. A. Cappelli. Plasma-assisted stabilization of laminar premixed methane/air flames around the lean flammability limit. *Combust. Flame*, 159(10):3128–3137, Oct. 2012. 12, 13, 128

[17] S. Balay, S. Abhyankar, M. F. Adams, S. Benson, J. Brown, P. Brune, K. Buschelman, E. M. Constantinescu, L. Dalcin, A. Dener, V. Eijkhout, W. D. Gropp, V. Hapla, T. Isaac, P. Jolivet, D. Karpeev, D. Kaushik, M. G. Knepley, F. Kong, S. Kruger, D. A. May, L. C. McInnes, R. T. Mills, L. Mitchell, T. Munson, J. E. Roman, K. Rupp, P. Sanan, J. Sarich, B. F. Smith, S. Zampini, H. Zhang, H. Zhang, and J. Zhang. PETSc Web page. https://petsc.org/, 2021. URL https://petsc.org/. 46, 182

[18] D. R. Ballal and A. H. Lefebvre. The influence of flow parameters on minimum ignition energy and quenching distance. *Symposium (International) on Combustion*, 15(1):1473–1481, Jan. 1975. doi: 10.1016/s0082-0784(75)80405-x. URL https://doi.org/10.1016/s0082-0784(75)80405-x. 7, 17

[19] S. Barbosa, G. Pilla, D. A. Lacoste, P. Scouflaire, S. Ducruix, C. O. Laux, and D. Veynante. Influence of nanosecond repetitively pulsed discharges on the stability of a swirled propane/air burner representative of an aeronautical combustor. *Philosophical Transactions of the Royal Society A: Mathematical, Physical and Engineering Sciences*, 373(2048):20140335, Aug. 2015. doi: 10.1098/rsta.2014.0335. URL https://doi.org/10.1098/rsta.2014.0335. 11, 12

[20] Y. Bechane and B. Fiorina. Numerical investigations of turbulent premixed flame ignition by a series of nanosecond repetitively pulsed discharges. *P. Combust. Inst.*, 38(4):6575–6582, 2021. 12, 13, 128, 164

[21] Y. Bechane, N. Darabiha, V. R. Moureau, C. O. Laux, and B. Fiorina. Large eddy simulations of turbulent flame ignition by nanosecond repetitively pulsed discharges. In *AIAA Scitech 2019 Forum*. American Institute of Aeronautics and Astronautics, Jan. 2019. doi: 10.2514/6.2019-0742. URL https://doi.org/10.2514/6.2019-0742. 12, 13, 164

[22] A. Bellemans, N. Kincaid, N. Deak, P. Pepiot, and F. Bisetti. P-DRGEP: a novel methodology for the reduction of kinetics mechanisms for plasma-assisted combustion applications. *P. Combust. Inst.*, 38(4):6631–6639, 2021. ISSN 1540-7489. 146, 151

[23] V. P. Blanchard, N. Minesi, Y. Bechane, B. Fiorina, and C. O. Laux. Experimental and numerical characterization of a lean premixed flame stabilized by nanosecond discharges. In *AIAA SCITECH 2022 Forum*. American Institute of Aeronautics and Astronautics, Jan. 2022. doi: 10.2514/6.2022-2255. URL https://doi.org/10.2514/6.2022-2255. 142

[24] P. Bochev, K. Peterson, and X. Gao. A new control volume finite element method for the stable and accurate solution of the drift–diffusion equations on general unstructured grids. *Computer Methods in Applied Mechanics and Engineering*, 254:126–145, Feb. 2013. doi: 10.1016/j.cma.2012.10.009. URL https://doi.org/10.1016/j.cma.2012.10.009. 37

[25] A. Bogaerts, W. Wang, A. Berthelot, and V. Guerra. Modeling plasma-based CO2conversion: crucial role of the dissociation cross section. *Plasma Sources Science and Technology*, 25(5):055016, Aug. 2016. doi: 10.1088/0963-0252/25/5/055016. URL https://doi.org/10.1088/0963-0252/25/5/055016. 129

[26] M. Boileau, G. Staffelbach, B. Cuenot, T. Poinsot, and C. Berat. LES of an ignition sequence in a gas turbine engine. *Combustion and Flame*, 154(1-2):2–22, July 2008. doi: 10.1016/j.combustflame.2008.02.006. URL https://doi.org/10.1016/j.combustflame.2008.02.006. 29

[27] A. Bourdon, V. P. Pasko, N. Y. Liu, S. Celestin, P. Segur, and E. Marode. Efficient models for photoionization produced by non-thermal gas discharges in air based on radiative transfer and the helmholtz equations. *Plasma Sources Science and Technology*, 16(3):656–678, Aug. 2007. doi: 10.1088/0963-0252/16/3/026. URL https://doi.org/10.1088/0963-0252/16/3/026. 24

[28] D. Breden, L. L. Raja, C. A. Idicheria, P. M. Najt, and S. Mahadevan. A numerical study of high-pressure non-equilibrium streamers for combustion ignition application. *J. Appl. Phys.*, 114(8):083302, Aug. 2013. 11, 13, 36

[29] A. Burcat, B. Ruscic, Chemistry, and T. I. I. of Tech. Third millenium ideal gas and condensed phase thermochemical database for combustion (with update from active thermochemical tables). 7 2005. doi: 10.2172/925269. URL https://www.osti.gov/biblio/925269. 83

[30] D. Burnette, A. Montello, I. V. Adamovich, and W. R. Lempert. Nitric oxide kinetics in the afterglow of a diffuse plasma filament. *Plasma Sources Sci. T.*, 23(4):045007, June 2014. 109, 110, 111, 112

[31] I. M. Campbell and B. A. Thrush. Behaviour of carbon dioxide and nitrous oxide in active nitrogen. *Trans. Faraday Soc.*, 62:3366–3374, 1966. doi: 10.1039/TF9666203366. URL http://dx.doi.org/10.1039/TF9666203366. 134

[32] M. Capitelli, F. C.M., B. Gordiets, and A. Osipov. *Plasma Kinetics in Atmospheric Gases*. Springer, 2000. 87, 91, 92, 95, 96, 97, 112, 129, 132, 181

[33] T. A. Casey, J. Han, M. Belhi, P. G. Arias, F. Bisetti, H. G. Im, and J.-Y. Chen. Simulations of planar non-thermal plasma assisted ignition at atmospheric pressure. *P. Combust. Inst.*, 36(3):4155–4163, 2017. 11, 13

[34] M. Castela, B. Fiorina, A. Coussement, O. Gicquel, N. Darabiha, and C. O. Laux. Modelling the impact of non-equilibrium discharges on reactive mixtures for simulations of plasma-assisted ignition in turbulent flows. *Combustion and Flame*, 166:133–147, Apr. 2016. doi: 10.1016/j.combustflame.2016.01.009. URL https://doi.org/10.1016/j.combustflame.2016.01.009. 12, 13, 79, 128, 159, 160, 162, 164, 176, 181, 216

[35] M. Castela, S. Stepanyan, B. Fiorina, A. Coussement, O. Gicquel, N. Darabiha, and C. O. Laux. A 3-d DNS and experimental study of the effect of the recirculating flow pattern inside a reactive kernel produced by nanosecond plasma discharges in a methane-air mixture. *Proceedings of the Combustion Institute*, 36(3):4095–4103, 2017. doi: 10.1016/j.proci.2016.06.174. URL https://doi.org/10.1016/j.proci.2016.06.174. 12, 13, 208

[36] A. Cavaliere and M. de Joannon. Mild combustion. *Progress in Energy and Combustion Science*, 30(4):329–366, Jan. 2004. doi: 10.1016/j.pecs.2004.02.003. URL https://doi.org/10.1016/j.pecs.2004.02.003. 6

[37] Q. Cazères, P. Pepiot, E. Riber, and B. Cuenot. A fully automatic procedure for the analytical reduction of chemical kinetics mechanisms for computational fluid dynamics applications. *Fuel*, 303:121247, 2021. ISSN 0016-2361. 81, 145, 150, 181

[38] M. Champion, B. Deshaies, G. Joulin, and K. Kinoshita. Spherical flame initiation: Theory versus experiments for lean propane-air mixtures. *Combust. Flame*, 65(3):319–337, Sept. 1986. 218

[39] O. Chanrion and T. Neubert. A PIC-MCC code for simulation of streamer propagation in air. *Journal of Computational Physics*, 227(15):7222–7245, July 2008. doi: 10.1016/j.jcp.2008.04.016. URL https://doi.org/10.1016/j.jcp.2008.04.016. 25

[40] K.-L. Chen, M.-F. Tseng, M.-C. Lo, S. Hamaguchi, M.-H. Hu, Y.-M. Lee, and J.-S. Wu. Development of a massively parallelized fluid-based plasma simulation code with a finite-volume method on an unstructured grid. *IEEE Transactions on Plasma Science*, 49(1):104–119, Jan. 2021. doi: 10.1109/tps.2020.3013632. URL https://doi.org/10.1109/tps.2020.3013632. 36

[41] Z. Chen and Y. Ju. Theoretical analysis of the evolution from ignition kernel to flame ball and planar flame. *Combustion Theory and Modelling*, 11(3):427–453, Apr. 2007. doi: 10.1080/13647830600999850. URL https://doi.org/10.1080/13647830600999850. 9

[42] L. Cheng. *Detailed Numerical Simulation of Multi-Dimensional Plasma Assisted Combustion*. PhD thesis, 2022. INP Toulouse. 36, 38, 39, 182, 188, 190

[43] L. Cheng, N. Barleon, O. Vermorel, B. Cuenot, and A. Bourdon. AVIP: a low temperature plasma code. *arXiv preprint arXiv*, 2021. 36, 182, 188

[44] L. Cheng, N. Barleon, B. Cuenot, O. Vermorel, and A. Bourdon. Plasma assisted combustion of methane-air mixtures: Validation and reduction. *Combustion and Flame*, 2022. 79

[45] J. Choe and W. Sun. Plasma assisted ammonia combustion: enhanced flame stability and reduced NOx emission. In *AIAA SCITECH 2022 Forum*. American Institute of Aeronautics and Astronautics, Jan. 2022. doi: 10.2514/6.2022-1452. URL https://doi.org/10.2514/6.2022-1452. 10

[46] D. D. Cont-Bernard, M. Ruchkina, P. Ding, J. Bood, A. Ehn, and D. A. Lacoste. Femtosecond two-photon laser-induced fluorescence imaging of atomic hydrogen in a laminar methane–air flame assisted by nanosecond repetitively pulsed discharges. 29(6): 065011, June 2020. doi: 10.1088/1361-6595/ab9234. URL https://doi.org/10.1088/1361-6595/ab9234. 18, 127

[47] D. D. Cont-Bernard, T. F. Guiberti, and D. A. Lacoste. Laser induced fluorescence investigation of the chemical impact of nanosecond repetitively pulsed glow discharges on a laminar methane-air flame. 38(4):6641–6649, 2021. doi: 10.1016/j.proci.2020.07.097. URL https://doi.org/10.1016/j.proci.2020.07.097. 11, 64, 127

[48] P. C. Cosby. Electron-impact dissociation of nitrogen. *J. Chem. Physics*, 98(12):9544–9553, June 1993. 111, 112

[49] S. Célestin. *Study of the dynamics of streamers in air at atmospheric pressure*. PhD thesis, 2008. Ecole centrale de Paris. 19, 22, 23, 24, 25, 26, 27, 30, 36, 48, 56, 64, 66, 68, 194, 213, 215

[50] B. B. Dally, S. H. Shim, R. A. Craig, P. J. Ashman, and G. G. Szego. On the burning of sawdust in a MILD combustion furnace. *Energy & Fuels*, 24(6):3462–3470, May 2010. doi: 10.1021/ef901583k. URL https://doi.org/10.1021/ef901583k. 6

[51] A. C. DeFilippo and J.-Y. Chen. Modeling plasma-assisted methane-air ignition using pre-calculated electron impact reaction rates. *Combust. Flame*, 172:38–48, Oct. 2016. 11, 13, 115, 127, 128

[52] A. T. del Caz, V. Guerra, D. Goncalves, M. L. da Silva, L. Marques, N. Pinhao, C. D. Pintassilgo, and L. L. Alves. The LisbOn KInetics boltzmann solver. *Plasma Sources Sci. T.*, 28(4):043001, Apr. 2019. 85

[53] M. C. Drake, J. W. Ratcliffe, R. J. Blint, C. D. Carter, and N. M. Laurendeau. Measurements and modeling of flamefront no formation and superequilibrium radical concentrations in laminar high-pressure premixed flames. *Symposium (International) on Combustion*, 23(1):387–395, Jan. 1991. doi: 10.1016/s0082-0784(06)80283-3. URL https://doi.org/10.1016/s0082-0784(06)80283-3. 4

[54] J. W. Dreyer, D. Perner, and C. R. Roy. Rate constants for the quenching of $N_2(A_3,v=0,8)$ by CO, CO2, NH3, NO, and O_2. *The Journal of Chemical Physics*, 61(8):3164–3169, Oct. 1974. doi: 10.1063/1.1682472. URL https://doi.org/10.1063/1.1682472. 135

[55] S. Dujko, A. H. Markosyan, R. D. White, and U. Ebert. High-order fluid model for streamer discharges: I. derivation of model and transport data. *Journal of Physics D: Applied Physics*, 46(47):475202, oct 2013. doi: 10.1088/0022-3727/46/47/475202. URL https://doi.org/10.1088/0022-3727/46/47/475202. 26

[56] C. Dumitrache, A. Gallant, N. Minesi, S. Stepanyan, G. D. Stancu, and C. O. Laux. Hydrodynamic regimes induced by nanosecond pulsed discharges in air: mechanism of vorticity generation. *Journal of Physics D: Applied Physics*, 52(36):364001, July 2019. doi: 10.1088/1361-6463/ab28f9. URL https://doi.org/10.1088/1361-6463/ab28f9. 208

[57] D. Dunn-Rankin and P. Therkelsen. *Lean Combustion, Technology and Control, 2nd Edition*. 2016. 4

[58] J. Dutton. A survey of electron swarm data. *Journal of Physical and Chemical Reference Data*, 4(3):577–856, July 1975. doi: 10.1063/1.555525. URL https://doi.org/10.1063/1.555525. 56

[59] Z. Eckert. *Energy Transfer in Non-Equilibrium Reacting Gas Flows: Applications in Plasma Assisted Combustion and Chemical Gas Lasers*. PhD thesis, 2018. The Ohio State University. 116, 117, 127

[60] O. Eichwald, H. Bensaad, O. Ducasse, and M. Yousfi. Effects of numerical and physical anisotropic diffusion on branching phenomena of negative-streamer dynamics. *Journal of Physics D: Applied Physics*, 45(38):385203, Sept. 2012. doi: 10.1088/0022-3727/45/38/385203. URL https://doi.org/10.1088/0022-3727/45/38/385203. 30

[61] L. Esclapez. *Numerical Study of Ignition and Inter-Sector Flame Propagation in Gas Turbine*. PhD thesis, 2015. INP Toulouse. 7, 8

[62] A. Fridman. *Plasma Chemistry*. 2008. 9, 20, 22, 23

[63] G. E. Georghiou, R. Morrow, and A. C. Metaxas. A two-dimensional, finite-element, flux-corrected transport algorithm for the solution of gas discharge problems. *Journal of Physics D: Applied Physics*, 33(19):2453–2466, Sept. 2000. doi: 10.1088/0022-3727/33/19/316. URL https://doi.org/10.1088/0022-3727/33/19/316. 30

[64] L. Y. Gicquel, N. Gourdain, J.-F. Boussuge, H. Deniau, G. Staffelbach, P. Wolf, and T. Poinsot. High performance parallel computing of flows in complex geometries. *Comptes Rendus Mécanique*, 339(2):104 – 124, 2011. ISSN 1631-0721. doi: https://doi.org/10.1016/j.crme.2010.11.006. URL http://www.sciencedirect.com/science/article/pii/S163107211000207X. High Performance Computing. 29

[65] M. F. Golde and B. A. Thrush. Vacuum ultraviolet emission by active nitrogen. i. the formation and removal of $N_2(a_1)$. *Proceedings of the Royal Society of London. A. Mathematical and Physical Sciences*, 330(1580):79–95, Sept. 1972. doi: 10.1098/rspa.1972.0132. URL https://doi.org/10.1098/rspa.1972.0132. 91

[66] D. G. Goodwin, R. L. Speth, H. K. Moffat, and B. W. Weber. Cantera: An object-oriented software toolkit for chemical kinetics, thermodynamics, and transport processes. https://www.cantera.org, 2021. Version 2.5.1. 81

[67] C. Goy, S. James, and S. Rea. *Monitoring combustion instabilities: E. on uk's experience*. Progress in Astronautics and Aeronautics, 2005. 5

[68] M. Grofulović, L. L. Alves, and V. Guerra. Electron-neutral scattering cross sections for CO2: a complete and consistent set and an assessment of dissociation. *Journal of Physics D: Applied Physics*, 49(39):395207, Sept. 2016. doi: 10.1088/0022-3727/49/39/395207. URL https://doi.org/10.1088/0022-3727/49/39/395207. 129

[69] M. Grofulović, T. Silva, B. L. M. Klarenaar, A. S. Morillo-Candas, O. Guaitella, R. Engeln, C. D. Pintassilgo, and V. Guerra. Kinetic study of CO2 plasmas under non-equilibrium conditions. II. input of vibrational energy. *Plasma Sources Science and Technology*, 27(11):115009, Nov. 2018. doi: 10.1088/1361-6595/aadb60. URL https://doi.org/10.1088/1361-6595/aadb60. 129

[70] V. Guerra, A. T. del Caz, C. D. Pintassilgo, and L. L. Alves. Modelling N_2-O_2 plasmas: volume and surface kinetics. *Plasma Sources Sci. T.*, 28(7):073001, jul 2019. 95

[71] G. Hagelaar and G. Kroesen. Speeding up fluid models for gas discharges by implicit treatment of the electron energy source term. *Journal of Computational Physics*, 159(1): 1–12, Mar. 2000. doi: 10.1006/jcph.2000.6445. URL https://doi.org/10.1006/jcph.2000.6445. 48

[72] G. J. M. Hagelaar and L. C. Pitchford. Solving the Boltzmann equation to obtain electron transport coefficients and rate coefficients for fluid models. *Plasma Sources Sci. T.*, 14 (4):722–733, Oct. 2005. 27, 85, 88, 90, 93, 116, 130, 132, 133, 134

[73] G. J. M. Hagelaar, F. J. de Hoog, and G. M. W. Kroesen. Boundary conditions in fluid models of gas discharges. *Physical Review E*, 62(1):1452–1454, July 2000. doi: 10.1103/physreve.62.1452. URL https://doi.org/10.1103/physreve.62.1452. 40

[74] G. Hartmann. Theoretical evaluation of peek's law. *IEEE Transactions on Industry Applications*, IA-20(6):1647–1651, Nov. 1984. doi: 10.1109/tia.1984.4504655. URL https://doi.org/10.1109/tia.1984.4504655. 56

[75] Hayashi. HAYASHI database, www.lxcat.net/Hayashi, retrived on September 14, 2020, 2020. URL www.lxcat.net/Hayashi. 96, 115, 116

[76] M. Hayashi. *Swarm Studies and Inelastic Electron-Molecule Collisions*. Springer, 1985. 132

[77] S. Heijkers, M. Aghaei, and A. Bogaerts. Plasma-based CH_4 conversion into higher hydrocarbons and H_2: Modeling to reveal the reaction mechanisms of different plasma sources. *J. Phys. Chem. C*, 124(13):7016–7030, Mar. 2020. 116, 117

[78] J. T. Herron. Evaluated chemical kinetics data for reactions of N(2 D), N(2 P), and N_2(a3) in the gas phase. *Journal of Physical and Chemical Reference Data*, 28(5):1453–1483, Sept. 1999. doi: 10.1063/1.556043. URL https://doi.org/10.1063/1.556043. 91, 92, 135

[79] J. Heywood. *Internal Combustion Engines Fundamentals. McGraw-Hill, Inc.* 1988. 5

[80] C. Hirsch. *Numerical Computation of Internal and External Flows: The Fundamentals of Computational Fluid Dynamics*. Elsevier, second edition, 2007. 35, 39

[81] J. O. Hirschfelder, C. F. . Curtiss, and R. B. Bird. Molecular theory of gases and liquids. 1954. 82, 180

[82] S. Huang, Y. Wu, K. Zhang, J. Sun, D. Jin, and Y. Li. Experimental investigation on spray and ignition characteristics of plasma actuated bluff body flameholder. *Fuel*, 309: 122215, Feb. 2022. doi: 10.1016/j.fuel.2021.122215. URL https://doi.org/10.1016/j.fuel.2021.122215. 11

[83] W. M. Huo, T. L. Gibson, M. A. P. Lima, and V. McKoy. Schwinger multichannel study of the $^2\Pi_g$ shape resonance in N_2. *Phys. Rev. A*, 36:1632–1641, Aug 1987. 95, 96

[84] Y. Itikawa and N. Mason. Cross sections for electron collisions with water molecules. *Journal of Physical and Chemical Reference Data*, 34(1):1–22, 2005. doi: 10.1063/1.1799251. URL https://doi.org/10.1063/1.1799251. 131, 132

[85] D. J.L., F. C.M., and R. A. *Principles of Laser Plasmas*. Wiley, Ney York, 1976. 124

[86] V. Joncquieres, F. Pechereau, A. Alvarez Laguna, A. Bourdon, O. Vermorel, and B. Cuenot. chapter A 10-moment fluid numerical solver of plasma with sheaths in a Hall Effect Thruster. AIAA Propulsion and Energy Forum. American Institute of Aeronautics and Astronautics, Jul 2018. doi: 10.2514/6.2018-4905. URL https://doi.org/10.2514/6.2018-4905. 0. 29

[87] V. Joncquieres, O. Vermorel, and B. Cuenot. A fluid formalism for low-temperature plasma flows dedicated to space propulsion in an unstructured high performance computing solver. *Plasma Sources Science and Technology*, 29(9):095005, sep 2020. doi: 10.1088/1361-6595/ab62d8. URL https://doi.org/10.1088/1361-6595/ab62d8. 29

[88] Y. Ju and W. Sun. Plasma assisted combustion: Dynamics and chemistry. *Prog. Energ. Combust*, 48:21–83, June 2015. 7, 9, 10, 216

[89] M. Katsuki and T. Hasegawa. The science and technology of combustion in highly preheated air. *Symposium (International) on Combustion*, 27(2):3135–3146, Jan. 1998. doi: 10.1016/s0082-0784(98)80176-8. URL https://doi.org/10.1016/s0082-0784(98)80176-8. 6

[90] G. T. Kim, C. S. Yoo, S. H. Chung, and J. Park. Effects of non-thermal plasma on the lean blowout limits and CO/NOx emissions in swirl-stabilized turbulent lean-premixed flames of methane/air. *Combustion and Flame*, 212:403–414, Feb. 2020. doi: 10.1016/j.combustflame.2019.11.024. URL https://doi.org/10.1016/j.combustflame.2019.11.024. 10, 11, 127

[91] W. Kim and J. Cohen. Plasma-assisted combustor dynamics control at realistic gas turbine conditions. *Combustion Science and Technology*, 193(5):869–888, Oct. 2019. doi: 10.1080/00102202.2019.1676743. URL https://doi.org/10.1080/00102202.2019.1676743. 10, 11

[92] S. Kobayashi, Z. Bonaventura, F. Tholin, N. A. Popov, and A. Bourdon. Study of nanosecond discharges in H_2-air mixtures at atmospheric pressure for plasma assisted combustion applications. *Plasma Sources Sci. T.*, 26(7):075004, June 2017. 13, 148

[93] A. A. Konnov. On the role of excited species in hydrogen combustion. *Combust. Flame*, 162(10):3755–3772, Oct. 2015. 97

[94] I. A. Kossyi, A. Y. Kostinsky, A. A. Matveyev, and V. P. Silakov. Kinetic scheme of the non-equilibrium discharge in nitrogen-oxygen mixtures. *Plasma Sources Sci. T.*, 1(3): 207–220, Aug. 1992. 87, 91, 92, 112

[95] T. Kozák and A. Bogaerts. Splitting of CO_2 by vibrational excitation in non-equilibrium plasmas: a reaction kinetics model. *Plasma Sources Science and Technology*, 23(4): 045004, June 2014. doi: 10.1088/0963-0252/23/4/045004. URL https://doi.org/10.1088/0963-0252/23/4/045004. 128

[96] T. Kozák and A. Bogaerts. Evaluation of the energy efficiency of CO_2 conversion in microwave discharges using a reaction kinetics model. *Plasma Sources Science and Technology*, 24(1):015024, Dec. 2015. doi: 10.1088/0963-0252/24/1/015024. URL https://doi.org/10.1088/0963-0252/24/1/015024. 128

[97] A. Kulikovsky. A more accurate scharfetter-gummel algorithm of electron transport for semiconductor and gas discharge simulation. *Journal of Computational Physics*, 119(1): 149–155, June 1995. doi: 10.1006/jcph.1995.1123. URL https://doi.org/10.1006/jcph.1995.1123. 35, 36, 37, 42

[98] A. A. Kulikovsky. Positive streamer between parallel plate electrodes in atmospheric pressure air. *J. Phys. D Appl. Phys.*, 30(3):441–450, Feb. 1997. 19, 25, 26, 148

[99] A. A. Kulikovsky. The role of photoionization in positive streamer dynamics. *Journal of Physics D: Applied Physics*, 33(12):1514–1524, May 2000. doi: 10.1088/0022-3727/33/12/314. URL https://doi.org/10.1088/0022-3727/33/12/314. 22, 24

[100] M. J. Kushner. Modeling of microdischarge devices: Pyramidal structures. *Journal of Applied Physics*, 95(3):846–859, 2003. doi: 10.1063/1.1636251. URL https://doi.org/10.1063/1.1636251. 26

[101] D. Lacoste, D. Xu, J. Moeck, and C. Laux. Dynamic response of a weakly turbulent lean-premixed flame to nanosecond repetitively pulsed discharges. *Proceedings of the Combustion Institute*, 34(2):3259–3266, Jan. 2013. doi: 10.1016/j.proci.2012.07.017. URL https://doi.org/10.1016/j.proci.2012.07.017. 127

[102] D. A. Lacoste, J. P. Moeck, D. Durox, C. O. Laux, and T. Schuller. Effect of nanosecond repetitively pulsed discharges on the dynamics of a swirl-stabilized lean premixed flame. *Journal of Engineering for Gas Turbines and Power*, 135(10), Aug. 2013. doi: 10.1115/1.4024961. URL https://doi.org/10.1115/1.4024961. 12

[103] D. A. Lacoste, J. P. Moeck, C. O. Paschereit, and C. O. Laux. Effect of plasma discharges on nitric oxide emissions in a premixed flame. *Journal of Propulsion and Power*, 29(3): 748–751, May 2013. doi: 10.2514/1.b34819. URL https://doi.org/10.2514/1.b34819. 10, 11

[104] D. A. Lacoste, B. J. Lee, A. Satija, S. Krishna, S. A. Steinmetz, I. Alkhesho, O. Hazzaa, R. P. Lucht, M. S. Cha, and W. L. Roberts. Investigation of gas heating by nanosecond repetitively pulsed glow discharges used for actuation of a laminar methane-air

flame. *Combustion Science and Technology*, 189(11):2012–2022, May 2017. doi: 10.1080/00102202.2017.1333984. URL https://doi.org/10.1080/00102202.2017.1333984. 11

[105] N. Lamarque. *Schemas numeriques et conditions limites pour la simulation aux grandes echelles de la combustion diphasique dans les foyers d'helicoptere*. PhD thesis, 2007. INP Toulouse. 31, 44

[106] M. L. Lavadera, C. Brackmann, and A. A. Konnov. Experimental and modeling study of laminar burning velocities and nitric oxide formation in premixed ethylene/air flames. *P. Combust. Inst.*, 38(1):395–404, 2021. 96, 97

[107] A. H. Lefebvre and D. R. Ballal. *Gas Turbine Combustion*. CRC Press, Apr. 2010. doi: 10.1201/9781420086058. URL https://doi.org/10.1201/9781420086058. 7

[108] J. K. Lefkowitz and T. Ombrello. An exploration of inter-pulse coupling in nanosecond pulsed high frequency discharge ignition. *Combust. Flame*, 180:136–147, June 2017. 10, 11, 12, 127, 148

[109] J. K. Lefkowitz, S. D. Hammack, C. D. Carter, and T. M. Ombrello. Elevated OH production from NPHFD and its effect on ignition. *Proceedings of the Combustion Institute*, 38(4):6671–6678, 2021. doi: 10.1016/j.proci.2020.09.002. URL https://doi.org/10.1016/j.proci.2020.09.002. 10, 11

[110] C. Li, W. J. M. Brok, U. Ebert, and J. J. A. M. van der Mullen. Deviations from the local field approximation in negative streamer heads. *Journal of Applied Physics*, 101(12):123305, 2007. doi: 10.1063/1.2748673. URL https://doi.org/10.1063/1.2748673. 26

[111] C. Li, U. Ebert, and W. Hundsdorfer. Spatially hybrid computations for streamer discharges with generic features of pulled fronts: I. planar fronts. *Journal of Computational Physics*, 229(1):200–220, Jan. 2010. doi: 10.1016/j.jcp.2009.09.027. URL https://doi.org/10.1016/j.jcp.2009.09.027. 25

[112] Lisbon. IST-LISBON database, www.lxcat.net/IST-Lisbon, retrived on October 19, 2020, 2020. URL www.lxcat.net/IST-Lisbon. 95, 96

[113] D. X. Liu, P. Bruggeman, F. Iza, M. Z. Rong, and M. G. Kong. Global model of low-temperature atmospheric-pressure He + H_2O plasmas. *Plasma Sources Science and Technology*, 19(2):025018, Mar. 2010. doi: 10.1088/0963-0252/19/2/025018. URL https://doi.org/10.1088/0963-0252/19/2/025018. 128, 131, 135

[114] N. Liu. Effects of photoionization on propagation and branching of positive and negative streamers in sprites. *Journal of Geophysical Research*, 109(A4), 2004. doi: 10.1029/2003ja010064. URL https://doi.org/10.1029/2003ja010064. 36

[115] N. Liu. *Dynamics of positive and negative streamers in sprites*. PhD thesis, The Pennsylvania State University, 2006. 22, 30, 64, 74

[116] L. Loeb and J. Meek. The mechanism of spark discharge in air at atmospheric pressure. i. *Journal of Applied Physics, Volume 11, Issue 6, p.438-447*, 1940. doi: 10.1063/1.1712792. 20

[117] L. Loeb and J. M. Meek. The mechanism of spark discharge in air at atmospheric pressure. ii. *Journal of Applied Physics, Volume 11, Issue 7, p.459-474*, 1940. doi: 10.1063/1.1712796. 20

[118] J. Lowke and J. Rees. The drift velocities of free and attached electrons in water vapour. *Australian Journal of Physics*, 16(4):447, 1963. doi: 10.1071/ph630447. URL https://doi.org/10.1071/ph630447. 132

[119] Lu and C. K. Law. Systematic approach to obtain analytic solutions of quasi steady state species in reduced mechanisms. *The Journal of Physical Chemistry A*, 110(49):13202–13208, Nov. 2006. doi: 10.1021/jp064482y. URL https://doi.org/10.1021/jp064482y. 146

[120] A. Luque and U. Ebert. Density models for streamer discharges: Beyond cylindrical symmetry and homogeneous media. *Journal of Computational Physics*, 231(3):904–918, Feb. 2012. doi: 10.1016/j.jcp.2011.04.019. URL https://doi.org/10.1016/j.jcp.2011.04.019. 30

[121] Q. Malé, G. Staffelbach, O. Vermorel, A. Misdariis, F. Ravet, and T. Poinsot. Large eddy simulation of pre-chamber ignition in an internal combustion engine. *Flow, Turbulence and Combustion*, 103(2):465–483, Apr. 2019. doi: 10.1007/s10494-019-00026-y. URL https://doi.org/10.1007/s10494-019-00026-y. 7, 29

[122] R. Maly and M. Vogel. Initiation and propagation of flame fronts in lean CH4-air mixtures by the three modes of the ignition spark. *Symposium (International) on Combustion*, 17 (1):821–831, Jan. 1979. doi: 10.1016/s0082-0784(79)80079-x. URL https://doi.org/10.1016/s0082-0784(79)80079-x. 8

[123] X. Mao and Q. Chen. Effects of vibrational excitation on nanosecond discharge enhanced methane–air ignition. *AIAA Journal*, 56(11):4312–4320, Nov. 2018. 11, 13

[124] W. Marinelli, W. Kessler, B. Green, and W. Blumberg. Quenching of $N_2(a^1\pi_g$, v' = o) by N_2, O_2, CO, CO_2, CH_4, H_2 and Ar. *J. Chem. Physics*, 90:9, 02 1989. 91, 92, 94, 134, 135

[125] A. H. Markosyan, J. Teunissen, S. Dujko, and U. Ebert. Comparing plasma fluid models of different order for 1d streamer ionization fronts. *Plasma Sources Science and Technology*, 24(6):065002, oct 2015. doi: 10.1088/0963-0252/24/6/065002. URL https://doi.org/10.1088/0963-0252/24/6/065002. 26

[126] J. M. Meek. A theory of spark discharge. *Physical Review, Volume 57, Issue 8, p.722-728*, 1940. doi: 10.1103/PhysRev.57.722. URL https://link.aps.org/doi/10.1103/PhysRev.57.722. 20

[127] L. Merotto, M. Balmelli, W. Vera-Tudela, and P. Soltic. Comparison of ignition and early flame propagation in methane/air mixtures using nanosecond repetitively pulsed discharge and inductive ignition in a pre-chamber setup under engine relevant conditions. *Combustion and Flame*, 237:111851, Mar. 2022. doi: 10.1016/j.combustflame.2021.111851. URL https://doi.org/10.1016/j.combustflame.2021.111851. 7

[128] G. J. Micklow, S. Roychoudhury, H. L. Nguyen, and M. C. Cline. Emissions reduction by varying the swirler airflow split in advanced gas turbine combustors. In *Volume 3: Coal, Biomass and Alternative Fuels; Combustion and Fuels; Oil and Gas Applications; Cycle Innovations*. American Society of Mechanical Engineers, 1992. doi: 10.1115/92-gt-110. URL https://doi.org/10.1115/92-gt-110. 6

[129] R. C. Millikan and D. R. White. Systematics of vibrational relaxation. *J. Chem. Physics*, 39(12):3209–3213, 1963. 95, 160, 181

[130] N. Minesi. *Thermal spark formation and plasma-assisted combustion by nanosecond repetitive discharges*. PhD thesis, Université Paris-Saclay, 2020. 11, 136, 208, 214

[131] E. I. Mintoussov, S. J. Pendleton, F. G. Gerbault, N. A. Popov, and S. M. Starikovskaia. Fast gas heating in nitrogen–oxygen discharge plasma: II. Energy exchange in the afterglow of a volume nanosecond discharge at moderate pressures. *J. Phys. D Appl. Phys.*, 44(28):285202, June 2011. ISSN 0022-3727. 94

[132] M. M.J. and P. L.F. *Chemistry of the Atmosphere*. Halsted, New York, 1975. 124

[133] A. Montello, Z. Yin, D. Burnette, I. V. Adamovich, and W. R. Lempert. Picosecond CARS measurements of nitrogen vibrational loading and rotational/translational temperature in non-equilibrium discharges. *J. Phys. D Appl. Phys.*, 46(46):464002, Oct. 2013. 64, 107, 108, 109

[134] Morgan. MORGAN database, www.lxcat.net/Morgan, retrived on October 6, 2020, 2020. URL www.lxcat.net/Morgan. 96

[135] A. S. Morillo-Candas, T. Silva, B. L. M. Klarenaar, M. Grofulović, V. Guerra, and O. Guaitella. Electron impact dissociation of CO2. *Plasma Sources Science and Technology*, 29(1):01LT01, Jan. 2020. doi: 10.1088/1361-6595/ab6075. URL https://doi.org/10.1088/1361-6595/ab6075. 128

[136] R. Morrow and J. J. Lowke. Streamer propagation in air. *J. Phys. D: Appl. Phys*, 30(4): 614–627, Feb. 1997. 19, 27, 50, 66, 67, 156, 180, 191, 192, 193

[137] G. V. Naidis. Modelling of transient plasma discharges in atmospheric-pressure methane-air mixtures. *J. Phys. D Appl. Phys.*, 40(15):4525–4531, July 2007. 148

[138] J. C. Nedelec. Mixed finite elements in ?3. *Numerische Mathematik*, 35(3):315–341, Sept. 1980. doi: 10.1007/bf01396415. URL https://doi.org/10.1007/bf01396415. 37

[139] K. F. Ness and R. E. Robson. Transport properties of electrons in water vapor. *Physical Review A*, 38(3):1446–1456, Aug. 1988. doi: 10.1103/physreva.38.1446. URL https://doi.org/10.1103/physreva.38.1446. 132

[140] S. Nijdam, G. Wormeester, E. M. van Veldhuizen, and U. Ebert. Probing background ionization: positive streamers with varying pulse repetition rate and with a radioactive admixture. *Journal of Physics D: Applied Physics*, 44(45):455201, 2011. doi: 10.1088/0022-3727/44/45/455201. URL https://doi.org/10.1088/0022-3727/44/45/455201. 50, 190

[141] D. Z. Pai, G. D. Stancu, D. A. Lacoste, and C. O. Laux. Nanosecond repetitively pulsed discharges in air at atmospheric pressure - the glow regime. *Plasma Sources Sci. T.*, 18 (4):045030, Oct. 2009. 19

[142] D. Z. Pai, D. A. Lacoste, and C. O. Laux. Nanosecond repetitively pulsed discharges in air at atmospheric pressure - the spark regime. *Plasma Sources Sci. T.*, 19(6):065015, Nov. 2010. 64, 148, 189

[143] S. Pancheshnyi. Role of electronegative gas admixtures in streamer start, propagation and branching phenomena. *Plasma Sources Science and Technology*, 14(4):645–653, aug 2005. doi: 10.1088/0963-0252/14/4/002. URL https://doi.org/10.1088/0963-0252/14/4/002. 25, 26

[144] E. Pannier, T. Yong, M. Cappelli, and C. Laux. Efficiency of CO_2 dissociation in high pressure nanosecond repetitively pulsed (nrp) discharge. 07 2016. 129

[145] P. Pepiot. *Automatic strategies to model transportation fuel surrogates*. PhD thesis, Stanford University, 2008. 145

[146] P. Pepiot-Desjardins and H. Pitsch. An efficient error-propagation-based reduction method for large chemical kinetic mechanisms. *Combustion and Flame*, 154(1-2):67–81, July 2008. doi: 10.1016/j.combustflame.2007.10.020. URL https://doi.org/10.1016/j.combustflame.2007.10.020. 146

[147] P. Pepiot-Desjardins and H. Pitsch. An automatic chemical lumping method for the reduction of large chemical kinetic mechanisms. *Combustion Theory and Modelling*, 12 (6):1089–1108, Nov. 2008. doi: 10.1080/13647830802245177. URL https://doi.org/10.1080/13647830802245177. 146

[148] Phelps. PHELPS database, www.lxcat.net/Phelps, retrived on July 30, 2020, 2020. URL www.lxcat.net/Phelps. 88, 89, 90, 95, 96, 124, 129, 131

[149] T. X. Phuoc and F. P. White. An optical and spectroscopic study of laser-induced sparks to determine available ignition energy. *Proceedings of the Combustion Institute*, 29(2): 1621–1628, Jan. 2002. doi: 10.1016/s1540-7489(02)80199-7. URL https://doi.org/10.1016/s1540-7489(02)80199-7. 8

[150] G. Pilla, D. Galley, D. A. Lacoste, F. Lacas, D. Veynante, and C. O. Laux. Stabilization of a turbulent premixed flame using a nanosecond repetitively pulsed plasma. *IEEE Transactions on Plasma Science*, 34(6):2471–2477, Dec. 2006. doi: 10.1109/tps.2006.886081. URL https://doi.org/10.1109/tps.2006.886081. 127

[151] L. G. Piper. Quenching rate coefficients for N_2(a'1). *J. Chem. Physics*, 87(3):1625–1629, Aug. 1987. 91, 94, 135

[152] L. G. Piper. Energy transfer studies on N_2(x, v) and N_2(b). *The Journal of Chemical Physics*, 97(1):270–275, July 1992. doi: 10.1063/1.463625. URL https://doi.org/10.1063/1.463625. 92, 135

[153] S. Pischinger and J. B. Heywood. A model for flame kernel development in a spark-ignition engine. *Symposium (International) on Combustion*, 23(1):1033–1040, Jan. 1991.

doi: 10.1016/s0082-0784(06)80361-9. URL https://doi.org/10.1016/s0082-0784(06)80361-9. 17

[154] T. Poinsot and S. Lele. Boundary conditions for direct simulations of compressible viscous flows. *J. Comput. Phys*, 101(1):104 – 129, 1992. 188, 215

[155] T. Poinsot and D. Veynante. *Theoretical and Numerical Combustion*. R.T. Edwards Inc., 2005. 180

[156] L. Polak and D. Slovetsky. Electron impact induced electronic excitation and molecular dissociation. *International Journal for Radiation Physics and Chemistry*, 8(1-2):257–282, Jan. 1976. doi: 10.1016/0020-7055(76)90070-x. URL https://doi.org/10.1016/0020-7055(76)90070-x. 129, 131

[157] N. Popov. Fast gas heating in a nitrogen–oxygen discharge plasma: I. kinetic mechanism. *J. Phys. D Appl. Phys., Volume 44, Issue 28*, 2011. 11, 90, 91, 92, 93, 94, 96, 97, 134

[158] N. Popov. Fast gas heating initiated by pulsed nanosecond discharge in atmospheric pressure air. 01 2013. ISBN 978-1-62410-181-6. 11, 13, 100, 101, 102, 104, 105, 106, 107, 161, 162, 163, 181, 188, 190, 197

[159] N. A. Popov. Investigation of the mechanism for rapid heating of nitrogen and air in gas discharges. *Plasma Phys. Rep.*, 27(10):886–896, Oct. 2001. 11, 90, 91, 93, 94

[160] N. A. Popov. Pulsed nanosecond discharge in air at high specific deposited energy: fast gas heating and active particle production. *Plasma Sources Sci. T.*, 25(4):044003, May 2016. 11, 13, 90, 91, 101, 105, 163, 194

[161] A. A. Quader. What limits lean operation in spark ignition engines: flame initiation or propagation. 1 1976. URL https://www.osti.gov/biblio/6718804. 7

[162] Y. Raizer. *Gas Discharge Physics*. 1991. 20

[163] J. Rax. *Physique des Plasma*. Dunod, 2005. 26

[164] M. D. Renzo, J. Urzay, P. D. Palma, M. D. de Tullio, and G. Pascazio. The effects of incident electric fields on counterflow diffusion flames. *Combustion and Flame*, 193: 177–191, July 2018. doi: 10.1016/j.combustflame.2018.03.001. URL https://doi.org/10.1016/j.combustflame.2018.03.001. 8

[165] K. R.J., C. M.E., G. P., and Z. H. *Chemically Reacting Flow: Theory, Modeling, and Simulation*. Wiley, 2017. 81, 82, 83

[166] D. Rusterholtz. *Nanosecond Repetitively Pulsed Discharges in Atmospheric Pressure Air*. PhD thesis, 2012. Ecole centrale de Paris. 100, 203

[167] D. Rusterholtz, D. Lacoste, G. Stancu, D. Pai, and C. Laux. Ultrafast heating and oxygen dissociation in atmospheric pressure air by nanosecond repetitively pulsed discharges. *J. Phys. D Appl. Phys.*, 46:4010–, 11 2013. 18, 49, 64, 91, 92, 100, 101, 102, 104, 105, 106, 107, 128, 137, 148, 150, 151, 152, 161, 162, 163, 187, 188, 189, 192, 194, 195, 196, 198, 199, 201, 203, 204, 209, 210, 222

[168] H. Ryzko. Drift velocity of electrons and ions in dry and humid air and in water vapour. *Proceedings of the Physical Society*, 85(6):1283–1295, June 1965. doi: 10.1088/0370-1328/85/6/327. URL https://doi.org/10.1088/0370-1328/85/6/327. 132

[169] F. D. Sabatino and D. A. Lacoste. Enhancement of the lean stability and blow-off limits of methane-air swirl flames at elevated pressures by nanosecond repetitively pulsed discharges. *Journal of Physics D: Applied Physics*, 53(35):355201, June 2020. doi: 10.1088/1361-6463/ab8f54. URL https://doi.org/10.1088/1361-6463/ab8f54. 11, 18, 127

[170] D. Scharfetter and H. Gummel. Large-signal analysis of a silicon read diode oscillator. *IEEE Transactions on Electron Devices*, 16(1):64–77, Jan. 1969. doi: 10.1109/t-ed.1969.16566. URL https://doi.org/10.1109/t-ed.1969.16566. 35, 36

[171] T. Schonfeld and M. Rudgyard. Steady and unsteady flow simulations using the hybrid flow solver AVBP. *AIAA Journal*, 37(11):1378–1385, 1999. doi: 10.2514/2.636. URL https://doi.org/10.2514/2.636. 29

[172] A. Sharma, V. Subramaniam, E. Solmaz, and L. L. Raja. Coupled computational studies of non-thermal plasma based combustion ignition. In *AIAA Scitech 2019 Forum*. American Institute of Aeronautics and Astronautics, Jan. 2019. doi: 10.2514/6.2019-0746. URL https://doi.org/10.2514/6.2019-0746. 11, 13, 30, 36

[173] S. Shcherbanev, T. Moriniere, R. Solana-Perez, M. Weilenmann, Y. Xiong, U. Doll, and N. Noiray. Anchoring of premixed jet flames in vitiated crossflow with pulsed nanosecond spark discharge. *Applications in Energy and Combustion Science*, 1-4:100010, Dec. 2020. doi: 10.1016/j.jaecs.2020.100010. URL https://doi.org/10.1016/j.jaecs.2020.100010. 10, 11, 12

[174] A. Shioyoke, J. Hayashi, R. Murai, N. Nakatsuka, and F. Akamatsu. Numerical investigation on effects of nonequilibrium plasma on laminar burning velocity of ammonia flame. *Energy & Fuels*, 32(3):3824–3832, Feb. 2018. doi: 10.1021/acs.energyfuels.7b02733. URL https://doi.org/10.1021/acs.energyfuels.7b02733. 10

[175] I. Shkurenkov, D. Burnette, W. R. Lempert, and I. V. Adamovich. Kinetics of excited states and radicals in a nanosecond pulse discharge and afterglow in nitrogen and air. *Plasma Sources Sci. T.*, 23(6):065003, Aug. 2014. 101, 105, 109, 110, 111, 112

[176] H. Sitaraman and R. Grout. Premixed combustion simulations with a self-consistent plasma model for initiation. In *54th AIAA Aerospace Sciences Meeting*. American Institute of Aeronautics and Astronautics, Jan. 2016. doi: 10.2514/6.2016-2158. URL https://doi.org/10.2514/6.2016-2158. 12, 13

[177] G. P. Smith, D. M. Golden, M. Frenklach, N. W. Moriarty, B. Eiteneer, M. Goldenberg, C. T. Bowman, R. K. Hanson, S. Song, W. C. Gardiner, J. V. V. Lissianski, and Z. Qin, 2020. URL http://www.me.berkeley.edu/gri_mech/. 96, 119

[178] S. Starikovskaia, E. Kukaev, A. Kuksin, M. Nudnova, and A. Starikovskii. Analysis of the spatial uniformity of the combustion of a gaseous mixture initiated by a nanosecond discharge. *Combust. Flame*, 139(3):177–187, Nov. 2004. 10, 11, 96, 121, 124, 127, 150

[179] A. Starikovskiy and N. Aleksandrov. Plasma-assisted ignition and combustion. *Progress in Energy and Combustion Science*, 39(1):61 – 110, 2013. ISSN 0360-1285. 89, 95

[180] W. Sun, X. Gao, B. Wu, and T. Ombrello. The effect of ozone addition on combustion: Kinetics and dynamics. *Progress in Energy and Combustion Science*, 73:1–25, July 2019. doi: 10.1016/j.pecs.2019.02.002. URL https://doi.org/10.1016/j.pecs.2019.02.002. 119

[181] P. K. Sweby. High resolution schemes using flux limiters for hyperbolic conservation laws. *SIAM Journal on Numerical Analysis*, 21(5):995–1011, Oct. 1984. doi: 10.1137/0721062. URL https://doi.org/10.1137/0721062. 39

[182] J. Teunissen and U. Ebert. Simulating streamer discharges in 3d with the parallel adaptive afivo framework. *Journal of Physics D: Applied Physics*, 50(47):474001, Oct. 2017. doi: 10.1088/1361-6463/aa8faf. URL https://doi.org/10.1088/1361-6463/aa8faf. 25, 30

[183] J. Teunissen, A. Sun, and U. Ebert. A time scale for electrical screening in pulsed gas discharges. *Journal of Physics D: Applied Physics*, 47(36):365203, Aug. 2014. doi: 10.1088/0022-3727/47/36/365203. URL https://doi.org/10.1088/0022-3727/47/36/365203. 48

[184] F. Tholin. *Numerical simulation of nanosecond repetitively pulsed discharges in air at atmospheric pressure : Application to plasma-assisted combustion*. PhD thesis, 2012. Ecole centrale de Paris. 19, 22, 23, 25, 26, 30, 36, 40, 48, 49, 50, 66, 190, 211, 213, 215

[185] F. Tholin, D. A. Lacoste, and A. Bourdon. Influence of fast-heating processes and o atom production by a nanosecond spark discharge on the ignition of a lean –air premixed flame. *Combustion and Flame*, 161(5):1235–1246, May 2014. doi: 10.1016/j.combustflame.2013.11.007. URL https://doi.org/10.1016/j.combustflame.2013.11.007. 11, 13

[186] A. C. Tibère-Inglesse, S. D. McGuire, and C. O. Laux. Inferring the gas temperature from the rotational temperatures of $N_2(B)$ and $N_2(C)$. *To be submitted*, 2021. 100, 102

[187] J. Townsend. *The theory of ionization of gases by collision*. 1910. 20

[188] Triniti. TRINITI database, www.lxcat.net/TRINITI, retrived on September 14, 2020, 2020. URL www.lxcat.net/TRINITI. 96, 132

[189] J. C. Tully. Reactions of $O(^1D)$ with atmospheric molecules. *J. Chem. Physics*, 62(5): 1893–1898, Mar. 1975. 135

[190] M. Uddi. *Non-equilibrium kinetic studies of repetitively pulsed nanosecond discharge plasma assisted combustion*. PhD thesis, 2008. The Ohio State University. 116, 127

[191] M. Uddi, N. Jiang, E. Mintusov, I. Adamovich, and W. Lempert. Atomic oxygen measurements in air and air/fuel nanosecond pulse discharges by two photon laser induced flourescence. In *46th AIAA Aerospace Sciences Meeting and Exhibit*. American Institute of Aeronautics and Astronautics, Jan. 2008. 18, 117, 118, 119, 150, 151

[192] J. van Dijk, K. Peerenboom, M. Jimenez, D. Mihailova, and J. van der Mullen. The plasma modelling toolkit plasimo. *Journal of Physics D: Applied Physics*, 42(19):194012, Sept. 2009. doi: 10.1088/0022-3727/42/19/194012. URL https://doi.org/10.1088/0022-3727/42/19/194012. 30

[193] J. E. Velazco, J. H. Kolts, and D. W. Setser. Quenching rate constants for metastable argon, krypton, and xenon atoms by fluorine containing molecules and branching ratios for XeF and KrF formation. *The Journal of Chemical Physics*, 65(9):3468–3480, Nov. 1976. doi: 10.1063/1.433573. URL https://doi.org/10.1063/1.433573. 124

[194] C. Verheyen, T. Silva, V. Guerra, and A. Bogaerts. The effect of H_2O on the vibrational populations of CO_2 in a CO_2/H_2O microwave plasma: a kinetic modelling investigation. *Plasma Sources Science and Technology*, 29(9):095009, Sept. 2020. doi: 10.1088/1361-6595/aba1c8. URL https://doi.org/10.1088/1361-6595/aba1c8. 131

[195] W. Wang, R. Snoeckx, X. Zhang, M. S. Cha, and A. Bogaerts. Modeling plasma-based CO_2 and CH_4 conversion in mixtures with N_2, O_2, and H_2O: The bigger plasma chemistry picture. *The Journal of Physical Chemistry C*, 122(16):8704–8723, Jan. 2018. doi: 10.1021/acs.jpcc.7b10619. URL https://doi.org/10.1021/acs.jpcc.7b10619. 128, 131, 134, 135

[196] J. F. Wilson, F. J. Davis, D. R. Nelson, R. N. Compton, and O. H. Crawford. Electron transport and ion clustering reactions in water vapor and deuterated water vapor. *The Journal of Chemical Physics*, 62(10):4204–4212, 1975. doi: 10.1063/1.430302. URL https://doi.org/10.1063/1.430302. 132

[197] C. Winters, Z. Eckert, Z. Yin, K. Frederickson, and I. V. Adamovich. Measurements and kinetic modeling of atomic species in fuel-oxidizer mixtures excited by a repetitive nanosecond pulse discharge. *J. Phys. D Appl. Phys.*, 51(1):015202, Dec. 2017. 100

[198] S. Yang, S. Nagaraja, W. Sun, and V. Yang. Multiscale modeling and general theory of non-equilibrium plasma-assisted ignition and combustion. *J. Phys. D Appl. Phys.*, 50 (43):433001, Sept. 2017. 11, 13

[199] M. Yousfi and M. D. Benabdessadok. Boltzmann equation analysis of electron-molecule collision cross sections in water vapor and ammonia. *Journal of Applied Physics*, 80 (12):6619–6630, Dec. 1996. doi: 10.1063/1.363785. URL https://doi.org/10.1063/1.363785. 132

[200] M. Zakari. *Modélisation Volumes-Finis en maillages non-structurés de décharges électriques à la pression atmosphérique.* Ph.d. thesis, Institut National Polytechnique de Toulouse - INPT, Dec. 2013. URL https://tel.archives-ouvertes.fr/tel-00940096. 30, 48

[201] S. Zare, H. W. Lo, S. Roy, and O. Askari. On the low-temperature plasma discharge in methane/air diffusion flames. *Energy*, 197:117185, Apr. 2020. doi: 10.1016/j.energy.2020.117185. URL https://doi.org/10.1016/j.energy.2020.117185. 10, 11

[202] M. B. Zhelezniak, A. K. Mnatsakanian, and S. V. Sizykh. Photoionization of nitrogen and oxygen mixtures by radiation from a gas discharge. *Teplofizika Vysokikh Temperatur*, 20:423–428, Nov. 1982. 24